Interface Electronic State Characterization of

Plasma Enhanced Atomic Layer Deposited Dielectrics on GaN

by

Jialing Yang

A Dissertation Presented in Partial Fulfillment
of the Requirements for the Degree
Doctor of Philosophy

Approved April 2014 by the
Graduate Supervisory Committee:

Robert Nemanich, Chair
Tingyong Chen
Xihong Peng
Fernando Ponce
David Smith

ARIZONA STATE UNIVERSITY

May 2014

ABSTRACT

In this dissertation, the interface chemistry and electronic structure of plasma-enhanced atomic layer deposited (PEALD) dielectrics on GaN are investigated with x-ray and ultraviolet photoemission spectroscopy (XPS and UPS). Three interrelated issues are discussed in this study: (1) PEALD dielectric growth process optimization, (2) interface electronic structure of comparative PEALD dielectrics on GaN, and (3) interface electronic structure of PEALD dielectrics on Ga- and N-face GaN. The first study involved an in-depth case study of PEALD Al_2O_3 growth using dimethylaluminum isopropoxide, with a special focus on oxygen plasma effects. Saturated and self-limiting growth of Al_2O_3 films were obtained with an enhanced growth rate within the PEALD temperature window (25-220 ℃). The properties of Al_2O_3 deposited at various temperatures were characterized to better understand the relation between the growth parameters and film properties. In the second study, the interface electronic structures of PEALD dielectrics on Ga-face GaN films were measured. Five promising dielectrics (Al_2O_3, HfO_2, SiO_2, La_2O_3, and ZnO) with a range of band gap energies were chosen. Prior to dielectric growth, a combined wet chemical and *in-situ* H_2/N_2 plasma clean process was employed to remove the carbon contamination and prepare the surface for dielectric deposition. The surface band bending and band offsets were measured by XPS and UPS for dielectrics on GaN. The trends of the experimental band offsets on GaN were related to the dielectric band gap energies. In addition, the experimental band offsets were near the calculated values based on the charge neutrality level model. The third study focused on the effect of the polarization bound charge of the Ga- and N-face

GaN on interface electronic structures. A surface pretreatment process consisting of a NH_4OH wet chemical and an *in-situ* NH_3 plasma treatment was applied to remove carbon contamination, retain monolayer oxygen coverage, and potentially passivate N-vacancy related defects. The surface band bending and polarization charge compensation of Ga- and N-face GaN were investigated. The surface band bending and band offsets were determined for Al_2O_3, HfO_2, and SiO_2 on Ga- and N-face GaN. Different dielectric thicknesses and post deposition processing were investigated to understand process related defect formation and/or reduction.

DEDICATION

To my wife and the whole family

ACKNOWLEDGMENTS

First of all, I would like to express my appreciation to my supervisor, Professor Robert Nemanich, for his continued support and encouragement during my study and for the opportunity to work in his research team. I would also like to thank Professor Robert Nemanich for his guidance and enthusiasm in these years, which always inspires me and will benefit me for my whole life.

In addition, I also appreciate the helps and suggestions from the rest of the committee members: Dr. Tingyong Chen, Dr. Xihong Peng, Dr. Fernando Ponce, and Dr. David Smith. I could not finish the dissertation without their helps.

I would like to thank all the group members at the Nanoscience Laboratory. I want to give my special thanks to Dr. Chiyu Zhu and Franz Koeck, who gave me valuable suggestions on my research and taught me the knowledge about the vacuum technique and equipment maintenance. I also want to thank Dr. Fu Tang, who built up the PEALD system and helped me to solve the related problems. In addition, I appreciate the helps from Dr. Xin Liu and Dr. Tianyin Sun, who trained me for the use of lab equipment and provided insight of the problems I met. I also want to thank Brianna Eller, who helped me with the experiment, problem solving, and paper writing. I would like to extend my appreciation to the rest of the previous and present group members, including Dr. Yang Sun, Dr. Anna Zaniewski, Manpuneet Kaur, Xingye Wang, Chris England, Joseph Shammas, and Sean Caudle, who helped me with the questions I got.

I would like to thank the staff working in the Department of Physics: Araceli Vizcarra, Ebony Shalley, Rose Murrietta, Ixchell Paape, Jane Laux, and Deborah Denson, who helped me to solve many problems during the five years study at ASU. I also appreciate the help from Dr. Emmanuel Soignard for x-ray reflectivity measurement, Dr. Barry Wilkens for Rutherford backscattering spectroscopy measurement, and Dr. Diana Convey for spectroscopic ellipsometry measurement at LeRoy Eyring Center for Solid State Science.

This research is supported by the Office of Naval Research through the DEFINE MURI program, N00014-10-1-0937. I would like to appreciate the opportunity to participate this program and I want to thank all the people working under this research project, especially Dr. Xiang Liu and Dr. Umesh Mishra from University of California, Santa Barbara, Dr. Rathnait Long from Stanford University, Dr. Siddharth Rajan from Ohio State University, and Jie Yang and Dr. Tso-Ping Ma from Yale University, who helped me with the problem solving, sample supply, and device characterization.

Finally, I would like thank my parents and parents in law, other family members, and all the friends for their love and support all these years. I am grateful for my mother and grandmother, who gave me life, brought me up, and taught me how to be a right person. Furthermore, I want to give my special thanks to my wife, who accompanies me to overcome all the difficult time in the past five years and will give birth to my baby girl soon.

TABLE OF CONTENTS

Page

CHAPTER Page

CHAPTER Page

LIST OF TABLES

Table Page

LIST OF FIGURES

Figure Page

Figure Page

Figure Page

Figure Page

Figure Page

Figure Page

CHAPTER 1

INTRODUCTION

1.1 Background

GaN based electronic structures are attractive for next generation power devices due to their excellent material properties, including large band gap, high breakdown field, and high saturation velocity [1,2,3]. However, device performance is plagued by a large concentration of defect states, which leads to a high leakage current and significant current collapse. The leakage current could be reduced by applying an appropriate dielectric layer under the gate to create an additional barrier layer for electron tunneling. The potential barrier of dielectrics on GaN should be greater than 1 V to effectively decrease the leakage current [4]. Therefore, the band alignment of dielectrics on GaN will play a significant role in determining the confinement properties of carriers in the semiconductor and ultimately the device performance. On the other hand, the current collapse phenomena could be mitigated with a suitable dielectric passivation layer between the gate and drain to limit charge transfer to/from the surface states [1]. Therefore, high quality dielectric growth is crucial for development of GaN electronics [1,2]. Plasma-enhanced atomic layer deposition (PEALD), as a robust and highly manufacturable method, can enable uniform and conformal growth with atomic scale thickness control compared with other deposition methods, such as sputtering or chemical vapor deposition [5]. Therefore, understanding the PEALD growth mechanisms and developing the dielectric deposition process is crucial to obtain dielectric films with reduced impurity and defect densities. In addition, the interface properties of dielectrics

on GaN are of great importance for determining the semiconductor carrier confinement properties and ultimately improving the device performance.

Prior to dielectric growth, the surface preparation process will have significant effect on improving device performance [2]. Although surface preparation processes for metal/GaN Schottky contacts have been investigated for years, the requirements may be quite different from dielectric/GaN applications [2]. For instance, plasma or ion sputtering could introduce point defects such as donor-like N vacancies, which would shift the Fermi level towards the conduction band minimum and subsequently improve the ohmic contact properties [6]. In addition, some wet chemical residuals (e.g., S, Cl) may improve adhesion of the metal layer to GaN [2]. While these defects or species may improve the performance of metal/GaN Schottky contacts, they may degrade the dielectric/GaN interface through introducing electronic active defects. Therefore, a detailed study of the surface chemistry and electronic structure of GaN is needed to understand the development of surface states. Furthermore, post deposition processes may also reduce interface and dielectric defects, which will have a profound effect on reducing leakage current and current collapse.

On the other hand, GaN has a strong spontaneous polarization, which generates a large polarization bound charge (~2.1 x10^{13} charges/cm^2) [7] and further complicates the interface electronic structure. In fact, the role of the polarization bound charge and its effect on interface states and band offsets is a major theme of this dissertation. The compensating charges and states are at least partially responsible for the device failure mechanisms. The location and concentration of the charges and defects and how they can be altered by the different processing will be reflected in the compensation mechanism

and the surface band bending. The study of polarization charge effects on the GaN surface electronic structure and the dielectric/GaN interface electronic structure during different processing is anticipated to be critical to improving device performance.

In this study, different surface preparation processes, PEALD dielectric growth processes, and post deposition processes are developed to investigate their effect on the charge compensation mechanisms and the interface electronic states. A major advantage of this research is the use of an integrated ultra high vacuum system that combines the surface preparation and PEALD systems with chambers for photoemission spectroscopy to characterize the electronic states.

1.2 Thesis approach

In chapter 2, a review of nitride semiconductor properties and interface phenomena is introduced to better understand the surface and/or interface electronic properties of GaN. The topics include: GaN based electronic device structures, GaN crystal structure and polarization, device failure mechanisms, processing effects, and interface band alignment theory.

In chapter 3, basic information about the instrumentation is introduced, including the remote plasma surface preparation system, the remote PEALD system, and the ultraviolet and x-ray photoemission spectroscopy (UPS and XPS) systems. In addition, the method used to determine the band alignment of dielectrics on GaN is presented.

In chapter 4, a detailed case study of PEALD Al_2O_3 growth using a non-pyrophoric precursor, dimethylaluminum isopropoxide (DMAI), is reported with a specific focus on the oxygen plasma effects. Saturated and self-limiting growth of Al_2O_3

films with an enhanced growth rate of ~1.5Å/cycle within a temperature window of 25-220 ℃ is achieved. The higher growth rate of PEALD than that reported for thermal ALD is related to the higher reactivity of the oxygen plasma species compared with H_2O and the adsorption of active oxygen species residual from the plasma exposure. In addition, room temperature Al_2O_3 film growth with low carbon impurities is obtained by including an extended oxygen plasma pulse in the growth cycle. The properties of Al_2O_3 films are measured to achieve a better understanding of the relation of the growth parameters and film properties and to enable tuning of film properties to meet requirements of different applications.

In chapter 5, a comprehensive comparison of five PEALD dielectrics on n-type, Ga-face GaN is reported to investigate the dielectric confinement properties on GaN. These dielectrics have different properties on GaN, including large band gap, high dielectric constant, good chemical and thermal properties, or low interface state density on GaN. The large diversity in the band gap of the investigated dielectrics (3.4 - 8.9 eV) enables a better understanding of the relation between the interface band alignment of dielectric/GaN and the dielectric band gap. The study addresses different cleaning processes to obtain well characterized surfaces and understand polarization charge compensation mechanism. After dielectric deposition, the chemical and electronic properties of the dielectric/GaN interfaces are studied. The trends of the valence and conduction band potential barrier of dielectrics on GaN are related to the band gap of dielectrics. In addition, the effect of post deposition processes on polarization charge compensation and interface bonding and states are also investigated. Plasma-induced defects were also observed for the different dielectrics, which could be removed by

annealing. The experimental band offset results are compared with theoretical results based on EA and CNL model.

In chapter 6, n-type, Ga- and N-face GaN are studied to further investigate the charge compensation mechanism and the effect of polarization charge on interface properties. The surface band bending of both Ga- and N-face GaN is measured, and the polarization compensation mechanism is discussed. In addition, the chemical and electronic properties of three dielectrics (Al_2O_3, HfO_2, and SiO_2) with relatively large potential barriers and good chemical stability on GaN are investigated. Similar band offset results are obtained for dielectrics on both Ga-face and N-face GaN, regardless of dielectric thickness and processing conditions. The experimental band offset results are close to the theoretical calculation based on the CNL model. The results indicate that surface states compensate the polarization charge and mitigate the effect of polarization charge on band offset.

In chapter 7, the most significant results of this dissertation are summarized and future work based on current studies is also proposed.

The studies of this dissertation add together to provide a more complete understanding of the effects of polarization charge on the dielectric/GaN interfaces and the surface process involved in PEALD dielectric growth.

Reference

[1] R. D. Long and P. C. McIntyre, *Materials* **5**, 1297 (2012).

[2] B. S. Eller, J. Yang, and R. J. Nemanich, *J. Vac. Sci. Technol. A* **31** 050807 (2013).

[3] U. K. Mishra, P. Parikh, and Y. F. Wu, *Proc. IEEE* **90**, 1022 (2002).

[4] J. Robertson, *J. Vac. Sci. Technol. B* **18**, 1785 (2000).

[5] H. B. Profijt, S. E. Potts, M. C. M. van de Sanden, and W. M. M. Kessels, *J. Vac. Sci. Technol. A* **29**, 050801 (2011).

[6] H. W. Jang, C. M. Jeon, J. K. Kim, and J. L. Lee, *Appl. Phys. Lett*. **78**, 2015 (2001).

[7] A. Zoroddu, F. Bernardini, P. Ruggerone, and V. Fiorentini, *Phys. Rev. B* **64**, 045208 (2001).

CHAPTER 2

NITRIDE SEMICONDUCTOR PROPERTIES AND DEVICES

2.1 GaN based electronic devices

GaN is a wide band gap (~3.4 eV) semiconductor with high breakdown field (~3 MV/cm) and high saturation velocity (~10^7 cm/s), which is suitable for high frequency, high power, and high temperature electronic applications [1,2,3]. The major physical properties of GaN and its competing opponents as power electronics are listed in Table 2.1 [4]. The subsequent advantages of GaN power devices are listed in Table 2.2 [4]. The first column is the required performance for power devices; the second column shows the enabling features of GaN related to the required performance; and the third column summarizes the technology advantages. The high power/unit width allows smaller devices, which have higher impedance and are easier to fabricate. The high breakdown field feature enables high voltage operation, which reduces the demands for voltage conversion and improves the efficiency by lowering power requirements and simplifying cooling [4]. In addition, as a direct band gap material, GaN has been widely used in light emitting diode electronics [5], which can help reduce the development cost of power devices due to the potential overlap of the technologies.

Table 2.1. The major material properties of Si, GaAs, SiC, and GaN, where μ is the electron mobility, ε is the dielectric constant, E_g is the band gap energy, BFOM ratio is the Baliga figure of merit (related to material parameters to minimize the conduction loss in low-frequency unipolar transistors), JEM ratio is the Johnson figure of merit (related to the product of power and frequency for a low voltage transistor), and Tmax is the maximum temperature before the degradation of the semiconductor [4]. U. K. Mishra, et. al., *Proc. IEEE* **90**, 1022 (2002). Copyright © 2002, IEEE.

	μ (cm^2/V s)	**ε**	**E_g** (eV)	**BFOM Ratio**	**JEM Ratio**	**T_{max}** (℃)
Si	1300	11.4	1.1	1.0	1.0	300
GaAs	5000	13.1	1.4	9.6	3.5	300
SiC	260	9.7	2.9	3.1	60	600
GaN	1500	9.5	3.4	24.6	80	700

Table 2.2. Competitive advantages of GaN based power devices, where the most important benefits are highlighted in the table [4]. U. K. Mishra, et. al., *Proc. IEEE* **90**, 1022 (2002). Copyright © 2002, IEEE.

Need	**Enabling Feature**	**Performance Advantage**
High Power/Unit Width	wide band gap, high field	compact, ease of matching
High Voltage Operation	high breakdown field	eliminate/reduce step down
High Linearity	HEMT technology	optimum band allocation
High Frequency	high electron velocity	bandwidth μ-wave/mm-wave
High Efficiency	high operating voltage	power saving, reduced cooling
Low Noise	high gain, high velocity	high dynamic range receivers
High Temperature Operation	wide band gap	rugged, reliable, reduced cooling needs
Thermal Management	SiC substrate	high power devices with reduced cooling needs
Technology Leverage	direct band gap, enabler for lighting	driving force for technology low cost

There are two promising GaN-based power device structures which have been extensively studied, including AlGaN/GaN heterostructure high electron mobility transistors (HEMTs) and metal insulator/oxide semiconductor field effect transistors (MISFETs or MOSFETs) [2]. Fig. 2.1 shows schematics of these two devices. For AlGaN/GaN HEMTs, there is a two-dimensional electron gas (2DEG) at the AlGaN and GaN interface, which enhances the electron mobility. However, the intrinsic normally-on status of AlGaN/GaN HEMTs increases the power consumption. The normally-on condition is also not suitable for power switching applications that require fail-safe operation [6]. On the other hand, the GaN MOSFETs (or MISFETs) could be operated at normally-off condition but it does not have the enhanced electron mobility of AlGaN/GaN HEMT devices. In addition to the intrinsic properties of the different devices, the properties of GaN and the dielectric (oxide) layer could affect the device performance significantly, which requires better understanding.

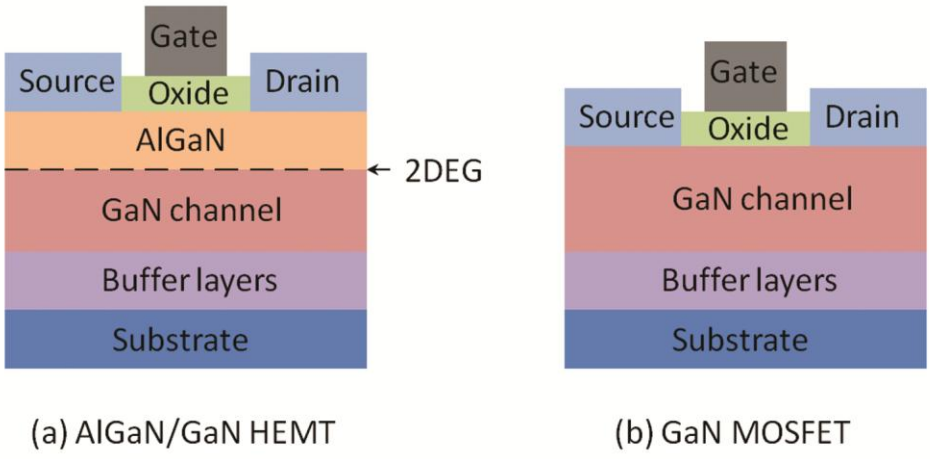

Figure 2.1. A schematic illustration of (a) AlGaN/GaN HEMT and (b) GaN MOSFET devices. The dimensions of the different layers are not to scale.

2.2 GaN crystal structure

The GaN investigated in this study has a wurtzite crystal structure as shown in Fig. 2.2, which is also the most used crystal structure for GaN power devices. The hexagonal crystal structure is defined by the height c of the hexagonal prism, the edge length a of the basal hexagon, and the internal parameter u, the anion-cation bond length along the [0001] axis in units of c. The lack of inversion symmetry in the (0001) plane of the ionic GaN compound enables two different sequences of atomic layering along the [0001] axis, which gives rise to the spontaneous polarization $\mathbf{P_{SP}}$ and two surface terminations: (0001) or Ga-face (+c plane) formed by cations and $(000\bar{1})$ or N-face (-c plane) formed by anions. The $\mathbf{P_{SP}}$ is defined as the dipole moment per unit volume of the sample. The direction of the dipole moment points from negatively charged N atom to positively charged Ga atom, which is along the +c direction. The $\mathbf{P_{SP}}$ can be calculated by the following equation [7]:

$$\vec{P}_{SP} = \frac{\vec{P}_b}{\Omega} = \left(\frac{\vec{P}_{b//} + 3\vec{P}_{b\perp}\cos(\theta)}{\Omega} \cdot \hat{c}\right)\hat{c} \tag{2.1}$$

where $\vec{P}_b$ is the net dipole moment along the c axis of the unit cell; Ω is the unit cell volume; $\vec{P}_{b//}$ is the dipole moment for the bond along c axis, which is directed along the -c direction; $\vec{P}_{b\perp}$ is the dipole moment for the bond oriented at angel θ along the +c direction; and $\hat{c}$ is the unit vector along the +c direction [7]. The calculation suggests the

spontaneous polarization in GaN points from positively charged Ga-face to negatively charged N-face [7,8,9]. Even for the ideal wurtzite crystal structure ($c/a=(8/3)^{1/2}$, u=0.375, θ =109.47 °), the value of $(\vec{P}_{b//}+3\vec{P}_{b\perp}\cos(\theta))\cdot\hat{c}$ is not zero. Zoroddu *et al.* [10] has confirmed this point by calculating the spontaneous polarization of GaN using ideal wurtzite crystal structure parameters and they find a value of ~ -0.018C/m^2, which is about ~55% of its actual value. This suggests that the nonvanishing spontaneous polarization in III-N crystal is not caused by a non-ideal wurtzite crystal structure. However, the increased nonideality of wurtzite crystal structure (u increases and c/a decreases) from GaN (~-0.033 C/m^2) to InN (~-0.042 C/m^2) and AlN (~-0.095 C/m^2), could lead to an increase of spontaneous polarization [10].

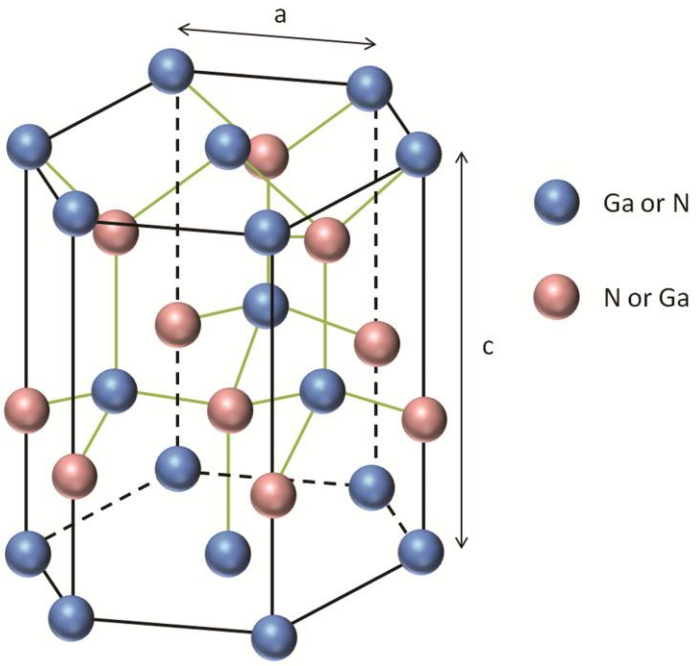

Figure 2.2. The wurtzite crystal structure of GaN. The size of the Ga and N atoms are not to scale.

In addition, there is also a piezoelectric polarization, $\mathbf{P}_{PZ}$, in unrelaxed GaN. The $\mathbf{P}_{PZ}$ will be along the -c or +c axis when GaN is in tensile or compressive strain, respectively (Fig. 2.3). Therefore, in the absence of an external electric field, the total macroscopic polarization **P** will be the sum of $\mathbf{P}_{PZ}$ and $\mathbf{P}_{SP}$, and the polarization induced charge density ρ_p will be given by the following relation:

$$\rho_P = -\nabla \cdot \vec{P} = -\nabla \cdot (\vec{P}_{SP} + \vec{P}_{PZ}) \tag{2.2}$$

However, GaN films are typically grown above a critical thickness (~10nm) and only a small residual stain remains in the films [11]. The corresponding $\mathbf{P_{PZ}}$ (=0.002 C/m^2) is typically negligible compared with $\mathbf{P}_{SP}$ (=-0.033 C/m^2) [12], and $\mathbf{P_{PZ}}$ will not be discussed in this study. Considering that the spontaneous polarization points from Ga-face to N-face, there will be a negative or positive polarization induced bound sheet charge at the Ga- or N-face, respectively. According to Eq. 2.2, the polarization bound sheet charge density is ~ 2.1x10^{13} charges/cm^2 [10]. For n-type GaN, the free electrons tend to compensate the positive bound sheet charge at the N-face; on the other hand, the positive ionized donor will only partially compensate the negative bound sheet charge at the Ga-face as calculated by the following relation [13]:

$$\frac{\sigma_{inv}}{e} = \frac{\sigma}{e} - \frac{1}{e}\sqrt{2E_g N_D \varepsilon \varepsilon_0} \tag{2.3}$$

where σ_{inv} is the compensating positive sheet charge density; σ is the polarization induced negative bound sheet charge density; N_D is the ionized donor; and ε is the dielectric constant of GaN. One theoretical study [13] suggests that ~0.1 eV downwards band bending at the N-face would enable nearly complete compensation by free electrons, fixing the conduction band close to the Fermi level. In contrast, ~3.4 eV upward band bending would be required at the Ga-face due to the lack of sufficient ionized donors or free holes. However, the experimental results suggests that there is an upward band bending of ~0.3-1.5 eV at the Ga-face [14,15,16,17] and ~0.1-1.0 eV at the N-face [15,17]. This suggests surface defects play a greater role in screening the polarization charge than ionized donors or free carriers. The surface defects may include structural defects, surface contamination, surface states, or adsorbates [13].

For typical GaN epitaxial growth on sapphire, the molecular beam epitaxy (MBE) method can enable the deposition of N-face GaN directly and Ga-face GaN by using an AlN buffer layer [18]. For the metal organic chemical vapor deposition (MOCVD) method, the initial nitridation step will enable Ga-face GaN deposition while an initial Ga exposure instead will lead to the growth of N-face GaN [17]. The difference could be explained by the different bond strength between Al-O and Al-N bonds, and Ga-N and Ga-O bonds, respectively [19]. For typical MBE deposition processes, oxygen terminated substrates resist the nitridation process, and the first deposited layer will be Ga or Al metals. For a Ga layer, it will become part of the first GaN layer due to the stronger bond strength of Ga-N bonds compared with Ga-O bonds, which leads to N-face GaN deposition. On the other hand, the first Al layer will belong to the substrate due to the stronger bond strength of Al-O bonds compared with Al-N bonds, which suggests the

next N layer will be the initial surface of the AlN layer and lead to Al-face AlN and subsequently Ga-face GaN deposition. Therefore, the polarities of MBE GaN can be inverted by applying an AlN buffer layer. For MOCVD processes, the nitridation process at higher deposition temperature causes the deposition of a thin AlN buffer layer, which leads to the deposition of Ga-face GaN. On the other hand, using an initial Ga pulse will result similar growth process to the MBE N-face GaN deposition process [19].

After deposition, the Ga- and N-face GaN could be distinguished by different methods, including convergent beam electron diffraction (CBED) [20], and wet chemical etching and physical morphology [21]. Specifically, the CBED is used to determine the point and space group based on the zone-axis diffraction patterns symmetries [20]. The experimental patterns could be compared with the simulated patterns of a particular GaN polarity to determine the sample polarity [20]. In addition, the wet chemical and surface morphology is also an effective method to distinguish the polarity of GaN. The wet chemicals (e.g., KOH [22], NaOH [23]) can selectively etch the N-face GaN, causing degradation of surface morphology [22]. For Ga-face GaN, the three occupied dangling bonds of nitrogen atoms under the first Ga layer may exhibit strong repulsion against OH^- ions and prevent their attacking the Ga atoms. On the other hand, for N-face GaN, the OH^- ions may more readily attack the back bond Ga atoms due to the single occupied dangling bond of nitrogen [22]. This etch process on N-face GaN will lead to degradation of the surface morphology, which can be used to distinguish the N-face GaN.

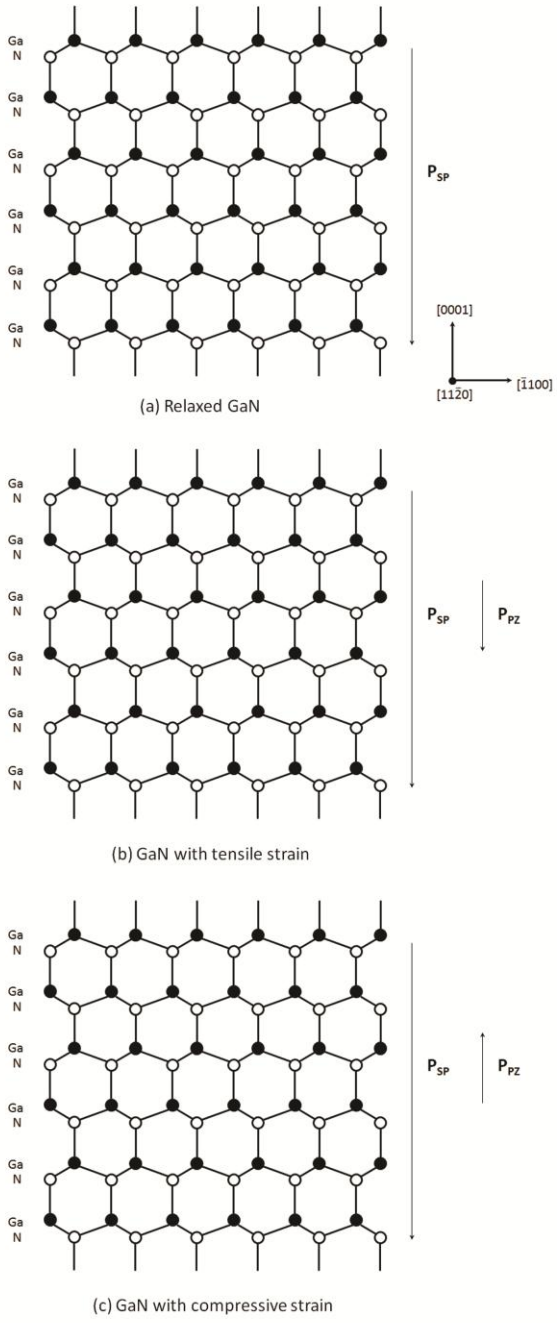

Figure 2.3. Schematic illustration of spontaneous polarization and piezoelectric polarization in Ga-face GaN in the case of (a) relaxed structure, (b) tensile strain, and (c) compressive strain.

2.3 Device reliability

Although GaN-based materials show great potential in power electronic devices, there are still limitations for these structures, including large gate leakage current and significant current collapse. To mitigate these limitations and improve the device performance, a better understanding of the failure mechanisms is needed.

2.3.1 Gate leakage

Gate leakage is electron tunneling through the gate which leads to current loss and degradation of the power efficiency and noise performance [3]. Several gate leakage mechanisms have been proposed, including thermionic emission [24], thermionic field emission [25], dislocation-assisted tunneling [26], Frenkel-Poole emission [27], Fowler-Nordheim tunneling [28], space charged limited current [29], and trap-assisted tunneling [24]. Some of the typical gate leakage mechanisms are shown in Fig. 2.4 [3]. It is suggested that the leakage current is caused by defect assisted thermionic emission and/or thermionic field emission. The interface and bulk states may serve as trapping states, enhancing the tunneling effect. The dominant mechanism may be dependent on the specific temperature, device structure, interface properties, and bias condition [3].

Alternatively, Hasegawa et al. [30] proposed a model where a thin Schottky barrier (TSB) leads to gate leakage current as shown in Fig. 2.5 [30]. The TSB will lead to enhanced electron tunneling through thermionic field emission in both forward and reverse bias conditions. In other words, the gate leakage will be enhanced by the interface and bulk states, which serve as trapping centers or pinning states.

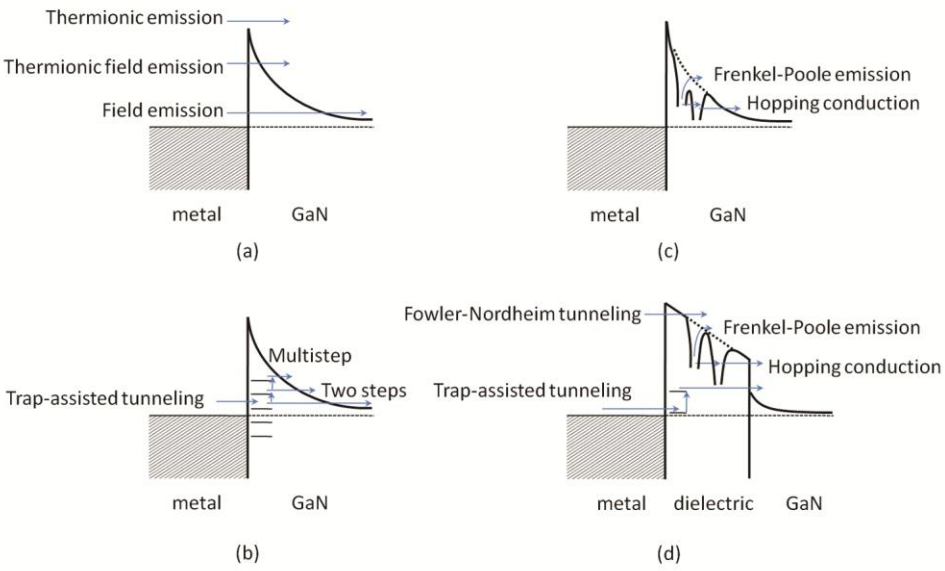

Figure 2.4. Schematic illustration of the possible gate leakage current mechanisms in GaN based electronic devices [3].

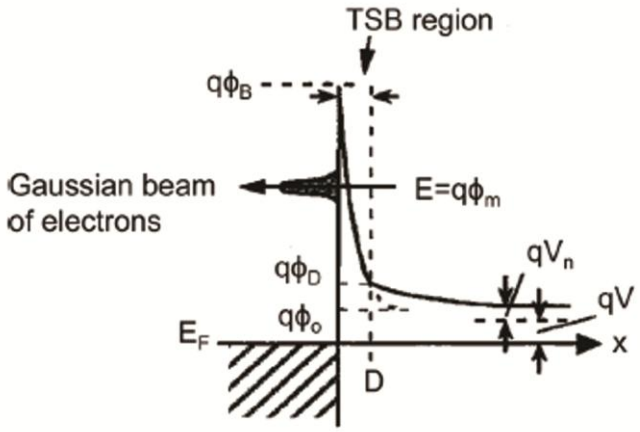

Figure 2.5. The TSB model for current transport at the Schottky interface [30].

2.3.2 Current collapse

Current collapse is another obstacle limiting the performance of GaN based devices. The effect refers to the drain current reduction under large amplitude high

frequency gate swings [3,31]. Vetury *et al.* [31] proposed the virtual gate model to explain current collapse in AlGaN/GaN based electronics. The effect is related to the reduction of positively charged surface states, as shown in Fig. 2.6. The donor-like surface states are likely a source of the 2DEG in AlGaN/GaN, while the net positive polarization charge at AlGaN/GaN interface confines the 2DEG at the interface. It is worth noting that the 2DEG can also be confined at N-face GaN/AlGaN interfaces, which enables the application of N-face GaN/AlGaN HEMTs [18,32]. If the positive surface states were decreased either by trapping electrons or removal of the positive surface defects, the surface potential becomes negative, and acts like a negatively biased metal gate, or virtual gate. This virtual gate will lead to an increase of the depletion region, the decrease in the electric field at the gate edge, and subsequently a decrease of the drain current.

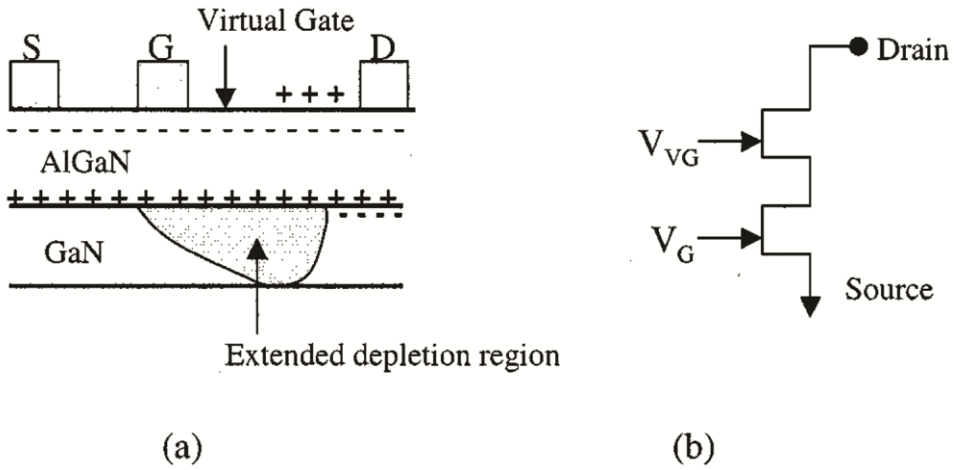

Figure 2.6. Schematic illustration of virtual gate in the AlGaN/GaN electronic structure [31]. R. Vetury, et.al, *IEEE Trans. Electron Devices* **48**, 560 (2001). Copyright © 2001, IEEE.

These failure mechanisms are related to the interface and bulk electronic states, which may be mitigated by appropriate processing, including surface cleaning, dielectric growth, and post deposition treatment. Specifically, the dielectric (oxide) layer as shown in Fig. 2.7 can serve as an additional barrier layer for electron tunneling under the gate and/or passivation layer between the gate and drain to prevent the trapping of electrons or the removal of positively charged surface states, which can significantly reduce the gate leakage and/or current collapse significantly. Suitable cleaning and post deposition treatment could also improve the device performance by removing the electronic states responsible for the failure mechanisms.

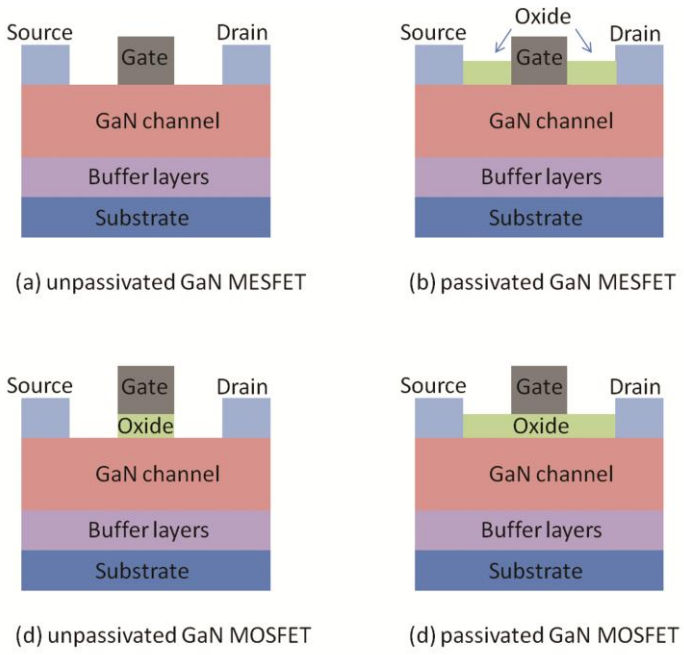

Figure 2.7. Schematic of (a) unpassivated GaN metal semiconductor field effect transistor (MESFET); (b) passivated GaN MESFET; (c) unpassivated GaN MOSFET; and (d) passivated GaN MOSFET.

2.4 Processing effect

2.4.1 Surface cleaning

As previously mentioned, the electronic states responsible for failure mechanisms may include bulk defects, structural defects, adsorbates, surface contamination, oxide layer, surface states, etc. These states could be affected by different processing treatments including: surface cleaning, gate dielectric and/or dielectric passivation growth, and post deposition and/or metallization annealing. For instance, carbon contamination could contribute to current collapse and degrade the device performance, which could be mitigated during the cleaning process [33,34].

There has been extensive study of cleaning processes of GaN and AlGaN to remove surface contamination and passivate bulk defects. These processes have addressed carbon contamination, native oxides, adsorbates, residual species, N-vacancy related defects, etc [3,35]. The *ex-situ* cleaning methods include solvents, various acids and bases, and UV/O_3. On the other hand, *in-situ* cleaning methods involve room temperature or elevated temperature sputtering or plasma treatment (e.g., O_2, Ne, Ar, Xe, H_2, N_2, and NH_3), vacuum, gas, or flux (e.g., H_2, N_2, NH_3, and Ga flux) annealing [3]. The typical cleaning process consists of an *ex-situ* wet chemical treatment and an *in-situ* process.

Various wet chemical treatments were investigated to remove oxides and carbon contamination from the surface, including H_2SO_4, HCl, HF, buffered HF, H_2S, HNO_3, NH_4F, $(NH_4)_2S$, NH_4OH, NaOH, KOH, H_2O_2, etc [3]. Specifically, HF was found to be the most efficient chemical to remove carbon contamination. On the other hand, HF, NH_4OH, HCl, and $(NH_4)_2S$ could effectively remove the oxides. However, the HCl and

$(NH_4)_2S$ treatments will leave Cl and S groups on the surface [36], which could prevent the surface from being reoxidized. In addition, the selection of specific pH and oxide-reduction potential of the etchant solution and the control of etching time are significant to obtaining an oxide-free and balanced-stoichiometry GaN surface [37].

However, oxygen and carbon contamination has not been completely removed by *ex-situ* cleaning method alone. According to the research by Smith and King *et al.* [38,39], vacuum annealing is not an effective method to remove carbon and oxide from GaN due to the high desorption temperature (~900 ℃) of the contaminants. At this temperature, the GaN starts to decompose, which creates dangling bonds and generates surface defects. Alternatively, Ga deposition or N_2+ sputtering followed by high temperature annealing [40,41], NH_3 gas annealing [14], N_2 [42], H_2/N_2 [43], or NH_3 [44] plasma annealing could remove the contamination layer, passivate N-vacancy related defects, and/or passivate bulk defects with incorporated H. However, the incorporation of H in p-type GaN is not desired, since the carrier concentration would be degraded by the formation of the Mg-H complex [45].

2.4.2 Gate dielectric and dielectric passivation deposition

After suitable cleaning process, various materials have been investigated as gate dielectrics and/or passivation layers to further decrease the leakage current and/or current collapse, including nitrides (SiN_x [46], low-temperature (LT) GaN [47], AlN [48]), SiO_2 [49], Al_2O_3 [50], Ga_2O_3 [51], HfO_2 [52], La_2O_3 [53], Sc_2O_3 [54], MgO [54], ZnO [55], and other oxides [56,57]. Specifically, the nitrides have similar lattice constant (e.g., LT GaN and AlN), avoid oxidization processes, and can effectively suppress current collapse

by reducing the formation of N-vacancy related defects. However, the relatively smaller band gaps of the nitrides are not sufficient to suppress the leakage current. On the other hand, oxides, such as Al_2O_3 and SiO_2, have good thermal and chemical stability, and a large band gap to suppress leakage current. An N-based plasma process can be applied before the deposition of the oxides to passivate the surface defects and suppress current collapse [58]. However, the relatively low dielectric constant of these oxides leads to a significant reduction in the transconductance of devices. It may be more suitable to use them as the interfacial layer between GaN or AlGaN and oxides with higher dielectric constant (e.g., HfO_2). Alternatively, they could also be used as capping layer on top of chemical unstable oxides (e.g., La_2O_3, MgO). In one word, there is no perfect dielectric, that has both the lower leakage current and smaller current collapse than other dielectrics. In addition, the performance of the dielectrics will also depend on the specific device structures, GaN bulk properties, surface pretreatments, dielectric growth method, and post deposition treatment.

2.4.3 Post deposition and metallization annealing

In addition to using N-based cleaning process to passivate the surface and bulk defects, N-based annealing processes (e.g., NH_3, N_2, or H_2/N_2) have also been applied after dielectrics or metal gate deposition to decrease the bulk deep level traps and interface states [59,60,61]. Zhou *et al*. [59] reported improved DC performance of ALD Al_2O_3/AlGaN/GaN based MOSHEMTs after a 10 min, 600℃ post deposition anneal (PDA) in an N_2 atmosphere. The maximum transconductance and gate drain breakdown voltage was increased, which was attributed to a reduction of deep-level traps. Peng *et al*.

[60] found that the direct current, radio frequency small signal, and power performance of SiN_x passivated AlGaN/GaN HEMTs was improved after a 3 min post metallization rapid thermal annealing (PMA) in N_2 ambiance at 350 ℃. It was suggested that PMA in N_2 suppresses current collapse by passivating the N-vacancies, and reducing leakage current by recovering dry-etch damage at the Schottky metal/AlGaN interface. In one word, PDA or PMA in some form of nitrogen atmosphere appears to help to reduce the current collapse and leakage current by suppressing the interface and bulk defects.

2.5 Band alignment methods

For carrier confinement, the band offset of dielectrics on GaN should be greater than 1 eV to create a sufficient potential barrier for current leakage [62]. Therefore, the band alignment of dielectrics on GaN will play a critical role in determining the confinement properties of carriers in the semiconductor and ultimately the device performance.

The theory of metal-semiconductor interface band alignment was first presented by Schottky and Mott independently in the 1938-1940 period [63,64]. The models are summarized schematically in Fig. 2.8. There is a depletion region in the semiconductor after contact if the original Fermi levels of the metal and semiconductor do not align, and the resultant band bending leads to diode electrical characteristics.

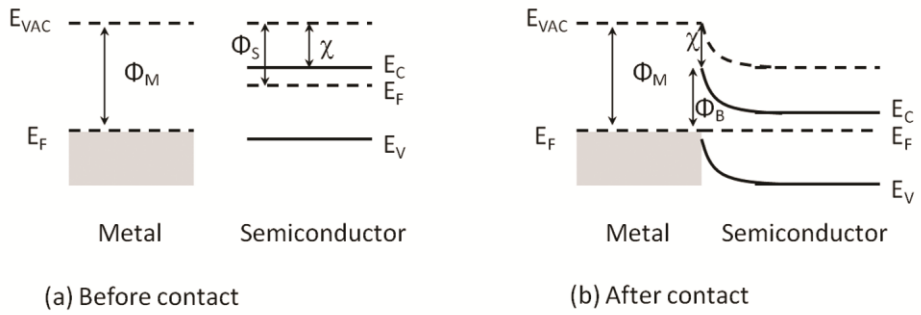

Figure 2.8. The interface of a metal and n-type semiconductor before (a) and after (b) contact; where E_{VAC} is the vacuum level; E_C is the conduction band maximum; E_F is the Fermi level; E_V is the valence band minimum; Φ_M is the work function of the metal; Φ_S is the work function of the semiconductor; χ is the electron affinity of the semiconductor; and Φ_B is the Schottky barrier height.

The electron affinity or vacuum alignment model neglects interface interactions. The Schottky barrier height (SBH) can be given by the following equation:

$$\Phi_B = \Phi_M - \chi \tag{2.4}$$

More recent models have developed approaches to account for the interactions by considering an interface dipole [65]. Therefore, the corresponding SBH is expressed in the following equation:

$$\Phi_B = \Phi_M - \chi - \Delta \tag{2.5}$$

where Δ is the interface dipole induced by charge transfer. Anderson [66] adapted the interface alignment theory of metal/semiconductor to semiconductor/semiconductor interfaces, which can equally be applied to dielectric/semiconductor interfaces. Due to the complexity of the semiconductor interface electronic states, a unified theory has not been explored. Some models, like electron affinity model, suggest there is no charge transfer at the semiconductor interfaces. Others are exploring the nature of the interface charge transfer, such as charge neutrality level model.

2.5.1 Electron affinity model

The electron affinity (EA) model proposed by Anderson is based on the assumption that the vacuum levels of the two materials align at the interface after contact [66]. Therefore, the CBO (ΔE_C) of the dielectric/GaN interface could be estimated using the following equation:

$$\Delta E_C = \chi_{GaN} - \chi_{dielectric} \tag{2.6}$$

where χ is the electron affinity. Several photoemission spectroscopy studies have reported that Ga-face GaN has a electron affinity varying from 2.9-3.6 eV [12,16,67,68]. The electron affinity could be affected by different surface chemistry and electronic structure, which may be affected by different deposition methods and/or surface pretreatment processes. The corresponding VBO (ΔE_V) after considering the band gap (E_g) of GaN and dielectric could be determined by the following equation:

$$\Delta E_V = (E_{g,dielectric} + \chi_{dielectric}) - (E_{g,GaN} + \chi_{GaN}) = I_{dielectric} - I_{GaN} \quad (2.7)$$

where I is the photo threshold energy, which is the sum of the electron affinity and band gap. Depending on the different values of VBO and CBO, two typical types of band alignment are shown in Fig. 2.9.

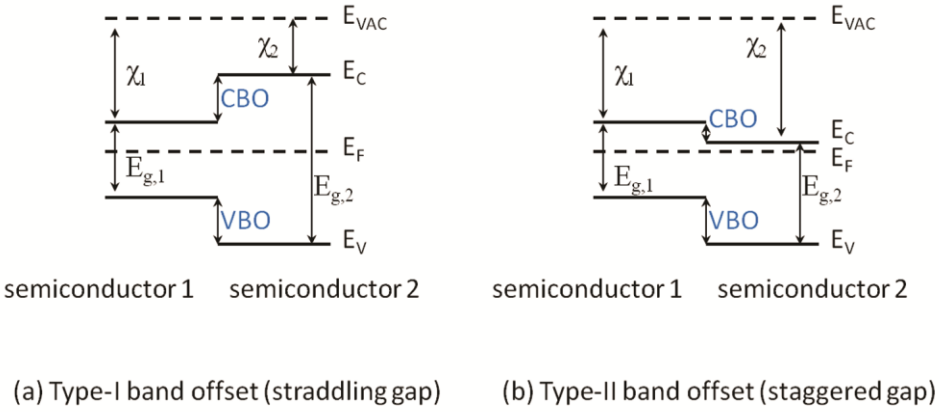

Figure 2.9. The illustration of two typical types of band offset as predicted by EA model.

2.5.2 Charge neutrality level model

The EA model assumes there is no interface dipole after alignment, which is the ideal case. An alternative model, first presented by Tejedor and Flores [69] and later described by Tersoff [70], is based on metal-induced gap states (MIGS) at the metal/semiconductor interface. The MIGS refers as the dangling bond states of the broken surface bonds dispersed across the band gap of semiconductor or is induced by the attenuated metal wave function into the band gap of semiconductor [65,71,72]. When the metal contacts with semiconductor, a charge transfer between metal and interface gap

states will create interface dipole, which is shown in Fig. 2.10 [73]. The charge neutrality level (CNL) is like the Fermi level of the interface states. The charge transfer then tends to align the Fermi level of the metal and CNL of the semiconductor together [72].

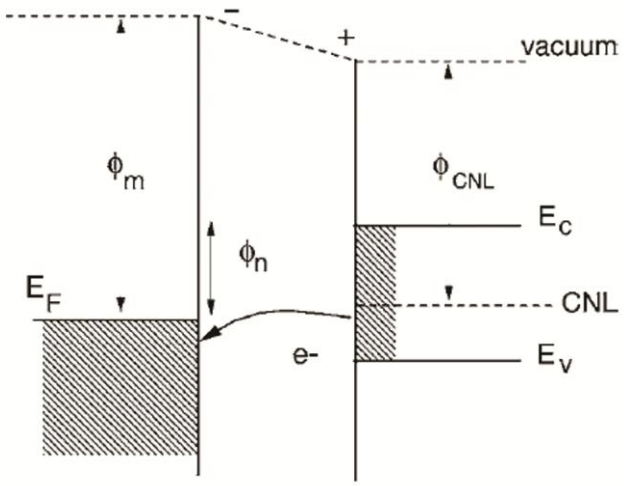

Figure 2.10. The illustration of the charge transfer and created dipole at the interface of metal/semiconductor [73].

For semiconductor/semiconductor or dielectric/semiconductor interfaces, the CNL is the point where the contribution from the valence and conduction band density of states is equal, as shown in Fig. 2.11 [73]. The charge transfer at the interface tends to align the CNLs of heterostructures. This model was further refined to include an empirical factor S [72], which was suggested to depend on the optical dielectric constant (ε_∞) in the following relation [74,75].

$$S = \frac{1}{1 + 0.1(\varepsilon_\infty - 1)^2} \tag{2.8}$$

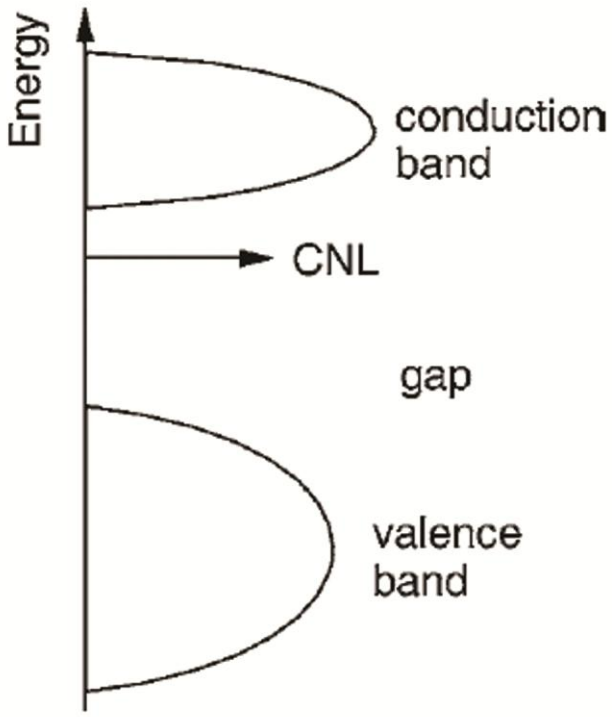

Figure 2.11. The CNL is the weighted average of the density of states of conduction and valence band [73].

The VBO of dielectric on GaN could then be calculated by the following relation:

$$\begin{aligned}\Delta E_V &= E_{CNL,dielectric} - E_{CNL,GaN} - S[(E_{g,GaN} + \chi_{GaN}) - (E_{g,dielectric} + \chi_{dielectric}) \\ &\quad -(E_{CNL,GaN} - E_{CNL,dielectric})] \\ &= E_{CNL,dielectric} - E_{CNL,GaN} - S[I_{GaN} - I_{dielectric} - (E_{CNL,GaN} - E_{CNL,dielectric})]\end{aligned} \tag{2.9}$$

where $E_{CNL,GaN}$ and $E_{CNL,dielectric}$ are the charge neutrality levels of GaN and dielectric with respect to VBM. For a GaN and dielectric interface, the dimensionless factor S of the wider band gap material is used. In the Bardeen limit of strong pinning (S=0), the heterostructure are aligned at the CNL; while in the Schottky limit of no pinning (S=1), there is no charge transfer creating interface dipole and therefore the heterostructure align at the vacuum level. These two cases are shown in Fig. 2.12.

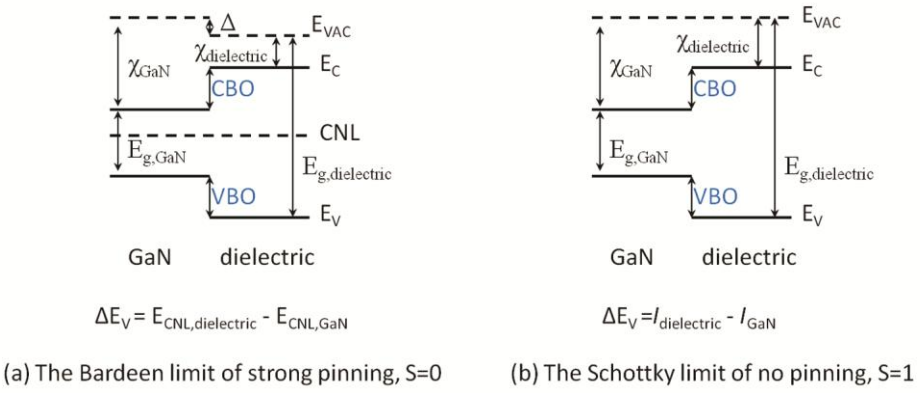

Figure. 2.12. An illustration of the band alignment based on the CNL model in the (a) Bardeen limit of strong pining (i.e. CNL alignment) and (b) Schottky limit of no pinning (i.e. vacuum level alignment).

J. Robertson and B. Falabretti reported a calculation of a series of band offset results of dielectrics on GaN based on CNL model, which are summarized in Table 2.3 [73]. In this calculation, the specific interface bonding is not considered, which may contribute to band offset errors.

Table 2.3. The valence and conduction band offsets of dielectrics on GaN based on CNL model [73].

Material	Band Offset	
	VBO	CBO
AlN	0.4	2.4
Al_2O_3	3.0	2.4
Ga_2O_3	0.7	0.5
Gd_2O_3	0.7	1.9
HfO_2	1.6	1.1
$HfSiO_4$	1.7	1.6
$LaAlO_3$	1.3	1.1
La_2O_3	0.7	2.0
$PbTiO_3$	-0.2	0.4
Sc_2O_3	0.7	2.0
Si_3N_4	0.8	1.3
SiO_2	3.1	2.6
$SrTiO_3$	0.2	-0.1
Ta_2O_5	1.1	0.1
Y_2O_3	0.8	1.9
ZnO	0.9	-0.7
ZrO_2	1.6	1.1

2.6 Summary and comments

The GaN is a promising candidate for power electronics due to its excellent material properties. However, the large concentration of surface defects causes a large leakage current and significant current collapse, degrading device performance and reliability. On the other hand, the large polarization induced bound sheet charge is apparently compensated by surface defects, which may be related to the failure mechanisms. The failure mechanisms could be mitigated by appropriate cleaning processes, dielectric growth, and post deposition annealing as previously discussed. The

surface band bending of GaN can be related to the location and concentration of charges and defects near the surface, which may be affected by these processes.

In this study, different cleaning processes are applied and evaluated to obtain an effective cleaning method to remove carbon contamination, retain thin oxygen coverage, and potentially passivate N-vacancy related defects. The effect of cleaning processes on surface chemistry and electronic structures was measured by photoemission spectroscopy. In addition, the plasma enhanced atomic layer deposition method is developed to obtain uniform and conformal dielectric films with atomic scale thickness control and reduced impurities and defects. The band alignments of several promising dielectrics on Ga-face GaN are measured by photoemission spectroscopy to determine the confinement properties of carriers in the heterostructures. The experimental band offset results are also compared with theoretical calculations to understand the semiconductor interface alignment properties. The effect of processing induced defects on the interface electronic structure is also discussed.

Furthermore, the surface chemistry and electronic structures of GaN with different polarities is studied to better understand effects related to polarization charge on surface and interface electronic states. The effects of cleaning processes and post deposition processing on surface chemistry, electronic structure, and charge compensation mechanism are discussed. In addition, the effect of the polarization induced charge on band alignment between the dielectric and GaN is also investigated.

Reference

[1] S. J. Pearton, J. C. Zolper, R. J. Shul, and F. Ren, *J. Appl. Phys*. **86**, 1 (1999).

[2] R. D. Long and P. C. McIntyre, *Materials* **5**, 1297 (2012).

[3] B. S. Eller, J. Yang, and R. J. Nemanich, *J. Vac. Sci. Technol. A* **31** 050807 (2013).

[4] U. K. Mishra, P. Parikh, and Y. F. Wu, *Proc. IEEE* **90**, 1022 (2002).

[5] F. A. Ponce, and D. P. Bour, *Nature* **386**, 351 (1997).

[6] Y. Niiyama, S. Ootomo, J. Li, T. Nomura, S. Kato and T. P. Chow, *Semicond. Sci. Technol.* **25** 125006 (2010).

[7] S. Y. Davydov, *Phys. Solid State*, **51** 1231 (2009).

[8] F. Bernardini, V. Fiorentini, and D. Vanderbilt, *Phys. Rev. B.* **56** R10 024 (1997).

[9] *O. Ambacher, J. Smart, J. R. Shealy, N. G. Weimann, K. Chu, M. Murphy,* W. J. Schaff*, L. F. Eastman, R. Dimitrov, L. Wittmer, M. Stutzmann, W. Rieger and* J. Hilsenbeck*, J. Appl. Phys.* **85**, 3222 (1999).

[10] A. Zoroddu, F. Bernardini, P. Ruggerone, and V. Fiorentini, *Phys. Rev. B* **64**, 045208 (2001).

[11] A. D. Bykhovski, B. L. Gelmont, and M. S. Shur, *J. Appl. Phys.* **81**, 6332 (1997).

[12] T. E. Cook, Jr., C. C. Fulton, W. J. Mecouch, K. M. Tracy, and R. F. Davis, E. H. Hurt, G. Lucovsky, and R. J. Nemanich, *J. Appl. Phys*. **93**, 3995 (2003).

[13] U. Karrer, O. Ambacher, and M. Stutzmann, *Appl. Phys. Lett.* **77**, 2012 (2000).

[14] K. M. Tracy, W. J. Mecouch, R. F. Davis, and R. J. Nemanich, *J. Appl. Phys.* **94**, 3163 (2003).

[15] P. Lorenz, T. Haensel, R. Gutt, R. J. Koch, J. A. Schaefer, and S. Krischok, *Phys. Status Solidi B* **247**, 1658 (2010).

[16] C. I. Wu, A. Kahn, N. Taskar, D. Dorman, and D. Gallagher, *J. Appl. Phys.* **83**, 4249 (1998).

[17] H. W. Jang, J. H. Lee, and J. L. Lee, *Appl. Phys. Lett.* **80**, 3955 (2002).

[18] R. Dimitrov, M. Murphy, J. Smart, W. Schaff, J. R. Shealy, L. F.Eastman, O.Ambacher , and M. Stutzmann, *J. Appl. Phys.* **87**, 3375 (2000).

[19] M. Stutzmann, O. Ambacher, M. Eickhoff, U. Karrer, A. Lima Pimenta, R. Neuberger, J. Schalwig, R. Dimitrov, P.J. Schuck, R.D. Grober, *Phys. Stat. Sol. (b)* **228** 505 (2001).

[20] F. A. Ponce, D. P. Bour, W. T. Young, M. Saunders, and J. W. Steeds, *Appl. Phys. Lett*. **69**, 337 (1996).

[21] D. Zhuang, and J.H. Edgar, *Mat. Sci. Eng. R* **48** 46 (2005).

[22] D. Li, M. Sumiya, S. Fuke, D. Yang, D. Que, Y. Suzuki, and Y. Fukuda, *J. Appl. Phys.* **90** 4219 (2001).

[23] A. R. Smith, R. M. Feenstra, D. W. Greve, M.-S. Shin, M. Skowronski, J. Neugebauer, and J. E. Northrup, *Appl. Phys. Lett.* **72**, 2114 (1998).

[24] J. C. Carrano, T. Li, P. A. Grudowski, C. J. Eiting, R. D. Dupuis, and J. C. Campbell, *Appl. Phys. Lett.* **72**, 542 (1998).

[25] S. Oyama, T. Hashizume, and H. Hasegawa, *Appl. Surf. Sci.* **190**, 322 (2002).

[26] H. Zhang, E. J. Miller, and E. T. Yu, *J. Appl. Phys.* **99**, 023703 (2006).

[27] C. F. Shih, K. T. Hung, C. Y. Hsiao, S. C. Shu, and W. M. Li, *J. Alloys Compd.* **480**, 541 (2009).

[28] Z. H. Liu, G. I. Ng, S. Arulkumaran, Y. K. T. Maung, and H. Zhou, *Appl. Phys. Lett.* **98**, 163501 (2011).

[29] V. Lebedev, G. Cherkashinin, G. Ecke, I. Cimalla, and O. Ambacher, *J. Appl. Phys.* **101**, 033705 (2007).

[30] H. Hasegawa, T. Inagaki, S. Ootomo, and T. Hashizume, *J. Vac. Sci. Technol. B* **21**, 1844 (2003).

[31] R. Vetury, N. Q. Zhang, S. Keller, and U. K. Mishra, *IEEE Trans. Electron Devices* **48**, 560 (2001).

[32] M. Abraham, X. Weng, W. H.Choi, B. P. Downey, and S. E. Mohney, *Appl. Phys. Lett.* **101**, 243504 (2012).

[33] J. A. Bardwell, S. Haffouz, W. R. McKinnon, C. Storey, H. Tang, G. I. Sproule, D. Roth, and R. Wang, *Electrochem. Solid-State Lett.* 10, H46 (2007).

[34] M. J. Uren, J. Möreke, and M Kuball, *IEEE Trans. Electron Devices* **59**, 3327 (2012).

[35] T. Hashizume, S. Ootomo, T. Inagaki and H. Hasegawa, *J. Vac. Sci. Technol. B* **21**, 1828 (2003).

[36] M. Diale, F. D. Auret, N. G. Van der Berg, R. Q. Odendaal, and W. D. Roos, *Appl. Surf. Sci.* 246, 279 (2005).

[37] A. N. Hattori, F. Kawamura, M. Yoshimura, Y. Kitaoka, Y. Mori, K. Hattori, H. Daimon, and K. Endo, *Surf. Sci.* **604**, 1247 (2010).

[38] L.L. Smith, S.W. King, R.J. Nemanich and R.F. Davis, *J. Electron. Mater.* **25**, 805 (1996).

[39] S. W. King, J. P. Barnak, M. D. Bremser, K. M. Tracy, C. Ronning, R. F. Davis, and R. J. Nemanich, *J. Appl. Phys.* **84**, 5248 (1998).

[40] V.M. Bermudez, R. Kaplan, M. Asif Khan, and J.N. Kuznia, *Phys. Rev. B* **48**, 2436 (1993).

[41] V.M. Bermudez, T.M. Jung, K. Doverspike, and A.E. Wickenden, *J. Appl. Phys.* **79**, 110 (1996).

[42] T. Inagaki, T. Hashizume, and H. Hasegawa, *Appl. Surf. Sci.* **216**, 519 (2003).

[43] K.N. Lee, S.M. Donovan, B. Gila, M. Overberg, J.D. Mackenzie, C.R. Abernathy, and R.G. Wilson, *J. Electrochem. Soc.* **147**, 3087 (2000).

[44] J. Kim, H. Choi, M. Ha, H. Song, C. Roh, J. Lee, J. Park, and C. Hahn, *Jpn. J. Appl .Phys.* **49** 04DF05 (2010).

[45] S. Nakamura, N. Iwasa, M. Senoh, and T. Mukai, *Jpn. J. Appl. Phys.* **31**, 1258 (1992).

[46] R. Nakasaki, T. Hashizume and H. Hasegawa, *Physica E (Amsterdam)* **7**, 953 (2000).

[47] C. J. Kao, M. C. Chen, C. J. Tun, G. C. Chi, J. K. Sheu, W. C. Lai, M. L. Lee, F. Ren, and S. J. Pearton, *J. Appl. Phys*. **98**, 064506 (2005).

[48] T. Hashizume, E. Alekseev, D. Pavlidis, K. S. Boutros, and J. Redwing, *J. Appl. Phys*. **88**, 1983 (2000).

[49] C. J. Kirkpatrick, B. Lee, R. Suri, X. Yang and V. Misra, *IEEE Electr Device L* **33**, 1240 (2012).

[50] P.D. Ye, B. Yang, K.K. Ng, J. Bude, G.D. Wilk, S. Halder and J.C.M. Hwang, *Appl. Phys. Lett.* **86**, 063501 (2005).

[51] D J. Fu, Y.H. Kwon, T.W. Kang, C.J. Park, K.H. Baek, H.Y. Cho, D.H. Shin, C.H. Lee and K.S. Chung, *Appl. Phys. Lett.* **80**, 446 (2002).

[52] C. Liu, E.F. Chor and L.S. Tan, *Appl. Phys. Lett.* **88**, 173504 (2006).

[53] J. S. Jur, V. D. Wheeler, D. J. Lichtenwalner, J. P. Maria, and M. A. L. Johnson, *Appl. Phys. Lett*. 98, 042902 (2011).

[54] B. Luo, J.W. Johnson, J. Kim, R.M. Mahandru, F. Ren, B.P. Gila, A.H. Onstine, C.R. Abernathy, S.J. Pearton, A.G. Baca, R.D. Briggs, R.J. Shul, C. Monier and J.Han, *Appl. Phys. Lett.* **80**, 1661 (2002).

[55] Y. Chiou and C. Lee, *IEEE T Electron Dev.* **58**, 3869 (2011).

[56] K. Balachander, S. Arulkumaran, H. Ishikawa, K. Baskar and T. Egawa, *Phys. Status Solidi A* **202**, R16 (2005).

[57] C. Hu, M. Lin, T. Wu, F. Adriyanto, P. Sze, C. Wu and Y. Wang, *IEEE T Electron Dev.* **59,** 121 (2012).

[58] T. Hashizume, S. Ootomo, and H. Hasegawa, *Appl. Phys. Lett.* **83**, 2952 (2003).

[59] H. Zhou, G. I. Ng, Z. H. Liu, and S. Arulkumaran, *Appl. Phys. Express*. **4** 104102 (2011).

[60] M.Z. Peng , Y.K. Zheng, K. Wei, and X.Y. Liu. *Microelectron Eng*. **87** 2638 (2010).

[61] Y.Q. Wu, T. Shen, P.D. Ye and G.D. Wilk, *Appl. Phys. Lett.* **90**, 143504 (2007).

[62] J. Robertson, *J. Vac. Sci. Technol. B* **18**, 1785 (2000).

[63] W. Schottky, *Phys. Z* **41**, 570 (1940).

[64] N. F. Mott, *Math. Proc. Cambridge* **34**, 568 (1938).

[65] J. Bardeen, *Phys. Rev*. **71**, 717 (1947).

[66] R. L. Anderson, *Solid-State Electron*. **5**, 341 (1962).

[67] S. P. Grabowski, M. Schneider, H. Nienhaus, W. Monch, R. Dimitrov, O. Ambacher, and M. Stutzmann, *Appl. Phys. Lett.* **78**, 2503 (2001).

[68] V. M. Bermudez, *J. Appl. Phys.* **80**, 1190 (1996).

[69] C. Tejedor and F. Flores, *J. Phys. C: Solid State Phys.* **11**, L19 (1978).

[70] J. Tersoff, *Phys. Rev. B* **30**, 4874 (1984).

[71] V. Heine, *Phys. Rev.* **138**, A1689 (1965).

[72] J. Robertson, *J. Vac. Sci. Technol. B* **18**, 1785 (2000).

[73] J. Robertson and B. Falabretti, *J. Appl. Phys.* **100**, 014111 (2006).

[74] W. Mönch, *Phy. Rev. Lett.* **58**, 1260 (1987).

[75] W. Mönch, *J. Vac. Sci. Technol. B* **6**, 1270 (1988).

CHAPTER 3

INSTRUMENTS AND ANALYSIS METHOD

3.1 Introduction

The experiments in this study are mainly completed *in-situ* with various ultra high vacuum (UHV) instruments, including semiconductor processing, film deposition, and photoemission spectroscopy characterization. All of the systems are connected to a ~20 m UHV transfer line with a base pressure ~$4x10^{-10}$ Torr, as shown in Fig. 3.1.

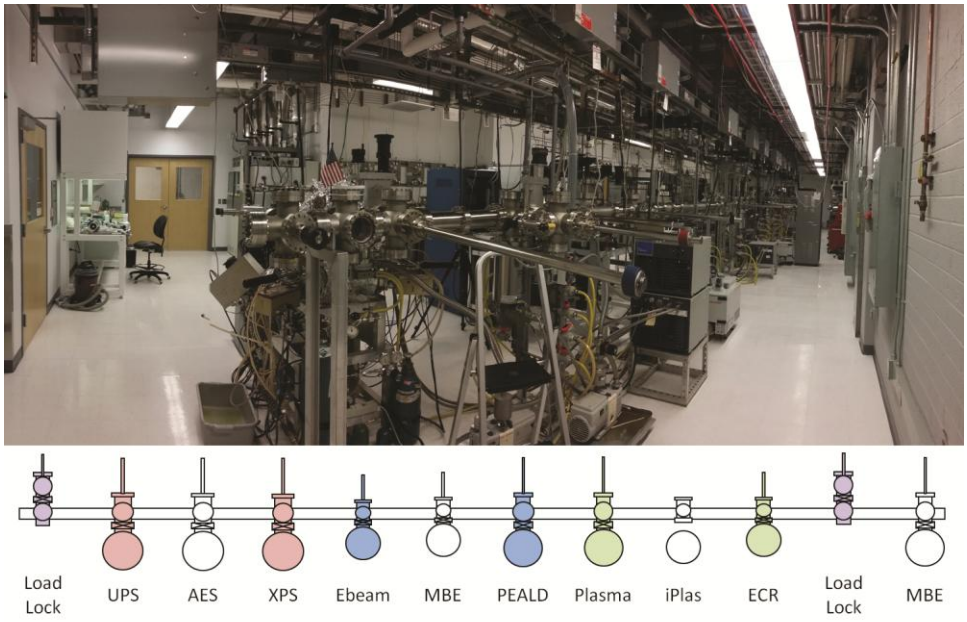

Figure 3.1. A photograph and schematic of the UHV transfer line and integrated UHV system.

After *ex-situ* wet chemical clean, the sample was mounted onto a 1 inch sample holder, put into the load lock, and then transferred into different UHV systems through

the transfer line. In this research, the following UHV instruments were used, including a remote plasma system for sample cleaning and/or post deposition treatment, a remote plasma-enhanced atomic layer deposition (PEALD) system for dielectric deposition and/or post deposition processing, and an ultra-violet and x-ray photoemission spectroscopy (UPS and XPS) system for electronic structure characterization.

Other *ex-situ* facilities employed in this study included the wet chemical treatment for sample cleaning, atomic force microscopy (AFM) for surface morphology measurement, x-ray reflectivity (XRR) for film density and thickness measurement, Rutherford backscattering spectroscopy (RBS) for atomic concentration measurement, and spectroscopic ellipsometry (SE) for film thickness and optical property measurement.

3.2 Remote plasma processing chamber

The remote plasma processing chamber used for sample cleaning and annealing is illustrated in Fig. 3.2. The base pressure for this chamber was ~2.0×10^{-9} Torr, and the chamber pressure was increased to ~60 mTorr during sample processing as controlled by a throttle valve in front of the turbo pump. The processing gas used in this research included H_2, N_2, mixed H_2 and N_2, He, and NH_3 with a flow rate of 90 standard cubic centimeters per minute (sccm). The plasma was generated by a radio frequency (rf) source (100 W, 13.56 MHz) applied to a helical copper coil wrapped around a ~32 mm diameter quartz tube. The time-varying magnetic field caused by the time-varying electric current passing through the coil generates an azimuthal electric current of the ions and electrons in the processing gas, which sustain the plasma. The remote plasma generator was ~25 cm above the sample, which provided a sufficient flux of excited molecular

species and radicals, while reducing the plasma damage caused by ion bombardment and plasma radiation [1].

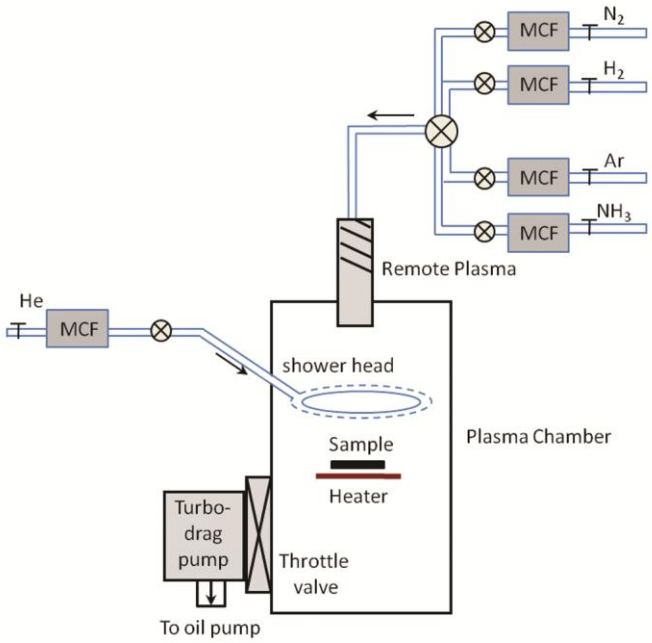

Figure 3.2. The schematic illustration of the remote plasma processing system.

For cleaning purpose, the samples were usually treated with 15 min NH_3, H_2, N_2, or mixed H_2 and N_2 plasma, and additional 15 min gas annealing at 600-700 ℃. For post deposition treatment, the samples were annealed at ~600 ℃ for 30 min in vacuum, NH_3, H_2, N_2, or mixed H_2 and N_2 gas or treated with 5-20 min room temperature He plasma.

3.3 Remote plasma-enhanced atomic layer deposition

3.3.1 Atomic layer deposition

Atomic layer deposition (ALD) is a vapor-phase deposition method, which is based on the sequential use of gas phase chemical process [2]. The chemicals, called precursors, react with the sample surface in two sequential half cycles, separated by an inert purge gas, typically Ar or N_2 gas. The chemical reactions in these two half cycles are self-limiting, which suggests the amount of deposited material is constant in each half cycle. The purge gas employed after each half cycle is to remove excess dosed precursor and gas phase reaction byproduct from the chamber. By repeating the two half-cycle self-limiting reactions, films with atomic layer precision can be deposited on the substrate. The typical growth rate for ALD, expressed as growth per cycle (GPC), is between 0.5-1.5 Å/cycle. In addition to atomic scale thickness control, ALD can enable relatively low deposition temperature compared with chemical vapor deposition, and fulfill uniform growth over large substrate and conformal deposition in structures with high aspect ratio as long as applying sufficient dosing and purge time [2].

3.3.2 Plasma-enhanced atomic layer deposition

For oxide ALD, the oxidizer is usually water, and the surface reactions are thermally driven by elevated substrate temperature, which is called thermal ALD. Plasma-enhanced ALD (PEALD) is an energy-enhanced ALD method [1]. By using activated oxygen species (e.g., O_2*, O*) generated by a plasma, PEALD can not only decrease deposition temperature and film impurities, but also increase the growth rate and film density [3,4].

The typical PEALD deposition process is shown in Fig. 3.3. At first, the metal precursor is delivered into the chamber by carrier gas, typically Ar or N_2, and reacts with the surface group to form submonolayer ~ monolayer chemisoprtion; then a purge step is applied to remove non-reacted molecules and gas phase by-product; in the second half-cycle, the O_2 plasma is excited and delivered into the chamber and oxidizes the chemisorbed molecular on the surface; the second purge step is employed to remove excess O_2, gas phase by-products, and provide a fresh surface for the next cycle of PEALD deposition [2].

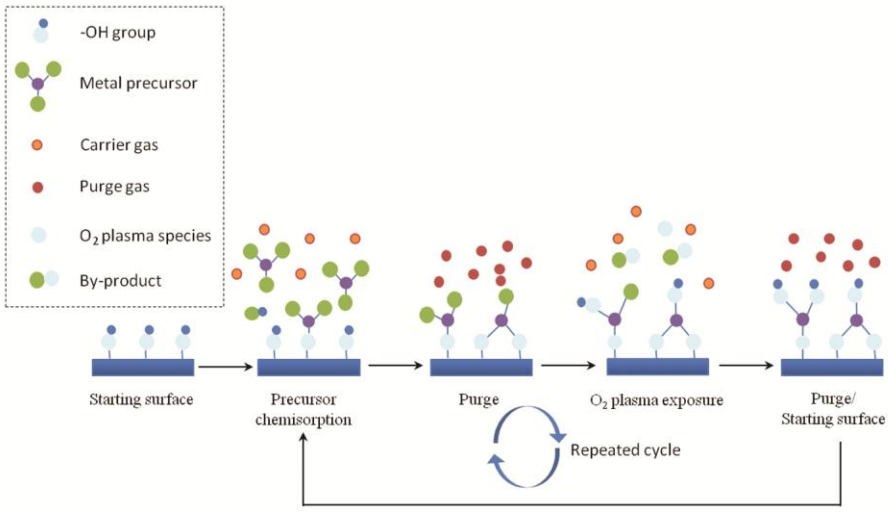

Figure 3.3. The schematic illustration of typical PEALD process.

To optimize these processes, the precursor dose time, purge time, and O_2 plasma dose time is varied to achieve saturated and self-limiting growth. Initially, the metal organic precursor dose time is increased until the growth rate saturates. For the second half-cycle reaction, the O_2 plasma dose time is increased until the growth rate is constant

which indicates that the chemisorbed precursor was fully oxidized. On the other hand, the purge time is increased until the growth rate is minimized indicating purging of excess precursor.

In addition, the substrate temperature also has a significant effect on the growth rate, as shown in Fig. 3.4. When the substrate temperature is below T_1, the growth rate could be increased or decreased which has been attributed to precursor condensation on the surface or incomplete reaction caused by insufficient thermal energy, respectively. On the other hand, for temperatures above T_2, the growth rate could also be increased or decreased by precursor decomposition or precursor desorption on the surface, respectively. The temperature window between T_1 and T_2, in which the surface reaction is self-limiting and the growth rate might be constant, is called the PEALD growth window. Therefore, it is required to achieve saturated and self-limiting growth within the PEALD growth window during deposition by optimizing the precursor dose time, O_2 plasma time, purge time, and substrate temperature. However, due to different chemical properties and reaction mechanisms, there may be no obvious growth window for some precursors during ALD deposition.

Fig. 3.5 shows a schematic of the home-built remote PEALD system used in this study. The PEALD chamber has a base pressure of ~6.0×10^{-9} Torr, and during the deposition, the pressure was set to be ~100 mTorr as controlled by a throttle valve in front of the turbo pump. The metal organic precursors were installed in different bubblers, which were maintained at different temperatures to provide sufficient vapor pressure for PEALD deposition. The precursor was delivered into the reaction chamber by Ar carrier gas through a bypass when the vapor pressure of the precursor was high or through the

bubbler when the vapor pressure of the precursor was low. During deposition, the delivery line was maintained at ~20 ℃ higher than that of the specific bubbler temperature, and the chamber was maintained at ~110 ℃ to prevent condensation during precursor exposure. Ultra high purity grade O_2 with a flow rate of 35 sccm was used as the oxygen source, and research grade N_2 with a flow rate of 35 sccm was used as the purge gas. The remote oxygen plasma was generated by an rf-source (200 W, 13.56 MHz) ~25 cm above the sample. The deposition process was controlled by a computer running a LabVIEW program, which operated the pulse time schedule shown in Fig. 3.6. The precursor pulse time was ~0.1-1 s followed by 20-40 s N_2 purge time. A 6s O_2 purge to reach 100 mTorr pressure inside the chamber preceded an ~8 s plasma, which was followed by ~20-40 s N_2 purge again to prepare for the next cycle of growth. In this dissertation, five different dielectrics were deposited by using the PEALD system, including Al_2O_3, HfO_2, SiO_2, La_2O_3, and ZnO.

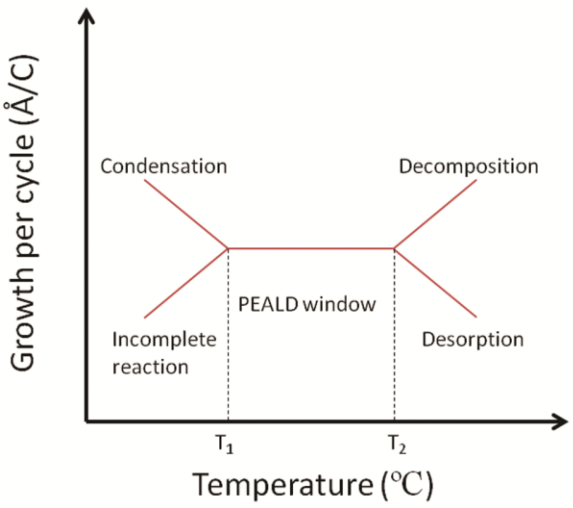

Figure 3.4. The schematic illustration of the relation between the PEALD growth rate and substrate temperature.

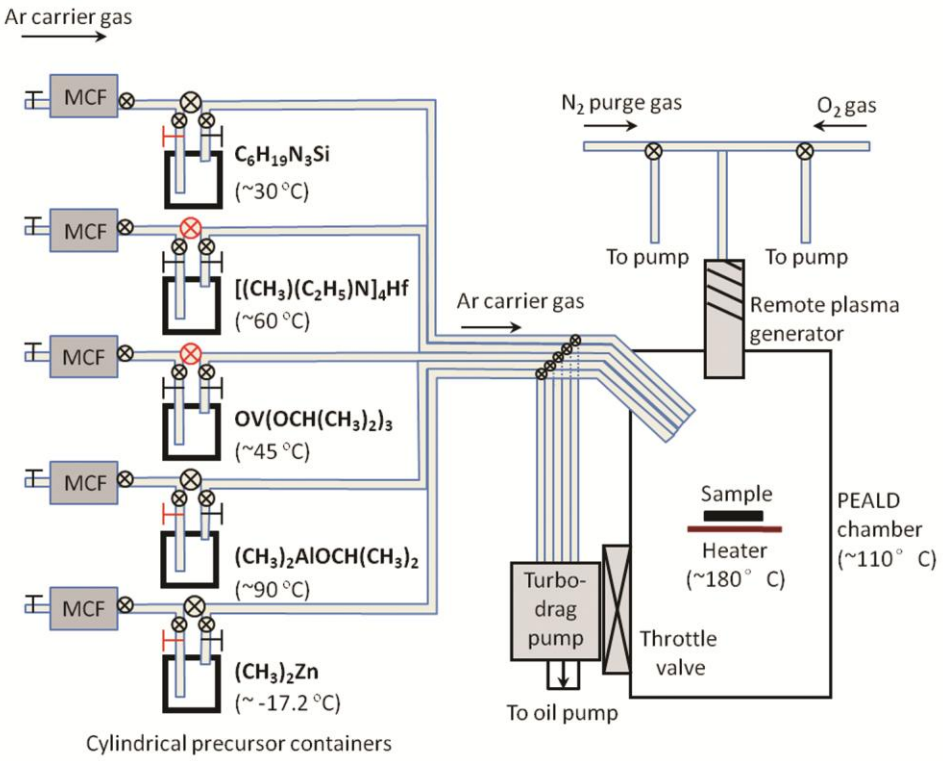

Figure 3.5. The schematic of the remote PEALD system, where the red symbols represents closed values.

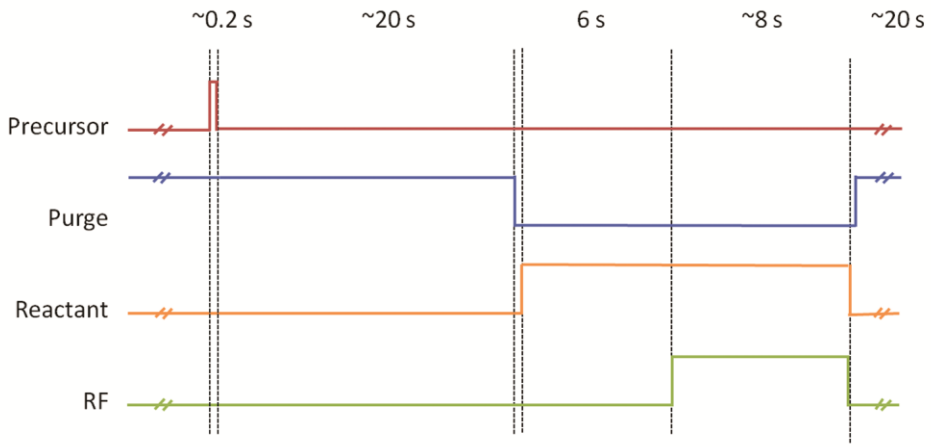

Figure 3.6. The schematic illustration of the pulse time schedule for PEALD deposition.

3.4 Photoemission spectroscopy

3.4.1 Principle of photoemission spectroscopy

Photoemission spectroscopy analysis is an application of the photoelectric effect, which applies photons to strike the sample and excite the electrons to emit from the surface. Fig. 3.7 shows a schematic of the photoemission spectroscopy system, which consists of a photon source, electron optics, an electron energy analyzer, and an electron multiplier detector in an UHV chamber. Most of the excited electrons do not escape from the sample due to energy losses caused by scattering and/or recombination. Fig. 3.8 shows the relation between the electron inelastic mean free path (escape depth) and its initial kinetic energy [5]. Subsequently, the electrons close to the sample surface could escape into vacuum, if they have enough kinetic energies to overcome the work function of the sample. In the meantime, some scattered electrons with sufficient kinetic energies could also escape from the surface as secondary electrons, which contribute to the background in the spectrum. The electron optics, typically consist of a set of electrostatic lenses to collect the electrons and focus them onto the analyzer entrance slit. A bias is applied to the two concentric hemispherical plates of the analyzer, which can allow the electrons with certain energy, called pass energy, to arrive at the detector. Inside the multiplier detector, the electrons are accelerated to strike a surface, which introduces secondary electron emission. This process is repeated to create an electron avalanche and finally a measurable current pulse.

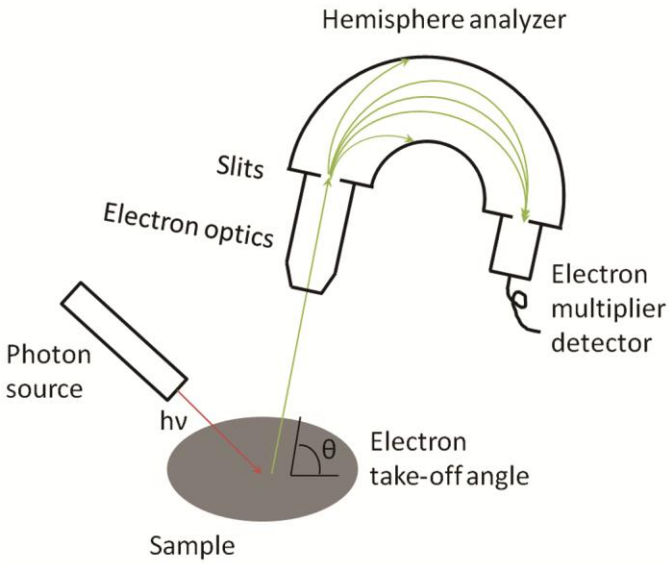

Figure 3.7. The schematic illustration of the photoemission spectroscopy system.

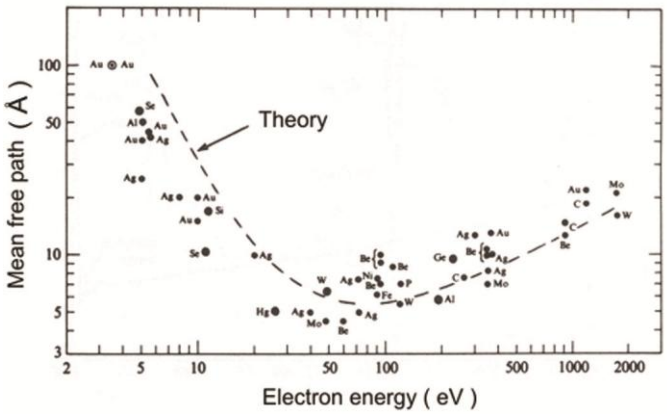

Figure 3.8. The relation between electron inelastic mean free path (escape depth) and its kinetic energy [5].

The two operation modes for the optic lens and hemisphere analyzer are the fixed retard ratio (FRR) and fixed analyzer transmission (FAT). For FRR mode, both the lens and the analyzer pass energy are adjusted to maintain a constant ratio of electron kinetic

energy and analyzer pass energy. This leads the energy interval accepted by the detection system to increase with electron kinetic energy, typically used in Auger electron spectra. On the other hand, for FAT mode, the analyzer pass energy is maintained at constant, and the transfer lens is adjusted to retard the selected electron kinetic energy to the accepted range by the analyzer, which gives a constant resolution.

Photoelectron spectroscopy could be subdivided into x-ray and ultraviolet photoemission spectroscopy (XPS and UPS) according to the different energies of the photon sources. Considering x-rays have much higher energy than that of ultraviolet photon, the XPS is used to investigate the core level states with high binding energy while UPS is focused on the electronic structure in valence band range as shown in Fig. 3.9.

The relation between the electron binding energy in the sample and the kinetic energy after emitting from the surface in photoemission spectroscopy can be expressed as Eq. 3.1.

$$BE = h\nu - KE - \Phi_W \tag{3.1}$$

Where BE is the binding energy of the electron in the sample; hν is the photon energy; KE is the emitted electron kinetic energy; and Φ_W is the work function of the spectrometer. Here the Fermi level is defined to be the zero point of the binding energy. For UPS measurements, a negative bias is applied between the sample and analyzer to enable the low kinetic energy photoelectrons to overcome the work function of the spectrometer. Therefore, Eq. 3.1 is modified as follows.

$$BE = h\nu - KE - \Phi_W - qV \tag{3.2}$$

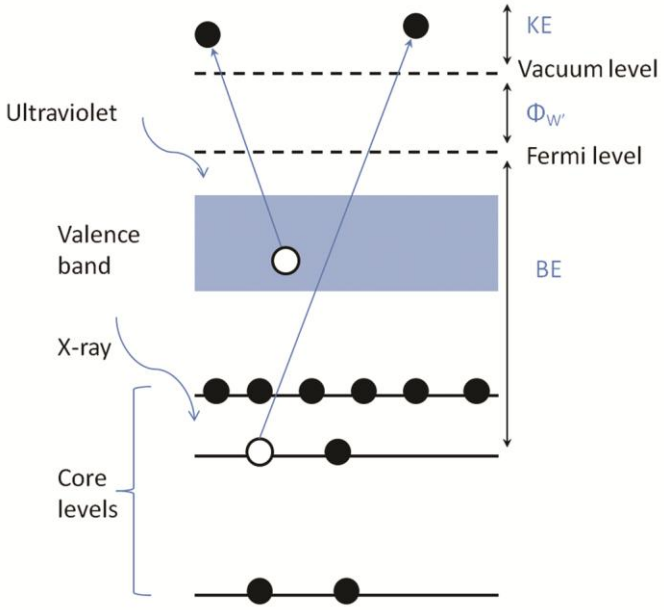

Figure 3.9. Illustration of electron excitations in XPS and UPS, where $\Phi_{W'}$ is the work function of the sample.

3.4.2 X-ray photoelectron spectroscopy

The XPS system used in this study was equipped with a VG XR3E2 dual anode x-ray source, with Mg and Al sources. The electrons emitted from the hot filament were accelerated in a 13kV electric field to strike the Mg or Al coated anode, which emitted Mg Kα (=1253.6 eV) or Al Kα (=1486.6 eV) x-rays respectively. The core level electrons excited by high energy x-rays within the ~5-10 nm sample depth could escape from the sample surface. A VG Microtech Clam II analyzer was operated at FAT mode with a pass

energy of 20 eV and a resolution of 1.0 eV. The binding energy position of the core levels could be resolved to ~ 0.1 eV through the curve fitting of the core level peaks.

3.4.3 Ultraviolet photoelectron spectroscopy

The UPS system was equipped with a VSW 50mm mean radius hemispherical analyzer operated at FAT mode with 15 eV pass energy. The photon source used He I radiation generated from research grade He gas in an UV discharge lamp operated at 1 kV and a 20 mA discharge current. During the measurement, the VSW HAC 300 controller operated at an energy resolution of 0.15 eV was used to scan the kinetic energy range from 26 to 4 eV with 0.1 eV steps when applying a negative 8 V bias to the sample. The valence band maximum (VBM) of the semiconductor could be determined by the binding energy difference between the low binding energy cut-off of the UPS spectra and the Fermi level. In addition, the electron affinity of the semiconductor could be calculated using the following equation:

$$\chi = h\nu - W - E_g \tag{3.3}$$

where hν is the ultraviolet photon energy; W is the spectrum width; and E_g is the band gap of the semiconductor.

3.4.4 Calibration of x-ray and ultraviolet photoemission spectroscopy

It is of great importance to calibrate the XPS and UPS system routinely to make sure the obtained binding energy positions are consistent. There are normally two ways to

calibrate the systems: one is to measure the core level peak of a standard sample (e.g., clean gold foil) and align it to its standard position as recorded in the literature; another method is to align the Fermi level to zero binding energy position. For XPS system calibration, the first method was employed. Fig. 3.10 shows the Au $4f_{7/2}$ peak of a clean gold foil excited by Mg and Al x-rays, which gave a binding energy position of 84.1 and 84.2 eV, respectively. Considering the standard binding energy position for Au $4f_{7/2}$ peak should be at 84.0 eV, the calibration was suggested to be -0.1 and -0.2 eV for Mg and Al source respectively.

For UPS calibration, the second method was used due to the clear cut-off at the Fermi level (e.g., clean gold foil) in the spectra. Since the obtained spectra were usually expressed as signal intensity vs photoelectron kinetic energy, Eq. 3.2 was used to convert the kinetic energy of the photoelectron to its binding energy, which suggested the work function of the spectrometer had to be calibrated. Fig 3.11 shows the He I UPS result of the high kinetic energy cut-off region of a clean gold foil with -8V bias, which indicated that the Fermi level position obtained by the intersection at A or B was at 24.9 ± 0.05 eV. By using Eq. 3.2, the work function of the spectrometer was calibrated to be 4.3 eV.

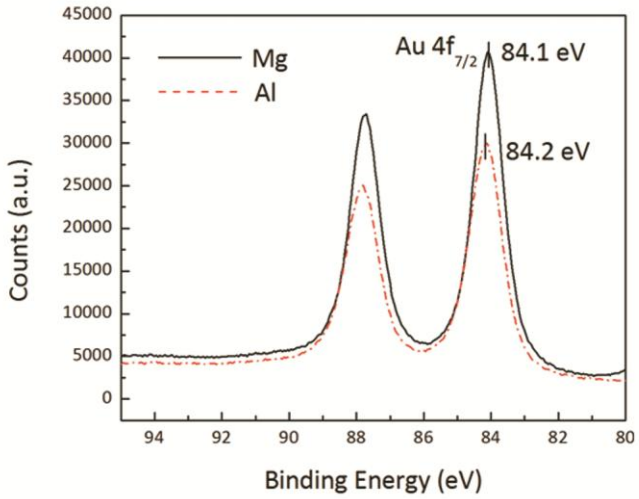

Figure 3.10. The XPS Au $4f_{7/2}$ peak of clean gold foil using Mg and Al Kα x-ray source.

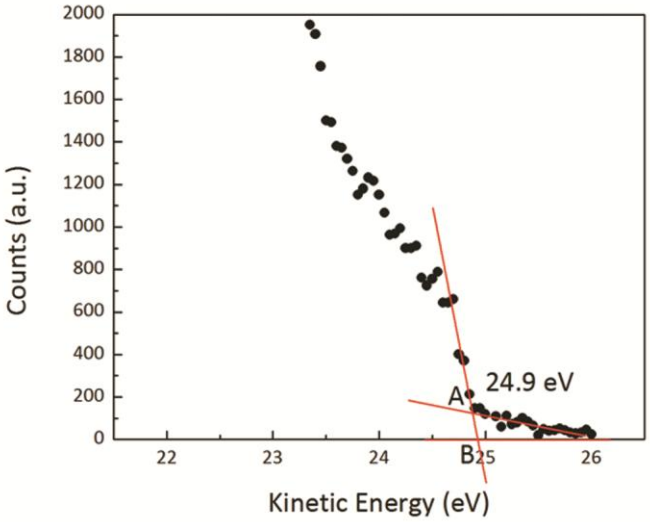

Figure 3.11. The He I UPS result of the high kinetic energy cut-off region of a clean gold foil.

3.5 Band Alignment Measurement Method

To determine the valence band offset (VBO) of dielectrics on GaN, the following relation proposed by Waldrop and Grant [6], and Kraut [7] *et al.* is used in this study.

$$\Delta E_V = (E_{CL} - E_V)_{GaN} - (E_{CL} - E_V)_{dielectric} + \Delta E_{CL} \quad (3.4)$$

Where ΔE_V is the VBO; $(E_{CL}\text{-}E_V)_{GaN}$ and $(E_{CL}\text{-}E_V)_{dielectric}$ are the binding energy difference between the core level and VBM in GaN and dielectric respectively; and ΔE_{CL} is the subsequent binding energy difference in the core levels of the dielectric and GaN. The value of $(E_{CL}\text{-}E_V)_{GaN\ or\ dielectric}$ is constant and virtually independent of band bending.

Fig 3.12 shows a case study of the VBO determination of Al_2O_3 on GaN. The binding energy difference between Ga 3d and VBM in GaN is presumed to be 17.8 eV, which has been reported by Waldrop and Grant [6]. After Al_2O_3 deposition, the XPS was used to measure the Ga 3d and Al 2p core levels, and the UPS was then used to measure the valence band electronic structure, including the VBM relative to the Fermi level and electron affinity. This gives the information about the GaN surface band bending and the value of $\Delta E_{Al\ 2p\text{-}Ga\ 3d}$ and $(E_{Al\ 2p}\text{-}E_V)_{Al2O3}$. Subsequently, the VBO of Al_2O_3 on GaN could be calculated according to Eq. 3.4.

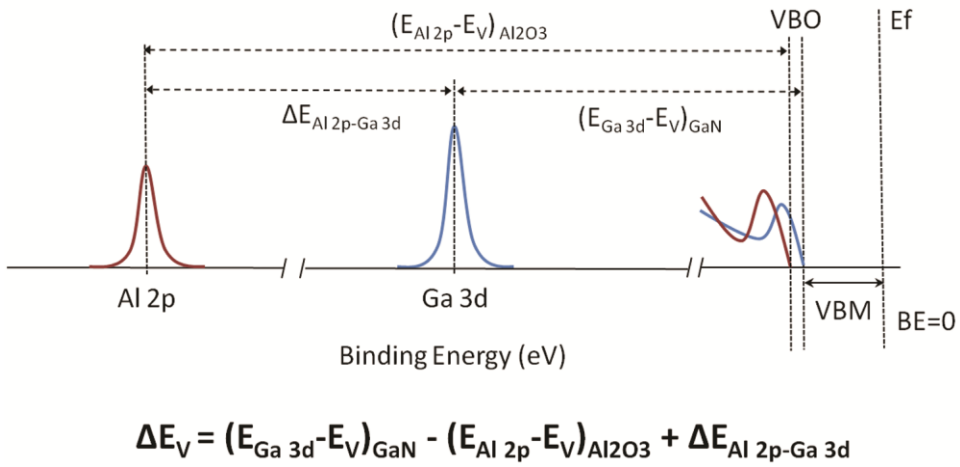

Figure 3.12. The illustration of VBO determination of Al_2O_3 on GaN.

For other PEALD dielectrics investigated in this study, the core levels used in the band offset calculation were Hf $4f_{7/2}$ in HfO_2, Si 2s in SiO_2, La $3d_{5/2}$ in La_2O_3, and Zn 3d in ZnO. Once the values of the binding energy differences between the core level and VBM in the dielectrics are determined, the VBO could be calculated by only measuring the binding energy differences of the dielectrics and GaN core levels using XPS.

The conduction band offset (CBO) of dielectrics on GaN could be calculated by the following equation.

$$\Delta E_C = E_{g,dielectric} - E_{g,GaN} - \Delta E_V \tag{3.5}$$

Where ΔE_C is the CBO; and $E_{g,dielectric}$ and $E_{g,GaN}$ is the band gap of dielectric and GaN, respectively. GaN has an energy band gap of 3.4 eV, which will be used in this study directly. For dielectric (oxide), the energy band gap could be measured from XPS O 1s

energy loss spectroscopy (ELS). The photoexcited O 1s electrons can suffer energy loss due to single particle excitations (band to band transitions) and collective oscillations (plasmons) [8,9]. The plasmon loss exhibits a broad and smooth spectral related to the O 1s core level peak with a shift to higher binding energy by the plasmon energy. After aligning the O 1s core level to zero binding energy, the onset energy of electron excitations from valence band to conduction band indicates the energy band gap of the dielectrics. Therefore, both valence and conduction band offset could be measured by photoemission spectroscopy system.

References

[1] H. B. Profijt, S. E. Potts, M. C. M. van de Sanden, and W. M. M. Kessels, *J. Vac. Sci. Technol. A* **29**, 050801 (2011).

[2] R. L. Puurunen, *J. Appl. Phys.* **97**, 121301 (2005).

[3] J. W. Lim and S. Yun, *Electrochem. Solid-State Lett.* **7**, F45 (2004).

[4] J. Yang, B.S. Eller, M. Kaur, and R.J. Nemanich, *J. Vac. Sci. Technol. A*. **32**, 021514 (2014).

[5] D. Briggs, et. al., Practical Surface Analysis, Vol. 1 Auger and X-ray Photoelectron Spectroscopy, 2nd edition (John Wiley & Sons, West Sussex, 1990).

[6] J. R. Waldrop and R. W. Grant, *Appl. Phys. Lett*. **68**, 2879 (1996).

[7] E. A. Kraut, R. W. Grant, J. R. Waldrop and S. P. Kowalczyk, *Heterojunction Band Discontinuities: Physics and Device Applications*, edited by F. Capasso and G. Margaritondo (Elsevier, New York, 1987).

[8] F. G. Bell and L. Ley, *Phys. Rev. B* **37**, 8383 (1988).

[9] H. Nohira, W. Tsai, W. Besling, E. Young, J. Petry, T. Conard, W. Vandervorst, S. De Gendt, M. Heyns, J. Maes, and M. Tuominen, *J. Non-Cryst. Solids* **303**, 83 (2002).

CHAPTER 4

CHARACTERIZATION OF PLASMA-ENHANCED ATOMIC LAYER DEPOSITION OF ALUMINUM OXIDE USING DIMETHYLALUMINUM ISOPROPOXIDE

4.1 Abstract

In this research, Al_2O_3 films were grown by remote plasma-enhanced atomic layer deposition (PEALD) using a non-pyrophoric precursor, dimethylaluminum isopropoxide (DMAI), and oxygen plasma. After optimization, the growth rate was determined to be ~1.5 Å/cycle within a growth window of 25-220 ℃; the higher growth rate than reported for thermal ALD was ascribed to the higher reactivity of the plasma species compared with H_2O and the adsorption of active oxygen at the surface, which was residual from the oxygen plasma exposure. Both effects enhance DMAI chemisorption and increase the saturation density. In addition, a longer oxygen plasma time was required at room temperature to complete the reaction and decrease the carbon contamination below the detection limit of x-ray photoemission spectroscopy. The properties of the subsequent Al_2O_3 films were measured for different temperatures. When deposited at 25 ℃ and 200 ℃, the Al_2O_3 films demonstrated a single Al-O bonding state as measured by x-ray photoemission spectroscopy, a similar band gap of 6.8 ± 0.2 eV as determined by energy loss spectroscopy, a similar index of refraction of 1.62 ± 0.02 as determined by spectroscopic ellipsometry, and uniform growth with a similar surface roughness before and after growth as confirmed by atomic force microscopy. However, the room

temperature deposited Al_2O_3 films had a lower mass density (2.7g/cm^3 compared with 3.0 g/cm^3) and a higher atomic ratio of O to Al (2.1 compared with 1.6) as indicated by x-ray reflectivity and Rutherford backscattering spectroscopy, respectively.

4.2 Introduction

Thin films of Al_2O_3 have been used as dielectric layers for Si and III-V microelectronics. [1 - 5]. The potential of Al_2O_3 for this application is linked to advantageous dielectric properties such as a large band gap (~6.5 eV) [6,7], relatively high dielectric constant (~8) [1,8], high breakdown field (~10 MV/cm), chemical and thermal stability, and adhesion to many surfaces. In addition to metal-oxide-semiconductor structures, Al_2O_3 has also been considered for a range of applications, including corrosion protection on metallic substrates [9,10], passivation of solar cells [11,12], coatings of optical devices [13,14], and diffusion barriers in organic electronics [15,16]. Given the significant potential and range of applications associated with Al_2O_3, there has been considerable effort during the last several decades to establish and develop methods for Al_2O_3 deposition, including chemical vapor deposition (CVD) [17], physical vapor deposition (PVD) [15], and, one of the most promising, atomic layer deposition (ALD). ALD has often been preferred as an advanced thin film deposition technique due to the high-quality films obtained. More specifically, ALD films have been achieved at low temperatures with low impurity content and uniform and conformal coverage [18,19].

ALD is based on the sequential use of gas phase chemical processes [1,18]; assuming a binary reaction mechanism, there are two precursors that interact with the

surface independently as they are separated by purge steps. Consequently, this process results in flux-independent, self-limiting, layer-by-layer deposition with precise atomic-scale thickness control of conformal and uniform films on large diameter and/or high aspect ratio substrates [18,20]. Explicitly, this ALD process includes the following four steps: first, a self-limiting reaction between the surface -OH groups and precursor; second, a purge step to remove non-reacted precursor and gaseous by-products; third, a self-limiting reaction between a H_2O reactant and the surface groups; and lastly, a second purge step, resulting in a fresh starting surface for subsequent cycles.

For ALD of Al_2O_3, the binary reaction between trimethylaluminum (TMA, $Al(CH_3)_3$) and H_2O in thermal ALD remains one of the most extensively studied [1,18].

$$\mathrm{II}-OH_{(ads)} + Al(CH_3)_{3(g)} \rightarrow \mathrm{II}-OAl(CH_3)_{2(ads)} + CH_{4(g)}$$

$$\mathrm{II}-Al(CH_3)_{(ads)} + H_2O_{(g)} \rightarrow \mathrm{II}-Al(OH)_{(ads)} + CH_{4(g)} \qquad (4.1)$$

In these equations, "II-" represents surface bound species, "ads" chemisorbed molecules, and "g" gas phase chemicals and by-products. This is an advantageous process as the reactivity results in self-limiting behavior. Furthermore, TMA is thermally stable with a high vapor pressure at room temperature (9 Torr at 16.8 ℃ [21]) leading to reliable chemisorption, and the by-products of the reaction (e.g. CH_4) do not interfere with the deposition or purity of the film.

Despite the extensive use of TMA-based ALD processes, the safety of TMA remains a concern; it is not only pyrophoric but also highly reactive with H_2O. Reports from Eindhoven University of Technology have presented a detailed study of ALD Al_2O_3 using TMA [22 - 25] and alternative non-pyrophoric precursor, dimethylaluminum isopropoxide (DMAI, $[(CH_3)_2AlOCH(CH_3)_2]_2$) [21].

The properties of TMA and DMAI have been reported [21]. DMAI has a vapor pressure appropriate for ALD processes, it is not pyrophoric, and it is more stable than TMA. Unlike TMA, DMAI is not a symmetric molecule. Thus, there are several surface reactions that may occur during ALD deposition; the most likely have been reported as:

$$\mathrm{II}-OH_{(ads)} + \tfrac{1}{2}[(CH_3)_2 AlOCH(CH_3)_2]_{2(g)} \rightarrow \mathrm{II}-OAl(CH_3)OCH(CH_3)_{2(ads)} + CH_{4(g)}$$

$$\mathrm{II}-AlOCH(CH_3)_{2(ads)} + H_2O \rightarrow \mathrm{II}-Al(OH)_{(ads)} + HOCH(CH_3)_{2(g)} \qquad (4.2)$$

and/or

$$\mathrm{II}-OH_{(ads)} + \tfrac{1}{2}[(CH_3)_2 AlOCH(CH_3)_2]_{2(g)} \rightarrow \mathrm{II}-OAl(CH_3)_{2(ads)} + HOCH(CH_3)_{2(g)}$$

$$\mathrm{II}-Al(CH_3)_{(ads)} + H_2O_{(g)} \rightarrow \mathrm{II}-Al(OH)_{(ads)} + CH_{4(g)} \qquad (4.3)$$

Evidence suggests that these different surface reactions (e.g. Eq. 4.2 and 4.3) occur simultaneously [21].

In addition to altering the precursor, researchers at Eindhoven University of Technology have also evaluated the effects of various oxidizers. The study was

completed using both TMA and DMAI to deposit Al_2O_3 in plasma enhanced atomic layer deposition (PEALD). PEALD is an energy enhanced ALD method [3,19] that uses an activated plasma species (e.g. O_2*, O*) as the oxidizer rather than H_2O. The plasma process offers advantages over the thermal process, where the reactivity of the oxygen species results in not only an increased growth rate and film density but also a decreased impurity concentration and growth temperature [26,27]. Consequently, PEALD with O_2 plasma allows for a wider range of substrates that may require a low temperature deposition process, such as plastic based flexible displays and polymers [28,29], as well as more stable precursors that may not be reactive with H_2O [19]. Additionally, O_2 is more readily purged than H_2O, which improves the growth efficiency and reduces cycle time. PEALD also enables better control of film composition than thermal ALD as the technique permits the admixing of gases into the plasma [19,26] or adjusting other parameters such as plasma power and working pressure [19,30,31].

For plasma-enhanced atomic layer deposition, Langereis and Potts *et al*. [23,21] identified the following reactions using TMA as:

$$\mathrm{II}-OH_{(ads)} + Al(CH_3)_{3(g)} \rightarrow \mathrm{II}-OAl(CH_3)_{2(ads)} + CH_{4(g)}$$

$$\mathrm{II}-Al(CH_3)_{(ads)} + 4O^*_{(g)} \rightarrow \mathrm{II}-Al(OH)_{(ads)} + H_2O_{(g)} + CO_{2(g)} \qquad (4.4)$$

and DMAI as:

$$\mathrm{II}-OH_{(ads)} + \tfrac{1}{2}[(CH_3)_2 AlOCH(CH_3)_2]_{2(g)} \rightarrow \mathrm{II}-OAl(CH_3)OCH(CH_3)_{2(ads)} + CH_{4(g)}$$

$$\mathrm{II}-AlOCH(CH_3)_{2(ads)} + 9O^*_{(g)} \rightarrow \mathrm{II}-Al(OH)_{(ads)} + 3H_2O_{(g)} + 3CO_{2(g)} \quad (4.5)$$

and/or

$$\text{II}-OH_{(ads)} + \tfrac{1}{2}[(CH_3)_2 AlOCH(CH_3)_2]_{2(g)} \rightarrow \text{II}-OAl(CH_3)_{2(ads)} + HOCH(CH_3)_{2(g)}$$

$$\text{II}-Al(CH_3)_{(ads)} + 4O^*_{(g)} \rightarrow \text{II}-Al(OH)_{(ads)} + H_2O_{(g)} + CO_{2(g)} \quad (4.6)$$

where these two binary reactions (e.g. Eq. 5 and 6) are likely to occur simultaneously [21]. This indicates that the surface is presumable terminated by -OH groups after O_2 plasma exposure.

While plasma-enhanced ALD processes have the potential to alter the chemical reactions and the surface reaction mechanisms, there are a range of results that appear inconsistent. For instance, thermal ALD with DMAI has a reported Al_2O_3 growth rate that is greater than that for PEALD with DMAI [21]. More significantly, the growth rate of Al_2O_3 using PEALD and DMAI (~0.9-1.2 Å/cycle) has been reported to be lower than PEALD using TMA (1.4 Å/cycle) [21,32]. XPS studies of the different films have shown multiple O bonding configurations and in some cases multiple Al bonding configurations [21]. The same studies have shown differences in the residual carbon concentrations.

Even with the extensive prior studies, there is still disagreement or apparently conflicting results on (1) the PEALD growth rate using DMAI; (2) the bonding configurations of the deposited Al atoms; and (3) the presence of carbon impurities. These uncertainties may have limited the acceptance of DMAI for ALD applications.

In this research, the uncertainties noted above have been addressed through a detailed study of PEALD-DMAI Al_2O_3 film deposition with a specific focus on the O_2

plasma conditions, which has not been extensively reported to date. In addition, this study includes results on film morphology and band gap measurement to better characterize the films. Our results establish that the growth rate of the PEALD DMAI process could be equivalent to the PEALD TMA process; the growth rate of the plasma process could be higher than the thermal process; the films exhibit predominantly a single Al bonding configuration; the carbon contamination could be reduced to the x-ray photoemission spectroscopy (XPS) detection limit; the film morphology reflected the substrate roughness; and the band gap was comparable to the ALD Al_2O_3 using TMA.

4.3 Experiment

Al_2O_3 films were deposited by remote PEALD using DMAI and O_2 plasma on oxidized n-type Si (100) substrates. The PEALD Al_2O_3 was completed in a custom system shown schematically in Fig. 4.1 [3,33]. The system base pressure was ~$6.0x10^{-9}$ Torr, and during deposition, the pressure increased to ~100 mTorr as controlled by a throttle valve in front of the turbo pump. The DMAI precursor was heated to 90 ℃ in the bubbler to provide sufficient vapor pressure and was delivered to the chamber with an Ar carrier gas at a flow rate of 90 standard cubic centimeters per minute (sccm). To prevent condensation during precursor exposure, the chamber and delivery lines were maintained at ~110 ℃. Research grade N_2 with a flow rate of 35 sccm was used as the purge gas, and UHP grade O_2 with a flow rate of 35 sccm was used as the oxidizer. A 6 s O_2 purge preceded exciting the plasma. The remote plasma was generated by an inductively

coupled rf-source (200 W, 13.56 MHz) ~25 cm above the sample, which reduces the ion concentration while providing a sufficient flux of excited molecular species and radicals.

The timing of the gas pulses and plasma power were first varied to ensure saturated adsorption and self-limiting growth for a substrate temperature expected to be within the growth window. The ALD growth window was then determined, where the substrate temperature was varied between 25 ℃ and 350 ℃ (measured using a thermocouple and infrared pyrometer). For room temperature growth, both the substrate and chamber temperature were reduced to room temperature, but the bubbler and delivery line were maintained at 90 and 110 ℃ to provide consistent vapor pressure and prevent precursor condensation. However, even with the elevated precursor temperature, the thermocouple near the sample consistently indicated room temperature during deposition.

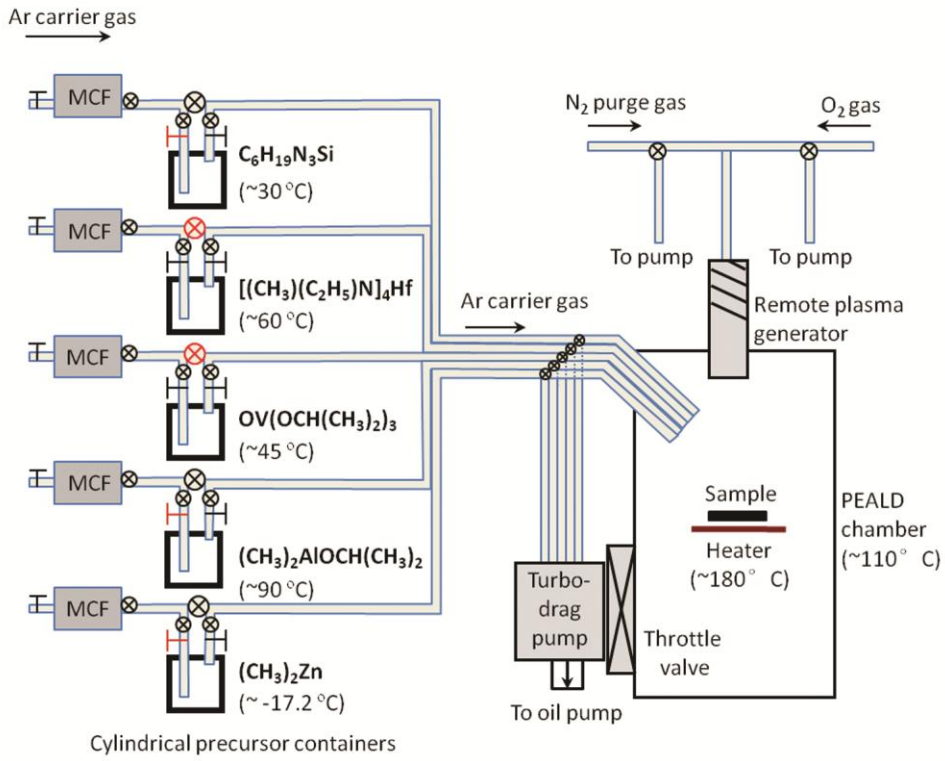

Figure 4.1. Schematic of the remote plasma-enhanced atomic layer deposition chamber.

Film thicknesses were determined with an *in-situ* quartz crystal microbalance (QCM) and XPS core level intensities and corroborated by comparison with *ex-situ* x-ray reflectivity (XRR), Rutherford backscattering spectroscopy (RBS), and spectroscopic ellipsometry (SE). The chemical states and composition of the films were then analyzed using *in-situ* XPS and ultraviolet photoemission spectroscopy (UPS) [3, 34]. Other material properties such as thin film density, surface morphology, index of refraction, and band gap energy were determined from XRR, AFM, SE, and energy loss spectroscopy (ELS), respectively.

4.4 Results and Discussion

4.4.1 PEALD Al_2O_3 growth

A. Self-limiting growth

To ensure uniform and conformal ALD growth, each half-reaction must be fully saturated and self-limiting within the ALD growth window; therefore, PEALD of Al_2O_3 using DMAI was first optimized with regards to the timing of the reactants and purge gases for a substrate temperature of 200 ℃, which was within the reported growth window [21,32].

As shown in Fig. 4.2a, the growth rate of Al_2O_3 at 200 ℃ reached self-limiting behavior when the DMAI precursor pulse was ≥0.2 s, the O_2 plasma was generated for ≥6 s, and the N_2 purge time was ≥18 s. Therefore, a 0.6 s DMAI precursor pulse and 8 s O_2 plasma exposure were employed for other processes at 200 ℃. This timing ensured DMAI chemisorption was saturated, and O_2 plasma reacted fully with the adsorbed species at this temperature. A longer N_2 pulse time (20 s) was chosen to ensure ample purge time, thus limiting CVD-like reactions between the reactants and removing gas-phase by-products from the chamber. The relationship between the growth rate and O_2 plasma power was also investigated in this study as shown in Fig. 4.2b. The results indicated that the growth rate increased with plasma power between 30 to 150 W and stabilized for power >150 W. Consequently, a plasma power of 200 W was adopted for subsequent growth conditions.

Film thicknesses, and thus the growth per cycle (GPC), were determined *in-situ* by QCM and XPS core level intensities. These measurements were then corroborated with XRR, RBS, and SE of thicker Al_2O_3 films (>25 nm) grown under the same

conditions. Fig. 4.3 shows the XRR data for 200 cycles Al_2O_3 deposited at 200 ℃, indicating a film thickness of 30.4 nm. These results thus imply a GPC of ~1.5 Å/cycle.

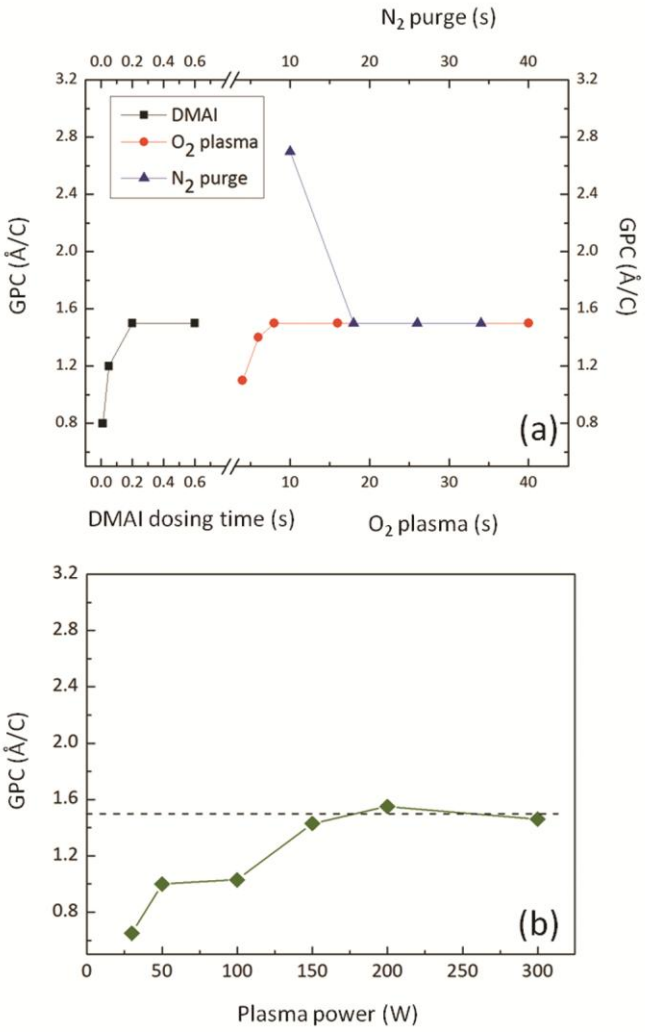

Figure 4.2. Al_2O_3 growth rate vs. (a) DMAI dose time (aquare), N_2 purge time (triagnle), and O_2 plasma exposure time (circle); (b) vs. plasma power (diamond) at a substrate temperature of 200 ℃.

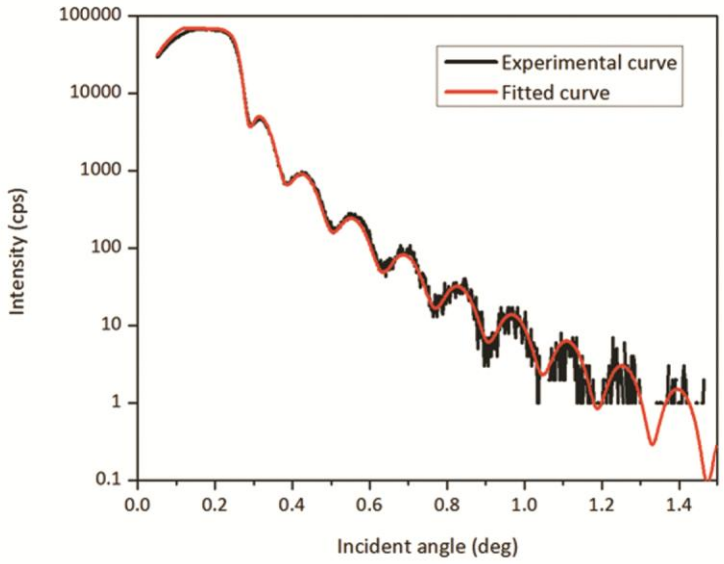

Figure 4.3. XRR of ~30 nm Al_2O_3 film deposited with optimized growth parameters on Si. The line with noise refers to the measured data, and the smooth line refers to the fitted results.

This growth rate is higher than the growth rates measured by other groups using DMAI for thermal ALD, ~0.7-1.2 Å/cycle at temperatures ~150-200 ℃ [21,35]. The larger growth rate associated with PEALD has been previously documented and related to the higher reactivity of the oxygen species compared with H_2O and active oxygen groups remaining on the surface after the plasma step [21,24,26,36]. There are three mechanisms that could account for the increased growth rate [21,26,36]: an increase in the reactivity of the oxygen species, an increase in the density of surface reactive sites, and/or a reduction of steric hindrance, where the ligands of the DMAI monomer or dimer (e.g. isopropoxide group) overlap with available reactive sites and prevent chemisorptions [21,37, 38]. The increased reactivity represents an increase in the kinetics of the process, while the other effects increase the available absorption sites. The excess

active oxygen groups, perhaps -OH groups, could serve as additional reactive sites and thus increase the density of chemisorbed DMAI molecules. In addition, the active oxygen species could react with ligands from depositing precursor molecules thus reducing steric hindrance and exposing additional reactive sites for chemisorption or generating additional surface sites. Consequently, the active oxygen plasma species could accelerate the surface reactions, increase the surface density of -OH sites, and/or reduce steric hindrance through reactions with precursor ligands. This hypothesis may also explain the relationship between the growth rate and O_2 plasma power, where the increase in plasma power increases the concentration of activated oxygen species and thus the growth rate. Under the experimental conditions, the PEALD growth rate using DMAI was improved by 30-80% compared with some prior studies [21,32], and is then comparable with PEALD using a TMA process (1.4 Å/cycle) [32].

One of the concerns about the enhanced growth rate of PEALD is that it could result in non-uniform growth. AFM was thus used to determine the morphology of the surfaces before and after growth of 6 nm and 33 nm thick PEALD Al_2O_3 films grown at 200 °C and 25 °C, respectively. These results are shown in Fig. 4.4. The RMS roughness was ~0.77±0.05 nm for the cleaned Si wafer (Fig. 4.4a), 0.76±0.05 nm for Al_2O_3 films grown at 200 °C (Fig. 4.4b), and 0.86±0.05 nm for Al_2O_3 films deposited at 25 °C (Fig 4.4c). These results indicated uniform and conformal deposition of Al_2O_3 films, where neither the O_2 plasma nor the increased growth rate resulted in increased surface roughness.

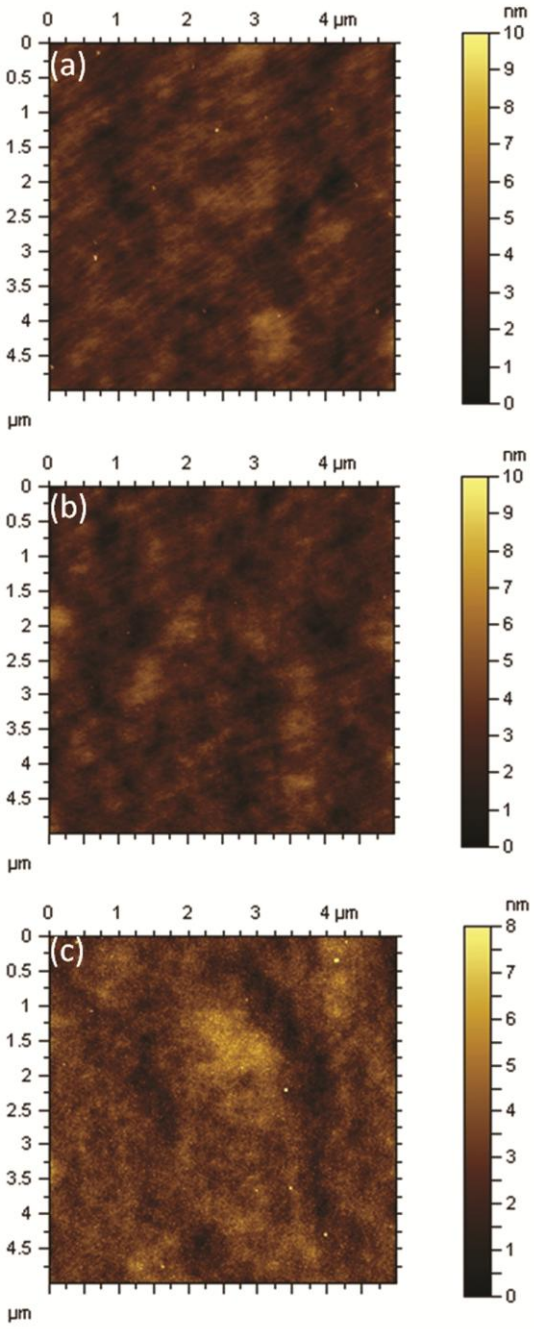

Figure 4.4. AFM images of (a) degreased Si wafer, (b) as-grown 6 nm Al_2O_3 film deposited at 200 ℃, and (c) as-grown 33 nm Al_2O_3 film deposited at 25 ℃. Images are 5 µm x 5 µm. The RMS roughnesses were ~0.77±0.05, 0.76±0.05, and 0.86±0.05 nm, respectively.

B. PEALD growth window

To further explore the growth properties at different conditions, the number of Al atoms deposited per cycle at different growth temperatures was determined by RBS and the results are shown in Fig. 4.5a. The Al atoms deposited per cycle increased with temperature above 200 ℃, and decreased when the temperature was reduced below 100 ℃. Within the temperature range of 150-200 ℃, the Al atoms deposited per cycle was similar.

The substrate temperature growth window was also investigated. As shown in Fig 4.6, these growth conditions resulted in a PEALD temperature window of ~25 to 220 ℃. Within the temperature window, the growth is self-limiting with a constant growth rate, as shown by the linear relationship between the film thickness and number of PEALD cycles at 200 ℃. At temperatures >220 ℃, the growth rate increased with substrate temperature, suggesting DMAI thermally decomposed on the surface. In contrast, at room temperature, the growth rate was slightly reduced, suggesting an incomplete reaction. In this case, an incomplete reaction could refer to when DMAI molecules were not effectively bonded to the surface groups and thus purged out of the chamber, and/or the O_2 plasma did not complete the oxidation reaction as a result of insufficient thermal energy.

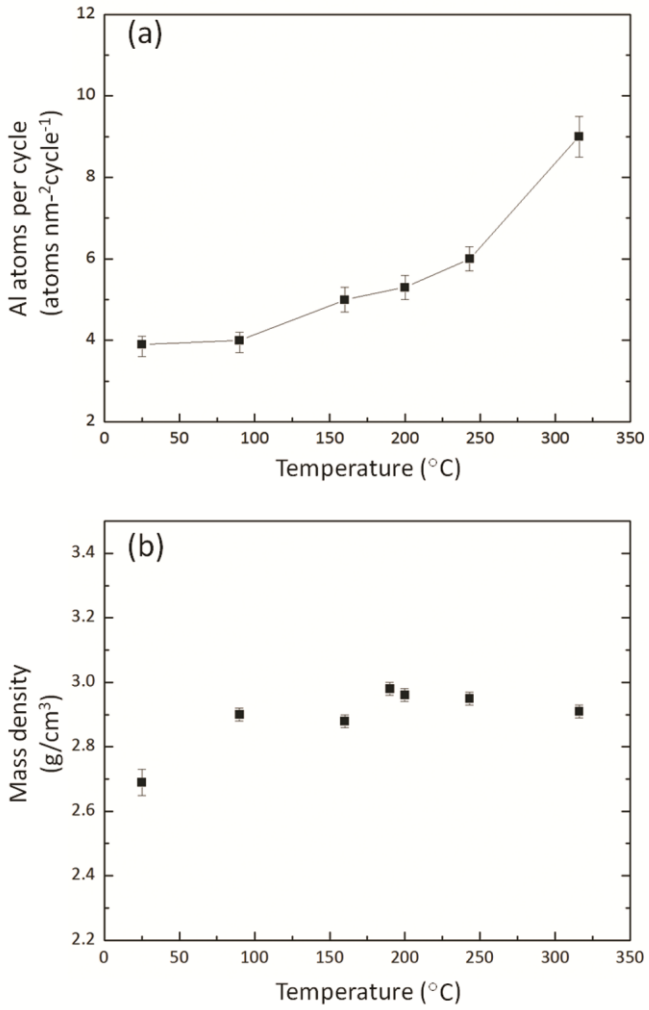

Figure 4.5. The number of Al atoms deposited per cycle (a) as determined by RBS and the film mass density, and (b) as measured by XRR for PEALD Al_2O_3 film using DMAI at different deposition temperatures.

For the room temperature growth, if the DMAI chemisorption was not complete, then increasing the DMAI pulse time may lead to an increased growth rate. Conversely, if the incomplete reactions were limited by the oxidation process, then increasing the oxygen plasma exposure could lead to an increased growth rate. To investigate this point,

Al_2O_3 films were grown with an increased DMAI dosing time of 1.2 s and N_2 purge time of 30-50 s to prevent CVD-like reactions. These deposition parameters again resulted in a growth rate of ~1.4 Å/cycle at room temperature, which suggested the longer DMAI dose time did not increase the DMAI chemisorption at this temperature. (The growth rate of Al_2O_3 at 200 ℃ under these same conditions remained at 1.5 Å/cycle, further confirming saturation at 200 ℃). On the other hand, increasing the O_2 plasma exposure from 8 to 40 s increased the 25 ℃ Al_2O_3 growth rate by ~10% to ~1.5 Å/cycle. This suggested that a longer oxygen plasma time is required to drive the chemical reaction at the lower temperature.

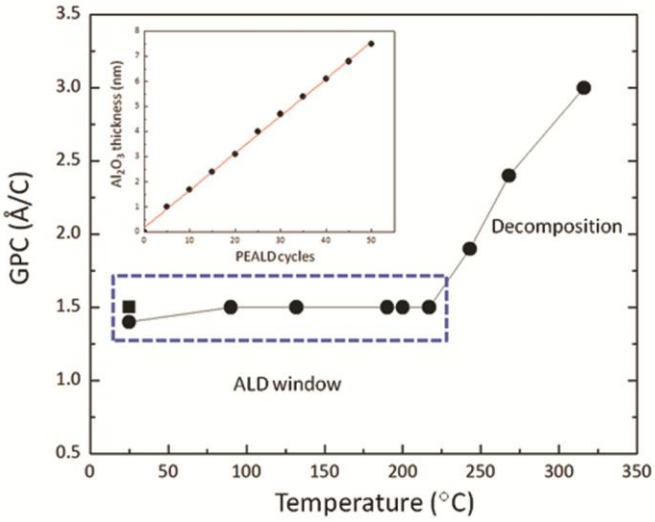

Figure 4.6. Al_2O_3 growth rate vs. substrate temperature, determining the ALD window of 25 to 220 ℃. The square represents the increased growth rate with the longer plasma pulse time. The inset shows the film thickness vs. number of PEALD cycles for the sample at 200 ℃.

Comparing the Al_2O_3 films deposited at 25 ℃ and 200 ℃, even though the concentration of Al atoms per cycle deposited at 25 ℃ was 26% smaller than that at 200 ℃ (3.9 ± 0.2 at.nm^{-2}cycle^{-1} compared with 5.3 ± 0.3 at.nm^{-2}cycle^{-1}), the growth rates were similar. Other characteristics of the 25 ℃ growth were a 10% lower film density (~2.7 g/cm^3 compared with 3.0 g/cm^3) and higher O to Al ratio (2.1 compared with 1.6) compared to the 200 ℃ growth. The molar mass for films deposited at 25 ℃ and 200 ℃ would be defined by the formula weight of the films. At 25 ℃ the $Al_2O_{4.2}$ formula mass is 15.2 % larger than that of $Al_2O_{3.2}$ at 200 ℃. Consequently this analysis suggests a growth rate of 1.5 Å/cycle at 200 ℃ and a growth rate of ~1.4 Å/cycle at 25 ℃, which are consistent with the measured results. Consequently, the higher O to Al atomic ratio and lower thin film density compensate for the lower value of Al atoms deposited per cycle and similar growth rates are obtained at both 25 and 200 ℃.

Given the complicated relationship between the deposition parameters and the growth window, it is difficult to compare growth rates across studies. For example, for PEALD using DMAI, one study reported a growth rate of ~0.9 Å/cycle within 25-400 ℃ [21], while another reported 1.2 Å/cycle within 160-250 ℃ [32]. Both vary from the results reported in this study. These differences in growth rate may be due to the different plasma power, plasma time, flow rate, chamber pressure, equipment setup, all of which may affect the concentration of active oxygen plasma species and thus the growth rate, or the different bubbler temperature. It is evident that a more systematic approach needs to be taken. Unfortunately, these factors are often overlooked, and thus, such disparities in growth rate and window are not uncommon. Even for the well-established TMA-H_2O

process, reported values for the growth rate at some temperatures can fluctuate up to 0.5 Å/cycle [23].

4.4.2 Spectroscopic measurement of thin film properties

Since the atomic ratios and the film densities were dependent on temperature even within the growth window, it was reasonable to suggest that other film properties may also be dependent on the deposition conditions. Thus, additional characterization techniques were used to determine the film properties of Al_2O_3 deposited within the growth window. More specifically, XPS was used to determine film composition and chemical states, ELS to determine the band gap, UPS to determine the electron affinity, and SE to determine the index of refraction. The goal of these measurements was to obtain a better understanding of the relation between deposition parameters and film properties, and ultimately enable tuning of desired film characteristics.

Film composition and impurity concentrations were determined by XPS on three different samples. Fig. 4.7 shows the respective XPS survey scan (a), and core level peaks for C 1s (b), Al 2p (c), and O 1s (d) of (i) an as-grown 10nm Al_2O_3 film deposited at 200 ℃ and (ii) after 600 ℃ annealing, and an as-grown 10nm Al_2O_3 film deposited at 25 ℃ with (iii) 8s and (iv) 40s O_2 plasma exposure durations. In the survey scan, only Al and O signals were evident with the carbon contamination at or below the XPS detection limit. A low C impurity density was indicated for the 200 ℃ PEALD Al_2O_3 growth process as shown in Fig. 4.7b. However, sample (iii) had a weak C peak, which was ascribed to carboxide groups. Compared with sample (iv), the longer oxygen plasma

process led to a reduction of the C peak. Therefore, the conditions of the oxygen plasma can be tuned to improve the film quality and reduce the C impurity density.

Through fitting the peaks with Gaussian-Lorentzian curves, the spectral composition and positions of the Al 2p and O 1s peaks were determined and summarized in Table 4.1. All the samples were characterized by a single Al-O bonding state. This result differs from other results of PEALD Al_2O_3 using DMAI [21], in which $Al(OH)_3$, AlO(OH), and $Al(CO_x)_y$ configurations were detected for room temperature Al_2O_3, but agrees with another study of room temperature ECR-PEALD Al_2O_3 using TMA [39]. The difference in the bonding states and impurities was likely a result of the different plasma conditions.

Table 4.1. XPS Al 2p and O 1s core level of Al_2O_3 films deposited at 200 ℃ and 25 ℃ before and after annealing. The main core levels and shoulder peaks are differentiated with the full width at half maximum (FWHM) included. All energies are given in eV.

Growth Temperature		**As-grown Al_2O_3**				**Annealed Al_2O_3**			
		Main	FWHM	Shoulder	FWHM	Main	FWHM	Shoulder	FWHM
200 ℃	Al 2p	75.2	1.8	-	-	76.4	1.8	-	-
(8s O_2 plasma)	O 1s	531.6	2.1	533.3	2.2	532.9	2.0	535.4	1.7
25 ℃	Al 2p	76.2	1.8	-	-				
(8s O_2 plasma)	O 1s	532.7	2.1	534.0	2.1				
25 ℃	Al 2p	75.3	1.8	-	-	76.6	1.8	-	-
(40s O_2 plasma)	O 1s	531.9	2.1	533.2	2.2	533.2	2.1	535.7	1.9

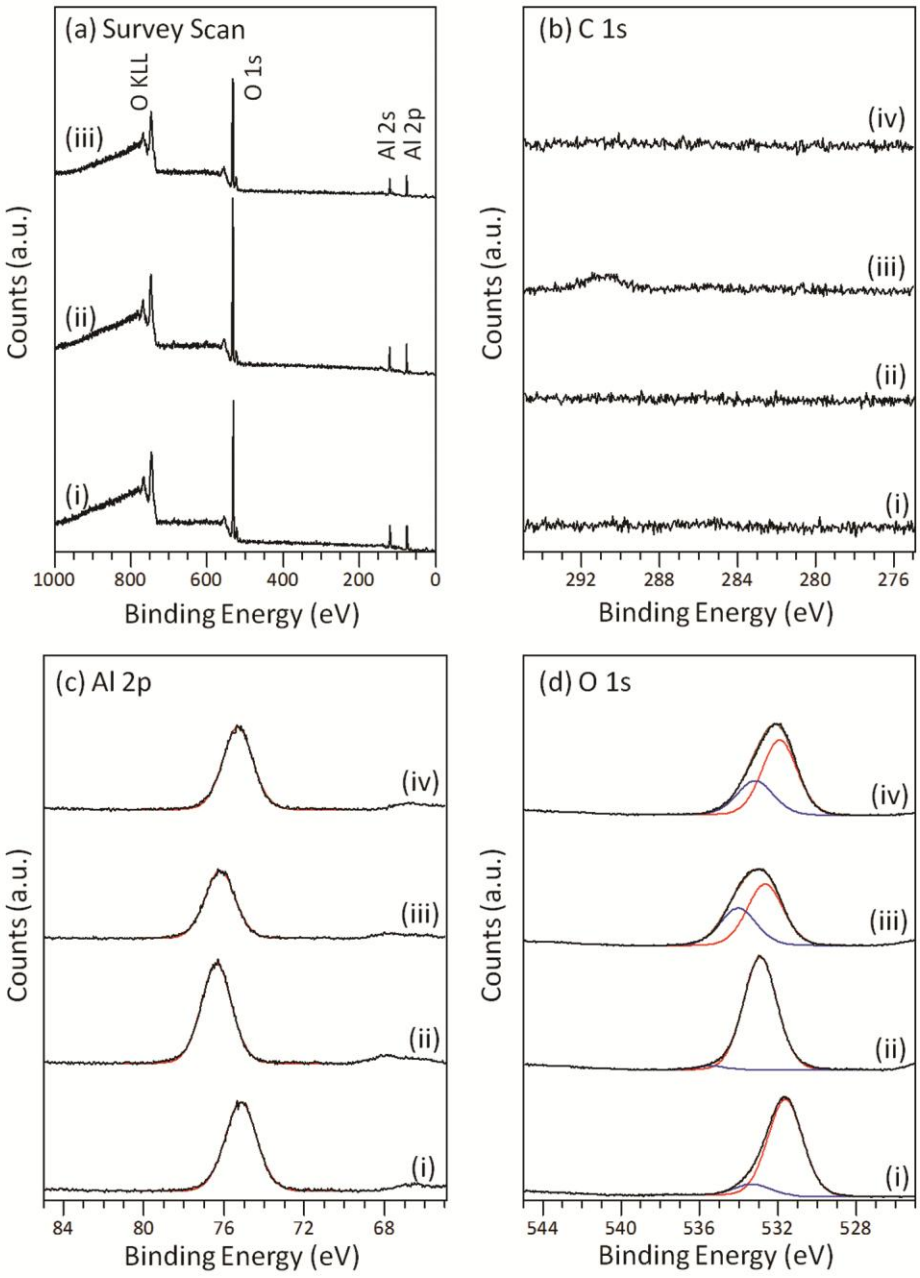

Figure 4.7. The respective XPS survey scans (a), and core level peaks for C 1s (b), Al 2p (c), and O 1s (d) of (i) an as-grown 10nm Al_2O_3 film deposited at 200 ℃ and (ii) after 600 ℃ annealing, and as-grown 10nm Al_2O_3 films deposited at 25 ℃ with (iii) 8s and (iv) 40s O_2 plasma exposure durations.

On the other hand, the O 1s peaks showed evidence of multiple oxygen bonding states with a distinct shoulder peak at higher binding energy. This peak was likely due to excess oxygen in the film, probably –OH groups. For the 25 ℃ Al_2O_3 film, the O 1s peak was much broader than that of the 200 ℃ Al_2O_3 film, which indicated an enhanced oxygen concentration. There may also be a small amount of carbon-based oxide groups, which could be reduced by the longer oxygen plasma process. The increased oxygen concentration was evident in the O to Al atomic ratio, which varied from ~2.1 to 1.9 for the 8 and 40 s O_2 plasma processed 25 ℃ Al_2O_3 films. This is to be compared with ~1.6 for the 200 ℃ Al_2O_3 film. It has been suggested that the -OH groups may not be readily removed at lower temperatures [21], which potentially accounts for the increased oxygen concentration.

The Al 2p and O 1s peak positions were not the same for all the samples. However, the binding energy difference between these two peaks was always 456.5±0.1 eV, which indicated the shifts were caused by different band bending in the SiO_2/Si layers. A previous study has suggested the oxygen plasma process could introduce acceptor-like defects, which may lead to electron transfer from the Si substrate and the formation of an electric field across the SiO_2 layer [40,41]. In this study, the core level of the 200 ℃ Al_2O_3 film shifted to higher binding energy by ~1.2 eV after 600 ℃ annealing, suggesting these states could be removed with the annealing process. In the mean time, the relative intensity of the excess oxygen peak decreased from ~10% to 3% after annealing, indicating these acceptor-like states may be related to excess oxygen [40]. For the 25 ℃ Al_2O_3 film, the shorter oxygen plasma exposure time may induce fewer acceptor-like defects, which apparently resulted in reduced shifts.

Additional characterization was completed for Al_2O_3 deposited on Si at 25 ℃ and 200 ℃ as summarized in Table 4.2. ELS was used to determine the band gap. Since ALD Al_2O_3 is amorphous [31,42], the band gap is typically significantly smaller than that of crystalline sapphire (~8.8 eV) and has been shown to be dependent on the growth method [43,44]. In this study, the O 1s ELS was used to deduce the band gap of Al_2O_3 as shown in Fig. 4.8. The O 1s ELS measurement was obtained from a 10 nm Al_2O_3 film deposited on Si at 200 ℃ and annealed at 600 ℃. A fraction of the emitted O 1s photoelectrons suffer energy loss due to collective oscillations (plasmons) and single particle excitations (band to band transitions) [45,46]. The plasmon loss showed a smooth and broad spectral component related to the O 1s core level but shifted to higher binding energy by the plasmon energy. Aligning the O 1s peak to the point of zero energy loss, the onset energy of electron excitations from valence band to conduction band indicated the energy band gap of the films. The band gap was thus determined to be 6.7 ± 0.1 eV. For the annealed, room temperature Al_2O_3 with 40 s O_2 plasma process, the band gap was 6.9 ± 0.1 eV. These values are comparable to other results (6.5-7.0 eV) [6,9,47].

Table 4.2. Al_2O_3 film properties on Si substrates grown by remote PEALD and DMAI at 25 ℃ and 200 ℃

PEALD	**25** ℃	**200** ℃
Growth per cycle	1.5 Å/cycle	1.5 Å/cycle
Al atoms per cycle	3.9 ±0.3 at.nm^{-2}cycle^{-1}	5.3 ±0.3 at.nm^{-2}cycle^{-1}
Mass density	2.69 ±0.04 g/cm^3	2.96 ±0.02 g/cm^3
[O]/[Al] ratio	2.1 ±0.1	1.6 ±0.1
Refractive index (630nm)	1.61 ±0.01	1.63 ±0.02
Band gap	6.9 ±0.1 eV	6.7 ±0.1 eV
Electron affinity	-	2.2 ±0.1 eV

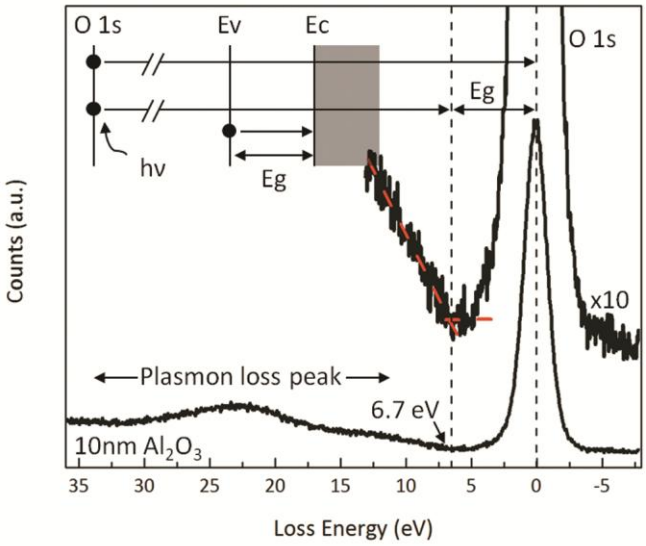

Figure 4.8. O 1s energy loss spectra from 10 nm Al_2O_3 on Si deposited at 200 ℃ and annealed at 600 ℃. The zero loss energy represents the O 1s core level. Ev is the valence band maximum; Ec is the conduction band minimum; and Eg is the band gap [9].

The band gap value could then be used in conjunction with UPS to determine the electron affinity. The UPS spectrum of 1.5nm annealed Al_2O_3 on Si deposited at 200 ℃ shown in Fig. 4.9 is similar to that reported for γ-Al_2O_3 films [48]. The high and low binding energy cutoff could be determined by an extrapolation of a linear fit to the UPS spectrum. The photo threshold energy or ionization energy of VBM electrons was calculated to be 8.9 eV for Al_2O_3 films, which was determined from the energy difference between the photon energy (He I=21.2 eV) and the UPS spectral width (12.3 eV). This is also the sum of the band gap and electron affinity, as shown schematically in Fig. 4.9. Using the measured band gap of Al_2O_3, the electron affinity of Al_2O_3 grown at 200 ℃ was determined to be 2.2±0.1 eV, which is similar to other reports [6,49].

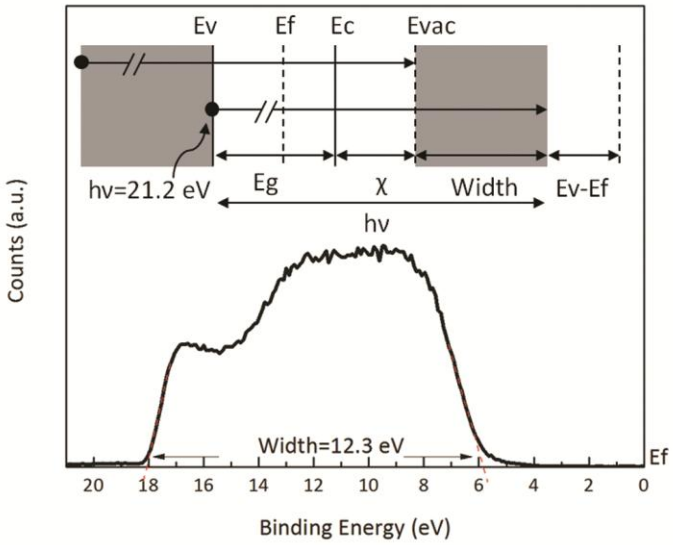

Figure 4.9. UPS scan of 1.5 nm Al_2O_3 on Si deposited at 200 ℃ and annealed at 600 ℃. The zero binding energy represents the Fermi level, and the low energy cutoff is the valence band maximum. Ef is the Fermi level; Evac is the vacuum level; and χ is the electron affinity.

Additionally, the optical properties of the films were determined by SE, where the index of refraction was 1.63±0.02 for films deposited at 200 ℃ and 1.61±0.01 for films deposited at 25 ℃, which was also consistent with reported results (1.62±0.02) for PEALD DMAI Al_2O_3 [21]. This slight increase with temperature also followed a trend for thermal ALD growth of Al_2O_3 (using TMA) [50]. In that case, the index of refraction increased slightly with growth temperature (from 1.57 to 1.60), and a corresponding increase of the film density from 2.7 to 3.0 g/cm^3 was also observed.

4.5 Conclusion

In this study, Al_2O_3 films were grown on Si by remote PEALD using O_2 plasma and DMAI as an alternative to pyrophoric TMA. The growth parameters—including the DMAI pulse time, O_2 plasma exposure time, N_2 purge time, O_2 plasma power, and substrate temperature—were varied to achieve self-limiting saturated growth, giving a growth rate of ~1.5 Å/cycle within the growth window of 25 ℃ to 220 ℃. The growth rate increased with an increase of plasma exposure time and power until the reaction was saturated. This increase was attributed to an increased concentration of active oxygen species on the surface. For deposition at room temperature, a longer plasma pulse time was required to achieve saturated growth. Furthermore, the room temperature deposited Al_2O_3 film with a longer O_2 plasma process displayed a single Al-O bonding state and carbon contamination below the XPS detection limit. Within these optimized growth parameters, conformal, uniform, and nearly stoichiometric Al_2O_3 films were obtained at 200 ℃ with a film density of ~2.96±0.02 g/cm^3, an index of refraction of 1.63±0.2, and a

band gap of 6.7±0.1 eV. Conformal and uniform Al_2O_3 films were also obtained at room temperature with a higher O:Al ratio of 2.1, a film density of ~2.69±0.04 g/cm^3, and an index of refraction of 1.61±0.1. The PEALD-DMAI process, with the significant advantage of a non-pyrophoric precursor, is comparable to PEALD-TMA in both process parameters and film properties.

Reference

[1] M. D. Groner, J. W. Elam , F. H. Fabreguette, and S. M. George, *Thin Solid Films* **413**, 186 (2002).

[2] M. M. Frank, G. D. Wilk, D. Starodub, T. Gustafsson, E. Garfunkel, Y. J. Chabal, J. Grazul, and D. A. Muller, *Appl. Phys. Lett.* **86**, 152904 (2005).

[3] J. Yang, B. S. Eller, C. Zhu, C. England, and R. J. Nemanich, *J. Appl. Phys.* **112**, 053710 (2012).

[4] P. D. Ye, B. Yang, K. K. Ng, J. Bude, G. D. Wilk, S. Halder, and J. C. M. Hwang, *Appl. Phys. Lett.* **86**, 063501 (2005).

[5] B.S. Eller, J. Yang, R.J. Nemanich, *J. Vac. Sci. Technol. A* **31**, 050807 (2013).

[6] E. Bersch, S. Rangan, R. A. Bartynski, E. Garfunkel, and E. Vescovo, *Phys. Rev. B* **78**, 085114 (2008).

[7] N. V. Nguyen, S. Sayan, I. Levin, J. R. Ehrstein, I. J. R. Baumvol, C. Driemeier, C. Krug, L.Wielunski, P. Y. Hung, and A. Diebold, *J. Vac. Sci. Technol. A* **23**, 1706 (2005).

[8] K.-S. An, W. Cho, K. Sung, S. S. Lee, and Y. Kim, *Bull. Korean Chem. Soc.* **24**, 1659 (2003).

[9] R. Matero, M. Ritala, M. Leskelä, T. Salo, J. Aromaa, and O. Forsén, *J. Phys. IV* **9**, 493 (1999).

[10] A. I. Abdulagatov, Y. Yan, J. R. Cooper, Y. Zhang, Z. M. Gibbs, A. S. Cavanagh, R. G. Yang, Y. C. Lee, and S. M. George, *Appl. Mater. Interfaces*, **3**, 4593 (2011).

[11] P. Poodt, A. Lankhorst, F. Roozeboom, K. Spee, D. Maas, *Ad Vermeer*, *Adv. Mater*. **22** 3564 (2010).

[12]C. Prasittichai and J. T. Hupp, *J. Phys. Chem. Lett*. **1** 1611 (2010).

[13] M. D. Groner, S. M. George, R. S. McLean, and P. F. Carcia, *Appl. Phys. Lett.* **88**, 051907 (2006).

[14] Y. Matsuura and J. Harrington, *J. Opt. Soc. Am. A* **14**, 1255 (1997).

[15] R. Thielsch A. Gatto, J. Heber, and N. Kaiser, *Thin Solid Films* **410**, 86 (2002).

[16] P. F. Carcia, R. S. McLean, M. H. Reilly, M. D. Groner, and S. M. George, *Appl. Phys. Lett*. **89**, 031915 (2006).

[17] T. Maruyama and S. Arai, *Appl. Phys. Lett*. **60**, 322 (1992).

[18] R. L. Puurunen, *J. Appl. Phys.* **97**, 121301 (2005).

[19] H. B. Profijt, S. E. Potts, M. C. M. van de Sanden, and W. M. M. Kessels, *J. Vac. Sci. Technol. A* **29**, 050801 (2011).

[20] B. Lee, S.-Y. Park, H.-C. Kim, K. Cho, E. M. Vogel, M. J. Kim, R. M. Wallace, and J. Kim, *Appl. Phys. Lett.* **92**, 203102 (2008).

[21] S. E. Potts, G. Dingemans, C. Lachaud, and W. M. M. Kessels, *J. Vac. Sci. Technol. A* **30**, 021505 (2012).

[22] J. L. van Hemmen, S. B. S. Heil, J. H. Klootwijk, F. Roozeboom, C. J. Hodson, M. C. M. van de Sanden, and W. M. M. Kessels, *J. Electrochem. Soc*. **154**, G165 (2007).

[23] E. Langereis, J. Keijmel, M.C.M. van de Sanden, and W.M.M. Kessels, *Appl. Phys. Lett*. **92**, 231904 (2008).

[24] S. E. Potts, W. Keuning, E. Langereis, G. Dingemans, M. C. M. vande Sanden, and W. M. M. Kessels, *J. Electrochem. Soc.* **157**, 66 (2010).

[25] S. E. Potts, H. B. Profijt, R. Roelofs, and W. M. M. Kessels, *Chem. Vap. Deposition* **19** 125 (2013).

[26] J. W. Lim and S. Yun, *Electrochem. Solid-State Lett.* **7**, F45 (2004).

[27] A. J. M. Mackus, N. Leick, L. Baker, and W. M. M. Kessels, *Chem. Mater.* **24**, 1752 (2012).

[28] S. J. Lim, S. J. Kwon, H. Kim, and J. S. Park, *Appl. Phys. Lett.* **91**, 183517 (2007).

[29] E. Langereis, M. Creatore, S. B. S. Heil, M. C. M. van de Sanden, and W. M. M. Kessels, *Appl. Phys. Lett.* **89**, 081915 (2006).

[30] T. O. Kääriäinen and D. C. Cameron, *Plasma Process. Polym.* **6**, S237 (2009).

[31] J. G. Lee, H. G. Kim, and S. S. Kim, *Thin Solid Films* **534**, 515 (2013).

[32] J. Koo, S. Kim, S. Jeon, H. Jeon, Y. Kim, and Y. Wen, *J. Korean Phys. Soc.* **48**, 131 (2006).

[33] F. Tang, C. Zhu, D. J. Smith, and R. J. Nemanich, *J. Vac. Sci.Technol.A* **30**, 01A147 (2012).

[34] C. Zhu, S.L. Caudle, J. Yang, D.J. Smith, R.J. Nemanich, *J. Vac. Sci. Technol. B* **32**, 011203 (2014).

[35] W. Cho, K. Sung, K.-S. An, S. S. Lee, T.-K. Chung, and Y. Kim, *J. Vac. Sci. Technol. A* **21**, 1366 (2003).

[36] S. B. S. Heil, P. Kudlacek, E. Langereis, R. Engeln, M. C. M. van de Sanden, and W. M. M. Kessels, *Appl. Phys. Lett.* **89**, 131505 (2006).

[37] M. Ritala, M. Leskelä, L. Niinistö, and P. Haussalo, *Chem. Mater*. **5**, 1174 (1993).

[38] S. Y. Lee, B. Luo, Y. Sun, J. M. White, and Y. Kim, *Appl. Surf. Sci.* **222**, 234 (2004).

[39] Y. Xiong, L. Sang, Q. Chen, L. Yang, Z, Wang, Z. Liu, *Plasma Sci and Technol*, **15**, 52 (2013).

[40] C. C. Fulton, T. E. Cook, G. Lucovsky, and R. J. Nemanich, *J. Appl. Phys*. **96**, 2665 (2004).

[41] C. Zhu, D. J. Smith, and R. J. Nemanich, *J. Vac. Sci. Technol. B* **30**, 051807 (2012).

[42] M. L. Huang, Y. C. Chang, C. H. Chang, Y. J. Lee, P. Chang, J. Kwo, T. B. Wu, and M. Hong, *Appl. Phys. Lett*. **87**, 252104 (2005).

[43] I. Costina and R. Franchy, *Appl. Phys. Lett*. **78**, 4139 (2001).

[44] R. H. French, *J. Am. Ceram. Soc*. **73**, 477 (1990).

[45] F. G. Bell and L. Ley, *Phys. Rev. B* **37**, 8383 (1988).

[46] H. Nohira, W. Tsai, W. Besling, E. Young, J. Petry, T. Conard, W. Vandervorst, S. De Gendt, M. Heyns, J. Maes, and M. Tuominen, *J. Non-Cryst. Solids* **303**, 83 (2002).

[47] H. Y. Yu, M. F. Li, B. J. Cho, C. C. Yeo, M. S. Joo, D.-L. Kwong, J. S. Pan, C. H. Ang, J. Z. Zheng, and S. Ramanathan, *Appl. Phys. Lett.* **81**, 376 (2002).

[48] A. Jimenez-Gonzalez, D. Schmeisser, *Surf. Sci.*, **250,** 59 (1991).

[49] S. Miyazaki, *J. Vac. Sci. Technol. B* **19**, 2212 (2001).

[50] M. D. Groner, F. H. Fabreguette, J. W. Elam, and S. M. George, *Chem. Mater*. **16**, 639 (2004).

CHAPTER 5

COMPARATIVE BAND ALIGNMENT OF PLASMA-ENHANCED ATOMIC LAYER DEPOSITED DIELECTRICS ON GALLIUM NITRIDE

5.1 Abstract

Thin films of Al_2O_3, HfO_2, SiO_2, La_2O_3, ZnO, and HfO_2/Al_2O_3 stacked structures were deposited on n-type, Ga-face, GaN wafers using plasma-enhanced atomic layer deposition (PEALD). The wafers were first treated with a wet-chemical clean to remove organics and an *in-situ* combined H_2/N_2 plasma at 650 ℃ to remove residual carbon contamination, resulting in a clean, oxygen-covered surface. This cleaning process produced slightly upward band bending of 0.1eV. Additional 650 ℃ annealing after plasma cleaning increased the upward band bending by 0.2 eV. After the initial clean, dielectric films were deposited using PEALD at ~100-160 ℃. The valence band and conduction band offsets (VBO and CBO) of the Al_2O_3/GaN, HfO_2/GaN, SiO_2/GaN, La_2O_3/GaN, and ZnO/GaN structures were deduced from *in-situ* x-ray and ultraviolet photoemission spectroscopy (XPS and UPS). The VBOs were determined to be 1.8, 1.4, 3.2, 0.9, and 0.7 eV, while the deduced conduction band offsets were 1.3, 1.0, 2.3, 1.7, and -0.7 eV, respectively. These values are compared with theoretical calculations based on the electron affinity model and charge neutrality level model. Moreover, subsequent annealing had little effect on these offsets; however, the GaN band bending did change depending on the annealing and processing. The trends of potential barriers of dielectrics on GaN were related to the band gap energies of the dielectrics. Dielectrics with a band

gap larger than 5.8 eV are preferred for GaN to provide sufficient potential barriers for electrons. An Al_2O_3 layer was investigated as an interfacial passivation layer (IPL), which, as results suggest, may lead to improved stability, performance, and reliability of HfO_2/IPL/GaN structures. The VBOs were ~0.1 eV and 1.3 eV, while the deduced CBOs were 0.6 eV and 1.1 eV for HfO_2 with respect to Al_2O_3 and GaN, respectively.

5.2 Introduction

GaN-based transistors have shown great potential in a broad spectrum of electronics applications, including high frequency, high power, and high temperature electronics, due to their excellent properties such as a high saturated drift velocity and high breakdown field. However, a relatively high gate leakage has been one of the major factors that limits the performance and reliability of GaN based transistors [1]. This limitation is significantly mitigated with the use of metal/dielectric/III-N structures, which lowers the leakage current and improves the thermal stability. As a result, researchers have investigated the use of various dielectrics as gate insulators including Al_2O_3 [1,2,3,4,5], HfO_2 [6,7,8], SiO_2 [9,10], La_2O_3 [11,12], ZrO_2 [13], Sc_2O_3 [14,15,16,17], MgO [15,18,19,20], Gd_2O_3 [21], Ga_2O_3(Gd_2O_3) [22,23,24], and ZnO [25, 26]. However, these dielectrics are not ready for low-cost or high-yield manufacturing, which is largely a result of the deposition method [1]. Atomic layer deposition (ALD) is a robust and highly manufacturable method, which relies on self-limiting adsorption to control the layer-by-layer deposition of the dielectric material. This method is based on sequential gas phase exposure and surface chemical processes. The organometallic precursor and reactive gas—separated by a purge step—are delivered into

the chamber, where they react at the sample surface in a cyclic manner to form a thin film. This method not only increases uniformity and nanometer control but also decreases defect densities when compared to other deposition methods such as sputtering and electron-beam deposition. By using activated oxygen plasma species, plasma-enhanced ALD (PEALD) can not only significantly reduce the deposition temperature but also reduce the impurities and increase the growth rate and film density [27].

To advance the current understanding, we have used PEALD to investigate several promising dielectrics, including aluminum oxide (Al_2O_3), hafnium oxide (HfO_2), silicon oxide (SiO_2), lanthanum oxide (La_2O_3), and zinc oxide (ZnO). Specifically, Al_2O_3 has a large band gap (~6.5 eV) [28,29], low dielectric constant (~9), strong adhesion to many surfaces, and good chemical and thermal stability than HfO_2. The large band gap provides a sufficient barrier for carriers in the GaN valence and conduction bands, while the low dielectric constant causes significant reduction of transconductance; HfO_2, on the other hand, has a high dielectric constant (~20), which mitigate this problem, but HfO_2 is not as stable as Al_2O_3 [30,31]. Furthermore, the relatively narrow band gap associated with hafnium oxide (~5.8 eV) would not limit the leakage current as effectively and thus affect device performance. Considering the complementary characteristics of Al_2O_3 and HfO_2, devices could achieve lower leakage current and higher thermal stability by using Al_2O_3 as an interfacial passivation layer (IPL) between the semiconductor substrate and HfO_2 [30]. In addition, SiO_2, has a low dielectric constant (~3.9), large band gap (~8.9 eV), good chemical and thermal stability, and has been widely used in Si based technologies. La_2O_3, on the other hand, has a much larger dielectric constant (~18-27) and smaller band gap (4.3-6.0 eV), which varies depending on the film crystal structure

[32]. Similar to HfO_2, the high dielectric constant of La_2O_3 may mitigate the issue of transconductance reduction of the device. However, La_2O_3 absorbs H_2O and CO_2, which may degrade device performance [33,34]. ZnO has the same wurtzite crystal structure as GaN. It exhibits a similar band gap (~3.4 eV), and has a small lattice mismatch [32] when comparing with GaN, which may minimize the density of interface states and improve the device performance. In other words, these dielectrics are all potential gate dielectrics and/or passivation layers on GaN and AlGaN/GaN based heterostructure. In addition, the large diversity in the band gap energies (3.4-8.9 eV) of the investigated dielectrics enables a better understanding of the relation between the dielectric/GaN interface alignment and dielectric band gap.

Previous research has focused primarily on the preparation and cleaning of GaN surfaces using HCl, TCE, and annealing as well as various hydrogen and nitrogen treatments [35,36,37,38]. There has also been some investigation into band alignment of the dielectric/GaN interface with HfO_2 grown via molecular beam deposition (HBD) [8]. The band alignment characteristics play a critical role in determining the confinement properties of carriers in the semiconductor and ultimately the performance of electronic and optoelectronic devices. This study focuses on the band-alignment of the Al_2O_3/GaN, HfO_2/GaN, SiO_2/GaN, La_2O_3/GaN, ZnO/GaN, and Al_2O_3/HfO_2/GaN stacked structures grown via PEALD. Results for the surface band bending of the n-type, Ga-face GaN surface are consistent with other experimental studies and reveal that an additional annealing during the cleaning process increases the upward band bending. These measurements are well below the values expected based on the polarization bound charge and doping level. Apparently, structural defects, surface contamination, and surface states

contribute to Fermi level pinning or additional charge compensation, which screen the polarization charge. The results for the band alignment of the Al_2O_3, HfO_2, SiO_2, La_2O_3, and ZnO thin films are discussed in terms of the electron affinity and charge neutrality level models. The results of the stacked structure of HfO_2/Al_2O_3/GaN are also discussed. In addition to the band alignment of these interfaces, the effects of plasma treatment are also noted.

5.3. Experiment

5.3.1 Cleaning

The 5±1 μm thick, n-type, Ga-face, epitaxial, GaN wafers with a Si doping density of ~1 x 10^{17} cm^{-3}, obtained from and diced by READE Advance Materials, were grown via HVPE on sapphire substrates. For the nondegenerate GaN, the Fermi level E_F can be determined from the doping density N_D by the following equation.

$$E_C - E_F = kT * \ln(N_C - N_D) \tag{5.1}$$

Where E_C is the conduction band minimum (CBM); k is Boltzmann constant; T is the absolute temperature; and N_C is the conduction band effective density of states (=2.2x10^{18} cm^{-3}) [39]. Consequently, the GaN Fermi level is indicated at ~0.1 eV below the CBM. Prior to ALD deposition, the wafer sections were treated with an *ex-situ* wet-chemical clean. This process includes sonicating the wafer in separate acetone, methanol, and HCl acid baths for 10 minutes each; the acetone and methanol remove organics, while the HCl removes carbon and oxygen contamination from the surface [36]. An *in-*

situ remote plasma clean was further employed to remove remaining carbon contamination and reduce the surface defect density. The samples were exposed to an *in-situ* combined H_2 and N_2 (1:4) plasma treatment at 650 ℃ for 15 minutes, where the pressure and combined gas flow rate were maintained at 60 mTorr and 90 standard cubic centimeters per minute (sccm), respectively.

5.3.2 Plasma-enhanced atomic layer deposition

After cleaning, the sample was loaded into an ultra high vacuum (UHV) linear transfer-line and transferred to the PEALD system. A schematic illustration of the system is shown in Fig 5.1. The background pressure in the chamber was ~6.0×10^{-9} Torr. During deposition, the ALD software controlled the pulse time of the gases. During a 0.1-1.0 s precursor pulse, the precursor was delivered into the chamber with an argon carrier gas. This pulse was followed by 10-30 s of N_2 gas, used to purge excess precursor from the chamber. Then, O_2 gas was introduced into the chamber. Once the pressure reached 100 mTorr, the oxygen plasma was excited with 13.56 MHz rf-excitation applied to a helical copper coil wrapped around a 32 mm diameter quartz tube. The O_2 flow rate was sustained at 35 sccm, and the rf-power was maintained at 200 W. Subsequently, N_2 gas was used to purge the chamber again and prepare the chamber for the next growth cycle.

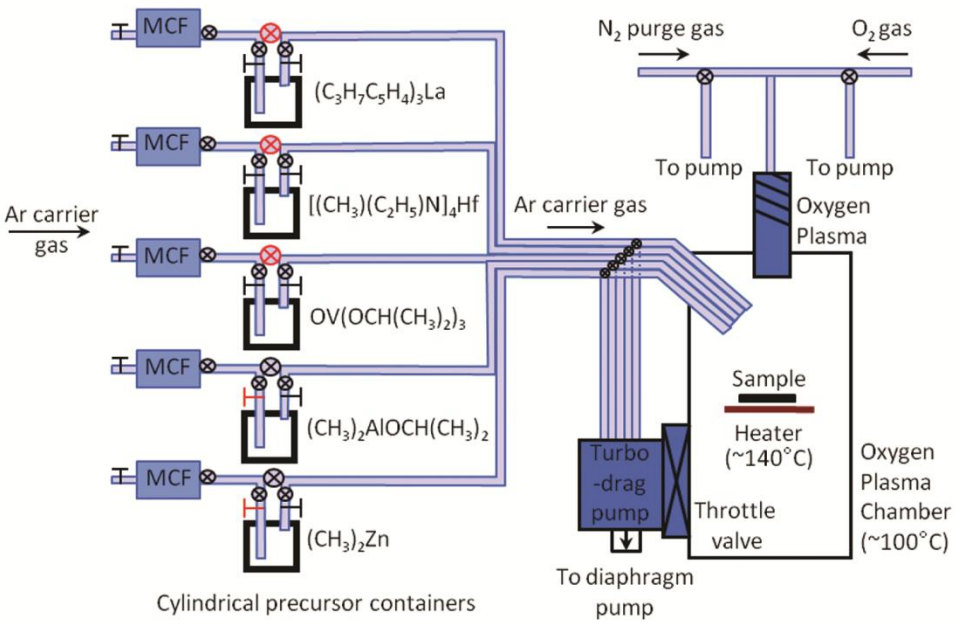

Figure 5.1. Schematic illustration of the PEALD system.

The precursors used for Al_2O_3, HfO_2, SiO_2, La_2O_3, and ZnO growth were dimethylaluminum isopropoxide (DMAI), tetrakis(ethylmethylamido)hafnium (TEMAH), octamethylcyclotetrasiloxane (OMCTS), tris(i-propylcyclopentadienyl) lanthanum (LaiPrCp3), and dimethylzinc (DMZ), respectively. To provide consistent vapor pressure for PEALD deposition, the bubbler temperatures were set to 80 °C for DMAI, 48 ℃ for TEMAH, 100 ℃ for OMCTS, and 168 ℃ for LaiPrCp3. The lines between the bubbler and the chamber were heated ~20 ℃ higher than the relevant bubbler temperature, and the chamber was heated to 110 ℃ to prevent precursor condensation. Considering the low boiling point of DMZ, the DMZ bubbler was maintained at -17.8 ℃ in coolant to reduce the vapor pressure during ZnO deposition. The substrate temperature was maintained at ~100-160 ℃ during growth depending on the deposition of different

dielectrics, and the respective growth rates were ~0.9, ~0.7, ~0.7, ~0.5, and ~2.0 Å/cycle for Al_2O_3, HfO_2, La_2O_3, SiO_2, and ZnO. The numbers of cycles were adjusted to deposit ~1-2 nm films on the GaN substrates. For the HfO_2/Al_2O_3/GaN stack structure, 1 nm Al_2O_3 was deposited on GaN and subsequently annealed in vacuum at 650 ℃, and then, 2 nm HfO_2 was grown over the Al_2O_3 layer.

5.3.3 Ultraviolet photoemission spectroscopy characterization

Ultraviolet photoemission spectra (UPS) were measured immediately following the ALD growth. The chamber base pressure was $8x10^{-10}$ Torr and He I, 21.2 eV radiation, was generated from research grade He gas using an DC plasma discharge lamp operated with an applied voltage of 1 kV and discharge current of 20 mA. The emitted electrons were dispersed with a VSW 50 mm hemispherical analyzer operated at a resolution of ~0.15 eV. Additionally, a negative 8 V bias was used to overcome the work function of the analyzer (4.4 V). The system was set to scan kinetic energy from 26 to 4 eV with 0.1 eV steps to obtain the valence band spectrum of the sample, which provided the electron affinity and valence band maximum of the film. The valence band maximum is determined by the energy difference between the Fermi level and the low binding energy cut-off of the UPS spectra, and the electron affinity is calculated by $\chi=h\nu-W-E_g$, where hν is the ultraviolet photon energy (21.2 eV), W is the UPS spectrum width between low and high binding energy cutoffs, and E_g is the band gap of the thin film.

5.3.4 X-ray photoemission spectroscopy characterization

In-situ x-ray photoemission spectroscopy (XPS) was used between various stages of the experimental process to characterize the core level binding energies of the samples' constituent elements. To investigate the GaN cleaning, XPS spectra of the C 1s and O 1s peaks were measured at a base pressure of $8x10^{-10}$ Torr. These spectra were used to determine the residual oxygen and carbon after various cleaning processes. To investigate the deposited films, XPS was utilized to measure the Ga 3d, Ga 3p, Ga 3s, N 1s, O 1s, C 1s, Al 2p, Hf 4f, La 3d, Si 2s, and Zn 3d core level spectra after each of the following steps: the standard cleaning process, PEALD dielectric thin-film growth, 30 minute vacuum annealing at 650 ℃, 5 minute room temperature oxygen plasma treatment, and finally, 30 minute vacuum annealing at 650 ℃. Note that throughout this process the sample was maintained in the UHV system. Mg Kα (=1253.6 eV) x-ray radiation was generally used as the source, except when scanning C 1s and Ga 3s peaks since the Ga Auger lines overlapped with the core level peaks. Therefore, Al Kα (=1486.6 eV) x-rays were used to scan the C 1s, Ga 3s, and Si 2s peaks. The x-ray source used a 4.4 A filament current, 16 mA emission current, and 13 kV accelerating voltage. The survey scans were repeated 30-80 times with a pass energy of 20 eV. The spectra were dispersed with a Fisons Clam II hemispherical analyzer with a resolution of ~1.0 eV. Through curve fitting of the core level peaks, the peak positions could be resolved to ±0.1 eV. These peak positions were then used to determine the valence band offsets.

Waldrop, Grant [40], and Kraut *et al.* [41] proposed a method to determine band offsets, which is based on the following relation:

$$\Delta E_V = (E_{CL} - E_V)_{GaN} - (E_{CL} - E_V)_{dielectric} + \Delta E_{CL} \quad (5.2)$$

where E_V represents the binding energy of the VBM; and E_{CL} is the binding energy of the core levels. In this analysis, ΔE_{CL} is the binding energy difference of the core levels of the GaN substrate and dielectric film; $(E_{CL}\text{-}E_V)_{GaN}$ and $(E_{CL}\text{-}E_V)_{dielectric}$ are the binding energy differences of the core level of Ga in GaN and the metal element in the dielectric with respect to its VBM. These $(E_{CL}\text{-}E_V)$ values are essentially independent of band bending, because the valence band maximum and core level bands would be affected equally. Once these values are measured, the VBO can be calculated using only the XPS core level difference of the dielectric and semiconductor. In this study, the value of $(E_{CL}\text{-}E_V)_{dielectric}$ is calculated from the VBM values from UPS and Hf, Al, Si, La, and Zn core level binding energy values from XPS. Because the surface of GaN is oxygen-covered, the valence band maximum (VBM) of GaN is not measured directly. According to prior studies of GaN [8,40,42], the Ga 3d core level is 17.7-17.8 eV below the valence band maximum, and 17.8 eV is adopted in this study for the value of $(E_{CL}\text{-}E_V)_{GaN}$. Accordingly, the evolution of the XPS core levels reflects the core level differences and can be used to determine the VBO and the band alignment at the interface.

5.4. Results

Using this method and the relationship between the energy bands and core levels, the band bending and alignment were calculated from the XPS and UPS data for seven different configurations: cleaned GaN, Al_2O_3/GaN, HfO_2/GaN, SiO_2/GaN, La_2O_3/GaN, ZnO/GaN, and HfO_2/Al_2O_3/GaN stacked structure.

5.4.1 Clean GaN

For GaN wafer, the band bending is dependent on surface contamination, which can significantly affect device performance. The contaminants on the material's surface, include absorbed molecules, organic contaminants, and native oxides. The goal in this study is to remove the carbon on the GaN but retain oxygen coverage, which results in an oxygen-covered surface. The surface oxygen can be removed with a high-temperature annealing ~900 ℃; however, at temperatures above ~800 ℃, Ga evaporation begins to occur leaving dangling bonds and increasing the surface defect concentration which in turn increases the interfacial defect concentration [36,37]. Retaining the oxygen-covered surface can therefore reduce the defects between the dielectric and GaN. Fig. 5.2 displays the XPS of the C 1s core level from the GaN surface after various *ex-situ* and *in-situ* cleaning processes.

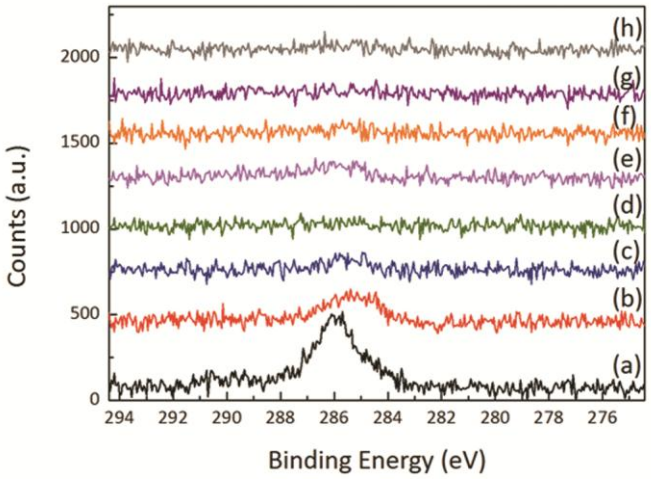

Figure 5.2. XPS spectra of C 1s core level from 5±1 μm n-type Ga-face GaN treated with (a) acetone and methanol; (b) acetone, methanol, HCl, and 400 ℃ annealing; (c) acetone, methanol, HCl, and 400 ℃ N_2 plasma annealing; (d) acetone, methanol, HCl, and 400 ℃ H_2/N_2 plasma annealing; (e) acetone, methanol, HCl, and room temperature H_2/N_2 plasma annealing; (f) acetone, methanol, and 400 ℃ H_2/N_2 plasma annealing; (g) acetone, methanol, HCl, UV/O_3, and 400 ℃ H_2/N_2 plasma annealing; and (h) acetone, methanol, HCl, and 650 ℃ H_2/N_2 plasma annealing.

In summary, the basic *ex-situ* clean involved acetone and methanol cleaning; however, this process left significant carbon contamination on the surface. This contamination was decreased with the various *in-situ* cleaning processes, where the 650 ℃ H_2/N_2 plasma process resulted in the least amount of carbon contamination. Using these two treatments as a baseline, the effects of HCl, UV/O_3, and higher temperature annealing were also considered and resulted in similar levels of carbon and oxygen on the surface. From these results, we established our baseline cleaning process: an *ex-situ*

cleaning process of sonication in an acetone, methanol, and HCl acid bath for 10 minutes each, and an *in-situ* cleaning process of a 15 minute 650 ℃ H_2/N_2 plasma process followed by an additional 30 minute 650 ℃ vacuum annealing.

The surface band bending of the oxygen-covered surface was also investigated. XPS curve fitting results of the oxygen-covered GaN surface gave the binding energy of the Ga 3d peak as 21.0 eV, which—assuming $(E_{CL}-E_V)_{GaN}$ is 17.8 eV—indicated the VBM of the GaN was 3.2 eV below the Fermi level. Using 3.4 eV as the GaN band gap, after *ex-situ* and *in-situ* cleaning, the bands were bent upward by 0.1 eV, which was smaller than other groups' values of 0.3 eV-1.5 eV [36,43,44,45]. However, an additional 30 minutes of annealing at 650 ℃ immediately following plasma cleaning decreased the binding energy of the Ga 3d core level to 20.8 eV, which indicated 0.3 eV upward band bending. The band schematic of oxygen-covered n-type Ga-face GaN is displayed in Fig. 5.3.

In an attempt to remove the residual oxygen contamination, the GaN wafer was treated with 200 W H_2/N_2 combined plasma at ~880 ℃ for 30 minutes and an additional 1 hour ~880 ℃ anneal. However, this treatment did not remove all the remaining oxygen. Fig. 5.4a shows the UPS spectra of this oxygen-covered GaN. The VBM and the width of the spectra were 2.8 eV and 14.4 eV, respectively. The photo threshold energy or ionization energy of the electrons in the VBM is equal to either the energy difference between the UPS photon energy and the spectral width or the sum of the electron affinity and band gap. This determined 6.8 eV as the ionization energy. Assuming 3.4 eV as the band gap, the electron affinity of oxygen-covered GaN was 3.4 eV, which is similar to another group's value of 3.3 eV [46]. The XPS of Ga 3d was 20.4 eV below the Fermi

level and therefore 17.6 eV in reference to the VBM. This was close to the previously reported value of 17.8 eV [8,40,42].

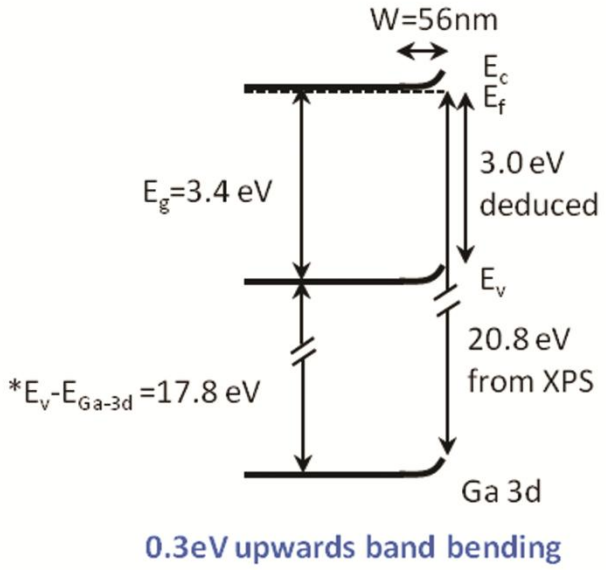

Figure 5.3. Band bending diagram of a cleaned, n-type, Ga-face GaN surface.

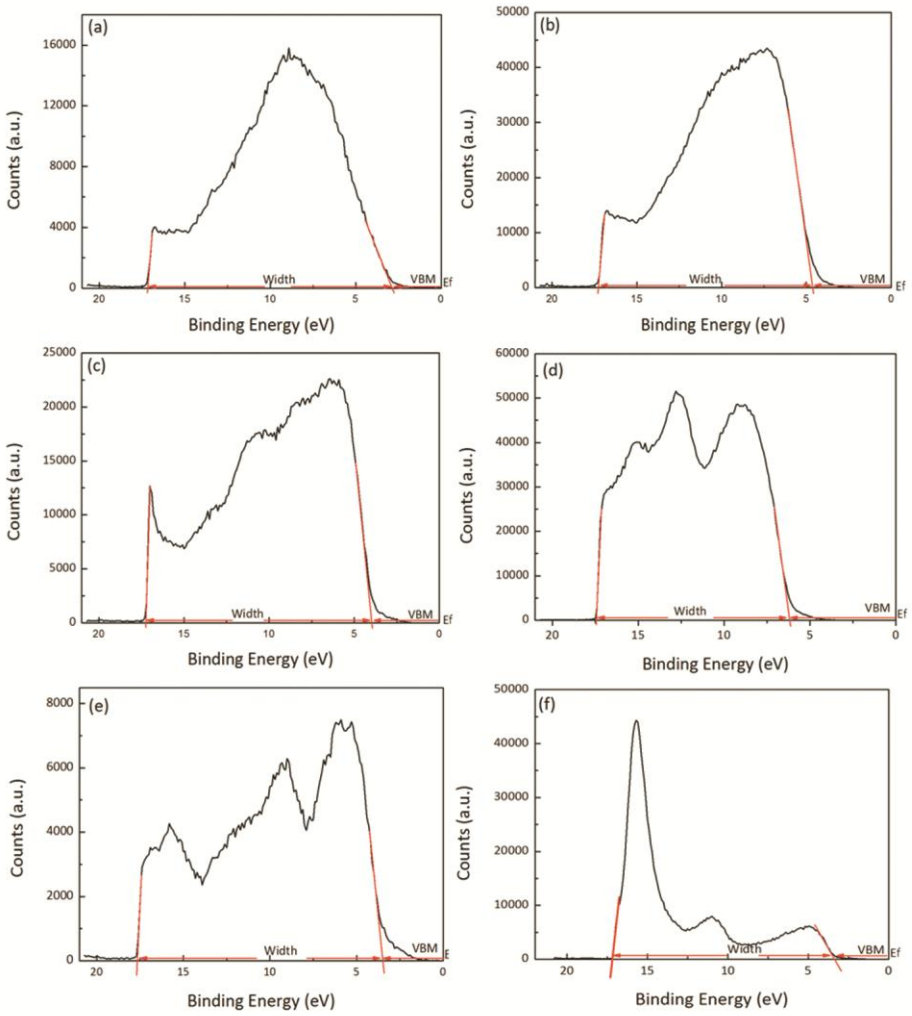

Figure 5.4. UPS spectra of (a) cleaned n-type, Ga-face GaN, (b) 1 nm as-deposited Al_2O_3 on n-type, Ga-face GaN, (c) 1 nm as-deposited HfO_2 on n-type, Ga-face GaN, (d) 1 nm as-deposited SiO_2 on n-type, Ga-face GaN, (e) 1.5 nm annealed La_2O_3 on n-type, Ga-face GaN, and (f) 1.6 nm as-deposited ZnO on n-type, Ga-face GaN, indicating the electron affinity and VBM. The VBM is the difference between the Fermi level and the low-binding energy cutoff, and the width of the spectrum, W, is used to calculate the electron affinity of the oxide.

5.4.2 Al_2O_3/GaN

The Al_2O_3 film deposited on GaN was ~1 nm thick. The UPS spectrum for this sample, shown in Fig. 5.4b, was used to determine the electron affinity and the VBM. It is worth mentioning here that the band gap of the amorphous Al_2O_3 thin film is not consistent with the bulk value of α-Al_2O_3 (8.8 eV) but is dependent on the method of oxide film growth. In other words, the amorphous thin film is characterized by a lower band gap than that of the bulk [28,29]. The decrease in the band gap has been associated with defect-induced states located in the band gap [47]. In the case of Al_2O_3, the VBM states are associated with the O 2p states, and the CBM states are associated with the Al 3s and 3p states [48]. Rehybridization between Al 3s, Al 3p, and O 2p, modifies the charge transfer between Al and O, and consequently decreases the band gap. A theoretical study used first-principles calculations to investigate amorphous Al_2O_3 model structures and showed that the smaller band gap could be due to the lower coordination numbers of the Al atoms in amorphous Al_2O_3 in comparison to those in crystalline α-Al_2O_3 [49]. For ALD grown Al_2O_3 thin films, the measured band gap is typically ~6.5 eV [50,51,52].

The evolution of the Ga 3d, Al 2p, N 1s, and O 1s core levels is shown in Fig. 5.5, and the XPS core level curve fitting results of Ga 3d, Ga $3p_{3/2}$, N 1s, O 1s, and Al 2p are summarized in Table 5.1. The results indicate the band bending development during the experimental process. After each annealing, the Ga and Al core levels shifted to high binding energies by ~0.6 eV. After oxygen plasma treatment of the thin films, the core levels shifted back to almost the original position measured before annealing. Accounting for the VBM of Al_2O_3, which was 4.5 eV below the Fermi level, the XPS spectrum

indicated the Al 2p core level at 74.9 eV below the Fermi level or 70.4 eV below the VBM. The binding energy difference of the Ga 3d and Al 2p core level peaks was measured as 54.6 eV. According to Eq. 5.2, the VBO of the GaN substrate and as-deposited Al_2O_3 film was 2.0 eV. Considering the 6.5 eV band gap of amorphous Al_2O_3, the corresponding conduction band offset (CBO) was 1.1 eV. After annealing, the core level difference between the Ga 3d and Al 2p peaks changed slightly to 54.4 eV, which indicated that the VBO decreased to 1.8 eV. Furthermore, the core level difference was unaltered by the oxygen plasma treatment, and thus the VBO and CBO values were equivalent to that of the annealed sample. For the final annealing step, ΔE_{CL} changed to 54.3 eV, which indicated a 1.7 eV VBO and 1.4 eV CBO.

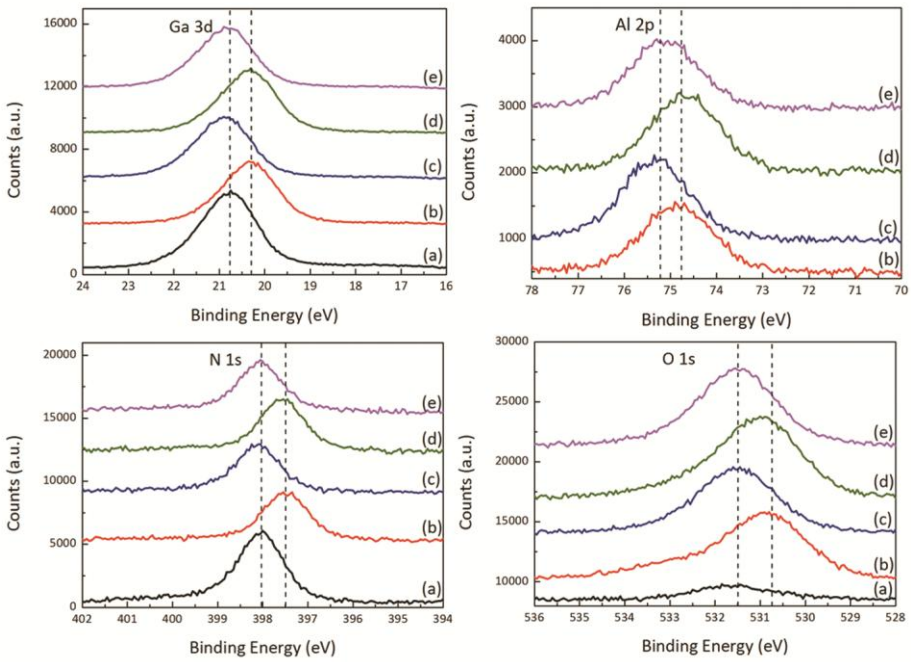

Figure 5.5. Ga 3d, Al 2p, N 1s, and O 1s XPS spectra for (a) cleaned GaN, (b) 1 nm Al_2O_3 as deposited, (c) 1 nm Al_2O_3 annealed, (d) oxygen plasma treated, (e) final annealing. The initial and final states of the core level peaks after Al_2O_3 growth are indicated with dashed lines.

Table 5.1. XPS fitting results for Ga 3d, Ga $3p_{3/2}$, N 1s, O 1s, and Al 2p core levels. All energies are given in eV.

Process	Ga 3d	Ga $3p_{3/2}$	N 1s	O 1s	Al 2p
Before growth	20.8	106.0	398.0	531.7	-
Al_2O_3 deposited	20.3	105.6	397.5	530.9	74.9
Al_2O_3 annealed	20.9	106.2	398.1	531.5	75.3
O_2 plasma	20.3	105.6	397.6	531.0	74.7
Final annealing	20.8	106.1	398.1	531.5	75.1

Fig. 5.6 shows the deduced band alignment diagrams of Al_2O_3 on n-type, Ga-face GaN. This figure demonstrates that although annealing and O_2 plasma treatment could change the screening of the polarization surface bound charge and alter the band bending conditions, the results of the band offset in this heterostructure were not significantly affected for these processes.

In Fig. 5.4b, the VBM of Al_2O_3 was found at 4.6 eV below the Fermi level. The width of the UPS spectrum was 12.7 eV, which indicated that the photo threshold energy and electron affinity of Al_2O_3 on GaN were 8.5 eV and 2.0 eV respectively. This electron affinity value was close to the value reported by O. Black *et al*. [53]. The related XPS Al 2p core level changed to 75.1 eV, which indicates the Al 2p core level was 70.5eV in reference to the VBM. This result was comparable to the previous experimental value and is consistent with other reports [28,54].

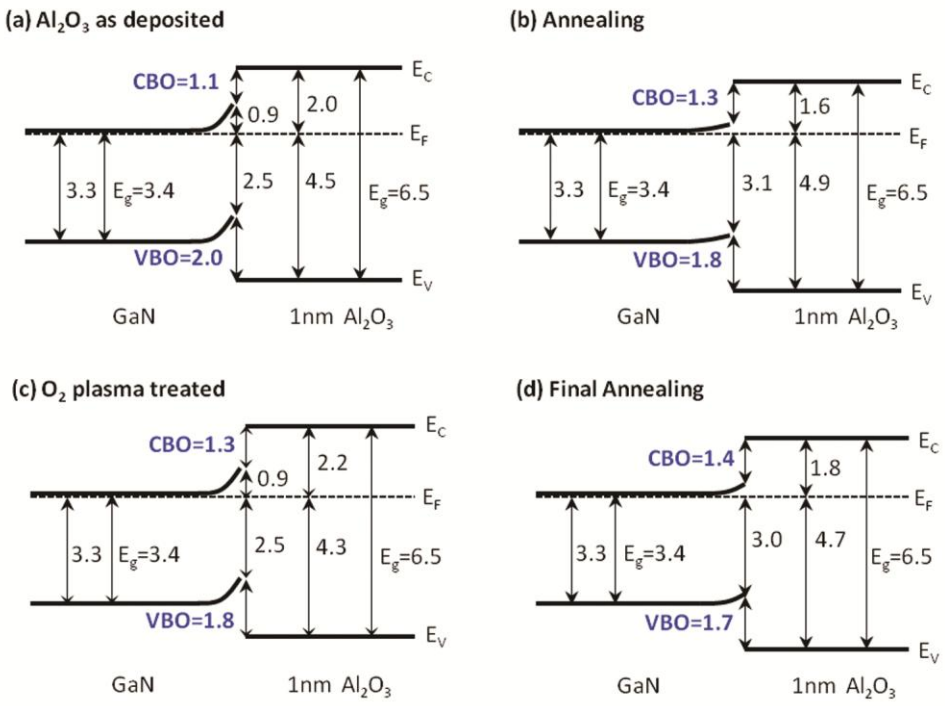

Figure 5.6. Deduced band alignment diagrams for Al_2O_3/GaN interface (a) as deposited, (b) after annealing, (c) O_2 plasma treated, and (d) final annealing, where all energies are given in eV.

5.4.3. HfO_2/GaN

Similarly, the results for HfO_2 are summarized in Fig. 5.4c, 5.7, and 5.8. Fig. 5.4c shows the UPS spectra for as-deposited HfO_2 on GaN. The VBM was determined to be 4.0 eV relative to the Fermi level. The UPS spectrum width was 13.2 eV, and the band gap of HfO_2 was assumed to be 5.8 eV. This band gap value was established according to other groups' experimental values, which are reported as 5.6-6.0 eV [28]. Therefore, the photo threshold energy and electron affinity were calculated to be 8.0 eV and 2.2 eV, which is consistent with other reports [8]. These values are summarized in Table 5.2

along with the UPS results of oxygen-covered GaN and Al_2O_3/GaN. The Hf $4f_{7/2}$ core level was 17.7 eV, meaning 13.7 eV below the VBM.

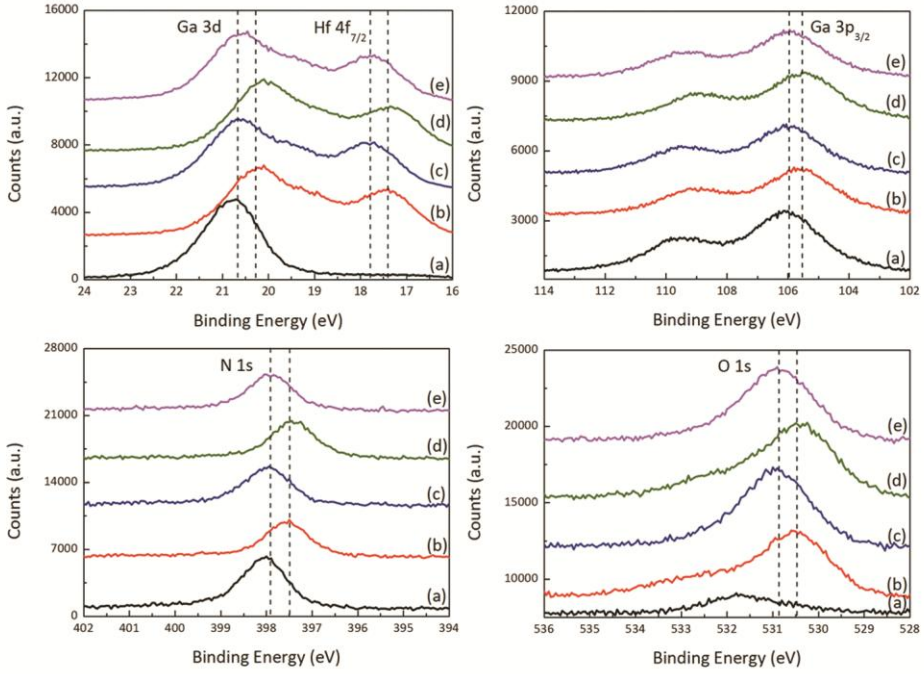

Figure 5.7. Ga 3d, Hf 4f, Ga 3p, N1s, and O 1s XPS spectra for (a) cleaned GaN, (b) 1 nm HfO_2 as deposited, (c) 1 nm HfO_2 annealed, (d) oxygen plasma treated, (e) final annealing. The initial and final positions of the core level peak after HfO_2 growth are indicated with dashed lines.

Fig. 5.7 displays the evolution of the Ga 3d, Hf 4f, Ga 3p, N1s, and O 1s core levels of 1 nm HfO_2/GaN during the various stages of the deposition process. The curve fitting results of these spectra are summarized in Table 5.3. Before growth, the Ga 3d core level was 20.8 eV, which indicated 0.3 eV upward band bending at the surface.

After the growth of 1 nm HfO_2 on GaN, the upward band bending of GaN was increased by 0.5 eV. These results were similar to Al_2O_3 deposited on GaN. The Hf $4f_{7/2}$ core level changed to 17.5 eV, and the VBM determined from UPS shifted to 3.9 eV, which indicated the value of $(E_{CL}\text{-}E_V)_{HfO2}$ was 13.6 eV. This value is consistently repeatable and agrees with a prior report [55]. The core level difference between Hf $4f_{7/2}$ and Ga 3d was -2.8 eV. Hence, the VBO of the as-deposited HfO_2/GaN heterostructure was 1.4 eV. Accounting for the 5.8 eV band gap of the HfO_2 thin film, the corresponding CBO was 1.0 eV. The annealing and oxygen plasma treatment following the growth result in the bands being shifted by almost the same values, and therefore the VBO and CBO were still ~1.4 eV and ~1.0 eV, respectively. Fig. 5.8 shows the deduced band alignment of HfO_2 on Ga face GaN with different experiment processes.

Table 5.2. UPS results of cleaned GaN, as-grown Al_2O_3/GaN and as grown HfO_2/GaN. All energies are given in eV.

	GaN	**Al_2O_3/GaN**	**HfO_2/GaN**	**SiO_2/GaN**	**La_2O_3/GaN**	**ZnO/GaN**
VBM	2.8	4.6	4.0	6.2	3.4	3.2
Spectral Width	14.4	12.7	13.2	11.3	14.3	13.9
Photo Threshold Energy	6.8	8.5	8.0	9.9	6.9	7.3
Band gap	3.4	6.5	5.8	8.9	6.0	3.4
Electron affinity	3.4	2.0	2.2	1.0	0.9	3.9

Table 5.3. XPS peak fitting results for Ga 3d, Ga $3p_{3/2}$, N 1s, O1s and Hf $4f_{7/2}$ core levels. All energies are given in eV.

Process	Ga 3d	Ga $3p_{3/2}$	N 1s	O 1s	Hf $4f_{7/2}$
Before growth	20.8	106.1	398.0	531.7	-
HfO_2 deposited	20.3	105.6	397.6	530.4	17.5
HfO_2 annealed	20.7	106.0	398.0	530.9	17.9
O_2 plasma	20.2	105.5	397.4	530.4	17.3
Final annealing	20.7	106.0	397.9	530.9	17.8

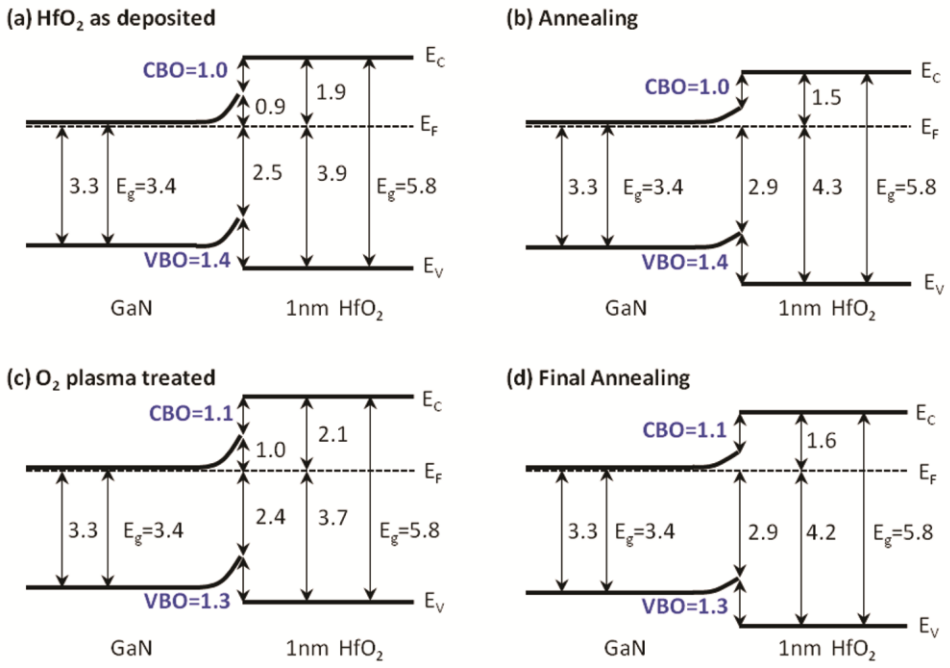

Figure 5.8. Deduced band alignment diagram for HfO_2/GaN interface (a) as deposited, (b) after annealing, (c) O_2 plasma treated, and (d) final annealing, where all energies are given in eV.

These values were different from previous HfO_2/GaN band offsets reported by Cook *et al.* [8], which give -0.1 eV and 0.3 eV as the VBO for as-grown and annealed

HfO_2/n-type, Ga-face GaN, respectively. (We note that the same photoemission systems were employed in both the prior and current study.) Further investigation revealed this difference stems from an ~0.5 eV difference in the Hf $4f_{7/2}$ core level with respect to the Ga core level and the energy separation between Hf $4f_{7/2}$ and VBM; these discrepancies culminated a ~1 eV difference in the VBOs. This disparity was likely the result of the different cleaning and deposition processes. In the previous work, the GaN was annealed in ammonia at a higher temperature to remove oxygen from the surface, while this research retained oxygen coverage on the GaN after cleaning, leaving an interstitial oxygen layer at the interface. The interlayer could change the electronegativity of the surface atoms and thus the interfacial dipole and subsequent electronic properties. Furthermore, in the previous study, the films were grown in 4 Å increments of MBD-deposited Hf followed by oxygen plasma; this suggests that the film may have a different structure than the films grown by PEALD. The dissimilar structure would explain the difference between the VBM and the Hf $4f_{7/2}$ core level as well as the shift in the Hf 4f core levels, while the O 1s and Ga core levels remained comparable.

5.4.4 SiO_2/GaN

Fig. 5.9 shows the evolution of the XPS Ga 3s, Si 2s, Ga 3d, O 1s, and C 1s core levels of 1 nm SiO_2/GaN during the various stages of the deposition process, including (a) as deposited, (b) first annealing, (c) O_2 plasma treatment, and (d) final annealing. The curve fitting results of these spectra are summarized in Table 5.4. After the deposition of SiO_2 films, the upward band bending of GaN was 0.5 eV, which was ~ 0.3 eV lower than that in Al_2O_3 and HfO_2/GaN. The Si 2s core level was at 154.9 eV, and the VBM was 6.0

eV, which suggested the value of $(E_{CL}-E_V)_{SiO2}$ was 148.9 eV. In addition, the core level difference between Si 2s and Ga 3d was 134.3 eV. Hence, the VBO of the as-deposited SiO_2/GaN heterostructure calculated from Eq. 5.2 was 3.2 eV, and the corresponding CBO was 2.3 eV. The annealing and oxygen plasma treatment after the deposition shifted the bands by only 0.1-0.2 eV, which was smaller than the shift of 0.5-0.6 eV observed for Al_2O_3/GaN or HfO_2/GaN. However, similar to the constant band offset in Al_2O_3 and HfO_2/GaN, the respective VBO and CBO of SiO_2/GaN were maintained at ~3.2 and ~2.3 eV regardless of the different processing. Fig. 5.10 shows the deduced band alignment of SiO_2 on Ga-face GaN for the different experimental processes.

Fig. 5.4d shows the UPS spectra for as-grown SiO_2/GaN. The VBM was determined to be 6.2 eV with respect to the Fermi level. The corresponding Si 2s binding energy was 155.1 eV respect to the Fermi level, which indicated a same value of $(E_{CL}-E_V)_{SiO2}$ (148.9 eV) as previously discussed. The UPS spectrum width was 11.3 eV, which indicated the photo threshold energy and electron affinity was 9.9 and 1.0 eV respectively (assuming 8.9 eV as the band gap). This value is consistent with other group's report (1.1.eV) [28].

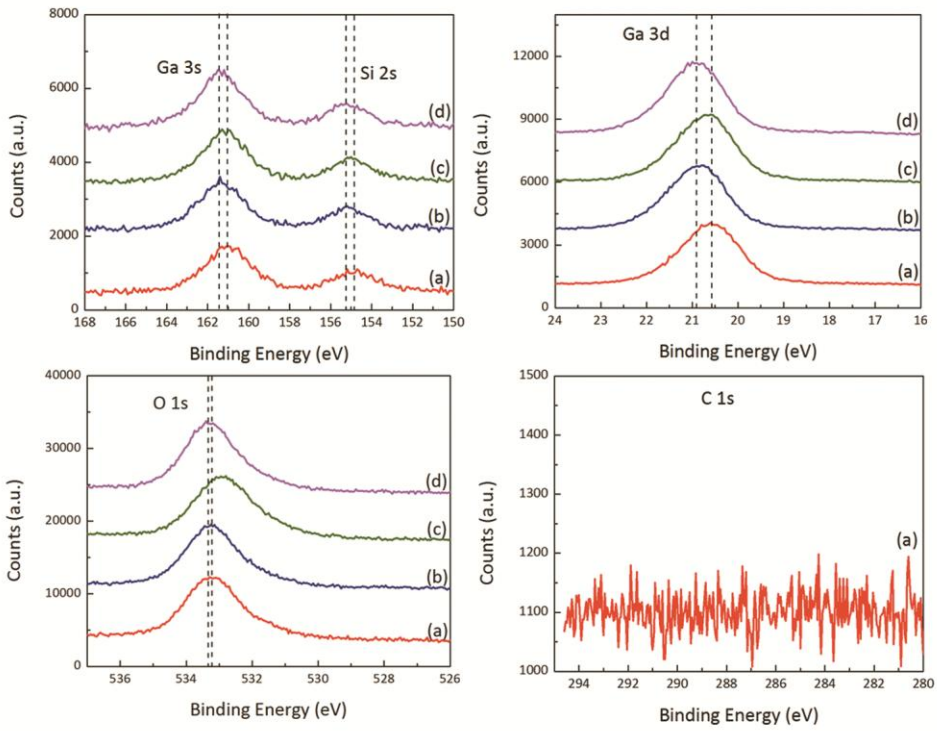

Figure 5.9. Ga 3s, Si 2s, Ga 3d, O 1s, and C 1s XPS spectra for (a) 1 nm SiO_2 as deposited, (b) 1 nm SiO_2 annealed, (c) oxygen plasma treated, (d) final annealing. The initial and final positions of the core level peak after SiO_2 growth are indicated with dashed lines.

Table 5.4. XPS peak fitting results for Ga 3d, Ga 3s, O 1s, and Si 2s core levels. All energies are given in eV.

Process	Ga 3d	Ga 3s	O 1s	Si 2s
SiO_2 deposited	20.6	161.0	533.2	154.9
SiO_2 annealed	20.8	161.3	533.3	155.2
O_2 plasma	20.7	161.2	532.9	155.0
Final annealing	20.9	161.4	533.3	155.2

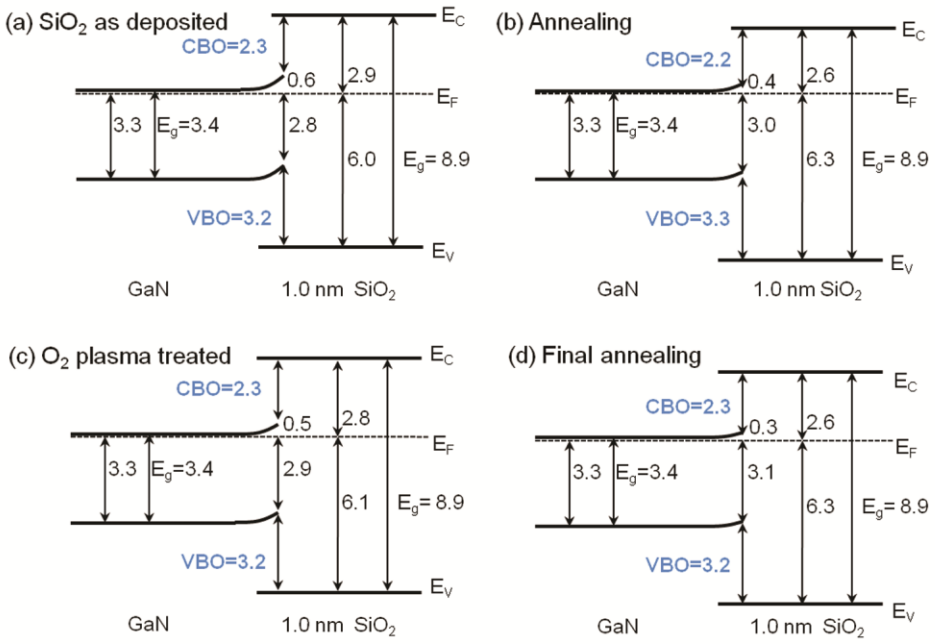

Figure 5.10. Deduced band alignment diagram for SiO_2/GaN interface (a) as deposited, (b) after annealing, (c) O_2 plasma treated, and (d) final annealing, where all energies are given in eV.

The band offset value was also different from previous SiO_2/GaN study reported by Cook [56], which gave the VBO as 2.3 eV if using 17.8 eV as the value of $(E_{CL}\text{-}E_V)_{GaN}$ in this study. This difference was similar to that of HfO_2/GaN, which could also be explained by the different surface pretreatment and growth methods applied in these two studies.

5.4.5 La_2O_3/GaN

Fig. 5.11 displays the evolution of the XPS La $3d_{5/2}$, Ga 3d, O 1s, and C 1s peaks of 1.5nm La_2O_3/GaN, including (a) before deposition, (b) after growth, (c) after 1 hour 700 ℃ annealing, and (d) three days exposure in air ambient. The curve fitting results are

summarized in Table 5.5. For the as-grown film, the respective La $3d_{5/2}$ and Ga 3d peaks were at 834.8 and 20.1 eV, suggesting 1.0 eV upward band bending at the interface. During post deposition treatment, the XPS Ga 3d and La $3d_{5/2}$ core levels shifted to higher binding energy by 0.2 and -0.6 eV after annealing, and further shifted to higher binding energy by -0.1 and 1.0 eV after three days ambient exposure, respectively. On the other hand, there were two observable oxygen peaks after deposition and exposure in the air, but only the one at lower binding energy remained after the annealing process.

Fig. 5.4e shows the UPS spectra of ~1.5 nm annealed La_2O_3 films on GaN. The VBM was determined to be 3.4 eV with respect to the Fermi level. The spectrum width of annealed La_2O_3 was 14.3 eV, which suggested the photo threshold energy and electron affinity was 6.9 and 0.9 eV respectively (assuming 6.0 eV as the band gap). The value of $(E_{CL}\text{-}E_V)_{La2O3}$ was then determined to be 831.4 eV. Considering the energy difference between La $3d_{5/2}$ and Ga 3d core levels was 813.9 eV, the VBO of La_2O_3/GaN was calculated to be 0.9 eV as shown in Fig 5.12, which was close to a other group's study (VBO=0.6 eV) [57]. Therefore, the CBO was calculated to be ~1.7 eV if using 6.0 eV as the band gap of La_2O_3.

The different shift directions of the Ga 3d and La 3d core levels after annealing suggested a change of film composition, which was also evidenced by the change of oxygen and carbon peak spectra. For the as-grown film, the oxygen peak at 529.8 eV was ascribed to La-O-La bonding, and the peak at 532.0 eV was due to La-$(OH)_x$ and/or La-CO_x groups, which could be removed after annealing. In addition, the carbon peak at 290.4 eV, ascribed to carboxide, could also be removed after annealing. The carbon contamination decreased ~40%, and the O impurity (OH and/or CO_x group)

concentration decreased from ~60% to the XPS detection limit after annealing, according to the integrated intensity calculation of XPS O 1s and C 1s spectra. Therefore, the film after annealing mainly consisted of La_2O_3. After several days exposure in the air, the La_2O_3 films had two oxygen and carbon peaks again, presumably due to the reaction with H_2O and/or CO_2 in air. The change in the film composition led to the different shifts in the Ga 3d and La 3d core levels.

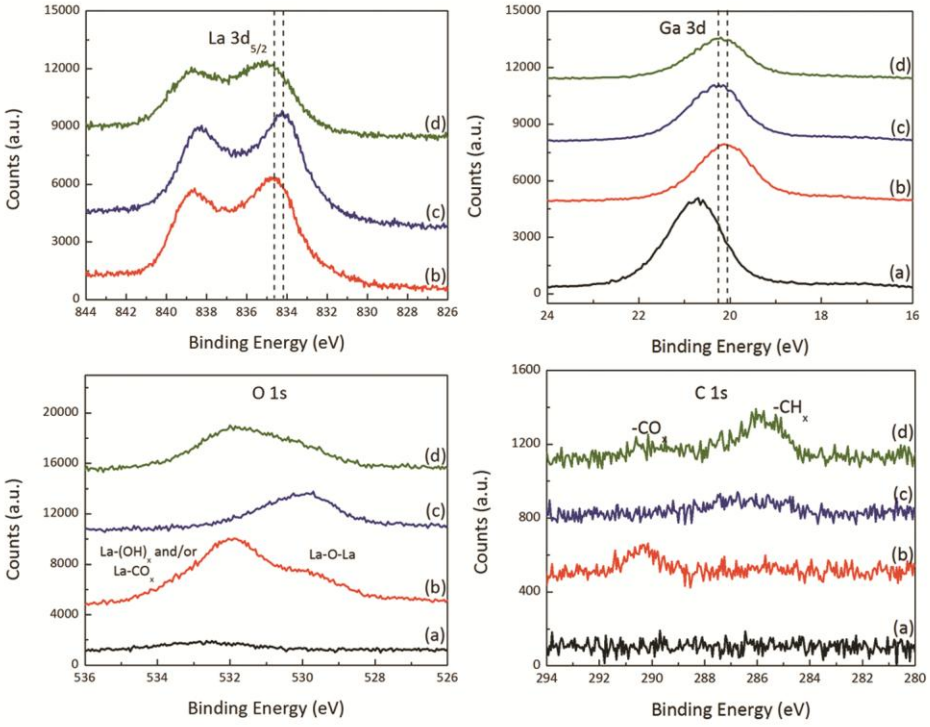

Figure 5.11. La $3d_{5/2}$, Ga 3d, O 1s, and C 1s XPS spectra for (a) cleaned GaN, (b) 1.5 nm La_2O_3 as deposited, (c) 1.5 nm La_2O_3 annealed at 700 ℃, (d) 3 days exposure in the air. The positions of the core level peak before and after annealing are indicated with dashed lines.

Table 5.5. XPS peak fitting results for La $3d_{5/2}$, Ga 3d, and O 1s core levels. All energies are given in eV.

Process	La $3d_{5/2}$	Ga 3d	O 1 (-OH)	O 1s (La-O-La)
Before growth	-	20.7	-	-
La_2O_3 deposited	834.8	20.1	532.0	529.8
La_2O_3 annealed	834.2	20.3	-	530.1
Air exposed	835.2	20.2	531.9	529.9

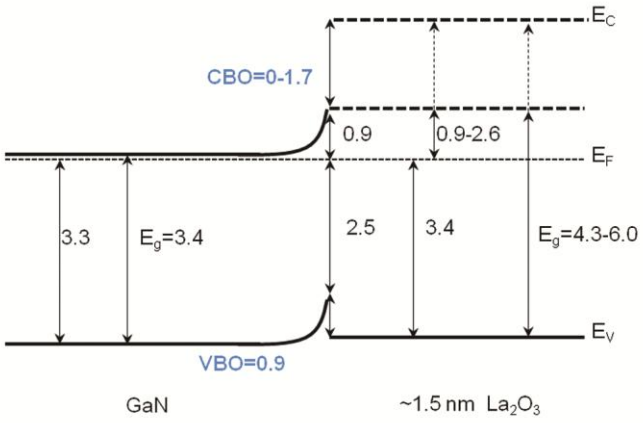

Figure 5.12. Deduced band alignment diagram for La_2O_3/GaN interface after 1 hour annealing at 700 ℃, where all energies are given in eV.

5.4.6 ZnO/GaN

Fig. 5.4f shows the UPS spectra of ~1.6nm as-grown ZnO films on GaN. The VBM was 3.3 eV from the Fermi level. The spectrum width was determined to be 13.9 eV, which suggested the respective photo threshold energy and electron affinity was 7.3 and 3.9 eV (assuming 3.4 eV as the band gap of ZnO).

Fig. 5.13 shows the XPS Ga 3d, Zn 3d, N 1s, O 1s, and C 1s peaks of as-grown and annealed ZnO on GaN. The curve fitting results are summarized in Table 5.6. After deposition, the Ga 3d core level was at 20.4 eV, suggesting a 0.7 eV upward band bending at the interface. The Zn 3d core level was at 10.9 eV, which indicated the binding energy difference between Ga 3d and Zn 3d core level was -9.5 eV and the value of $(E_{CL}-E_V)_{ZnO}$ was 7.6 eV. The respective VBO and CBO were then determined to be 0.7 and -0.7 eV, as shown in Fig. 5.14. This value is close to other reported results (VBO=0.7-0.8 eV) [58,59]

After annealing, the Ga 3d and Zn 3d core levels shifted to higher binding energy by 0.2 eV, indicating a constant band offset. For the oxygen peak, there was an evident shoulder peak at higher binding for the as-grown films, probably –OH groups, the concentration of which decreased from 34% to 17% after annealing. The carbon contamination was below the XPS detection limit during the processing.

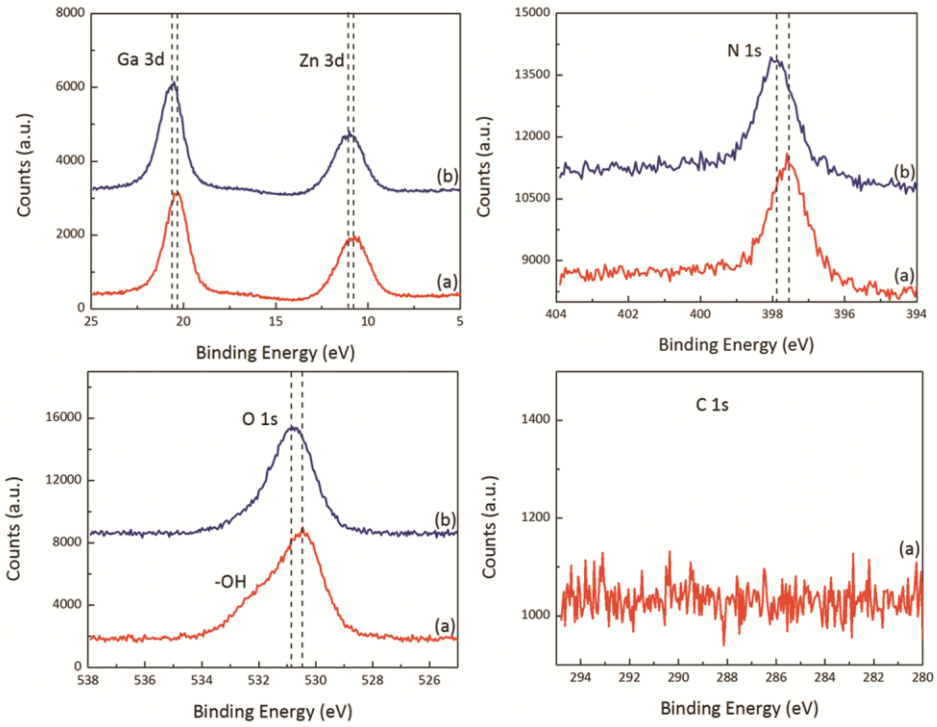

Figure 5.13. Ga 3d, Zn 3d, N 1s, O 1s, and C 1s XPS spectra for (a) 1.6 nm ZnO as deposited, (b) 1.6 nm ZnO annealed. The initial and final positions of the core level peaks after ZnO growth are indicated with dashed lines.

Table 5.6. XPS peak fitting results for Ga 3d, Zn 3d, N 1s, and O 1s core levels. All energies are given in eV.

Process	Ga 3d	Zn 3d	N 1s	O 1s	O 1s (-OH)
ZnO deposited	20.4	10.9	397.6	530.4	532.0
ZnO annealed	20.6	11.1	397.9	530.8	532.5

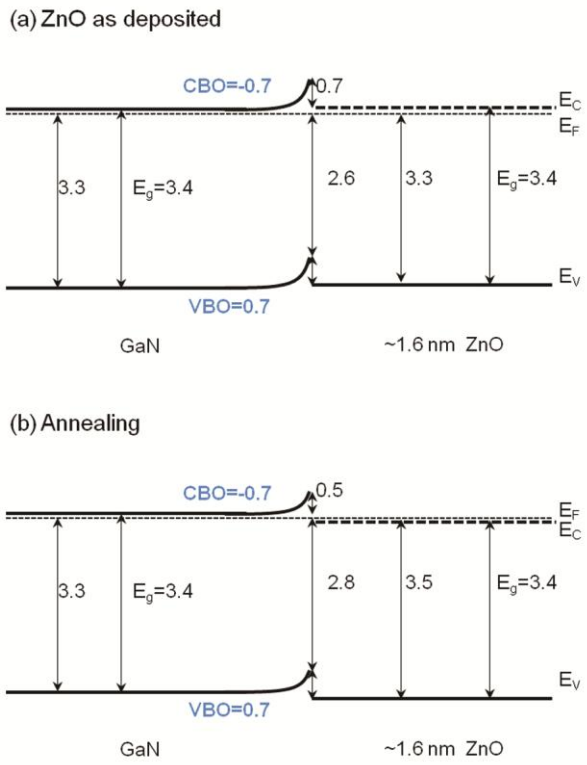

Figure 5.14. Deduced band alignment diagram for ZnO/GaN interface (a) as-deposited, and (b) after annealing, where all energies are given in eV.

5.4.7 $HfO_2/Al_2O_3/GaN$

The XPS core-level peak-fitting results for the stacked structures are shown in Table 5.7 for the Ga 3d, Ga $3p_{3/2}$, N 1s, O 1s, Al 2p, and Hf $4f_{7/2}$ peaks. These results were used to develop the band alignment diagrams for the stacked structure, which consisted of 2 nm HfO_2 on 1 nm Al_2O_3 on an n-type Ga-face GaN wafer. Fig. 5.15 illustrates the evolution of the XPS core level spectra. The values of $(E_{CL}\text{-}E_V)_{GaN}$, $(E_{CL}\text{-}E_V)_{Al2O3}$, and $(E_{CL}\text{-}E_V)_{HfO2}$ are fixed at 17.8 eV, 70.4 eV, and 13.6 eV, respectively. Assuming the charges were distributed only at the interfaces, the constructed bands of HfO_2 were flat and Al_2O_3 were

inclined indicating the presence of an electric field. Furthermore, the valence band offset of Al_2O_3 with respect to GaN was assumed to be 1.8 eV, unchanged from previous results.

Table 5.7. XPS peak fitting results for Ga 3d, Ga $3p_{3/2}$, N 1s, O 1s, Al 2p and Hf $4f_{7/2}$ core levels in eV.

Process	Ga 3d	Ga	N 1s	O 1s	Al 2p	Hf $4f_{7/2}$
HfO_2 deposited	20.3	105.6	397.6	530.5	74.4	17.2
HfO_2 annealed	20.6	105.9	397.9	530.7	74.9	17.7
O_2 plasma	20.3	105.6	397.5	530.3	74.4	17.3
Final annealing	20.7	106.0	397.9	530.7	74.9	17.8

From the fixed VBO of Al_2O_3/GaN and shift of GaN core levels, the core level values of Al_2O_3 at the Al_2O_3/GaN interface can be established. The XPS core level value of the Al 2p peak represented the average binding energy of the Al 2p core level in the interfacial layer, which can be used to determine the binding energy of the Al 2p core level in the middle of the Al_2O_3 interfacial layer, and the core level of the Al 2p at the HfO_2/Al_2O_3 interface can be ascertained from the inclined band property. After HfO_2 growth, the prominent Hf $4f_{5/2}$ peak overlapped with the Ga 3d peak, which obscured the Ga 3d peak fit. The values for the Ga 3d core levels were, therefore, obtained using the Ga $3p_{3/2}$ core level results according to the constant binding energy difference between the Ga 3d and Ga $3p_{3/2}$ core levels (85.3 eV). The modified Ga 3d peak value (20.3 eV) was then used to determine the VBM of GaN; accounting for $(E_{CL}\text{-}E_V)_{GaN}$=17.8 eV, the VBM of GaN was 2.5 eV below the Fermi level. Assuming the VBO at the Al_2O_3/GaN interface was 1.8 eV, the VBM of Al_2O_3 at the Al_2O_3/GaN interface was thus 4.3 eV below the Fermi level. According to the curve fitting value of the Al 2p core level, the

VBM in the middle of the Al_2O_3 film was 4.0 eV below the Fermi level. This value indicated the potential drop across the Al_2O_3 film was 0.6 eV, and the VBM of Al_2O_3 at the HfO_2/Al_2O_3 heterostructure was 3.7 eV. The VBM of HfO_2 was 3.6 eV below the Fermi level, which was determined from the XPS core level value of the Hf $4f_{7/2}$ peak. Therefore, the VBO and CBO at the HfO_2/Al_2O_3 interface were 0.1 eV and 0.6 eV respectively. Furthermore, the VBO and CBO between GaN and HfO_2 were 1.1 eV and 1.3 eV respectively. After annealing, the Ga $3p_{3/2}$ and Al 2p core levels moved to higher binding energy by 0.3 eV and 0.5 eV respectively, indicating a decrease of the potential drop across the Al_2O_3 film and charge accumulation presumably near the HfO_2/Al_2O_3 interface. The band diagrams of the stacked structure are depicted in Fig 5.16, and the results of the VBO and CBO of the various interfaces in the stacked structure are summarized in Table 5.8, where the band relations of HfO_2/GaN include the electric field in the dielectric. As suggested, the Al_2O_3 passivation layer provides enhanced thermodynamic stability and a sufficient valence band and conduction band potential barrier height (more than 1.3 V), which may improve the performance and decrease the leakage current of HfO_2/GaN structures.

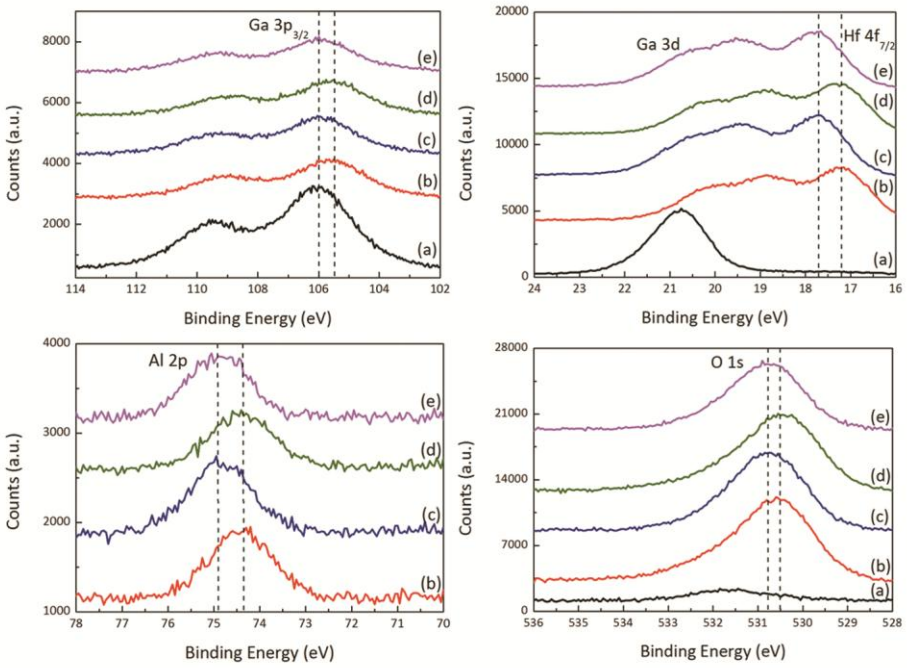

Figure 5.15. Ga 3p, Ga 3d and Hf 4f, Al 2p, and O 1s XPS core level spectra for (a) before growth, (b) $HfO_2/Al_2O_3/GaN$ as deposited, (c) $HfO_2/Al_2O_3/GaN$ annealed, (d) oxygen plasma treated, and (e) final annealing. The initial and final positions of the core level peaks after HfO_2 growth are indicated with dashed lines.

Table 5.8. Summary of band offset values for the $HfO_2/Al_2O_3/GaN$ structure, where all energies are given in eV. Note that the HfO_2/GaN the band relation includes the electric field in the dielectric.

Process	Al_2O_3-GaN		Al_2O_3-HfO_2		HfO_2-GaN	
	VBO	CBO	VBO	CBO	VBO	CBO
As deposited	1.8	1.3	0.1	0.6	1.1	1.3
Annealed	1.8	1.3	0.3	0.4	1.3	1.1
Oxygen plasma treated	1.8	1.3	0.0	0.7	1.2	1.2
Final annealing	1.8	1.3	0.1	0.6	1.3	1.1

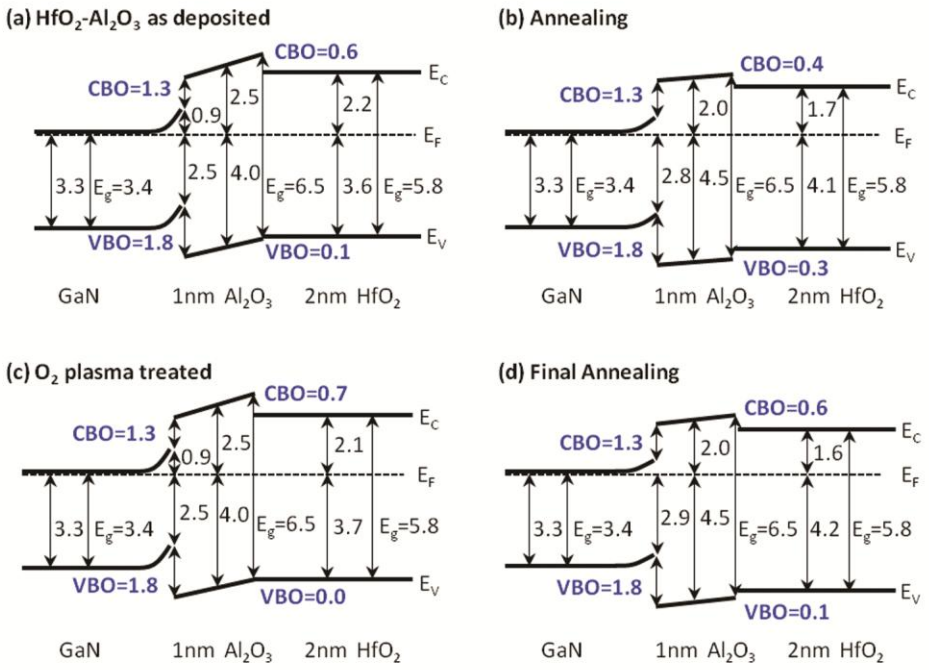

Figure 5.16. Band alignment diagram for $HfO_2/Al_2O_3/GaN$ interface (a) as deposited, (b) after annealing, (c) after oxygen plasma, and (d) after second annealing, where all energies are given in eV.

5.5. Discussion

As previously mentioned, the interface band alignment of two materials impacts the carriers confinement characteristics. Therefore, understanding the properties that influence band alignment can illuminate critical aspects of carrier behavior that may affect device performance and reliability. Consequently, there are several approaches, which attempt to explain the band bending and alignment; this includes the polarization, which determines the band bending of the bare wafer as well as the electron affinity and charge neutrality level models, which provide theoretical band alignments for dielectric/semiconductor interfaces. These models are discussed in this section in addition

to the elevated temperature annealing and various plasma treatments used throughout the experiment.

5.5.1 Polarization of GaN

Wurtzite GaN exhibits a large spontaneous polarization and piezoelectric polarization (P_{SP} and P_{PE}) [60,61], which contributes to band bending at the surface. The spontaneous polarization of Ga-face GaN (P_{SP}=-0.033 C/m^2) [62] points from the surface to the bulk. The piezoelectric polarization, on the other hand, is negligible in comparison. The polarization produces a negative bound surface charge at the Ga-face and positive bound charge at the N-face on the order of ~ 2.1x10^{13} charges/cm^2. The positive bound charge may be screened by free electrons, while the negative bound sheet charge is partially compensated by the positive ionized donors. If the negative bound sheet charge is completely compensated by the positive ionized donors, the thickness of the space charge region is equal to the bound sheet charge density (=2.1x10^{13} charges/cm^2) divided by the doping concentration (N_D=1x10^{17} cm^{-3}), which is 2.1 μm. Then, the surface potential Φ_S can be calculated by the following relation:

$$\Phi_S = -\frac{qN_D}{2\varepsilon\varepsilon_0}W^2 \tag{5.3}$$

where W is the depletion layer thickness, and ε(=9.5) is the dielectric constant of GaN. This calculation gives a surface potential of ~-420 V and an average electric field of ~200 MV/m, which would be represented as 420 eV upward band bending at the GaN surface.

In equilibrium, the large field will lead to inversion, which limits the band bending to the band gap value of the material, 3.4eV in this case. This analysis indicates the polarization bound charge cannot only be completely compensated by the positive ionized donors. The experimental upward band bending for Ga-face GaN is typically reported to be between 0.3 eV and 1.5 eV [36,43,44,45], well below the band gap value. This indicates that the surface is heavily compensated. In order to achieve the experimental band bending, the space charge region width and the area density of the ionized donors can be only between 56-126 nm and $5.6x10^{11}$-$1.3x10^{12}$ cm^{-2}, respectively. So the surface would have to be screened by ~$2x10^{13}$ charges/cm^2, which could include structural defects, Ga termination, surface contamination (such as absorbed oxygen atoms), surface states or absorbates causing Fermi level pinning, or additional charge compensation [63].

5.5.2 Oxygen coverage on GaN

After the standard cleaning process, oxygen termination was retained on the GaN surface. The oxygen coverage can be calculated from the following relation [64]:

$$\Theta_O = \frac{I_O}{I_{Ga}} \frac{S_{Ga}}{S_O} \sum_{n=0}^{\infty} Exp[\frac{-nd_{GaN}}{\lambda_{Ga} Cos[\varphi]}] \tag{5.4}$$

where Θ_O is the coverage or the number of absorbed oxygen per unit area (atoms/cm^2) divided by the number of Ga or N atoms per unit area (atoms/cm^2) in the c plane. One monolayer (ML) coverage refers to one oxygen atom per surface lattice site. The I_{Ga} and I_O are the integrated intensities of the Ga 3d and O 1s peaks; S_O and S_{Ga} is the atomic

sensitivity factor for O 1s and Ga 3d core levels, which is 0.66 and 0.31, respectively [65]; λ_{Ga} is the inelastic mean free path (IMFP) of Ga 3d electrons with kinetic energies ~1200 eV, which is estimated to be 24 Å [66]; ϕ is the angle between the normal direction and the analyzer, which is 20° for the XPS setup; and, d is the distance between two Ga planes, which is 2.6 Å. The sum of the exponential function in this relation represents the Ga 3d electrons from different Ga planes. The infinite limit can be replaced by a large number, such as 25, because the exponential function decreases rapidly with increased thickness and only surface Ga layers would contribute significantly to the sum. After cleaning, the oxygen coverage on the GaN surface was calculated to be 1.9±0.2 ML, which would correspond to ~0.4 nm Ga_2O_3. To remove the residual oxygen contamination, the GaN wafer was treated with 200 W H_2/N_2 combined plasma at ~880 ℃ for 30 minutes and an additional 1 hour ~880 ℃ annealing. However, the oxygen coverage on the surface of GaN was still ~1.5 ML.

5.5.3 Plasma treatment and annealing effects

As noted in the results, the plasma treatments altered the band bending. For example, the core levels of thin film and GaN substrate move to low binding energy by ~0.5 eV after oxygen plasma treatment. It is likely that the oxygen plasma introduces a high concentration of defects or interstitial oxygen atoms, which act as deep electron traps or acceptors, respectively [67]. These defects are compensated by ionized donors in the GaN and widen the depletion region, which increases the upward band bending. Elevated temperature annealing can remove the defects or excess interstitial oxygen from the film and subsequently reduce the upward band bending. Consequently, the core levels

shift back to higher binding energy, which is confirmed by the results. Compared to HfO_2/GaN and Al_2O_3/GaN, the SiO_2/GaN had a lower surface band bending after deposition and a smaller shift during post deposition treatment, which suggested that the oxygen plasma may not readily generate acceptor-like defects in SiO_2/GaN.

5.5.4 Band Alignment Models for Dielectrics/GaN

Modeling of semiconductor interfaces has been of interest since Schottky and Mott independently introduced their theories in 1938 [68]. However, despite this relatively long history, it is still subject to some debate. Presently, there are two common adaptations of interface modeling, which argue for a different point of alignment at the interface. In this paper, we identify these as the electron affinity model and the charge neutrality level model.

The electron affinity (EA) model, presented by Anderson [69], is based on the assumption that the vacuum levels of the two materials align at the interface. This premise can be extended to the semiconductor-semiconductor interface, or more specifically the high-k oxide/ GaN interfaces. Considering the vacuum-level alignment, the VBO,

$$\Delta E_V = (E_{g,dielectric} + \chi_{dielectric}) - (E_{g,GaN} + \chi_{GaN}) = I_{dielectric} - I_{GaN} \tag{5.5}$$

where E_g and χ are the energy band gap and the electron of the given semiconductor, respectively. The sum of these two values will give the photo threshold energy, *I*. For oxygen-covered GaN, Al_2O_3, HfO_2, SiO_2, La_2O_3, and ZnO, the photo threshold energies

are 6.8, 8.5, 8.0, 9.9, 6.9, and 7.3 eV, respectively. The calculated VBOs of the Al_2O_3, HfO_2, SiO_2, La_2O_3, and ZnO/GaN heterostructures are thus 1.7, 1.2, 3.1, 0.1, and 0.5 eV, in which the results of Al_2O_3/GaN, HfO_2/GaN, SiO_2/GaN, and ZnO/GaN were close to the experimental values. Moreover, the similarity in these values is potentially misleading as the model represents an idealized case that is not often physically realized. More explicitly, the EA model assumes no charge transfer at the interface.

An alternative model, first proposed by Tejedor and Flores [70] and later calculated by Tersoff [71], evaluates the available states at the interface. This model assumes the wave function of electrons in the metal decays exponentially across the interface and induces states in the gap. These gap states behave donor-like closer to the valence band and acceptor-like closer to the conduction band. The point where the contribution from both the acceptor- and donor-like states are equal is the branch point energy or charge neutrality level (CNL). The CNL then becomes the point of alignment at the heterostructure, assuming that there is some charge transfer, which creates an interfacial dipole. This model was further adapted to account for Fermi pinning at the interface [72], by considering the pining factor, S. This was empirically demonstrated [73,74] to obey the following relation:

$$S = \frac{1}{1 + 0.1(\varepsilon_\infty - 1)^2} \tag{5.6}$$

where ε_∞ is the optical dielectric constant of the material. This modifies the alignment of the energy levels at the interface, where the VBO is given by the following relation:

$$\Delta E_V = E_{CNL,dielectric} - E_{CNL,GaN} - S[I_{GaN} - I_{dielectric} - (E_{CNL,GaN} - E_{CNL,dielectric})] \quad (5.7)$$

where $E_{CNL,GaN}$ and $E_{CNL,dielectric}$ are the charge neutrality levels of the semiconductor and dielectrics measured from the VBM. When the CNLs of the materials are aligned, the calculation is modified by the dimensionless S factor of the wider band gap material, which accounts for Schottky pinning. In the Schottky limit of no pinning (S=1), there is no charge transfer, and the electron affinity model determines the VBO. In the Bardeen limit of strong pinning (S=0), the semiconductors are aligned at the CNL. For Al_2O_3, HfO_2, SiO_2, La_2O_3, and ZnO, the S factors are 0.69, 0.53, 0.86, 0.53, and 0.53 respectively [46]. The CNLs of GaN, Al_2O_3, HfO_2, SiO_2, La_2O_3, and ZnO calculated by local density approximation (LDA) are 2.3, 3.9, 3.7, 4.5, 2.4, and 3.3 eV [75,76] with respect to VBM. These CNLs determine the VBOs at the Al_2O_3/GaN, HfO_2/GaN, SiO_2/GaN, La_2O_3/GaN, and ZnO/GaN interfaces as 1.7, 1.3, 3.0, 0.1, and 0.7 eV. The results for Al_2O_3/GaN, HfO_2/GaN, SiO_2/GaN, and ZnO/GaN were close to the experimentally measured values. On the other hand, the empirically determined CNLs of GaN, Al_2O_3, HfO_2, SiO_2, and ZnO, 2.3 eV, 3.0 eV, 2.3 eV, 3.5 eV, and 2.8 eV, vary from the theoretical values [75]. Using the empirical values, the VBOs at the Al_2O_3/GaN, HfO_2/GaN, SiO_2/GaN, and ZnO/GaN interfaces are 1.4 eV, 0.6 eV, 2.5 eV, and 0.5 eV, smaller than the experimentally determined values of this report.

For the HfO_2/Al_2O_3/GaN stacked structure, the experimental VBO of HfO_2/Al_2O_3 was ~-0.2 eV, which was close to the calculated result based on CNL model (-0.4 eV). In addition, the VBO and CBO of HfO_2 with respect to GaN were ~1.3 eV and 1.1 eV respectively, which were close to the values in the HfO_2/GaN structure. The VBO of

HfO_2 and GaN in this stacked structure could be calculated by the difference of VBOs for HfO_2/Al_2O_3 and Al_2O_3/GaN, assuming there was no electric field in Al_2O_3 layer. Therefore, the difference for the VBOs of HfO_2 and GaN in HfO_2/GaN and HfO_2/Al_2O_3/GaN (Δ (ΔE_V)) could be calculated by the following equation.

$$\Delta(\Delta E_V) = (\Delta E_V)_{HfO2/GaN} - (\Delta E_V)_{HfO2/Al2O3/GaN}$$
$$= [(I_{GaN} - E_{CNL,GaN}) - (I_{HfO2} - E_{CNL,HfO2})]^*(S_{Al2O3} - S_{HfO2}) \quad (5.8)$$

The calculation suggested the difference was only ~0.032 eV due to the similar values for pinning factor S for Al_2O_3 and HfO_2 and similar CNL values with respect to vacuum level (I-E_{CNL}) for HfO_2 and GaN. This indicated the interfacial passivation layer did not significantly alter the band offset of the HfO_2/GaN heterostructure, if there was no significant field in the Al_2O_3 layer, as shown in Fig. 5. 17.

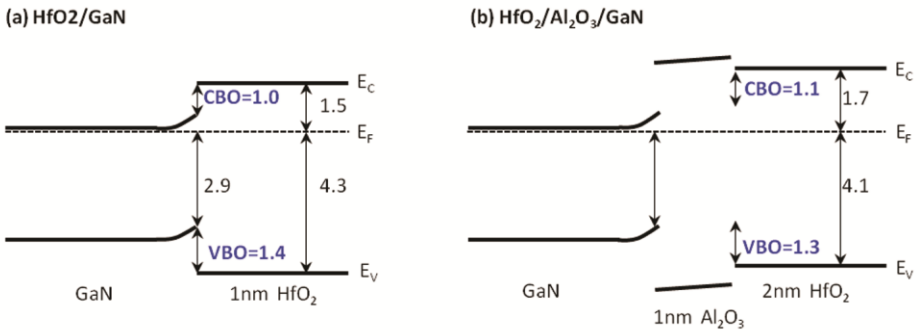

Figure 5.17. Band alignment diagram for (a) HfO_2/GaN and (b) HfO_2/Al_2O_3/GaN after annealing.

There is an additional factor to consider when evaluating the consistency of these models. Several researchers [77,78,79,80] have shown that the electron affinity of a material is dependent on the electronegativity of the adsorbed atoms. In other words, the electron affinity of the clean surface, which was used in the above calculations, is not necessarily an accurate representation of the electron affinity of that material at an interface. Investigation of the electronegativities of the elements involved suggests that the electron affinity of the dielectric will increase and/or the GaN substrate will decrease. Either of these changes will increase the VBOs determined by both models. Since both models report values lower than the experimentally determined VBOs, this correction further supports the experimentally determined VBOs.

The comparison between the theoretical band offsets calculated by Robertson *et al.* [46] and the experimental values in this research is shown in Fig. 5.18. Note that Robertson's original calculation for Al_2O_3 [46] were based on sapphire crystal structure and was modified with the parameters based on amorphous structure in this study. This figure indicates that the experimental band offset results for all five dielectrics are close to the theoretical calculations. The main difference in the calculations from this study and Robertson was the different photo threshold energy of GaN and dielectrics used.

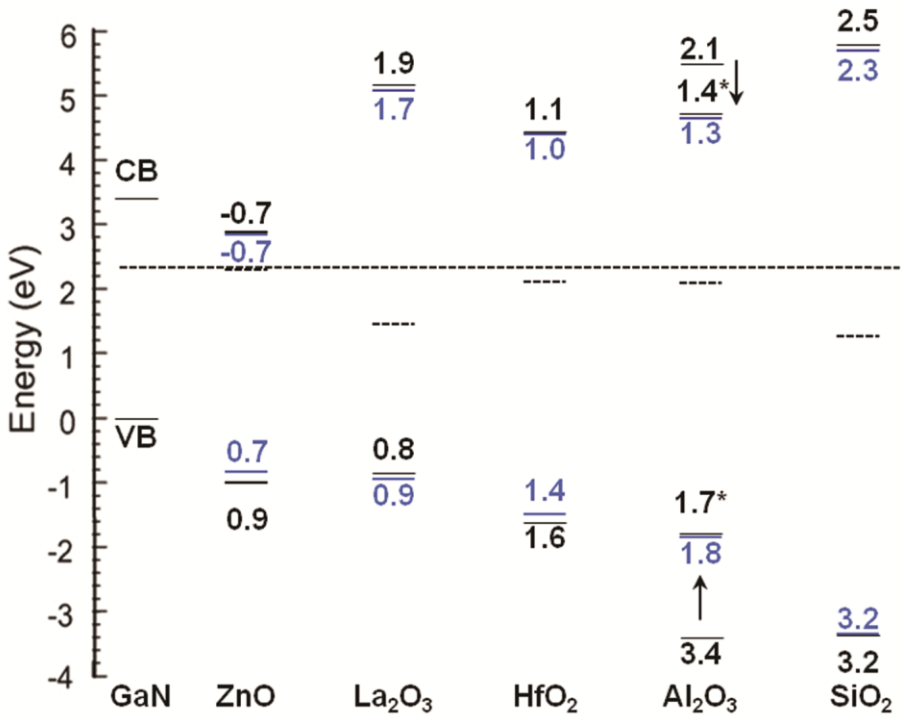

Figure 5.18. The experimental (blue solid line) and theoretical (black solid line) band offset results of dielectrics on GaN. The dash lines represent the CNL levels of the dielectrics and GaN.

In an attempt to better understand the similarity of these two models, the above calculations are considered in Fig. 5.19. The slight disparities of the charge neutrality levels and electron affinity levels are marked as Δ_{CNL} and Δ. These can be explained in terms of experimental error, inaccurate determination of the electron affinities, and Schottky pinning, which is not accounted for in this figure and will contribute to Δ_{CNL}.

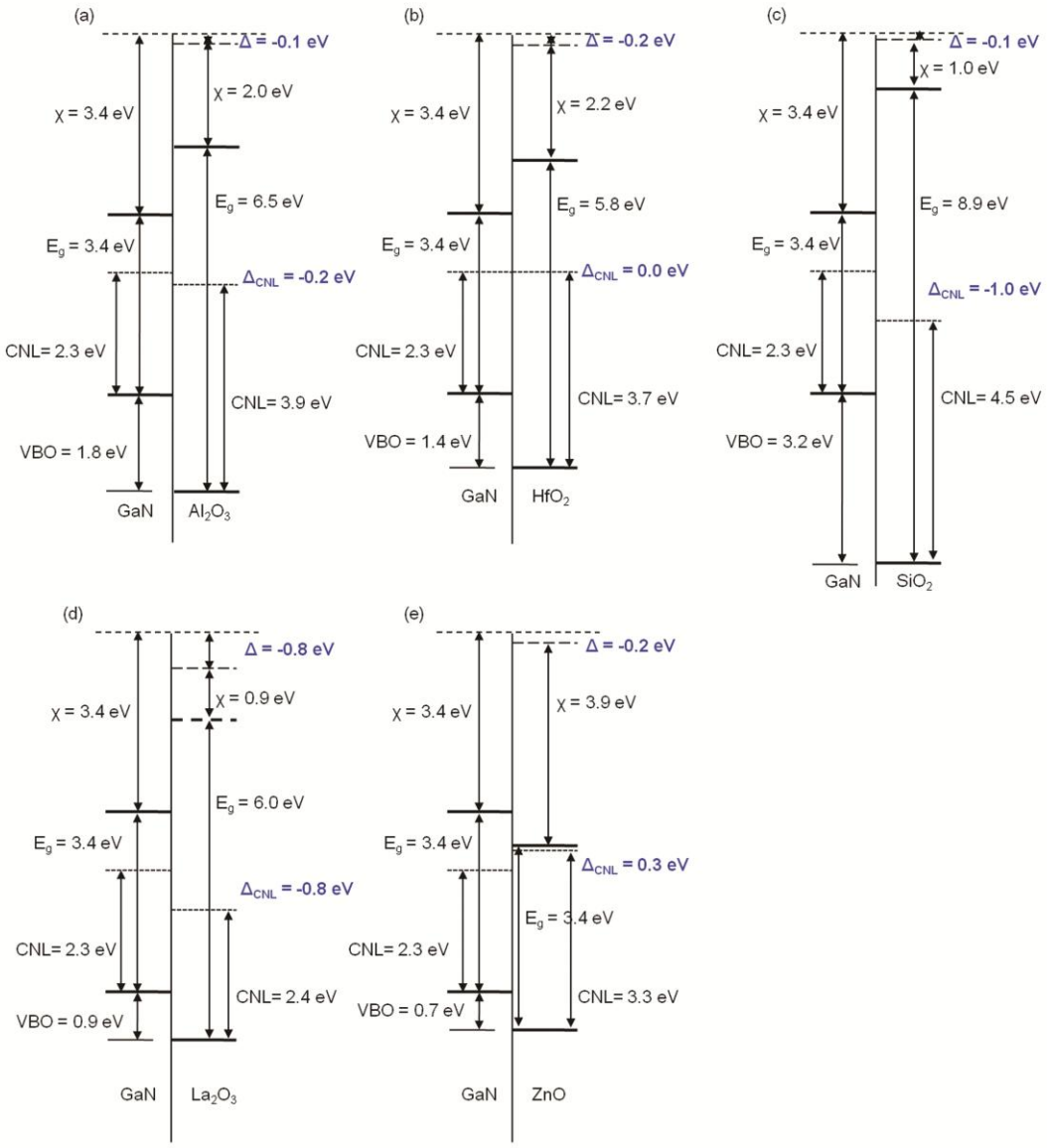

Figure 5.19. Band alignment diagram for (a) Al_2O_3/GaN, (b) HfO_2/GaN, (c) SiO_2/GaN, (d) La_2O_3/GaN, and (e) ZnO/GaN interfaces. The dashed line at the top of the figure corresponds to the vacuum level of GaN. The deviation from the electron affinity model is shown as Δ, and the deviation from the charge neutrality level model in the limit of strong pinning, S=0, is marked as Δ_{CNL}. The VBO was measured experimentally, and the charge neutrality levels of GaN, HfO_2, Al_2O_3, SiO_2, La_2O_3, and ZnO were provided by theoretical calculations [46,76].

5.5.5 Band offsets and dielectric band gap

The relation between the dielectric band gap and the band offsets of dielectrics on GaN is plotted in Fig. 5.20. In addition, it also suggests that the PEALD La_2O_3 in this study presumably has a band gap ~4.3 eV. To achieve low gate leakage current, the dielectrics on semiconductors need potential barrier over 1 V for electrons [81]. Fig. 5.20 shows the dielectric potential barrier for holes is larger than that for electrons on GaN. To provide more than 1 V potential barrier for holes, the dielectric should have a band gap greater than ~4.6 eV. However, the dielectrics should have a band gap larger than ~5.8 eV to build over 1 V potential barrier for electrons. This can be achieved by single large band gap dielectric (e.g. HfO_2, Al_2O_3, SiO_2), stacked structure (e.g. HfO_2-Al_2O_3 or SiO_2, La_2O_3-Al_2O_3 or SiO_2), or alloys (e.g. $LaAl_xO_y$, $LaSi_xO_y$, $HfSi_xO_y$).

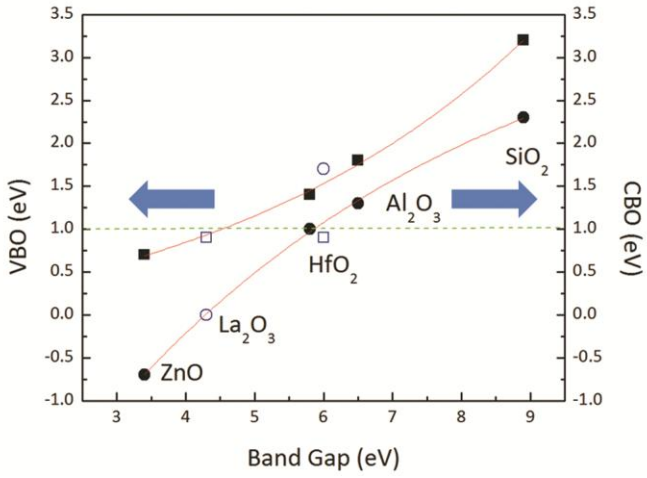

Figure 5.20. The dielectric band gap vs VBO and CBO on GaN. The square and circle symbols represent VBO and CBO respectively, and the open symbols represent La_2O_3 with band gap of 4.3 and 6.0 eV. The dashed and solid line serves as visual aid.

5.6 Conclusion

The band alignments of dielectrics, Al_2O_3, HfO_2, SiO_2, La_2O_3, and ZnO as well as the stacked structure HfO_2/Al_2O_3 on n-type, Ga-face GaN have been investigated. An *ex-situ* wet chemical clean with acetone, methanol, and HCl and an *in-situ* clean with 15 minute H_2/N_2 plasma and additional 30 minute annealing at 650 ℃ provided an oxygen-covered GaN surface with 1.9±0.2 ML of oxygen and 0.3 eV upward band bending. These values, while consistent with other groups' experiment data, are well below the calculation predicted from the polarization, which suggests that the surface is compensated at a level of ~10^{13} charges/cm^2. The electron affinity of Al_2O_3, HfO_2, SiO_2, La_2O_3, and ZnO was measured to be 2.0, 2.2, 1.0, 0.9, and 3.9 eV respectively. The respective valence band offsets at Al_2O_3/GaN, HfO_2/GaN, SiO_2/GaN, La_2O_3/GaN, and ZnO/GaN heterostructures were 1.8, 1.4, 3.2, 0.9, and 0.7 eV, which indicated corresponding conduction band offsets of 1.3, 1.0, 3.2, 1.7, and -0.7 eV. These band offset values are similar to the theoretical values calculated from the charge neutrality level model. The trends of potential barrier for dielectrics on GaN are related to the dielectric band gap. The dielectric potential barriers for holes are higher than that for electrons on GaN. To provide more than 1 V potential barriers for electrons, dielectric should have a band gap larger than 5.8 eV. Although the annealing and re-oxidization process could change the interface charges and alter the electric field in the dielectric and the band bending at the GaN interface, the band offset remained constant. For the HfO_2/Al_2O_3/GaN stacked structure, the valence band offset and conduction band offset of HfO_2 with respect to GaN were ~1.3 eV and 1.1 eV respectively. These values are close

to the values in the HfO_2/GaN structure and indicate the interfacial passivation layer does not significantly alter the band offset of between HfO_2 and GaN.

Reference

[1] P. D. Ye, B. Yang, K. K. Ng, J. Bude, G. D. Wilk, S. Halder and J. C. M. Hwang, *Appl*. *Phys*. *Lett*. **86**, 063501 (2005).

[2] S. Ootomo, T. Hashizume and H. Hasegawa, *Phys*. *Status Solidi* C **0**, 90 (2002).

[3] T. Hashizume, S. Ootomo and H. Hasegawa, *Appl*. *Phys*. *Lett*. **83**, 2952 (2003).

[4] Y. Z. Yue, Y. Hao, Q. Feng, J. C. Zhang, X. H. Ma and J. N. Ni, *Chin*. *Phys*. *Lett*. **24**, 2419 (2007).

[5] Y. Hao, Y. Z. Yue, Q. Feng, J. C. Zhang, X. H. Ma and J. N. Ni, *Chin*. *J*. *Semicond*. **28**, 1674 (2007).

[6] Y. C. Chang, H. C. Chiu, Y. J. Lee, M. L. Huang, K. Y. Lee, M. Hong, Y. N. Chiu, J. Kwo and Y. H. Wang, *Appl*. *Phys*. *Lett*. **90**, 232904 (2007).

[7] C. F. Shih, K. T. Hung, C. Y. Hsiao, S. C. Shu and W. M. Li, *J*. *Alloys Compd*. **480**, 541 (2009).

[8] T. E. Cook, Jr., C. C. Fulton, W. J. Mecouch, R. F. Davis, G. Lucovsky and R. J. Nemanich, *J*. *Appl*. *Phys*. **94**, 7155 (2003).

[9] S. Arulkumaran, T. Egawa, H. Ishikawa, T. Jimbo, and M. Umeno, *Appl.Phys. Lett.* **73**, 809 (1998).

[10] L. Pang, Y. Lian, D.-S. Kim, J.-H. Lee, and K. Kim, *IEEE Trans. Electron Devices* **59**, 2650 (2012).

[11] J. S. Jur, V. D. Wheeler, D. J. Lichtenwalner, J. P. Maria, and M. A. L. Johnson, *Appl. Phys. Lett*. **98**, 042902 (2011).

[12] H. C. Chiu, C. W. Lin, C. H. Chen, C. W. Yang, C. K. Lin, J. S. Fu, L. B. Chang, R. M. Lin, and K. P. Hsueh, *J. Electrochem. Soc.* **157**, H160 (2010).

[13] Y. Dora, S. Han, D. Klenov, P. J. Hansen, K. S. No, U. K. Mishra, S. Stemmer and J. S. Speck, *J. Vac. Sci. Technol. B* **24**, 575 (2006).

[14] R, Mehandru, B. Luo, J. Kim, F. Ren, B. P. Gila, A. H. Onstine, C. R. Abernathy, S. J. Pearton, D. Gotthold, R. Birkhahn, B. Peres, R. Fitch, J. Gillespie, T. Jenkins, J. Sewell, D. Via and A. Crespo, *Appl*. *Phys*. *Lett*. **82**, 2530 (2003).

[15] B. Luo, J. W. Johnson, B. P. Gila, A. Onstine, C. R. Abernathy, F. Ren, S. J. Pearton A. G. Baca, A. M. Dabiran, A. M. Wowchack and P. P. Chow, *Solid-State Electronics* **46**, 467 (2002).

[16] H. Cho, K. P. Lee, B. P. Gila, C. R. Abernathy, S. J. Pearton and F. Ren, *Solid-State Electronics* **47**, 1757 (2003).

[17] H. Cho, K. P. Lee, B. P. Gila, C. R. Abernathy, S. J. Pearton and F. Ren, *Electrochem. Solid-State Lett.* **6**, G149 (2003).

[18] J. Kim, R. Mehandru, B. Luo, F. Ren, B. P. Gila, A. H. Onstine, C. R. Abernathy, S. J. Pearton and Y. Irokawa, *Appl. Phys. Lett.* **80**, 4555 (2002).

[19] B. P. Gila, A. H. Onstine, J. Kim, K. K. Allums, F. Ren, C. R. Abernathy and S. J. Pearton, *J. Vac. Sci. Technol. B* **21**, 2368 (2003).

[20] B. P. Gila, J. Kim, B. Luo, A. Onstine, W. Johnson, F. Ren, C. R. Abernathy and S. J. Pearton, *Solid-State Electronics* **47**, 2139 (2003).

[21] M. Hong, J. Kwo, S. N. G. Chu, J. P. Mannaerts, A. R. Kortan, H. M. Ng, A. Y. Cho, K. A. Anselm, C. M. Lee and J. I. Chyi, *J. Vac. Sci. Technol. B* **20**, 1274 (2002).

[22] M. Hong, K. A. Anselm, J. Kwo, H. M. Ng, J. N. Baillargeon, A. R. Kortan, J. P. Mannaetrs, A. Y. Cho, C. M. Lee, J. I. Chyi and T. S. Lay, *J. Vac. Sci. Technol. B* **18**, 1453 (2000).

[23] F. Ren, C. R. Abernathy, J. D. Mackenzie, B. P. Gila, S. J. Pearton, M. Hong, M. A. Marcus, M. J. Schurman, A. G. Baca and R. J. Shul, *Solid-State Electronics* **42**, 2177 (1998).

[24] F. Ren, M. Hong, S. N. G. Chu, M. A. Marcus, M. J. Schurman, A. Baca, S. J. Pearton, and C. R. Abernathy, *Appl. Phys. Lett.* **73**, 3893 (1998).

[25] C.-T. Lee, Y.-L. Chiou, and C.-S. Lee, IEEE Electron Device Lett. **31**,1220 (2010).

[26] G. Vanko, M. Vallo, J. Bruncko, and T. Lalinský, Vacuum **86**, 672 (2012).

[27] H. B. Profijt, S. E. Potts, M. C. M. van de Sanden and W. M. M. Kessels, *J. Vac. Sci. Technol. A* **29**, 050801 (2011).

[28] E. Bersch, S. Rangan, R. A. Bartynski, E. Garfunkel and E. Vescovo, *Phys. Rev. B.* **78**, 085114 (2008).

[29] V. V. Afanas'ev and A. Stesmans, *J. Appl. Phys*. **102**, 081301 (2007).

[30] I. Kim, J. Koo, J. Lee and H. Jeon, *Jpn. J. Appl. Phys.* Part 1 **45**, 919 (2006).

[31] Y. Q. Wu, T. Shen, P. D. Ye and G. D. Wilk, *Appl. Phys. Lett*, **90**, 143504 (2007).

[32] B. S. Eller, J. Yang, and R. J. Nemanich, *J. Vac. Sci. Technol. A* **31** 050807 (2013).

[33] A. M. De Asha, J. T. S. Critchley and R. M. Nix, *Surf. Sci*. **405**, 201 (1998).

[34] T. Gougousi, M. J. Kelly, D. B. Terry, and G. N. Parsons, *J. Appl. Phys*. **93**, 1691 (2003).

[35] W. J. Mecouch, B. P. Wagner, Z. J. Reitmeier, R. F. Davis, C. Pandarinath, B. J. Rodriguez, and R. J. Nemanich, *J. Vac. Sci. Technol. A* **23**, 72 (2005).

[36] K. M. Tracy, W. J. Mecouch, R. F. Davis, and R. J. Nemanich, *J. Appl. Phys.* **94**, 3163 (2003).

[37] S. W. King, J. P. Barnak, M. D. Bremser, K. M. Tracy, C. Ronning, R. F. Davis, and R. J. Nemanich, *J. Appl. Phys*. **84**, 5248 (1998).

[38] L. L. Smith, S. W. King, R. J. Nemanich, and R. F. Davis, *J. Electron. Mater*. **25**, 805 (1996).

[39] W. Götz, N. M. Johnson, C. Chen, H. Liu, C. Kuo, and W. Imler, *Appl. Phys. Lett.* 68, 3144 (1996).

[40] J. R. Waldrop and R. W. Grant, *Appl. Phys. Lett*. **68**, 2879 (1996).

[41] E. A. Kraut, R. W. Grant, J. R. Waldrop and S. P. Kowalczyk, *Heterojunction Band Discontinuities: Physics and Device Applications*, edited by F. Capasso and G. Margaritondo (Elsevier, New York, 1987).

[42] J. Hedman and N. Mårtensson, *Phys. Scr*. **22**, 176 (1980).

[43] P. Lorenz, T. Haensel, R. Gutt, R. J. Koch, J. A. Schaefer and S. Krischok, *Phys. Status Solidi B* **247**, 1658 (2010).

[44] H. W. Jang, J. H. Lee and J. L. Lee, *Appl. Phys. Lett*. **80**, 3955 (2002).

[45] C. I. Wu, A. Kahn, N. Taskar, D. Dorman and D. Gallagher, *J. Appl. Phys*. **83**, 4249 (1998).

[46] J. Robertson and B. Falabretti, *J. Appl. Phys*. **100**, 014111 (2006).

[47] I. Costina and R. Franchy, *Appl. Phys. Lett.* **78**, 4139 (2001).

[48] R. H. French, *J. Am. Ceram. Soc*. **73**, 477 (1990).

[49] H. Momida, T. Hamada, Y. Takagi, T. Yamamoto, T. Uda and T. Ohno, *Phys. Rev. B.* **73**, 054108 (2006).

[50] H. Y. Yu, M. F. Li and D. L. Kwong. *Thin Solid Films.* **462**, 110 (2004).

[51] H. Y. Yu, M. F. Li, B. J. Cho, C. C. Yeo, M. S. Joo, D.-L. Kwong, J. S. Pan, C. H. Ang, J. Z. Zheng and S. Ramanathan, *Appl. Phys. Lett.* **81**, 376 (2002).

[52] N. V. Nguyen, O. A. Kirillov, W. Jiang, W. Wang, J. S. Suehle, P. D. Ye, Y. Xuan, N. Goel, K.-W. Choi, W. Tsai and S. Sayan. *Appl. Phys. Lett.* **93**, 082105 (2008).

[53] O. Blank, H. Reisinger, R. Stengl, M. Gutsche, F. Wiest, V. Capodieci, J. Schulze, and I. Eisele, *J. Appl. Phys*. **97**, 044107 (2005).

[54] M. Yoshitake, W. Song, J. Libra, K. Masek, F. Sutara, V. Matolin, and K. C. Prince, *J. Appl. Phys.* **103**, 033707 (2008).

[55] S. Suzer, S. Sayan, M. M. Banaszak Holl, E. Garfunkel, Z. Hussain and N. M. Hamdan. *J. Vac. Sci. Technol*. *A* **21,** 106 (2003).

[56] T. E. Cook, Jr., C. C. Fulton, W. J. Mecouch, K. M. Tracy, and R. F. Davis, E. H. Hurt, G. Lucovsky, and R. J. Nemanich, *J. Appl. Phys.* **93**, 3995 (2003).

[57] J. F. Ihlefeld, M. Brumbach, and S. Atcitty, *Appl Phys Lett.* **102**, 162903 (2013).

[58] S.-K. Hong, T. Hanada, H. Makino, Y. Chen, H.-J. Ko, T. Yao, A. Tanaka, H. Sasaki, and S. Sato, *Appl. Phys. Lett.* **78**, 3349 (2001).

[59] B. Kramm, A. Laufer, D. Reppin, A. Kronenberger, P. Hering, A. Polity, and B. K. Meyer, *Appl. Phys. Lett.* **100**, 094102 (2012).

[60] F. Bernardini, V. Fiorentini and D. Vanderbilt, *Phys. Rev. B,* **56**, 10024 (1997).

[61] F. Bernardini and V. Fiorentini, *Phys. Status Solidi B* **216**, 391 (1999).

[62] A. Zoroddu, F. Bernardini, P. Ruggerone and V. Fiorentini, *Phys. Rev. B* **64**, 045208 (2001).

[63] U. Karrer, O. Ambacher and M. Stutzmann, *Appl. Phys. Lett*. **77**, 2012 (2000).

[64] V.M. Bermudez, *J. Appl. Phys.* **80**, 1190 (1996).

[65] D. Briggs and M. P. Seah, Practical Surface Analysis, Vol. 1 Auger and X-ray Photoelectron Spectroscopy, 2nd edition (John Wiley & Sons, West Sussex, 1990).

[66] M. Krawczyk, L. Zommer, A. Jablonski, I. Grzegory and M. Bockowski *Surf. Sci*. **566-568**, 1234 (2004).

[67] O. Bierwagen, J. S. Speck, T. Nagata, T. Chikyow, Y. Yamashita, H. Yoshikawa, and K. Kobayashi, *Appl. Phys. Lett.* **98**, 172101 (2011).

[68] T.E. Cook, C.C. Fulton, W.J. Mecouch, R.F. Davis, G. Lucovsky and R.J. Nemanich, *J. High Speed Electron. Sys.* **14**, 107 (2004).

[69] R. L. Anderson, *Solid-State Electron*. **5**, 341 (1962).

[70] C. Tejedor and F. Flores, *J. Phys. C: Solid State Phys.* **11**, L19 (1978).

[71] J. Tersoff, *Phys. Rev. B* **30**, 4874 (1984).

[72] J. Roberston, *J. Vac. Sci. Technol. B* **18**, 1785 (2008).

[73] W. Mönch, *Phy. Rev. Lett.* **58**, 1260 (1987).

[74] W. Mönch, *J. Vac. Sci. Technol. B* **6**, 1270 (1988).

[75] W. Mönch, *J. Appl. Phys.* **109**, 113724 (2011).

[76] L. R. C. Fonseca, D. Liu and J. Robertson, *Appl. Phys. Lett.* **93**, 122905 (2008).

[77] J. Bardeen, *Phys. Rev.* **71**, 717 (1947).

[78] M. Schlüter, *Phys. Rev. B* **17**, 5044 (1978).

[79] S. Hashimoto, K. Egashira, T. Tanaka, R. Etoh, Y. Hata and R.T. Tung, *J. Appl. Phys.* **97**, 024911 (2005).

[80] Y. Li, W. Long and R.T. Tang , *Solid-State Commun.* **151**, 1641 (2011).

[81] J. Robertson , *J Non-Cryst Solids*, **303** 94 (2002).

CHAPTER 6

SURFACE BAND BENDING AND BAND ALIGNMENT OF PLASMA ENHANCED ATOMIC LAYER DEPOSITED DIELECTRICS ON GA-FACE AND N-FACE GALLIUM NITRIDE

6.1 Abstract

The effects of surface pretreatment, dielectric growth, and post deposition annealing on interface electronic structure and polarization charge compensation on Ga- and N-face GaN were investigated. The cleaning process consisted of an *ex-situ* wet chemical NH_4OH treatment and an *in-situ* elevated temperature NH_3 plasma process to remove carbon contamination, reduce oxygen coverage, and passivate N vacancy related defects. After the cleaning process, the carbon contamination was below the x-ray photoemission spectroscopy (XPS) detection limit, and oxygen coverage was stabilized at ~1 Monolayer on both Ga- and N-face GaN. After cleaning, the Ga- and N-face GaN had upward band bending of 0.8 ± 0.1 eV and 0.6 ± 0.1 eV respectively, which suggested the net charge of surface defects and polarization bound charge were almost the same on Ga- and N-face GaN with the same sign. In addition, three dielectrics (Al_2O_3, HfO_2, and SiO_2) were prepared by plasma-enhanced atomic layer deposition (PEALD) on Ga- or N-face GaN to investigate the polarization charge effect on the interface electronic structure and band offset through *in-situ* XPS and ultraviolent photoemission spectroscopy (UPS) characterization. In addition, the effect of different post deposition processing, included annealing in gas ambient (N_2, H_2/N_2 (10% H_2), or NH_3) and O_2 plasma treatment, on

interface electronic structure and polarization charge compensation mechanism was investigated. The respective valence band offsets of Al_2O_3, HfO_2, and SiO_2 with respect to Ga- and N-face GaN were 1.9 ± 0.2, 1.4 ± 0.1, and 3.1 ± 0.1 eV, regardless the dielectric thickness and processing conditions. The corresponding conduction band offset were 1.4 ± 0.2, 1.0 ± 0.1, and 2.4 ± 0.1 eV, respectively. The experimental band offset results were consistent with the theoretical calculations based on the charge neutrality level model. The effect of polarization charge on band offset was apparently screened by the surface defects on GaN. The O_2 plasma induced acceptor-like defects were $\sim 1.0 \pm 0.3 \times 10^{12}$ in Al_2O_3/GaN, HfO_2/GaN and SiO_2/GaN. For Al_2O_3/GaN and HfO_2/GaN, the negative defects could be removed by annealing; while for SiO_2/GaN, annealing in H-contained ambient (e.g., H_2/N_2 (10% H_2), or NH_3) was required to remove these defects effectively.

6.2. Introduction

GaN based transistors have shown great potential in high frequency, high temperature, and high power electronic devices due to their excellent material properties, such as large band gap (~3.4 eV), high breakdown field (~3 MV/cm), and high electron saturation velocity (~10^7 cm/s) [1,2,3,4]. There are two promising GaN based power electronic structures, GaN based metal semiconductor field-effect transistors (MESFETs) and GaN/AlGaN based high electron mobility transistors (HEMTs), which have been extensively studied [2,3]. However, these electronic structures suffer from a large leakage current and a significant current collapse, which are both attributed to a large concentration of surface defects [2,5,6,7,8].

On the other hand, the GaN has a bound charge due to a strong polarization effect, which further complicates this issue. GaN forms in the wurtzite crystal structure which exhibits a high degree of ionicity. The lack of inversion symmetry in the (0001) plane results in two different atomic layering sequences along the c-axis ([0001]), leading to a Ga-face ((0001) or +c plane) or N-face ($(000\bar{1})$ or -c plane) surface. These factors give rise to a large spontaneous polarization $\mathbf{P_{SP}}$, pointing from the Ga-face to N-face [9]. In addition, there may be also piezoelectric polarization $\mathbf{P_{PZ}}$ in GaN, which is along [0001] or $[000\bar{1}]$ direction when GaN is in compressive or tensile strain, respectively. Without an external electric field, the total polarization in GaN is the sum of the spontaneous and piezoelectric polarization. However, GaN films are typically grown above a critical thickness (~10nm), and there is only a small residual strain in the film [10]. Comparing with the large value of spontaneous polarization in GaN (=-0.033C/m^2) [11], the piezoelectric polarization (=0.002 C/m^2) is typically negligible, which will not be discussed in this study [12].

The GaN spontaneous polarization leads to negative and positive bound sheet charge (~2.1x10^{13} charges/cm^2) at the Ga- and N-face GaN respectively, which are typically compensated to avoid a large internal field in the material. For typical n-type GaN films, there was insufficient ionized donors to fully compensate the negative bound sheet charge at the Ga-face. Consequently, large band bending equal to the band gap would be required to invert the surface. In contrast for the N-face with a positive bound sheet charge, free electrons can compensate, leading to small downwards band bending [13]. However, experimental results to date show that the Ga-face exhibits an upward bending of 0.3-1.5 eV [14,15,16,17] and the N-face has an upward bending of 0.1-1.0 eV

[18,19,20]. This suggests that the internal compensation by ionized donor or free electrons do not play the major role. It appears that charged surface states play a greater role in polarization charge screening. These surface states may include structural defects, surface termination, surface oxides, contaminant, surface states, adsorbates, and additional charge screening [13].

The surface and bulk defect states, which may be related to the polarization charge screening, have a considerable effect on the failure mechanism. First of all, they may assist thermionic emission and/or thermionic field emission for electron tunneling by acting like trapping centers [2,21] or pinning states that causing a thin Schottky barrier [5,7]. On the other hand, the current collapse is ascribed to the formation of virtual gate, which describes the reduction of positive surface states [8]. The reduction in positive surface states may be caused by electron trapping or removal of positive states. Through proper cleaning process, dielectric growth, and post deposition annealing process, the related states may be passivated and the failure mechanisms may be mitigated [2].

Various surface treatments were investigated to mitigate the failure mechanism [2]. The cleaning process typically includes an *ex-situ* wet chemical clean and an *in-situ* elevated temperature process. The surface contamination on GaN and AlGaN usually consists of carbon contamination, oxides, absorbates, and residual species. Edwards *et al*. [22] reported there was a ~2-5 nm contamination layer on air-exposed GaN. Half of the contamination layer was organic and inorganic contaminants, and the rest were oxides, presumably native oxide. On one hand, several studies had shown that the carbon contamination and N-vacancy related defects play a role in current collapse and leakage current in GaN based devices [7,23,24,25]. On the other hand, the defects in the low

quality native oxide of GaN could also degrade device performance. The surface oxide could be removed with high temperature processes (800~900 ℃), while GaN may start to decompose at this temperature range, resulting in dangling bonds and other defects. Consequently, the goal of the surface pretreatment in this study is to remove carbon contamination, passivate N-vacancy related defects, and decrease oxide bulk defects while retaining oxygen coverage to stabilize the surface chemistry. For the wet chemical treatment, NH_4OH has demonstrated effective removal of native oxide since Ga_2O_3 easily dissolves in the alkali [26,27,28]. An *in-situ* relatively elevated temperature process is then employed to further reduce the surface impurities and defects and provide a surface appropriate for PEALD dielectric growth. Annealing GaN in a chemically active plasma has proven to be more effective to remove contamination and reduce defects than annealing in gas ambient. The plasma annealing also causes much less damage compared with ion sputtering. Hasegawa *et al.* [7,26] reported an *in-situ* N_2 plasma process can effectively passivate N-vacancy related defects and improve the device performance. In addition, some other groups [29,30,31] found that NH_3 plasma process could effectively remove carbon contamination an suppress current collapse. The effect was attributed to a reduction of N-vacancy related defects and introduction of interstitial H+, which can passivate bulk defects in GaN.

After cleaning process, suitable dielectric growth is also crucial to suppress leakage current and current collapse. The deposition of insulator (oxide) layer between GaN (or AlGaN) and metal gate could serve as additional barrier layer for electron tunneling, which could reduce the leakage current significantly [2,3]. Applying dielectric passivation layer between the gate and drain can prevent the charge transfer from/to the

surface and mitigate the current collapse [2]. Due to the advantages of applying the dielectric layer, various dielectrics have been studied on GaN devices, such as Al_2O_3 [17,32,33], HfO_2 [17,34,35], SiO_2 [36,37], La_2O_3 [38], Si_3N_4 [39,40], AlN [41], Sc_2O_3 [42,43], MgO [44,45], ZnO [46], and other oxides [2,3]. Among all the dielectrics, SiO_2, Al_2O_3, and HfO_2 have received extensive attention due to their excellent properties. They all have sufficient band gap energies (5.8 ~ 8.9 eV) to effectively reduce leakage current. In addition, SiO_2 has a relatively small dielectric constant (~3.9), and good chemical and thermal stability. Al_2O_3 has a relatively high dielectric (~9), high breakdown field (~10^7 V/cm), adhesion to AlGaN, and good chemical and thermal stability. On the other hand, HfO_2 has a higher dielectric constant (~20), but it is less thermally stable. The high dielectric constant of HfO_2 can mitigate the significant decrease in device transconductance [33, 47] and large threshold voltage shift [47].

In addition to the intrinsic properties of the dielectric, the deposition method also plays a critical role in determining the interface and bulk properties of dielectrics on GaN, and ultimately affecting the device performance. Atomic layer deposition (ALD) is based on sequential use of two half-cycle self-limiting surface reaction [48]. It can fulfill uniform growth over large substrate and conformal deposition on structures of high aspect ratio along with atomic layer scale thickness control [48,49], which has been preferred as the thin film deposition method. Plasma enhanced atomic layer deposition (PEALD) uses activated species generated by a plasma to oxidize the precursor, which can reduce the growth temperature and impurities, and increase the growth rate and film density [17,50,51,52]. In addition, it can have better control of the film composition by adding other gases into plasma [51,52]. There have been several studies about ALD SiO_2

and PEALD Al_2O_3 and HfO_2 on GaN and AlGaN/GaN based devices, which showed improved performance of suppressing leakage current and current collapse [36,53,54,55]. In addition to Ga-face AlGaN/GaN HEMTs, N-face GaN/AlGaN HEMTs exhibits a two-dimensional electron gas (2DEG) at the N-face GaN/AlGaN interface [56,57]. To better understand the confinement properties of carriers in the semiconductor, the interface electronic structure and band alignment of these PEALD dielectrics on Ga- and N-face GaN needs to be characterized. In addition, the effect of polarization charge on band offsets should also be better understood.

After dielectric growth, post deposition annealing in some form of N_2 ambient can further decrease the deep level traps and interface states in GaN and AlGaN/GaN heterostructures [58,59,60,61]. The different processing may change the location and/or the concentration of charged states. This could affect the polarization charge screening by internal ionized donors or electrons, which then affects the surface band bending of GaN.

In this research, the *ex-situ* and *in-situ* surface pretreatments prior to dielectric films growth are charazterized by the amount of residual carbon contamination, the oxygen coverage, and the band bending which reflects the changed surface states. An *in-situ* x-ray and ultraviolet photoemission spectroscopy (XPS and UPS) was used to characterize the surface chemistry and electronic structure. After cleaning, the interface electronic structures of three PEALD dielectrics Al_2O_3, HfO_2, and SiO_2 on both Ga- and N-face GaN were investigated to establish the interface band alignment and understand the effect of polarization charge on the band offset and band bending. Different post deposition processes were applied to investigate the effect of process induced defect formation and/or reduction. The results indicated that the surface band bending of both

Ga- and N-face GaN was ~0.6-0.8 eV after the cleaning processes, which suggested a large concentration of surface defects with opposite charge on the different surfaces. This large concentration of surface defects apparently screens the polarization charge and minimizes the effect of polarization on band offset between dielectric and GaN. The O_2 plasma could induce acceptor-like defects in Al_2O_3/GaN and HfO_2/GaN which could be removed by an annealing process; while for SiO_2/GaN, annealing in H-contained ambient was required to remove these defects effectively.

6.3 Experiment

6.3.1 GaN surface pretreatment

There were two types of GaN wafers investigated in this research. One was the n-type bulk GaN, which was ~450μm thick grown by hydride vapor phase epitaxy (HVPE) method. The Si doping density was ~$8x10^{17}$ cm^{-3}, which indicated the Fermi level was ~0.1 eV below the conduction band minimum (CBM). The other one was the n-type, Ga-face, GaN films (~500 nm) on Si (111) substrate grown by the HVPE, which was used to investigate the effects of different *ex-situ* wet chemical and *in-situ* plasma cleaning processes. The Si doping density was ~$1x10^{17}$ cm^{-3}, which indicated a similar Femi level position. The comparative Ga- and N-face GaN measurement were on the bulk GaN wafers.

The surface pretreatment processes included *ex-situ* wet chemical processes and *in-situ* elevated temperature remote NH_3 plasma processing. For the GaN/Si wafers, the wet chemical clean included sonicating in separate acetone, methanol, and NH_4OH or

HCl solutions for 10 min each, followed by a 10 s rinse in DI water and blow dry with ultra high purity (UHP) N_2 gas. After the chemical clean, the samples were loaded into the ultra high vacuum (UHV) system with a base pressure of $4x10^{-10}$ Torr. Following the *ex-situ* NH_4OH wet chemical clean, the surfaces were processed *in-situ* with 45 min vacuum annealing or NH_3 plasma and NH_3 gas annealing at 680 ℃. The substrate temperature was measured using a thermocouple and infrared pyrometer. The remote plasma was generated by a radio frequency (rf) source (100 W, 13.56 MHz) at ~ 25cm above the sample with a constant gas flow of 90 standard cubic centimeters per minute (sccm). The chamber pressure was maintained at 60 mtorr controlled by a throttle valve in front of the turbo pump. For Ga- and N-face GaN, the wet chemical clean included sonicating in separate acetone, methanol, and NH_4OH baths for 10 min each, followed by a 10 s rinse in DI water and blow dry with UHP N_2 gas. The *in-situ* cleaning process was 15min NH_3 plasma and 15min NH_3 gas annealing at 680 ℃.

6.3.2 PEALD dielectrics growth and post deposition treatment

After surface pretreatment, ~1.5 and 3.0 nm dielectric films (Al_2O_3, HfO_2, and SiO_2) were deposited on both Ga- and N-face GaN by PEALD method. The PEALD system has been discussed in detail elsewhere [50]. The precursors used for Al_2O_3, HfO_2, and SiO_2 growth were dimethylaluminum isoproxide (DMAI, $[(CH_3)_2AlOCH(CH_3)_2]_2$), tetrakis(ethylmethylamido) hafnium (TEMAHf, $Hf(NCH_3C_2H_5)_4$), and tris(dimethylamino) silane (TDMAS, $[(CH_3)_2N]_3SiH$), respectively. The DMAI, TEMAHf, and TDMAS bubblers were maintained at 90, 48, and 33 ℃, respectively, to

provide sufficient vapor pressure for PEALD deposition. The delivery line temperatures were maintained at ~20 ℃ higher than that of the specific bubbler to prevent precursor condensation inside the pipe. The growth rate for PEALD Al_2O_3, HfO_2, and SiO_2 films was ~ 1.5 Å/cycle, ~1.4 Å/cycle and ~0.5 Å/cycle when the substrate temperature was at ~180 ℃ [50], ~220 ℃, and ~200 ℃, respectively. After the dielectric growth, the samples were annealed in N_2, NH_3 or mixed H_2/N_2 (10% H_2) ambient at 600 ℃ for 30min. After annealing, the samples were treated with 5 min room temperature (RT) 100 w O_2 plasma to investigate the effect of O_2 plasma during the PEALD deposition.

6.3.3 X-ray and ultraviolent photoemission spectroscopy characterization

The *in-situ* XPS and UPS systems and measurement approaches were described previously [17,62]. XPS was used after each cleaning process to investigate the effect of different processes on the GaN chemical states. After dielectric growth, both XPS and UPS were used to characterize the interface electronic structure to determine the GaN surface band bending and band offsets.

The method of calculating the valence band offset (VBO) was developed by Waldrop, Grant and Kraut *et al*. [63,64], which is described in the following equation

$$\Delta E_V = (E_{CL} - E_V)_{GaN} - (E_{CL} - E_V)_{dielectric} + \Delta E_{CL} \quad (6.1)$$

where ΔE_V represents VBO; E_{CL} is the binding energy of the XPS core level; E_V is the valence band maximum (VBM); $(E_{CL}\text{-}E_V)_{GaN}$ or $(E_{CL}\text{-}E_V)_{dielectric}$ is the binding energy difference from VBM to core level in GaN or dielectric; and ΔE_{CL} is the binding energy difference between the core levels in GaN and dielectric (e.g., $\Delta E_{Al2p\text{-}Ga3d}$ for Al_2O_3/GaN, $\Delta E_{Hf4f7/2\text{-}Ga3d}$ for HfO_2/GaN, and $\Delta E_{Si2s\text{-}Ga3d}$ for SiO_2/GaN). The value of $(E_{CL}\text{-}E_V)$ is essentially independent of band bending. Once this value was measured, the change of ΔE_V and GaN surface band bending could be determined from the change of ΔE_{CL} and the Ga 3d core level, respectively.

6.4 Results

Using the method described above, the surface band bending and/or band alignment for the following samples were determined: cleaned Ga- and N-face GaN, cleaned GaN/Si, Al_2O_3/Ga-face GaN, Al_2O_3/N-face GaN, HfO_2/Ga-face GaN, HfO_2/N-face GaN, SiO_2/Ga-face GaN, and SiO_2/N-face GaN.

6.4.1 GaN surface pretreatment and surface band bending of Ga- and N-face GaN

A. GaN/Si

Fig. 6.1 shows the XPS C 1s and O 1s peaks of the GaN/Si surface after different cleaning processes. The *ex-situ* cleaning process included different combinations of solvent (acetone and methanol), HCl, and NH_4OH. Solvent cleans could remove part of the carbon contamination. After NH_4OH treatment, the O 1s peak intensity decreased slightly, which may be the result of dissolving Ga_2O_3 in NH_4OH [65]. Compared with

NH_4OH, HCl was more effective at removing the surface oxide from GaN [2,66], while it was less effective at removing carbon contamination. In addition, -Cl group could be residual on the surface, which may produce undesired electrically active defects at the interface or in the dielectric [66,67]. However, significant carbon peaks remained after *ex-situ* wet chemical cleaning [2]. It should be mentioned that additional carbon and oxygen may adsorb on the surface during sample preparation and loading into the UHV transfer line.

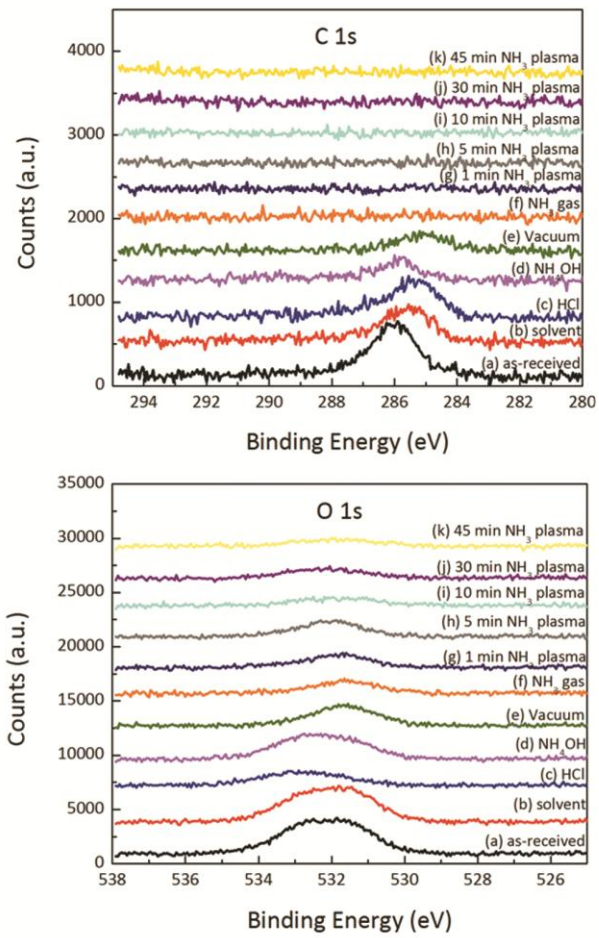

Figure 6.1. XPS C 1s and O 1s peak of Ga-face GaN on silicon substrate for (a) as received; (b) acetone and methanol cleaning; (c) acetone, methanol, and HCl cleaning; (d) acetone, methanol, and NH_4OH cleaning; (e) 45min vacuum annealing at 680 ℃; (f) 15min NH_3 gas annealing at 680 ℃; (g) 1 min NH_3 plasma and 15min NH_3 gas annealing at 680 ℃; (h) 5 min NH_3 plasma and 15min NH_3 gas annealing at 680 ℃; (i) 10 min NH_3 plasma and 15min NH_3 gas annealing at 680 ℃; (j) 30 min NH_3 plasma and 15min NH_3 gas annealing at 680 ℃; and (k) 45 min NH_3 plasma and 15min NH_3 gas annealing at 680 ℃. For all the *in-situ* high temperature processes, the combined *ex-situ* cleaning method is step (d).

All of the *in-situ* processes were based on the NH_4OH wet chemical treatment. The vacuum annealing led to a decrease of oxygen coverage, while the carbon contamination remained the same. The use of NH_3 gas and/or plasma in the elevated temperature process led to a significant reduction in both oxygen and carbon. The carbon contamination was below the XPS detection limit, and the oxygen concentration was almost the same after NH_3 plasma treatment.

B. Ga-face and N-face GaN

Fig. 6.2 shows the AFM images of as-received, chemical mechanical polished (CMP), Ga- and N-face bulk GaN. Topographical measurements showed the root mean square (rms) height for Ga- and N-face GaN was 0.42 ± 0.05 and 0.62 ± 0.05 nm respectively. Fig. 6.3 shows the XPS O 1s and C 1s peaks of Ga- and N-face GaN after the different cleaning processes. The as-received Ga- and N-face GaN showed similar carbon and oxygen coverage on the surface. After NH_4OH treatment, the oxygen peak intensity decreased for both Ga- and N-face GaN. However, there was no obvious decrease in carbon peak intensity, which was different from the effect of the NH_4OH treatment on GaN/Si. After *in-situ* 680 ℃ NH_3 plasma treatment, there was a significant decrease in the carbon and oxygen peak intensities on both surfaces. In particular, the carbon peak intensity was below the XPS detection limit. And the intensity of the XPS O 1s peak on both Ga- and N-face GaN was also similar to that on GaN/Si after the NH_3 plasma cleaning process.

The XPS Ga 3d, N 1s, O 1s, and C 1s core levels of Ga- and N-face GaN were summarized in Table 6.1. For the as-received samples, the C 1s main peak was centered at 285.7 ±0.1 eV (FWHM=1.8 ±0.1 eV) for both Ga- and N-face GaN, and there was also a shoulder peak at the higher binding energy side. For the O 1s peak, only a broad peak centered at 532.6-531.7 eV to 532.8-532.2 eV for Ga- and N-face GaN during the cleaning process was detected.

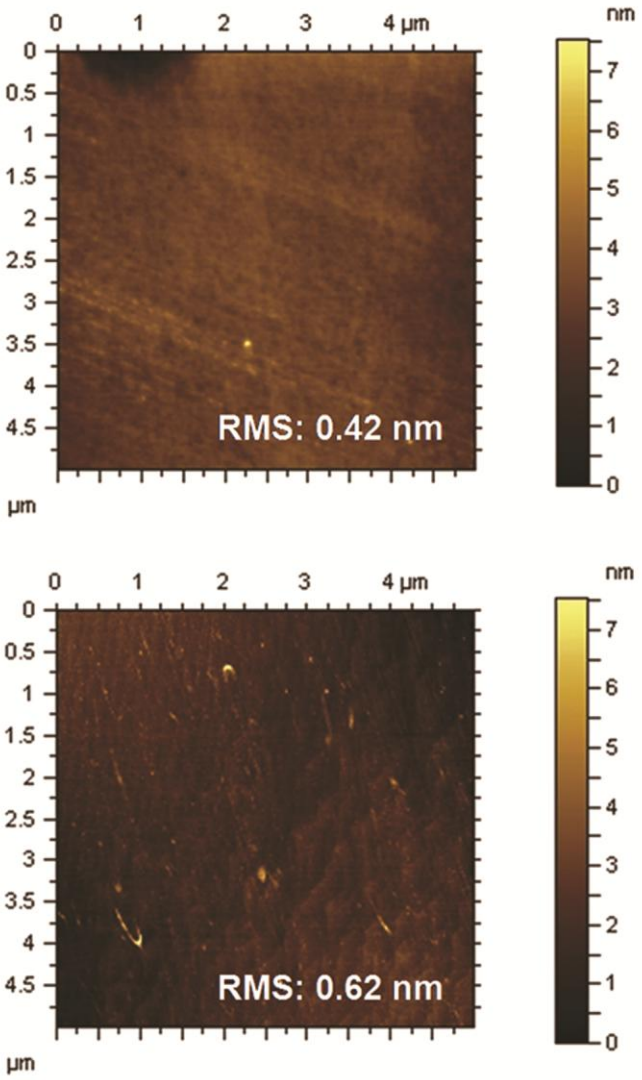

Figure 6.2. AFM images of as-received chemical mechanical polished Ga-face (top) and N-face (bottom) bulk GaN.

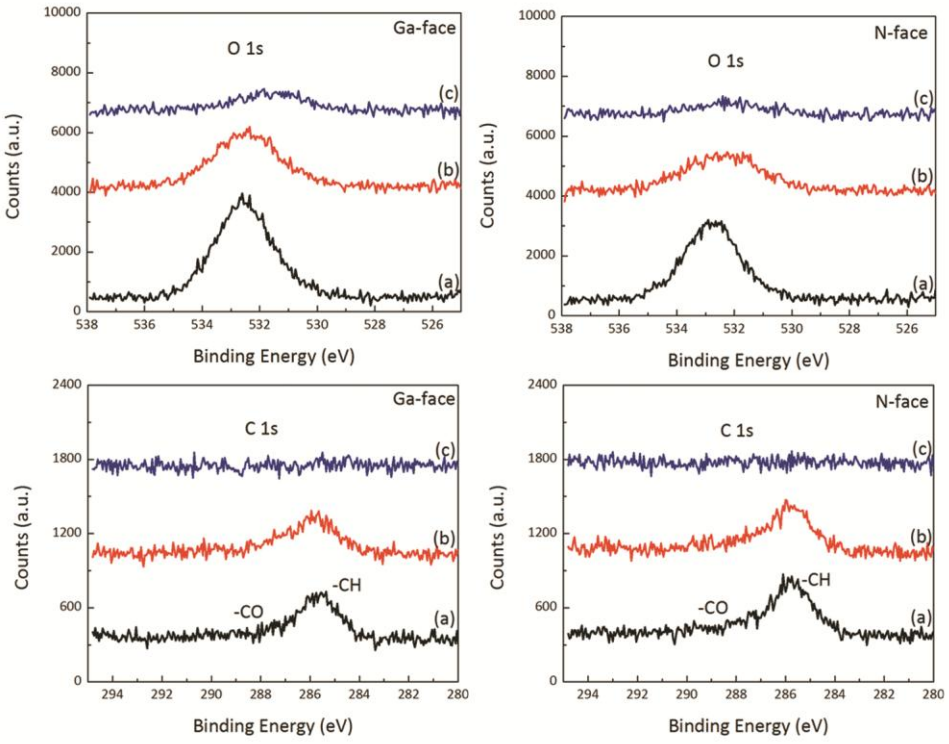

Figure 6.3. XPS results of O 1s and C 1s peak of (a) as received; (b) *ex-situ* wet chemical treated; and (c) *in-situ* NH_3 plasma treated Ga-face and N-face GaN.

Table 6.1. XPS results for as-received, wet-chemical cleaned, and NH_3 plasma cleaned Ga- and N-face bulk GaN.

	Ga-face GaN						**N-face GaN**					
	As received (±0.1 eV)		**Wet chemical (±0.1 eV)**		**NH_3 plasma (±0.1 eV)**		**As received (±0.1 eV)**		**Wet chemical (±0.1 eV)**		**NH_3 plasma (±0.1 eV)**	
	Center	**FWHM**	**Center**	**FWHM**	**Center**	**FWHM**	**Center**	**FWHM**	**Center**	**FWHM**	**Center**	**FWHM**
Ga 3d	**20.9**	**1.1**	**20.7**	**1.2**	**20.2**	**1.2**	**21.2**	**1.2**	**21.0**	**1.2**	**20.5**	**1.3**
N 1s	**398.2**	**1.1**	**398.0**	**1.1**	**397.5**	**1.2**	**398.6**	**1.1**	**398.3**	**1.0**	**397.8**	**1.0**
O 1s	**532.6**	**2.4**	**532.5**	**2.8**	**531.7**	**3.2**	**532.8**	**2.3**	**532.3**	**3.1**	**532.2**	**3.6**
C 1s	**285.6**	**1.9**	**285.8**	**2.0**	**-**	**-**	**285.7**	**1.8**	**285.7**	**1.8**	**-**	**-**

Fig. 6.4 shows the XPS Ga 3d and UPS results of Ga- and N-face GaN after NH_3 plasma cleaning. The VBM was determined from an extrapolation of a linear fit to the UPS low binding energy cutoff. The photo threshold energy of GaN was determined from the energy difference between the photon energy (He I=21.2 eV) and the UPS spectral width (or equivalently, the sum of electron affinity and the band gap of GaN). Therefore, the photo threshold energy of Ga- and N-face GaN after cleaning was 7.0 ± 0.1 and 6.9 ± 0.1 eV, respectively. Using 3.4 eV as the band gap of GaN, the electron affinity of Ga- and N-face GaN were determined to be 3.6 ± 0.1 and 3.5 ± 0.1 eV, respectively, which agreed with other group's result for Ga-face GaN (3.5 ± 0.1 eV) [68]. The binding energy difference between Ga 3d core level and VBM for both Ga- and N-face GaN was 17.8 eV, respectively, which was consistent with reported results [63,69,70]. This value was used for all of the following experiments to determine the surface band bending of GaN and the band offset of dielectric/GaN. For the as-received samples, the Ga 3d core level of Ga- and N-face GaN was centered at 20.9 and 21.2 eV respectively, which indicated 0.2 eV upward band bending and -0.1 eV downwards band bending, respectively. After cleaning, the Ga 3d core level shifted to lower binding energy for both faces, indicating an increase in the upward band bending. For Ga-face GaN, the respective upward bending values after NH_4OH clean and NH_3 plasma treatment were 0.4 and 0.9 eV, and for N-face GaN, they were 0.1 and 0.6 eV, respectively. These values are consistent with other group's results [14,15,16,17,18,19,20]. Fig. 6.5 shows a schematic of the surface band bending of Ga- and N-face GaN after *in-situ* NH_3 plasma treatment, where the Ga- and N-face GaN showed upward bending of 0.8 ± 0.1 eV and 0.6 ± 0.1 eV, respectively.

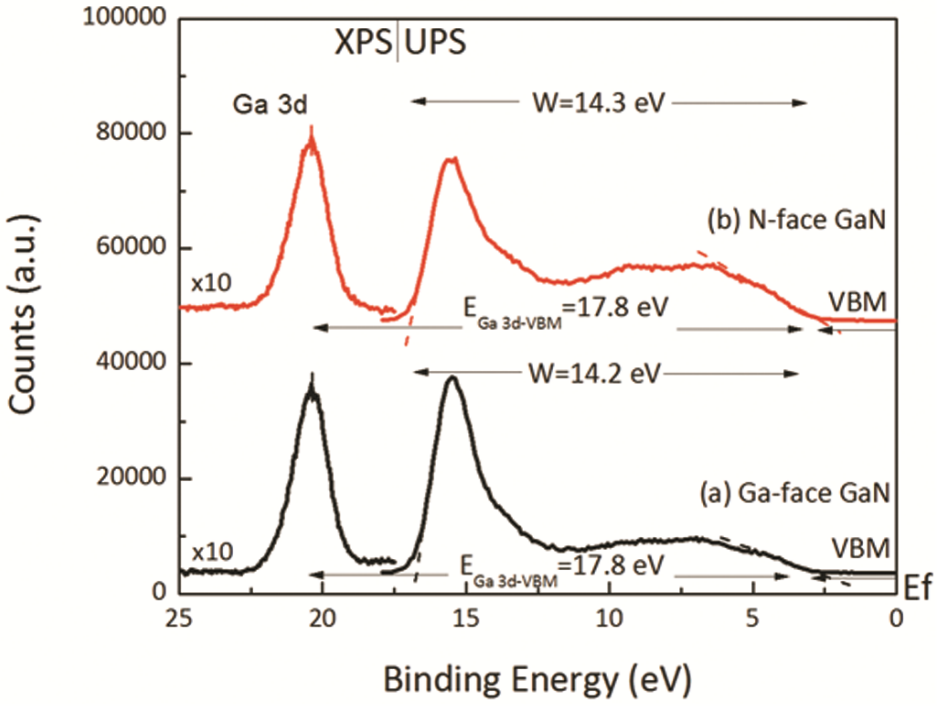

Figure 6.4. XPS Ga 3d and UPS results of (a) Ga-face and (b) N-face GaN after NH_3 plasma cleaning.

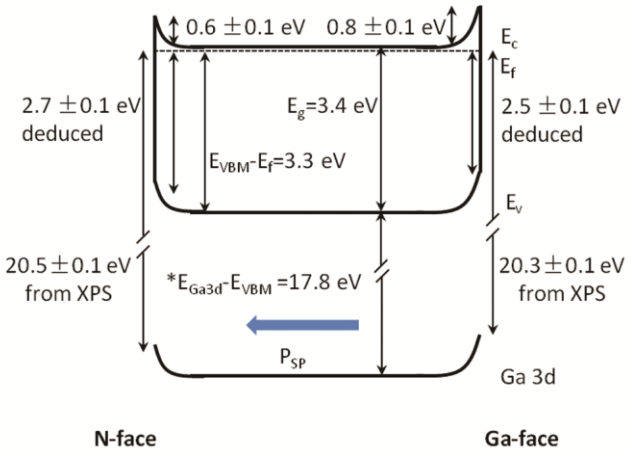

Figure 6.5. Surface band bending diagram of Ga- and N-face GaN after NH_3 plasma cleaning.

On the other hand, the upward band bending for as-received, HCl cleaned, and NH_4OH cleaned GaN/Si were 0.3, 0.2, and 0.4 eV respectively. The NH_4OH cleaned GaN exhibited similar surface band bending (~0.4 eV) as reported by Bermudez [71]. After NH_4OH cleaning, and following vacuum annealing the surface exhibited an upward band bending of 0.3 eV.

6.4.2 Surface band bending and band alignment of Al_2O_3/Ga- and N-face GaN

After surface pretreatment, ~1.5 nm Al_2O_3 films were deposited on both Ga- and N-face GaN by PEALD. FIG 6.6 shows the Al 2p and Ga 3d XPS core levels, and the UPS valence band spectra of Al_2O_3 on Ga- and N-face GaN (i and ii respectively) after different experimental processes. The binding energies of XPS core levels and VBM results are summarized in Table 6.2. The data was used to determine the surface band bending and VBOs.

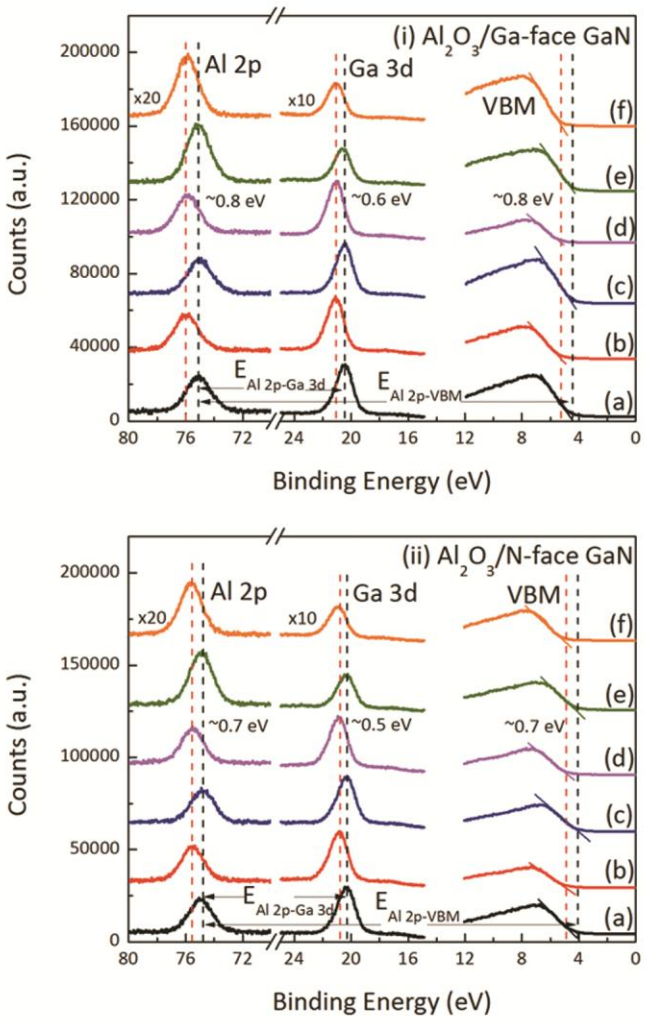

Figure 6.6. XPS Ga 3d and Al 2p core levels, and UPS low binding energy cut off spectra of Al_2O_3 on (i) Ga- and (ii) N-face GaN for (a) ~1.5nm as-grown Al_2O_3; (b) 30min 600 ℃ PDA in N_2 atmosphere; (c) 5min RT O_2 plasma; (d) 30min 600 ℃ PDA in N_2 atmosphere; (e) ~3.0nm as-grown Al_2O_3; (f) final 30min 600 ℃ PDA in N_2 atmosphere. The initial and final positions of the core level peaks and VBM after Al_2O_3 growth are indicated with dashed lines. The intensity of Al 2p and Ga 3d core levels are enlarged by 20 and 10 times respectively.

Table 6.2. XPS Ga 3d and Al 2p core levels, UPS VBM (relative to E_F), $(E_{Al2p}-E_V)_{Al2O3}$, and VBO results for Al_2O_3 on Ga- and N-face GaN. All energies are given in eV.

Process	Ga 3d		A1 2p		VBM		$(E_{Al2p}-E_V)_{Al2O3}$		VBO	
	Ga-face	N-face	Ga-face	N-face	Ga-face	N-face	Ga-face	N-face	Ga-face	N-face
as received	20.9	21.1	-	-	-	-	-	-	-	-
after clean	20.5	20.5	-	-	-	-	-	-	-	-
(a) 1.5 nm Al_2O_3	20.4	20.3	75.1	75.0	4.6	4.4	70.5	70.6	2.0	1.9
(b) N2 PDA	21.0	20.8	75.9	75.5	5.3	4.8	70.6	70.7	2.1	1.8
(c) O_2 plasma	20.4	20.3	75.0	74.8	4.5	4.1	70.5	70.7	1.9	1.6
(d) N2 PDA	21.0	20.8	75.9	75.5	5.3	4.8	70.6	70.7	2.1	1.8
(e) 3.0 nm Al_2O_3	20.5	20.3	75.1	74.9	4.5	4.2	70.6	70.7	1.8	1.7
(f) N_2 PDA	21.0	20.9	75.9	75.6	5.3	5.0	70.6	70.6	2.1	1.9

For Ga-face GaN, after 1.5 nm Al_2O_3 films deposition, the Ga 3d core level was at 20.4 eV, which indicated the VBM and surface band bending of GaN were 2.6 eV and 0.7 eV respectively. The VBM and Al 2p core level for Al_2O_3 was 4.6 eV and 75.1 eV, respectively, which indicates values of $(E_{Al2p}-E_V)_{Al2O3}$ and $\Delta E_{Al2p-Ga3d}$ of 70.5 and 54.7 eV. According to Eq. 6.1, the VBO between as-grown Al_2O_3 and Ga-face GaN was calculated to be 2.0 eV. After PDA in N_2, the Ga 3d core level shifted to higher binding energy by ~0.6 eV, and the N 1s peak (which was not shown here) also shifted to higher binding energy by ~0.7 eV. This shift was attributed to a change of the surface band bending, which changed from 0.7 to 0.1 eV after N_2 PDA. In the mean time, the Al 2p core level and VBM of Al_2O_3 films also shifted to higher binding energy by ~0.8 and 0.7 eV, respectively. The values of $(E_{Al2p}-E_V)_{Al2O3}$ and $\Delta E_{Al2p-Ga3d}$ were then changed to 70.6 eV

and 54.9 eV, respectively, which indicated the VBO changed to 2.1 eV. After 5 min RT O_2 plasma and second PDA, the values of surface band bending, $(E_{Al2p}-E_V)_{Al2O3}$, and VBO were 0.7 and 0.1 eV, 70.5 and 70.6 eV, and 1.9 and 2.1 eV, respectively, which were consistent with the values for the 1.5 nm Al_2O_3 and initial N_2 PDA. After an additional ~1.5 nm Al_2O_3 deposition, the ~3.0 nm Al_2O_3/Ga-face GaN had similar VBM, Al 2p core level, and Ga 3d core level energies with that of the 1.5 nm Al_2O_3 and oxygen plasma treated Al_2O_3/Ga-face GaN. After the final N_2 PDA, the values were consistent with those of the first and second N_2 PDA heterostructure. Throughout the whole experimental process, the surface band bending of Ga-face GaN was ~0.7 eV after plasma treatment and ~0.1 eV after N_2 PDA, indicating a ~0.6 eV shift in the surface band bending. The shift of the Al 2p core level and VBM in Al_2O_3 were both ~0.8 eV, which indicated the value of $(E_{Al2p}-E_V)_{Al2O3}$ was constant between 70.5 eV and 70.6 eV and independent of band bending. In addition, the VBO was almost constant, which was 1.9 and 2.1 eV for oxygen plasma treated and N_2 annealed Al_2O_3 on Ga-face GaN respectively, independent of the Al_2O_3 thickness.

The band gaps of Al_2O_3 and GaN (=3.4 eV) are necessary to calculate the conduction band offset (CBO). A previous study reported the band gap of PEALD Al_2O_3 as 6.7±0.1 eV, which was determined from XPS O 1s energy loss spectroscopy [50]. The result was consistent with other group's results [72,73]. Using 6.7 eV as the band gap of the Al_2O_3 films, the respective CBO was calculated to be 1.4 and 1.2 eV for oxygen plasma treated and N_2 annealed Al_2O_3/Ga-face GaN.

On the other hand, similar results were obtained for Al_2O_3/N-face GaN. The surface band bending of N-face GaN was ~0.8 and 0.3 eV upwards for the O_2 plasma

treated and N_2 annealed sample respectively. In addition, both the Al 2p core level and the VBM of Al_2O_3 shifted ~0.7 eV during the experimental processes, leading to a constant value of $(E_{Al2p}\text{-}E_V)_{Al2O3}$ (= ~70.6 eV). The VBO and CBO was ~1.7 and 1.6 eV for the oxygen plasma processed sample, and ~1.8 and 1.5 eV for the annealed sample, respectively. The deduced band alignment diagrams of Al_2O_3 films on Ga- and N-face GaN was summarized in Fig. 6.7.

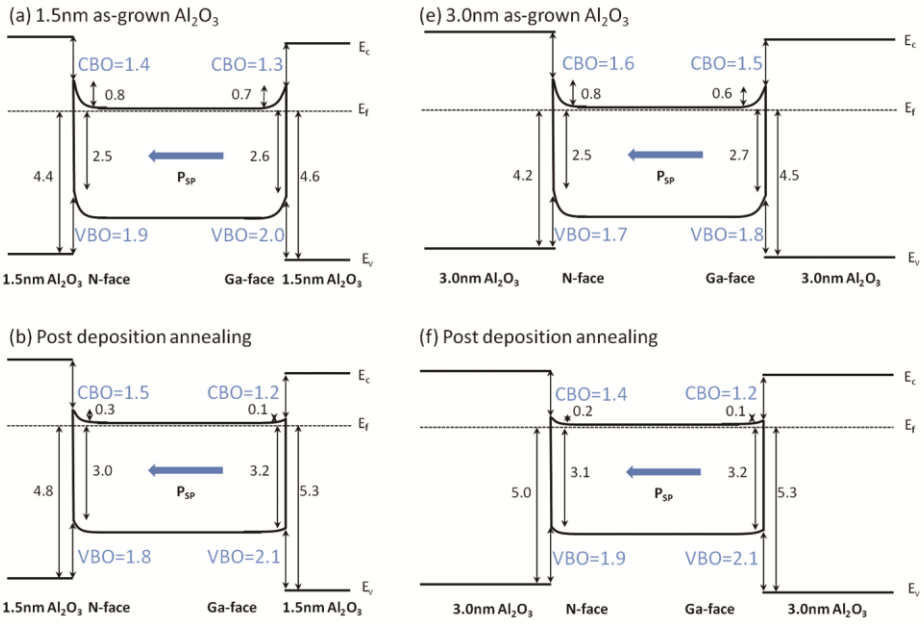

Figure 6.7. The deduced band alignment of (a) ~1.5nm as-grown Al_2O_3; (b) ~1.5nm annealed Al_2O_3; (e) ~3.0nm as-grown Al_2O_3; and (f) ~3.0nm annealed Al_2O_3, on Ga- and N-face GaN.

In addition to N_2, NH_3 is another promising annealing atmosphere. In this research, the effect of NH_3 as PDA ambient on surface band bending and band offsets of

Al_2O_3/Ga- and N-face GaN was also evaluated. The surface band bending for as-deposited ~1.5 and 3.0 nm Al_2O_3/Ga- and N-face GaN were ~0.8 and 0.7 eV respectively, which decreased to ~0.3 and 0.2 eV after 30 min PDA in NH_3 at 600 ℃. In addition to similar surface band bending after NH_3 PDA compared with N_2 PDA, the value of $(E_{Al2p}-E_V)_{Al2O3}$ and the band offset results were also similar. Specifically, the value of $(E_{Al2p}-E_V)_{Al2O3}$ was still 70.6 eV after NH_3 PDA; and the VBOs were ~1.9 and ~ 1.7 for O_2 plasma treated Al_2O_3/Ga- and N-face GaN, and ~2.1 and 1.9 eV for NH_3 annealed Al_2O_3/Ga- and N-face GaN, respectively. Furthermore, mixed H_2/N_2 gas annealing (10% H_2) was also used for Al_2O_3/Ga- and N-face GaN, which led to similar surface band bending and band offsets as the other two annealing ambients.

The photo threshold energies for as-grown and annealed Al_2O_3/Ga- and N-face GaN were 8.4±0.1 and 8.6±0.2 eV, respectively. This indicated the electron affinity of as-grown and annealed Al_2O_3 films were 1.7±0.1 and 1.9±0.2 eV respectively, which was consistent with our previous study (1.8 eV) [17] and other group's result (1.7 eV) [74].

To summarize, for PEALD Al_2O_3 films on GaN, the value of $(E_{Al2p}-E_V)_{Al2O3}$ was constant at 70.6±0.1 eV, which was consistent with our previous study (70.4-70.5 eV) [17] and other group's report (70.6 eV) [75]. The electron affinity of O_2 plasma processed and annealed Al_2O_3 films was 1.7±0.1 and 1.9±0.2 eV, respectively. The surface band bending for Ga- and N-face GaN after O_2 plasma processing was ~0.7±0.1 eV, which decreased to ~0.2±0.1 eV after PDA (N_2, N_2/H_2, and NH_3). The VBOs were similar on Ga- and N-face GaN, independent of the different processing and dielectric thickness, which were 2.0±0.1 eV for Al_2O_3/Ga-face GaN and 1.8±0.1 eV for Al_2O_3/N-face GaN. The subsequent CBOs were calculated to be 1.3±0.1 and 1.5±0.1 eV for Al_2O_3/Ga- and

N-face GaN, respectively. These values were consistent with our previous results for Al_2O_3 on Ga-face GaN films (=1.8±0.1 eV) [17].

6.4.3 Surface band bending and band alignment of HfO_2/Ga- and N-face GaN

Similar to Al_2O_3/GaN, ~1.5 nm HfO_2 films were deposited on Ga- and N-face GaN. Since the Hf 4f peaks overlap with the Ga 3d peak, and the binding energy difference between Ga 3d and N 1 s core level is constant, the N 1s core level was used to locate the Ga 3d peak position. Fig. 6.8 shows the XPS Hf 4f, Ga 3d, and N 1s core levels of PEALD HfO_2 on both Ga- and N-face GaN. After ~1.5 nm HfO_2 deposition, the Ga- and N-face GaN exhibited the same Ga 3d core level binding energy of 20.2 eV, which indicated the same upward band bending of 0.9 eV. The Hf $4f_{7/2}$ peak of HfO_2 was centered at 17.4 eV on both samples, which indicated the value of $\Delta E_{Hf4f7/2\text{-}Ga3d}$ was -2.8 eV. The value of $(E_{Hf4f7/2}\text{-}E_V)_{HfO2}$ was calculated from the binding energy difference between the XPS Hf $4f_{7/2}$ core level and the UPS VBM of HfO_2, which is shown in Fig. 6.9. The value was 13.7 eV for both as-grown and annealed HfO_2 films, which was consistent with our previous study (13.6-13.7 eV) [17] and other group's research (13.9 eV) [76]. The same value of $(E_{Hf4f7/2}\text{-}E_V)_{HfO2}$ was obtained for Ga-face GaN, which was not shown here. Therefore, the value of $(E_{Hf4f7/2}\text{-}E_V)_{HfO2}$ was set to be 13.7 eV for the band offset calculation. By using Eq. 6.1 and 5.8 eV as the band gap of HfO_2, the VBO and CBO was 1.3 and 1.1 eV, respectively, on Ga- and N-face GaN. After 30 min, 600 ℃ N_2 PDA, for HfO_2 on Ga- and N-face GaN, the Ga 3d core level shifted to higher binding energy by ~0.3 and 0.5eV, and the Hf $4f_{7/2}$ core level shifted to higher binding energy by

~ 0.5 and 0.7 eV, respectively. The subsequent VBO and CBO changed to 1.5 and 0.9 eV, respectively, on both Ga- and N-face GaN.

After O_2 plasma treatment and an additional 1.5 nm HfO_2 deposition, the Ga 3d and Hf $4f_{7/2}$ peaks were centered at 20.1 and 17.3 eV for both surfaces, respectively. It suggested the value of $\Delta E_{Hf4f7/2\text{-}Ga3d}$ changed back to -2.8 eV, and the subsequent VBO was calculated to be 1.3 eV for both Ga- and N-face GaN. For the second N_2 PDA, the Ga 3d and Hf $4f_{7/2}$ core levels were at 20.4 and 17.8 eV for Ga-face, and 20.6 and 17.9 eV for N-face, respectively. For the final N_2 PDA, the Ga 3d and Hf $4f_{7/2}$ core levels were at 20.5 and 17.9 eV for Ga-face, and 20.6 and 17.9 eV for N-face, respectively. These results indicated the value of $\Delta E_{Hf4f7/2\text{-}Ga3d}$ was -2.6 eV and -2.7 eV, and the VBO was 1.5 and 1.4 eV for annealed HfO_2/Ga- and N-face GaN, respectively. The related Ga 3d, N 1s, and Hf $4f_{7/2}$ core levels, and the VBO results were summarized in Table 6.3. The photo threshold energy for both as-deposited and annealed HfO_2 on GaN was 8.2 ± 0.1 eV, and the electron affinity was calculated to be 2.4 ± 0.1 eV, which was consistent with our previous result (2.2 eV) [17] and also close to the value of 2.5 eV reported by Bersch *et al.* [75].

The band alignment diagrams of HfO_2 on Ga- and N-face GaN are shown in Fig 6.10. The VBO and CBO of HfO_2 on GaN are 1.4 ± 0.1 eV and 1.0 ± 0.1 eV independent of GaN polarities, HfO_2 thickness and experimental process. The upward surface band bending was 0.9 ± 0.1 and 0.5 ± 0.1 eV for O_2 plasma processed and annealed HfO_2/Ga- and N-face GaN. For PEALD HfO_2 thin films, the energy difference between the Hf $4f_{7/2}$ peak and the VBM was 13.7 ± 0.1 eV, and the electron affinity was determined to be 2.4 ± 0.1 eV.

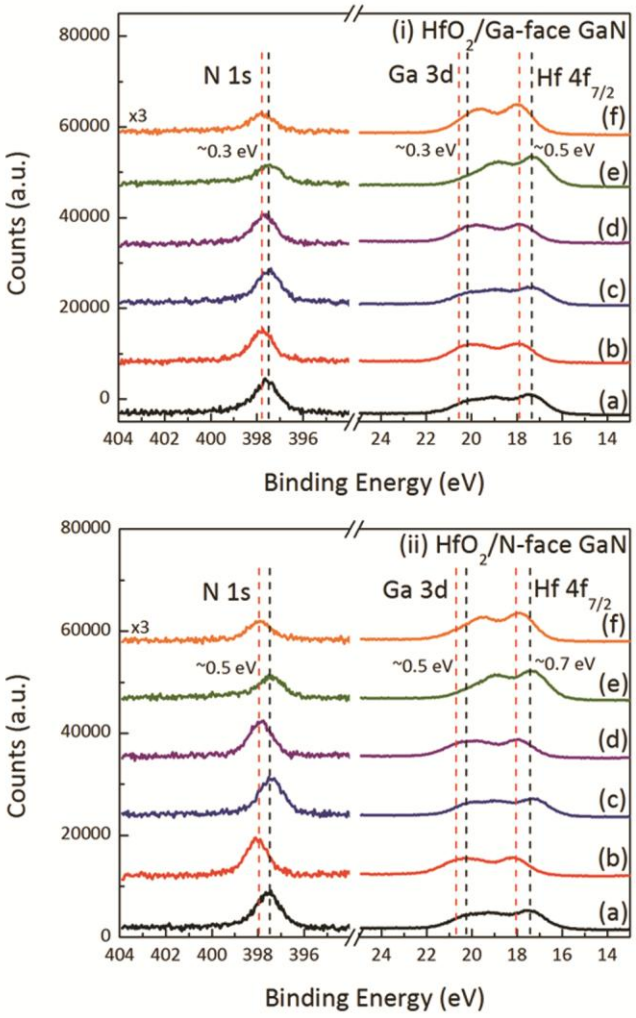

Figure 6.8. XPS Hf 4f, Ga 3d, and N 1s core levels of PEALD HfO_2 on both (i) Ga- and (ii) N-face GaN for (a) ~1.5nm as-grown HfO_2; (b) 30min 600 ℃ PDA in N_2 atmosphere; (c) 5min RT O_2 plasma; (d) 30min 600 ℃ PDA in N_2 atmosphere; (e) ~3.0nm as-grown HfO_2; and (f) final 30min 600 ℃ PDA in N_2 atmosphere. The initial and final positions of the core level peaks after HfO_2 growth are indicated with dashed lines. The intensity of N 1s core level is enlarged by 3 times.

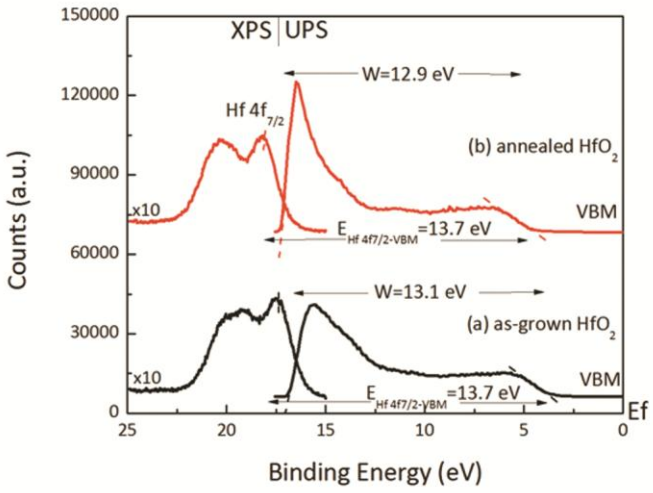

Figure 6.9. XPS Hf 4f and UPS results of (a) as-grown and (b) annealed PEALD HfO_2 on N-face GaN. The XPS signal intensity is enlarged by 10 times.

Table 6.3. XPS Ga 3d, N 1s, and Hf $4f_{7/2}$ core levels, and VBO results for HfO_2 on Ga- and N-face GaN. All energies are given in eV.

Process	Ga 3d		N 1s		Hf $4f_{7/2}$		VBO	
	Ga-face	N-face	Ga-face	N-face	Ga-face	N-face	Ga-face	N-face
after clean	20.3	20.5	397.5	397.8	-	-	-	-
(a) 1.5 nm HfO_2	20.2	20.2	397.5	397.5	17.4	17.4	1.3	1.3
(b) N_2 PDA	20.5	20.7	397.8	398.0	17.9	18.1	1.5	1.5
(c) O2 plasma	20.1	20.1	397.4	397.4	17.3	17.3	1.3	1.3
(d) N_2 PDA	20.4	20.6	397.7	397.9	17.8	17.9	1.5	1.4
(e) 3.0 nm HfO_2	20.1	20.1	397.4	397.4	17.3	17.3	1.3	1.3
(f) N_2 PDA	20.5	20.6	397.8	397.9	17.9	17.9	1.5	1.4

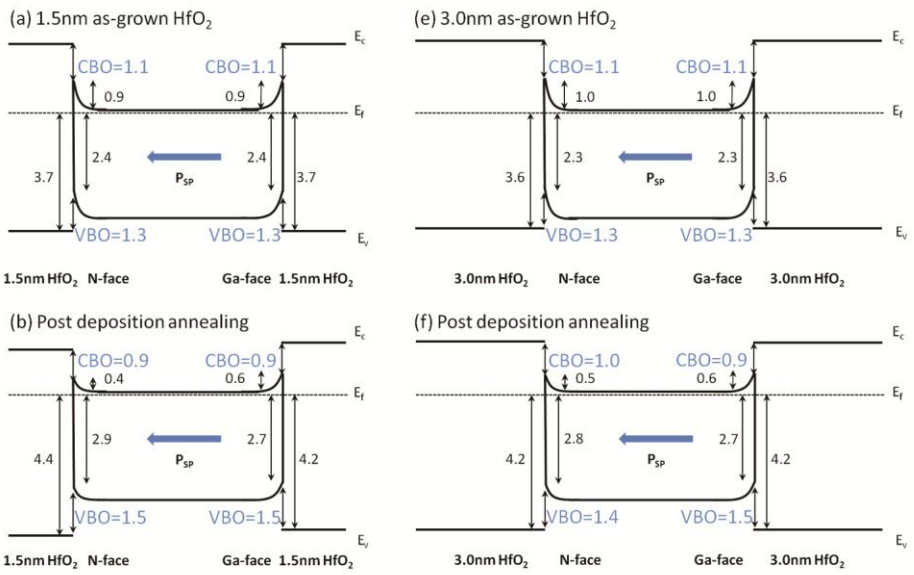

Figure 6.10. The deduced band alignment of (a) ~1.5nm as-grown HfO_2; (b) ~1.5nm annealed HfO_2; (e) ~3.0nm as-grown HfO_2; and (f) ~3.0nm annealed HfO_2 on Ga- and N-face GaN.

6.4.4 Surface band bending and band alignment of SiO_2/Ga-face and N-face GaN

To characterize PEALD SiO_2 on GaN, ~1.5 and 3.0 nm SiO_2 films were deposited on both Ga- and N-face GaN with the same experimental sequence used for Al_2O_3 and HfO_2. Since the Si 2p peak overlaps with Ga 3p peaks, the Si 2s core level was measured to indicate the band offset. To obtain both Ga 3s (~160 eV) and Si 2s peaks (~155 eV), the Al source was used to avoid Ga Auger features which occurs when using the Mg anode.

Fig. 6.11 shows the XPS Si 2s and UPS results of as-grown and annealed SiO_2 on N-face GaN. The two peaks centered at ~8 and 13 eV were characteristic of the O (2p)

and Si-O related features, respectively [77]. From the UPS measurement, the electron affinity of SiO_2 on GaN could be determined to be 1.1 ±0.1 eV. The value of $(E_{Si2s}\text{-}E_V)_{SiO2}$ was calculated to be 148.9 eV, which was consistent with previous result. The same value was obtained from SiO_2/Ga-face GaN, which was not shown here. Therefore, the value of $(E_{Si2s}\text{-}E_V)_{SiO2}$ was set to be 148.9 eV for the following calculations.

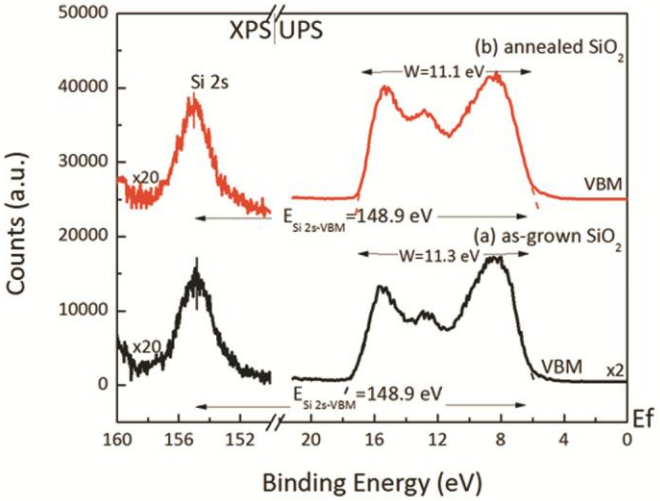

Figure 6.11. XPS Si 2s and UPS results of (a) as-grown and (b) annealed PEALD SiO_2 on N-face GaN. The XPS signal intensity and was enlarged by 20 times, and the UPS signal intensity for as-grown SiO_2 is enlarged by 2 times.

Fig. 6.12 shows the XPS Ga 3s, Si 2s, and Ga 3d core levels of SiO_2 on both Ga- and N-face GaN. After ~1.5 nm SiO_2 deposition, the Ga 3d of Ga- and N-face GaN was centered at 20.6 and 20.4 eV, respectively, which indicated a 0.5 and 0.7 eV upward band bending. The Si 2s peak of SiO_2 was located at 154.7 and 154.5 eV, which indicated a VBM of 5.8 and 5.6 eV, respectively. Therefore, the value of $\Delta E_{Si2s\text{-}Ga3d}$ was 134.1 eV for

both SiO_2/Ga- and N-face GaN. Using Eq. 6.1 and 8.9 eV as the band gap of SiO_2, the respective VBO and CBO of SiO_2 on both Ga- and N-face GaN were 3.0 and 2.5 eV. During post deposition processing, the Ga 3d and Si 2s peaks from SiO_2/N-face GaN shifted to higher binding energy ~0.4 eV together, while the Ga 3d and Si 2s peaks from SiO_2/Ga-face GaN shifted only ~0.1 eV. After an additional ~1.5 nm SiO_2 deposition, the Ga 3d of Ga- and N-face GaN were 20.6 and 20.7 eV, which indicated a 0.5 and 0.4 eV upward band bending, respectively. The Si 2s core level from SiO_2 on Ga- and N-face GaN were 154.9 and 155.0 eV, respectively, which indicated the VBO of SiO_2/Ga- and N-face GaN was 3.2 eV. After N_2 annealing, the Ga 3d and Si 2s core levels in both samples were essentially unchanged. After additional 30 min mixed H_2/N_2 (10% H_2) annealing, the Si 2s and Ga 3d core levels from Ga- and N-face GaN shifted to higher binding energy by ~0.4 eV. The Ga 3d core level changed to 21.0 eV on both Ga- and N-face GaN, indicating 0.1 eV upward band bending. The Ga 3d, Ga 3s and Si 2s binding energy values and VBO results are summarized in Table 6.4. The effect of different annealing ambient on the electronic structure of SiO_2/GaN/Si was also investigated. After SiO_2 deposition, the N_2 PDA and O_2 plasma step did not shift the core levels. However, the mixed H_2/N_2 (10% H_2) or NH_3 PDA resulted in a shift of the Si 2s and Ga 3d to higher binding energy by ~ 0.4 eV.

The band alignment diagram of SiO_2 on Ga- and N-face GaN is shown in Fig. 6.13. The VBO and CBO of SiO_2 on Ga- and N-face GaN were 3.1 ± 0.1 and 2.4 ± 0.1 eV, respectively, throughout the experimental processes. For PEALD SiO_2 films, the binding energy difference between Si 2s and VBM in SiO_2 was 148.9 eV and the electron affinity

of SiO_2 was 1.1±0.1 eV, which was consistent with prior study (1.1 eV) [78] and other group's result (1.3 eV) [75]

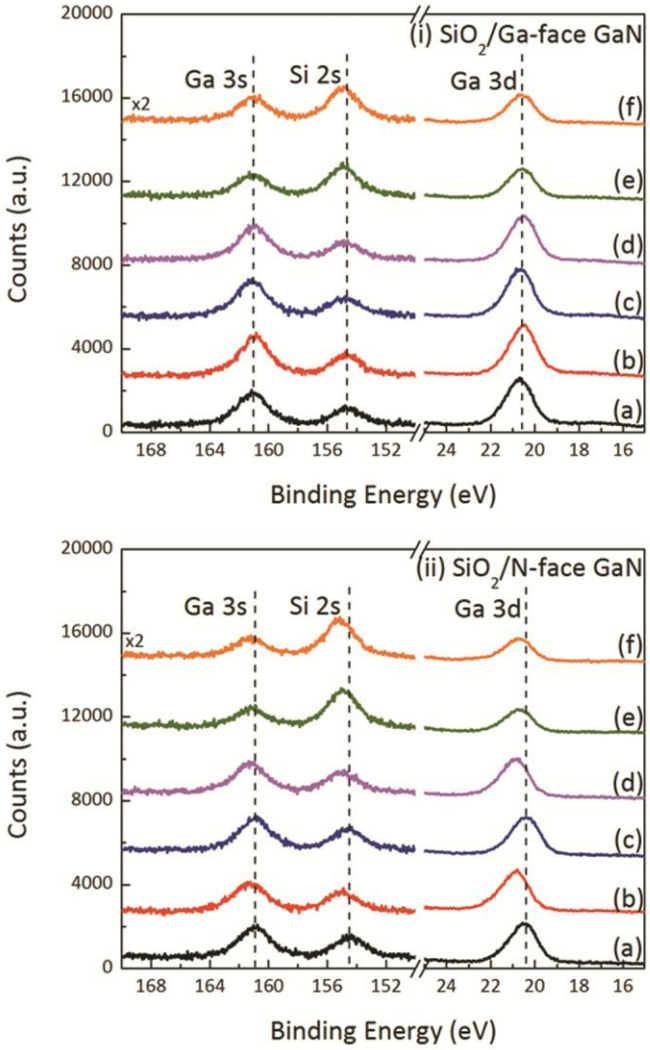

Figure 6.12. XPS Ga 3s, Si 2s, and Ga 3d core levels of PEALD SiO_2 on both (i) Ga- and (ii) N-face GaN for (a) ~1.5nm as-grown SiO_2; (b) 30min 600 ℃ PDA in N_2 atmosphere; (c) 5min RT O_2 plasma; (d) 30min 600 ℃ PDA in N_2 atmosphere; (e) ~3.0nm as-grown SiO_2; and (f) final 30min 600 ℃ PDA in N_2 atmosphere. The initial positions of the core level peaks after SiO_2 growth are indicated with dashed lines. The XPS Ga 3d and Si 2s peak intensity is enlarged by 2 times.

Table 6.4. XPS Ga 3d, Ga 3s and Si 2s core levels, and VBO results for SiO_2 on Ga- and N-face GaN. All energies are given in eV.

Process	Ga 3d		Ga 3s		Si 2s		VBO	
	Ga-face	N-face	Ga-face	N-face	Ga-face	N-face	Ga-face	N-face
after clean	**20.4**	**20.4**	**160.8**	**160.9**	-	-	-	-
(a) 1.5 nm SiO_2	**20.6**	**20.4**	**161.1**	**161.0**	**154.7**	**154.5**	**3.0**	**3.0**
(b) N_2 PDA	**20.5**	**20.8**	**161.0**	**161.3**	**154.7**	**155.0**	**3.1**	**3.1**
(c) O_2 plasma	**20.6**	**20.4**	**161.1**	**160.9**	**154.8**	**154.6**	**3.1**	**3.1**
(d) N_2 PDA	**20.5**	**20.8**	**161.0**	**161.3**	**154.8**	**155.0**	**3.2**	**3.1**
(e) 3.0 nm SiO2	**20.6**	**20.7**	**161.1**	**161.2**	**154.9**	**155.0**	**3.2**	**3.2**
(f) N_2 PDA	**20.6**	**20.7**	**161.0**	**161.2**	**154.9**	**155.1**	**3.2**	**3.3**
(g) N_2/H_2 PDA	**21.0**	**21.0**	**161.5**	**161.5**	**155.4**	**155.4**	**3.3**	**3.3**

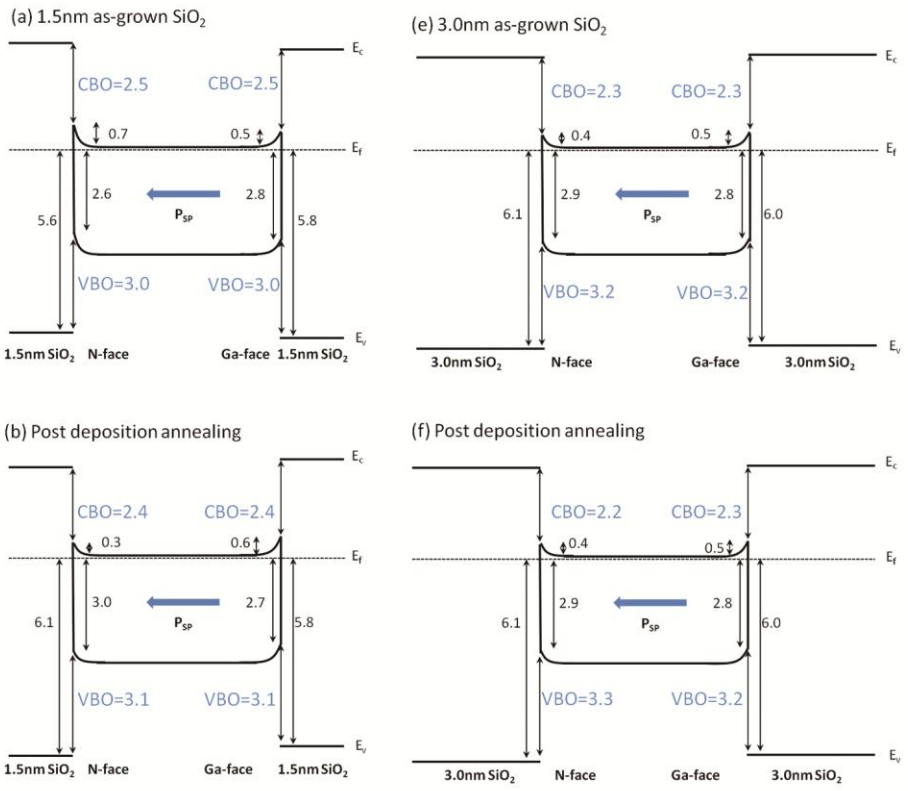

Figure 6.13. The deduced band alignment of (a) ~1.5nm as-grown SiO_2; (b) ~1.5nm annealed SiO_2; (e) ~3.0nm as-grown SiO_2; and (f) ~3.0nm annealed SiO_2, on Ga- and N-face GaN.

6.5 Discussion

The surface defects play a critical role in compensating the polarization bound sheet charge and subsequently affecting the surface band bending. In addition, the band offsets defined the carrier confinement properties in semiconductor and may determine device performance. Therefore, it is necessary to understand the effects of process conditions on polarization charge compensation and band offsets.

6.5.1 Surface electronic structure

A. Surface composition

For as-received GaN samples, the main C 1s peak was ascribed to hydrocarbon on the surface, and weaker peaks at higher binding energies (~290 eV) were attributed to carboxyl, such as C-O, C=O, and O-C=O, which is consistent with the results reported by Schulz *et al.* [79] and Gredelj *et al.* [80]. Vacuum annealing removed carboxyl peaks from the surface of GaN/Si, and an elevated temperature NH_3 process reduced the carbon contamination below the XPS detection limit [81]. The O 1s peak on GaN is a broad peak, which may consist of native oxide and -OH groups [2,66].

The surface composition on GaN/Si during the cleaning processes was shown in Fig. 6.14. The composition was calculated using the following equation:

$$\eta_x = \frac{I_x / S_x}{I_{Ga} / S_{Ga} + I_N / S_N + I_O / S_O + I_C / S_C} \tag{6.2}$$

where $I_{Ga,N,O,C}$ is the integrated area intensity of XPS Ga 3d, N 1s, O 1s, and C 1s peaks; $S_{Ga,N,O,C}$ is the atomic sensitive factor for Ga 3d, N 1s, O 1s, and C 1s photoelectrons, which is 0.31, 0.42, 0.66, and 0.25, respectively [82]; and η_x is the atomic concentration of element x.

For as-received GaN/Si, the atomic concentration of Ga, N, O, and C was 38.6%, 24.7%, 19.1%, and 20.5%, respectively. This indicated a similar amount of carbon and oxygen coverage on the surface, which was consistent with the study by Edwards *et al.*

[22]. On the other hand, the atomic ratio of N to Ga was only 0.64. For HCl cleaned GaN/Si, the atomic ratio of N/Ga increased to 0.81. This might be ascribed to the dissolving of Ga_2O_3 in HCl. In addition, the increase of N 1s peak intensity may be higher than that of Ga 3d peak intensity with the decrease of oxide and carbon surface coverage. This was ascribed to the lower value of inelastic mean free path (IMFP) of N 1s photoelectrons compared with that of Ga 3d photoelectrons. Compared with HCl, the NH_4OH cleaned GaN/Si had a higher N/Ga atomic ratio and a lower carbon concentration.

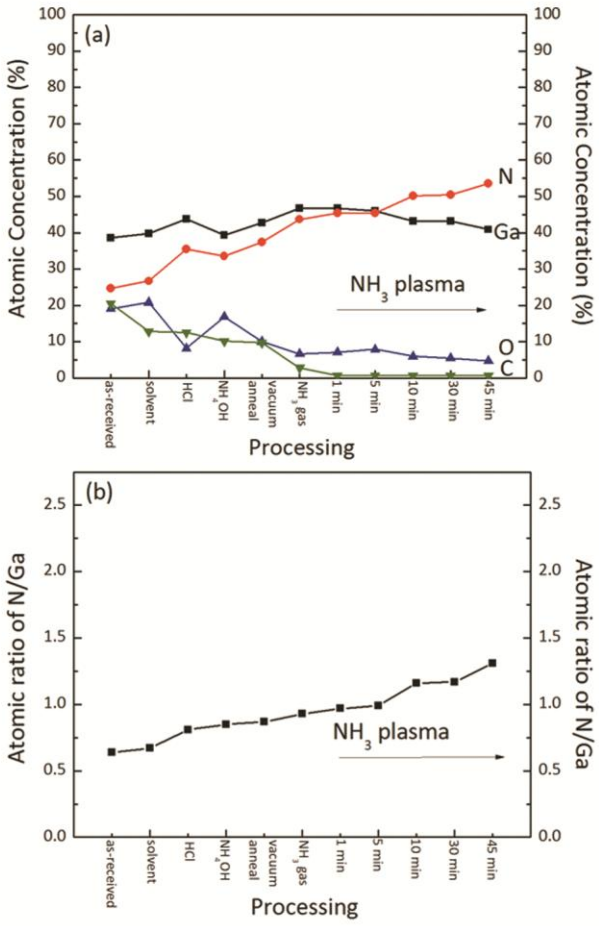

Figure 6.14. The (a) atomic concentration of Ga (square), N (circle), O (upper triangle), and C (lower triangle), and the atomic ratio for N to Ga of n-type, Ga-face GaN films on silicon with different cleaning processes. The different *ex-situ* cleaning process included as-received sample, solvent degreasing, solvent + HCl cleaning, and solvent + NH_4OH cleaning. All *in-situ* cleaning processes are combined with a prior solvent and NH_4OH clean.

The *in-situ* cleaning processes further decreased the C and O concentration and continued to change the N/Ga atomic ratio. The vacuum annealing process led to a ~50%

reduction of the oxygen and carbon remaining on the surface compared with as-received sample, and the N/Ga atomic ratio was ~0.87. For NH_3 gas annealing, the N/Ga atomic ratio was increased to 0.93. It may be speculated that the NH_3 plasma might passivate the N-vacancies. The N-vacancies related defects are thought to be donor-like defects, which tend to compensate the negative polarization bound charge. The passivation of N-vacancy related defects may lead to an increased depletion layer region to compensate the polarization charge, which would be characterized by an increase of surface band bending as shown in Fig. 6.15.

The atomic concentration of Ga- and N-face GaN was shown in Fig. 6.16. The surfaces have ~50% oxygen and carbon on the as-received Ga- and N-face GaN. After cleaning, the carbon contamination was below the detection limit of XPS (<1%) and the oxygen concentration decreased to ~5% on both Ga- and N-face GaN. The N/Ga atomic ratio on both Ga- and N-face GaN increased after the cleaning processes, which was shown in Fig. 6.17. For as-received Ga- and N-face GaN, the N/Ga atomic ratio was ~0.86 and 1.04, respectively, which was higher than that for as-received GaN/Si.

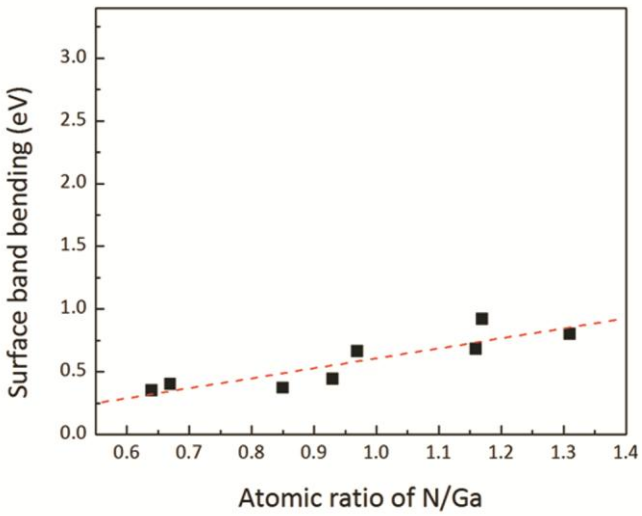

Figure 6.15. The relation of GaN surface band bending and the atomic ratio of N/Ga of GaN/Si. The dash line served as visual aid.

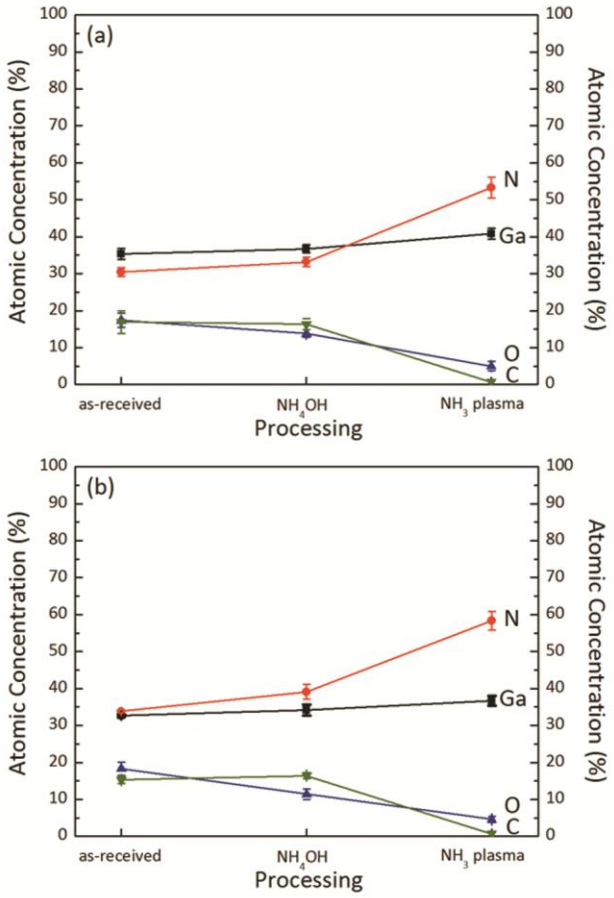

Figure 6.16. The atomic concentration of Ga (square), N (circle), O (upper triangle), and C (lower triangle) of (a) Ga-face and (b) N-face bulk GaN.

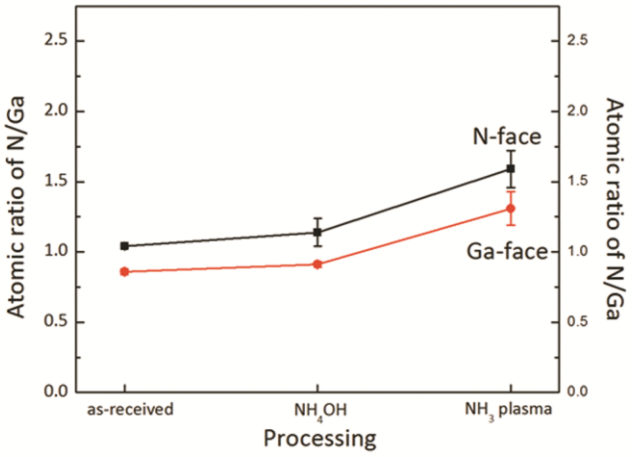

Figure 6.17. The atomic ratio of N to Ga for as-received, NH_4OH treated, and NH_3 plasma annealed Ga-face (square) and N-face (circle) GaN.

B. Oxygen coverage

After cleaning, the carbon contamination was below the XPS detection limit, and oxygen was still evident on the surface. By using the following equation [17,71], the oxygen coverage on the GaN surface could be calculated, where one monolayer (ML) oxygen coverage (Θ_O) indicates one oxygen atom per surface lattice site.

$$\Theta_O = \frac{I_O}{I_{Ga}} \frac{S_{Ga}}{S_O} \sum_{n=0}^{\infty} Exp[\frac{-nd_{GaN}}{\lambda_{Ga} Cos[\varphi]}] \qquad (6.3)$$

where φ is the angle between the normal direction of sample surface and analyze (which was 0 °in current XPS setup); λ_{Ga} (~2.4 nm) is the inelastic mean free path of the Ga 3d electrons with the kinetic energy of ~1200 eV; d (2.6 Å) is the distance between two Ga

planes in the c-axis direction; and n is the number of the Ga planes detected by XPS, where the upper limit could be replaced by a large number (such as 25). For N-face GaN, n was replaced by (n+0.25), since the first layer is N, and the distance between the first Ga and N layer was ~0.25d.

The oxygen coverage on Ga- and N-face GaN during cleaning processes was summarized in Table 6.5. For the as-received samples, there was 4.5 ± 0.5 and 5.1 ± 0.6 ML oxygen on the Ga- and N-face surfaces, which was presumably native oxide and absorbed oxygen (e.g. -OH, $-CO_x$). After NH_4OH cleaning, the oxygen coverage on Ga- and N-face GaN decreased to 3.4 ± 0.3 and 3.1 ± 0.4 ML, respectively. After *in-situ* NH_3 plasma treatment, the oxygen coverage further decreased to ~1.0 ML on both faces. After the cleaning processes, the O 1s core level shifted to lower binding energy, and this shift was consistent with that of the Ga 3d and N 1s core levels, which indicated the shift was related to the change in the surface band bending.

Bermudez [71] reported a study of oxygen chemisorptions on Ga-face GaN and calculated the surface normal dipole moment after oxygen saturation coverage according to the change of work function. The nonvanishing dipole moment suggested the O was bonded to Ga or N in a direction more nearly along the c axis [71]. Elsner *et al.* [83] has reported a theoretical calculation about O_2 chemisorption on Ga- and N-face GaN. For ideal Ga-face GaN, the stable oxygen coverage was ~ 0.375 ML, which could increase to 1 ML at very oxygen rich condition. They also reported a stable structure at Ga rich conditions with a Ga surface layer on top of the ideal Ga-face GaN. In this condition, all adsorbed oxygen atoms sat in three fold coordinated positions and the corresponding stable oxygen coverage was 1 ML, as shown in Fig. 6.18 [83]. On the other hand, for N-

face GaN, the calculation suggested that there was always 1ML of Ga atoms bonded to the N terminating atoms [83,84,85], as shown in Fig. 6.18. The corresponding stable oxygen coverage on N-face GaN was 0.75-1.0 ML depending on the oxygen chemical potential [83].

Table 6.5. The oxygen coverage on Ga- and N-face GaN.

Process	**Ga-face GaN**	**N-face GaN**
As-received	**4.5 ±0.5 ML**	**5.1 ±0.6 ML**
NH_4OH clean	**3.4 ±0.3 ML**	**3.1 ±0.4 ML**
NH_3 plasma clean	**1.1 ±0.2 ML**	**1.1 ±0.1 ML**

After the NH_3 plasma annealing process, the experimental oxygen coverage on both Ga- and N-face GaN surface was ~ 1 ML, which is consistent with the theoretical calculations based on the model with a Ga surface layer. The source of oxygen in the annealing chamber may come from the heater, sample holder, quartz tube, the chamber, or the sample itself.

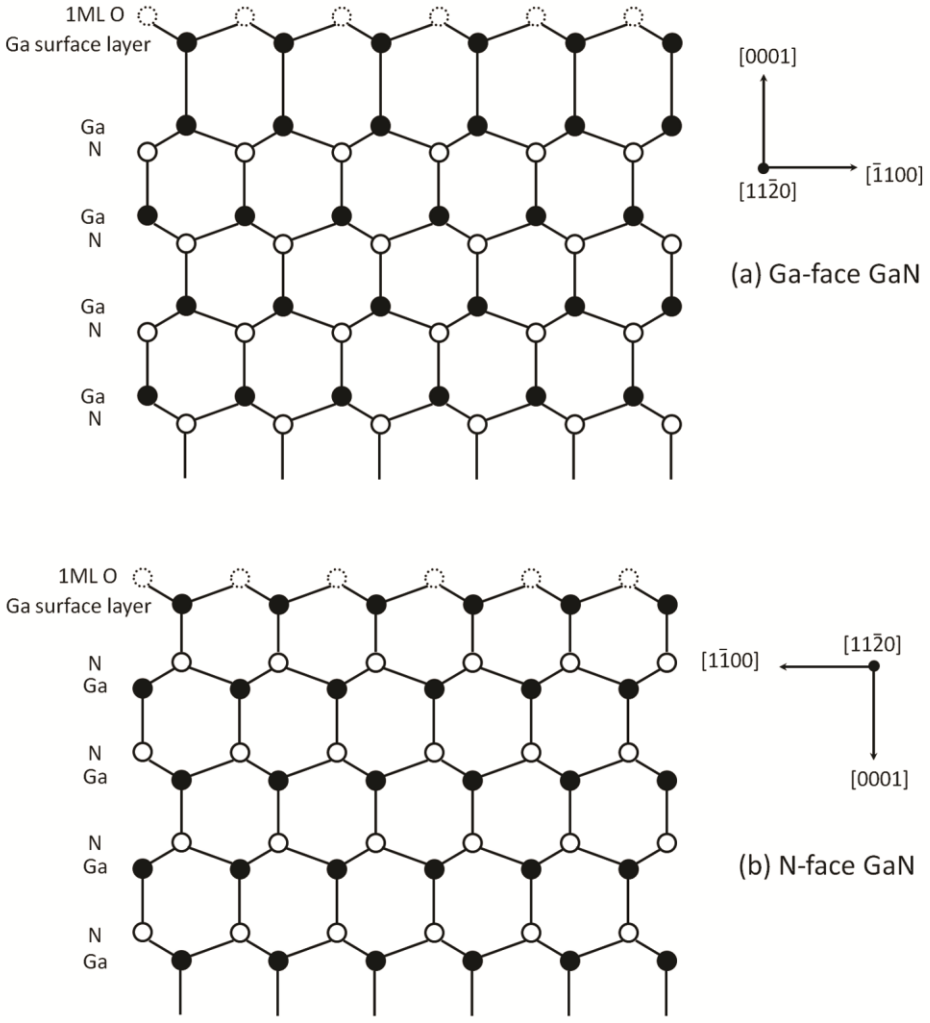

Figure 6.18. The schematic 1 ML stable oxygen coverage on both Ga- and N-face GaN with 1ML Ga surface layer on top of ideal structure [83].

C. Plasma effect

Comparing with H_2 plasma and N_2 plasma, the NH_3 plasma could better passivate the surface and bulk defects on GaN [29,30,31]. H_2 plasma may form volatile NH_x groups and cause N depletion and Ga clusters on GaN surface [7]. Among the different forms of nitrogen plasma, NH_3 plasma has advantages over N_2 or H_2/N_2 mixed plasma.

The N and H could more readily dissociate in NH_3, which could more effectively passivate N-vacancy related defects and the bulk defects in GaN [31]. In addition, the NH_3 plasma could stabilize the surface oxygen coverage to 1 ML, which avoids the presence of Ga dangling bonds that form during higher temperatures, and also decreased the defects in thicker surface oxides (~3 ML) after N_2 and H_2/N_2 plasma treatment.

D. Surface band bending and defect states

The effect of surface pretreatment on polarization charge compensation mechanism was investigated by monitoring the surface band bending. After NH_4OH treatment, the surface band bending for Ga- and N-face GaN, and GaN/Si were 0.4 ± 0.1, 0.1 ± 0.1, and 0.4 ± 0.1 eV upwards respectively. After *in-situ* NH_3 plasma treatment, the surface band bending was further increased to 0.8 ± 0.1, 0.6 ± 0.1, and 0.9 ± 0.1 eV respectively. The increase in upward band bending may be due to a reduction of the contamination layer and decrease of donor-like N-vacancy related defects. For vacuum annealed GaN/Si, which exhibited smaller surface band bending 0.3 ± 0.1 eV, the oxide thickness was higher and there may be more N-vacancy related defects. The upward band bending after NH_3 plasma treatment of these samples was close to the value (0.8 eV) reported by Bermudez *et al.* [71], who prepared the GaN samples by Ga deposition or 1 keV N_2^+ bombardment followed by UHV 900 ℃ annealing in both cases. Their investigation suggested that the surface Fermi level position that stable at ~0.7 eV below the bulk position might be caused by a balance between N vacancy (V_N, donor) and Ga vacancy (V_{Ga}, acceptor) defects [86,87]. The upwards band bending for N-face GaN indicated the surface defects overcompensated the positive bound sheet charge and the

net charge changed to negative, which needed compensating ionized donors. The acceptor-like Ga vacancy defects may be one of the reasons responsible for the negative defects.

The relation between the surface potential (Φ_S) and the depletion layer width (W) is given by the following relation:

$$\Phi_S = -\frac{qN_D}{2\varepsilon\varepsilon_o}W^2 \tag{6.4}$$

where N_D (=8x10^{17} cm^{-3}) is the doping density; ε (=9.5) is the dielectric constant of GaN; and ε_0 (=8.854x10^{-12} F/m) is the vacuum permeability. For respective ~0.8 and 0.6 eV upward band bending on Ga- and N-face GaN, the depletion layer width was ~32 and ~28 nm. This indicates the area density of ionized donors for Ga- and N-face GaN was ~2.6x10^{12} and 2.2x10^{12} charges/cm^{-3}, respectively. The similar internal charge compensation by ionized donors on both faces suggested a similar net charge of surface defects and polarization bound sheet charge. Therefore, the surface defects screened the polarization charge effects on Ga- and N-face GaN. The compensating surface states on Ga- and N-face GaN after cleaning was ~ 1.8x10^{13} and 2.3x10^{13} charges/cm^{-2} with opposite sign, respectively.

6.5.2 Interface electronic structure of dielectric on GaN

Our previous study has compared the experimental band offset of PEALD HfO_2 and Al_2O_3 on Ga-face GaN films with theoretical calculation based on the charge neutrality level (CNL) model [17]. The theoretical VBOs were calculated to be 1.7 and 1.3 eV respectively using the following equation

$$\Delta E_V = E_{CNL,dielectric} - E_{CNL,GaN} - S[I_{GaN} - I_{dielectric} - (E_{CNL,GaN} - E_{CNL,dielectric})] \quad (6.5)$$

where ΔE_V is the valence band offset; E_{CNL} is the charge neutrality level with respect to VBM; S is pinning factor of the wider band gap material; and I is the photo threshold energy. For the SiO_2/GaN VBO calculation, $E_{CNL,SiO2}$ and $E_{CNL,GaN}$ was 4.5 and 2.3 eV with respect to VBM [88]; S was 0.86 for SiO_2 [89]; and I_{GaN} and $I_{dielectric}$ were ~6.9 and 10.0 eV, respectively. Therefore the VBO for SiO_2 on GaN was calculated to be 3.0 eV.

Considering the CNL model does not include the effect of polarization charge, the dielectrics on Ga- and N-face should have the same band offsets based on this model [89]. In this study, the experimental VBO results for Al_2O_3, HfO_2, and SiO_2 on Ga- and N-face GaN were 2.0 ± 0.1 and 1.8 ± 0.1 eV, 1.4 ± 0.1 and 1.4 ± 0.1 eV, and 3.1 ± 0.1 and 3.1 ± 0.1 eV, respectively, which were close to the theoretical calculations. The experimental surface band bending results indicated a large concentration of surface defects screened the polarization charge. If the distance between the surface defects and the polarization bound charge was within several angstroms, the potential drop between them was only ~ 0.1V, which could not affect the surface electronic structure significantly. Therefore, the

polarization charge did not affect the band offset between dielectrics and GaN. In addition, the interfacial bonding states between GaN and dielectric (e.g., SiO_2) would be Ga-O-Si-O on both Ga- and N-face GaN. Therefore, similar band offset results should be obtained on both Ga- and N-face GaN.

The carbon impurities in dielectrics (HfO_2 and Al_2O_3) may introduce charge state transition levels close to GaN CBM, which may act as border traps and/or leakage current [90]. By using the PEALD method, the carbon impurities in the as-grown dielectrics (Al_2O_3, HfO_2, and SiO_2) on GaN were reduced below the XPS detection limit, which was expected to be beneficial for GaN power device application. Different post deposition treatments, including annealing in various ambient and RT O_2 plasma treatments, were applied to investigate their effects on surface band bending and band offsets. The oxygen interstitial (O_i) is an acceptor with (0/-2) transition level, which is below the midgap of the oxide (e.g., Al_2O_3 and HfO_2) [91]. In addition, the energy level of O_i in Al_2O_3 and HfO_2 is within the band gap of GaN after alignment, which suggests that the O_i would not act as a border trap [91]. The O_2 plasma process may induce acceptor-like defects, such as oxygen interstitial [17,92]. In addition, it appears that the oxygen interstitial could be removed during annealing process.

During this process, the Ga 3d and Al 2p core levels from 1.5 nm Al_2O_3 on Ga-GaN shifted by ~0.6 and 0.9 eV, respectively. On the other hand, for 1.5nm Al_2O_3 on N-face GaN, the respective Ga 3d and Al 2p core levels shifted by ~0.5 and 0.7 eV. The larger shift in Al_2O_3 than GaN indicated there may be an electric field across the interfacial layer, between GaN and Al_2O_3. In this case the shift of the Al 2p core level would be the sum of the shift of the Ga 3d from GaN and the potential drop across

interfacial layer. To investigate the possible charge distribution in Al_2O_3 films, an additional 1.5 nm Al_2O_3 was deposited on the original samples. If the charges were distributed in the oxide, they would generate an electric field across dielectric film and the shift of Al 2p core level during O_2 plasma treatment and annealing process would increase with the Al_2O_3 film thickness. However, the shift of the Ga 3d and Al 2p core levels was ~0.5 and 0.8 eV for 3.0 nm Al_2O_3/Ga-face GaN, and 0.5 and 0.7 eV for 3.0 nm Al_2O_3/N-face GaN, respectively. This indicated the shift of the Al 2p core level did not increase with Al_2O_3 thickness, which suggested the electric field may be near the Al_2O_3/GaN interfaces. In addition, considering different detection depth of XPS and UPS, if there was an electric field in the Al_2O_3 layer, the binding energy difference between the Al 2p and VBM in Al_2O_3 would be dependent on the Al_2O_3 thickness, which differed from the constant value measured in this study. Therefore the charges were likely located at or near the interface of GaN and Al_2O_3. Similar results were obtained from HfO_2 on Ga- and N-face GaN. The respective shift of Ga 3d and Hf $4f_{7/2}$ core levels was ~0.3 and 0.5 eV for HfO_2/Ga-face GaN, and ~0.5 and 0.7 eV for HfO_2/N-face GaN, regardless of the thicknesses of the HfO_2. This indicated the possible charge distribution at the interface, which could be removed with annealing process. The change of the interface charges could be calculated by the following equation, which is derived from Eq. 6.4.

$$A_I = N_D W_1 - N_D W_2 = \sqrt{2\varepsilon\varepsilon_o \Phi_{S1} N_D / q} - \sqrt{2\varepsilon\varepsilon_o \Phi_{S2} N_D / q} \qquad (6.6)$$

Where A_I is the area density of process induced charges; and the subscript 1 and 2 represents before and after annealing. The calculation suggested there were ~$1.0 \pm 0.3 \times 10^{12}$ charges/cm^2 induced by O_2 plasma at Al_2O_3/GaN or HfO_2/GaN interface, which could be removed by annealing.

However, results on SiO_2/GaN suggested the acceptor-like defects in the SiO_2/GaN structure were not readily removed as those in Al_2O_3/GaN and HfO_2/GaN structure. The core levels for 3 nm as-grown and N_2 annealed SiO_2 films on Ga- and N-face GaN were almost the same. After further H_2/N_2 PDA, the core levels shifted to higher binding energy by ~ 0.4 eV, which suggested H annealing could reduce these acceptor-like defects in SiO_2. This was further supported by the different shifts of Ga 3d core level of SiO_2 on GaN during different processing as shown in Fig. 6.19.

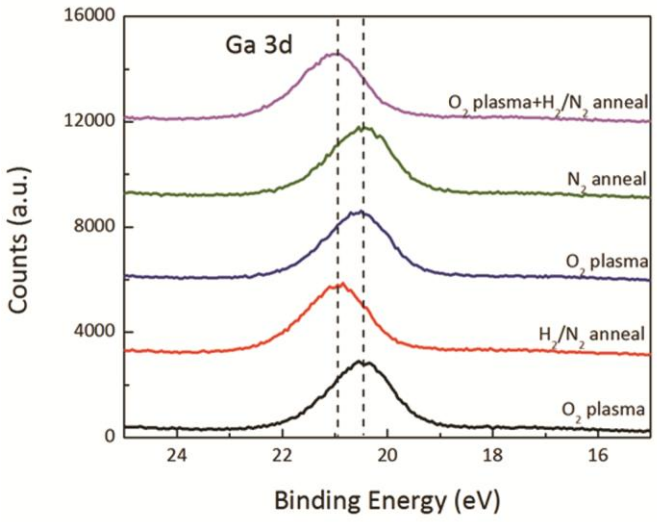

Figure 6.19. XPS Ga 3d core levels of SiO_2 on Ga-face GaN films during different processing.

6.6 Conclusion

In this research, Ga- and N-face GaN surfaces were cleaned to remove carbon contamination, reduce oxygen coverage, and passivate N-vacancy related defects. After surface pretreatment, both Ga- and N-face GaN were characterized by an upward band bending of 0.8 ± 0.1 eV and 0.6 ± 0.1 eV, respectively. The band bending demonstrated no obvious polarization dependence, which suggested a large concentration of compensating surface defects. In addition, the cleaning process led to undetectable carbon contamination by XPS and ~1 ML oxygen coverage on both Ga- and N-face GaN. The ~ 1ML oxygen coverage may indicate there was Ga surface layer on both Ga- and N-face GaN.

Three wide band gap PEALD dielectrics (Al_2O_3, HfO_2, and SiO_2) were deposited on Ga- and N-face GaN to investigate the effect of polarization charge on band offset. The carbon impurities for as-grown Al_2O_3, HfO_2, and SiO_2 on GaN were below the XPS detection limit. The effect of post deposition treatment, including PDA in N_2, mixed H_2/N_2 (10% H_2) or NH_3 ambient or O_2 plasma treatment, on interface electronic structure, polarization charge compensation, and band offset was studied. The respective valence band offsets of Al_2O_3, HfO_2, and SiO_2 on Ga- and N-face GaN were 1.9 ± 0.2, 1.4 ± 0.1, and 3.1 ± 0.1 eV, independent of the processing conditions and dielectric thicknesses, which indicated the polarization charge effect was screened by the surface defects and had little effect on band offset. The corresponding conduction band offset were 1.4 ± 0.2, 1.0 ± 0.1, and 2.4 ± 0.1 eV, respectively. These experimental values were consistent with theoretical calculations based on the charge neutrality level model. The plasma induced defects were $\sim 1.0 \pm 0.3 \times 10^{12}$ charges/cm^2 in Al_2O_3/GaN, HfO_2/GaN, and SiO_2/GaN. The

plasma induced defects in Al_2O_3/GaN and HfO_2/GaN were more readily removed with annealing. However, for SiO_2/GaN, the plasma induced defects may be removed with annealing in H-contained ambient.

Reference

[1] S. J. Pearton, J. C. Zolper, R. J. Shul, and F. Ren, *J. Appl. Phys*. **86**, 1 (1999).

[2] B. S. Eller, J. Yang, and R. J. Nemanich, *J. Vac. Sci. Technol. A* **31** 050807 (2013).

[3] R. D. Long and P. C. McIntyre, *Materials* **5**, 1297 (2012).

[4] U. K. Mishra, P. Parikh, and Y. F. Wu, *Proc. IEEE* **90**, 1022 (2002).

[5] T. Hashizume, J. Kotani, and H. Hasegawa, *Appl. Phys. Lett.* **84**, 4884 (2004).

[6] E. J. Miller, E. T. Yu, P. Waltereit, and J. S. Speck, *Appl. Phys. Lett.* **84**, 535 (2004).

[7] H. Hasegawa, T. Inagaki, S. Ootomo, and T. Hashizume, *J. Vac. Sci. Technol. B* **21**, 1844 (2003)

[8] R. Vetury, N. Q. Zhang, S. Keller, and U. K. Mishra, *IEEE Trans. Electron Devices* **48**, 560 (2001).

[9] A. Zoroddu, F. Bernardini, P. Ruggerone, and V. Fiorentini, *Phys. Rev. B* **64**, 045208 (2001).

[10] A. D. Bykhovski, B. L. Gelmont, and M. S. Shur, *J. Appl. Phys.* **81**, 6332 (1997).

[11] A. Zoroddu, F. Bernardini, P. Ruggerone, and V. Fiorentini, *Phys. Rev. B* **64**, 045208 (2001).

[12] T. E. Cook, Jr., C. C. Fulton, W. J. Mecouch, K. M. Tracy, and R. F. Davis, E. H. Hurt, G. Lucovsky, and R. J. Nemanich, *J. Appl. Phys*. **93**, 3995 (2003).

[13] U. Karrer, O. Ambacher, and M. Stutzmann, *Appl. Phys. Lett*. **77**, 2012 (2000).

[14] M. Hong, K. A. Anselm, J. Kwo, H. M. Ng, J. N. Baillargeon, A. R. Kortan, J. P. Mannaerts, A. Y. Cho, C. M. Lee, J. I. Chyi and T. S. Lay, *J. Vac. Sci. Technol. B* **18**, 1453 (2000).

[15] Y. Q. Wu, T. Shen, P. D. Ye, and G. D. Wilk, *Appl. Phys. Lett.* **90**, 143504 (2007).

[16] W. J. Mecouch, B. P. Wagner, Z. J. Reitmeier, R. F. Davis, C. Pandarinath, B. J. Rodriguez, and R. J. Nemanich, *J. Vac. Sci. Technol. A* **23**, 72 (2005).

[17] J. Yang, B. S. Eller, C. Zhu, C. England, and R. J. Nemanich, *J. Appl. Phys*. **112**, 053710 (2012).

[18] H.W. Jang, J.-H. Lee, and J.-L Lee, *Appl. Phys. Lett.* **80**, 3955 (2002).

[19] P. Lorenz, T. Haensel, R. Gutt, R. J. Koch, J. A. Schaefer and S. Krischok, *Physica Status Solidi B* **247**, 1658 (2010).

[20] V. M. Polyakov, F. S. Tautz, S. Sloboshanin, J. A. Schaefer, A. S. Usikoy, and B. Ja. Ber, *Semicond. Sci. Technol.* **13**, 1396 (1998).

[21] J. C. Carrano, T. Li, P. A. Grudowski, C. J. Eiting, R. D. Dupuis, and J. C. Campbell, *Appl. Phys. Lett.* **72**, 542 (1998).

[22] N. V. Edwards, M. D. Bremser, T. W. Weeks, R. S. Kern, R. F. Davis, and D. E. Aspnes, *Appl. Phys. Lett.* **69**, 2065 (1996).

[23] P. B. Klein, S. C. Binari, K. Ikossi, A. E. Wickenden, D. D. Koleske, and R. L. Henry, *Appl. Phys. Lett.* **79**, 3527 (2001).

[24] J. A. Bardwell, S. Haffouz, W. R. McKinnon, C. Storey, H. Tang, G. I. Sproule, D. Roth and R. Wang, *Electrochem. Solid-State Lett.* **10**, H46 (2007).

[25] J. Uren, J. Möreke, and M Kuball, *IEEE Trans. Electron Devices* **59**, 3327 (2012).

[26] R. Nakasaki, T. Hashizume, and H. Hasegawa, *Phys. E* **7**, 953 (2000).

[27] T. Hashizume, R. Nakasaki, S. Ootomo, S. Oyama, and H. Hasegawa, *Mater. Sci. Eng. B* **80**, 309 (2001).

[28] J. J. Kim, G. M. Yang, K.-H. Shim, and J. W. Yang, *Jpn. J. Appl. Phys.* **50**, 096501 (2011).

[29] S. Hoshi, T. Marui, M. Itoh, Y. Sano, and S. Seki, *IEICE Trans Electron*. **E89C**, 1052 (2006).

[30] J. Kim, H. Choi, M. Ha, H. Song, C. Roh, J. Lee, J. Park, and C. Hahn, *Jpn. J. Appl .Phys.* **49**, 04DF05 (2010).

[31] A. Hierro, S. A. Ringel, M. Hansen, J. S. Speck, U. K. Mishra, and S. P. DenBaars, *Appl. Phys. Lett.* **77**, 1499 (2000).

[32] Y. C. Chang, W. H. Chang, H. C. Chiu, L. T. Tung, C. H. Lee, K. H. Shiu, M. Hong, J. Kwo, J. M. Hong, and C. C. Tsai, *Appl. Phys. Lett.* **93**, 053504 (2008).

[33] P. D. Ye, B. Yang, K. K. Ng, J. Bude, G. D. Wilk, S. Halder, and J. C. M. Hwang, *Appl. Phys. Lett.* **86**, 063501 (2005).

[34] Y. C. Chang, W. H. Chang, Y. H. Chang , J. Kwo, Y. S. Lin , S. H. Hsu , J. M. Hong , C. C. Tsai, and M. Hong, *Microelectron Eng.* **87**, 2042 (2010).

[35] Y.C. Chang, H.C. Chiu, Y.J. Lee, M.L. Huang, K.Y. Lee, M. Hong, Y.N. Chiu, J. Kwo, and Y.H. Wang, *Appl. Phys. Lett.* **90**, 232904 (2007).

[36] C. J. Kirkpatrick, B. Lee, R. Suri, X. Yang, and V. Misra, *IEEE Electron Device Lett.* **33**, 1240 (2012).

[37] M. Sawada, T. Sawada, Y. Yamagata, K. Imai, H. Kimura, M. Yoshino, K. Iizuka, and H. Tomozawa, *J. Cryst. Growth* **189/190**, 706 (1998).

[38] J. S. Jur, V. D. Wheeler, D. J. Lichtenwalner, J. P. Maria, and M. A. L. Johnson, *Appl. Phys. Lett*. **98**, 042902 (2011).

[39] X. Hu, A. Koudymov, G. Simin, J. Yang, M. Asif Khan, A. Tarakji, M.S. Shur, and R. Gaska, *Appl. Phys. Lett*. **79**, 2832 (2001).

[40] H. Kim, R. M. Thompson, V. Tilak, T. R. Prunty, J. R. Shealy and L. F. Eastman, *IEEE Electron Device Lett.* **24**, 421 (2003).

[41] T. Hashizume, E. Alekseev, D. Pavlidis, K. S. Boutros, and J. Redwing, *J. Appl. Phys*. **88**, 1983 (2000)

[42] X. Wang, O. I. Saadat, B. Xi, X. Lou, R. J. Molnar, T. Palacios and R. G. Gordon, *Appl. Phys. Lett.* **101**, 232109 (2012).

[43] R. Mehandru, B. Luo, J. Kim, F. Ren, B. P. Gila, A. H. Onstine, C. R. Abernathy, S. J. Pearton, D. Gotthold, R. Birkhahn, B. Peres, R. Fitch, J. Gillespie, T. Jenkins, J. Sewell, D. Via, and A. Crespo, *Appl. Phys. Lett.* **82**, 2530 (2003).

[44] B. Luo, J.W. Johnson, J. Kim, R.M. Mehandru, F. Ren, B.P. Gila, A.H. Onstine, C.R. Abernathy, S.J. Pearton, A.G. Baca, R.D. Briggs, R.J. Shul, C. Monier and J. Han, *Appl. Phys. Lett.* **80**, 1661 (2002).

[45] A.Y. Polyakov, N.B. Smirnov, B.P. Gila, M. Hlad, A.P. Gerger, C.R. Abernathy, and S.J. Pearton, *J. Electrochem. Soc.* **154**, H115 (2007).

[46] Y. Chiou and C. Lee, *IEEE T Electron Dev.* **58**, 3869 (2011).

[47] M. Ochiai, M. Akita, Y. Ohno, S. Kishimoto, K. Maezawa, and T. Mizutani, *Jpn. J. Appl. Phys.* **42**, 2278 (2003).

[48] R. L. Puurunen, *J. Appl. Phys*. **97**, 121301 (2005).

[49] B. Lee, S. Park, H. Kim, K. Cho, E. M. Vogel, M. J. Kim, R. M. Wallace, and J. Kim, *Appl. Phys. Lett*. **92**, 203102 (2008).

[50] J. Yang, B. S. Eller, M. Kaur, R. J. Nemanich, *J. Vac. Sci. Technol. A* **32**, 021514 (2014)

[51] H. B. Profijt, S. E. Potts, M. C. M. van de Sanden, and W. M. M. Kessels, *J. Vac. Sci. Technol. A* **29**, 050801-1 (2011) .

[52] J. W. Lim and S. Yun, *J. Electrochem. Solid-State Lett.* **7**, F45 (2004).

[53] K.-Y. Park, H.-I. Cho, H.-C. Choi and J.-H. Lee, S.-B. Bae, Y.-H. Bae, J.-L. Lee, *J. Korean Phys. Soc.* **45**, S898 (2004).

[54] K.-Y. Park, H.-I. Cho, H.-C. Choi, Y.-H. Bae, C.-S. Lee,J.-L. Lee, and J.-H. Lee, *Jpn. J. Appl Phys.* **43**, L1433 (2004).

[55] J.-B. Ha, D.-S. Kim, K.-S. Im, K.-W. Kim, H.-S. Kang, K.-Y. Park1, and J.-H. Lee, *Jpn. J. Appl Phys.* **49**, 126501 (2010).

[56] M. Abraham, X. Weng, W. H.Choi, B. P. Downey, and S. E. Mohney, *Appl. Phys. Lett.* **101**, 243504 (2012)

[57] R. Dimitrov, M. Murphy, J. Smart, W. Schaff, J. R. Shealy, L. F.Eastman, O.Ambacher , and M. Stutzmann, *J. Appl. Phys.* **87**, 3375 (2000)

[58] C.F. Shih, K.T. Hung, C.Y. Hsiao, S.C. Shu, and W.M. Li, *J. Alloys Compd.* **480**, 541 (2009).

[59] M.Z. Peng, Y.K. Zheng, K. Wei, and X.Y. Liu, *Microelectron Eng.* **87**, 2638 (2010).

[60] H. Zhou, G. I. Ng, Z. H. Liu and S. Arulkumaran, *Appl. Phys. Express* **4**, 104102 (2011).

[61] K.-W. Kim, S.-D. Jung, D.-S. Kim, K.-S. Im, H.-S. Kang, J.-H. Lee, Y. Bae, D.-H. Kwon and S. Cristoloveanu, *Microelectron. Eng.* **88**, 1225 (2011).

[62] C. Zhu, S.L. Caudle, J. Yang, D.J. Smith, R.J. Nemanich, *J. Vac. Sci. Technol. B* **32**, 011203 (2014).

[63] J. R. Waldrop and R. W. Grant, *Appl. Phys. Lett.* **68**, 2879 (1996).

[64] E. A. Kraut, R. W. Grant, J. R. Waldrop, and S. P. Kowalczyk, Heterojunction Band Discontinuities: Physics and Device Applications, edited by F. Capasso and G. Margaritondo (Elsevier, New York, 1987).

[65] T. Hashizume, S. Ootomo, R. Nakasaki, S. Oyama, and M. Kihara, *Appl. Phys. Lett*. **76**, 2880 (2000).

[66] S. W. King, J. P. Barnak, M. D. Bremser, K. M. Tracy, C. Ronning, R. F. Davis, and R. J. Nemanich, *J. Appl. Phys.* **84**, 5248 (1998).

[67] Rathnait D. Long and Paul C. McIntyre, *Materials* **5**, 1297 (2012).

[68] C. I. Wu, A. Kahn, N. Taskar, D. Dorman, and D. Gallagher, *J. Appl. Phys*. **83**, 4249 (1998).

[69] T. E. Cook, Jr., C. C. Fulton, W. J. Mecouch, R. F. Davis, G. Lucovsky, and R. J. Nemanich, *J. Appl. Phys.* **94**, 7155 (2003).

[70] J. Hedman and N. Mårtensson, *Phys. Scr.* **22**, 176 (1980).

[71] V. M. Bermudez, *J. Appl. Phys.* **80**, 1190 (1996).

[72] H. Y. Yu, M. F. Li, B. J. Cho, C. C. Yeo, M. S. Joo, D.-L. Kwong, J. S. Pan, C. H. Ang, J. Z. Zheng, and S. Ramanathan, *Appl. Phys. Lett.* **81**, 376 (2002).

[73] N. V. Nguyen, O. A. Kirillov, W. Jiang, W. Wang, J. S. Suehle, P. D. Ye, Y. Xuan, N. Goel, K.-W. Choi, W. Tsai, and S. Sayan, *Appl. Phys. Lett.* **93**, 082105 (2008).

[74] O. Blank, H. Reisinger, R. Stengl, M. Gutsche, F. Wiest, V. Capodieci, J. Schulze, and I. Eisele, *J. Appl. Phys.* **97**, 044107 (2005).

[75] E. Bersch, S. Rangan, R. A. Bartynski, E. Garfunkel, and E. Vescovo, *Phys. Rev. B* **78**, 085114 (2008).

[76] S. Suzer, S. Sayan, M. M. Banaszak Holl, E. Garfunkel, Z. Hussain, and N. M. Hamdan, *J. Vac. Sci. Technol. A* **21**, 106 (2003).

[77] M. Brause, D. Ochs, J. Günster, Th. Mayer, B. Braun, V. Puchin, W. Maus-Friedrichs, and V. Kempter, *Surf Sci.* **383**, 216 (1997).

[78] T. E. Cook, Jr., C. C. Fulton, W. J. Mecouch, K. M. Tracy, and R. F. Davis, E. H. Hurt, G. Lucovsky, and R. J. Nemanich, *J. Appl. Phys.*, **93**, 3995 (2003)

[79] Ch. Schulz, S. Kuhr, H. Geffers, Th. Schmidt, J.I. Flege, T. Aschenbrenner, D. Hommel and J. Falta, *J. Vac. Sci. Technol. A* **29**, 011013 (2011).

[80] S. Gredelj, A. R. Gerson, S. Kumar, and G. P. Cavallaro, *Appl. Surf. Sci*. **174**, 240 (2001).

[81] F. C. Sauls, W. J. Hurley, L. V. Interrante, P. S. Marchetti, and G. E. Maciel, *Chem. Mater.* **7**, 1361 (1995).

[82] D. Briggs and M. P. Seah, Practical Surface Analysis, Vol. 1 Auger and X-ray Photoelectron Spectroscopy, 2nd edition (John Wiley & Sons, West Sussex, 1990).

[83] J. Elsner, R. Gutierrez, B. Hourahine, R. Jones, M. Haugk, Th. Frauenheim, *Solid State Commun.* **108** 953 (1998).

[84] A.R. Smith, R.M. Feenstra, D.W. Greve, M.S. Shin, M. Skowronski, J. Neugebauer, J.E. Northrup, *Appl. Phys. Lett.*, **72** 2114 (1998).

[85] J. Elsner, M. Haugk, G. Jungnickel, Th. Frauenheim, *Solid State Commun.*, **106** 739 (1998)

[86] V.M. Bermudez, D.D. Koleske, A.E. Wickenden, *Appl. Sur. Sci.*, **126** 69 (1998)

[87] J. Neugebauer, C.G. Van de Walle, Festkörperprobleme **35** 25 (1996)

[88] W. Mönch, *J. Appl. Phys.* **109**, 113724 (2011).

[89] J. Robertson and B. Falabretti, *J. Appl. Phys.* **100**, 014111 (2006).

[90] M. Choi, J. L. Lyons, A. Janotti, and C. G. Van de Walle, *Appl. Phys. Lett.* **102**, 142902 (2013).

[91] C. G. Van de Walle, M. Choi, J. Weber, J. Lyons, and A. Janotti, *Microelectron. Eng*. **109**, 211 (2013)

[92] O. Bierwagen, J. S. Speck, T. Nagata, T. Chikyow, Y. Yamashita, H. Yoshikawa, and K. Kobayashi, *Appl. Phys. Lett.* **98**, 172101 (2011).

CHAPTER 7

SUMMARY & FUTURE WORK

7.1 Summary

This dissertation mainly focuses on interface properties of PEALD dielectrics on GaN, which includes polarization charge compensation, interface states, and band offset of dielectrics on GaN. The effect of GaN surface pretreatment, dielectric deposition, and post deposition annealing processes on interface properties is investigated. The interface chemistry and electronic structures are mainly characterized by *in-situ* XPS and UPS. Results in the dissertation can be separated into three parts.

A detailed study was presented on remote PEALD Al_2O_3 film growth using non-pyrophoric precursor, DMAI, was investigated. Saturated and self-limiting growth of Al_2O_3 films were obtained with an enhanced growth rate of ~1.5 Å/cycle within a PEALD growth window that extends from room temperature to 220 ℃. The increased growth rate compared with thermal ALD was ascribed to a high concentration of active oxygen species remaining on the surface after plasma exposure and a higher reactivity of plasma species compared with water. The active oxygen species could accelerate surface reactions, increase the surface density of -OH groups, and/or reduce the steric hindrance through reactions with precursor ligands. Therefore, the active plasma species enhanced the DMAI molecular chemisorption saturation level and subsequently improved the growth rate. For room temperature Al_2O_3 deposition, carbon impurities were reduced below the XPS detection limit with an extended oxygen plasma time. The properties of Al_2O_3 films deposited at different temperatures were also characterized to achieve a

better understanding between the growth parameters and film properties. When deposited at 25 ℃ and 200 ℃, the Al_2O_3 films demonstrated a single Al-O bonding state as indicated by XPS, a similar band gap of 6.8±0.2 eV as determined from the O 1s ELS, a similar index of refraction of 1.62±0.02 as measured by spectroscopy ellipsometry, and a similar surface roughness before and after growth as indicated by AFM. However, compared with Al_2O_3 films deposited at 200 ℃, the room temperature Al_2O_3 films had a higher O to Al atomic ratio (2.1 compared with 1.6) and a lower mass density (2.7g/cm^3 compared with 3.0 g/cm^3) as confirmed by RBS and XRR, respectively.

PEALD could enable conformal and uniform amorphous Al_2O_3 film growth with atomic scale thickness control and reduced impurities compared with CVD or thermal ALD. Five promising PEALD dielectrics with variations in band gap energies were further investigated on GaN, including Al_2O_3, HfO_2, SiO_2, La_2O_3, and ZnO. Prior to dielectric growth, a surface pretreatment that consisted of an *ex-situ* wet chemical treatment of HCl and an *in-situ* high temperature H_2/N_2 plasma process was used to reduce carbon contamination below the XPS detection limit. After cleaning, the GaN surface had ~2.0 ML of oxygen coverage and an upward band bending ~ 0.3 eV. Considering a negative polarization bound charge (~2.1x10^{13} charges/cm^2) on the surface, the band bending value suggested positive surface compensating defects at a level of ~2x10^{13} charges/cm^2. The valence band offset of Al_2O_3, HfO_2, SiO_2, La_2O_3, and ZnO dielectrics on Ga-face GaN films were measured by *in-situ* XPS and UPS, and the respective values were 1.8, 1.4, 3.2, 0.9, and 0.7 eV. The corresponding respective conduction band offsets were 1.3, 1.0, 2.3, 1.7, and -0.7 eV. The trends of the potential barrier of dielectrics on GaN were related to the band gap of the dielectrics. The band

alignments suggested that the dielectric should have a minimum band gap of ~ 5.8 eV to create a sufficient potential barrier for electrons on GaN, and HfO_2, Al_2O_3, and SiO_2 fulfill this requirement. The measured band offset values were compared with calculated results based on electron affinity and charge neutrality level models. The results suggested that the experimental results were more close to the calculations based on the charge neutrality level model, which was more appropriate for heterostructure interfaces that exhibited an interface dipole. However, the experimental band offset values reported in the literature showed large variations, which may be related to different characterization methods and interface structures. The post deposition processing could shift the core levels of dielectrics and GaN by ~ 0.5 eV, while the band offset remained constant within the experimental errors. The effect was ascribed to the formation of acceptor-like defects during the oxygen plasma treatment. The defects could be removed by an annealing process. However, compared with Al_2O_3/GaN and HfO_2/GaN, the shift of core levels in SiO_2/GaN after processing was smaller, which indicated the O_2 plasma may introduce fewer acceptor-like defects or the acceptor-like defects may not be readily removed with the annealing process. The Al_2O_3 films were further investigated as an interfacial passivation layer between HfO_2 and GaN. For the HfO_2/Al_2O_3/GaN stacked structure, the valence and conduction band offsets of HfO_2 with respect to GaN were ~1.3 and 1.1 eV respectively. These values were similar to those for HfO_2/GaN. Therefore, the Al_2O_3 interfacial passivation layer did not significantly change the band offset of the HfO_2/GaN heterostructure.

To further investigate the effect of the polarization charge and the charge compensation mechanisms, bulk GaN substrates with both Ga-face and N-face surfaces

were investigated. Prior to dielectric growth, the Ga- and N-face GaN was cleaned with an *ex-situ* NH_4OH wet chemical and an *in-situ* elevated temperature NH_3 plasma process to remove carbon contamination, reduce oxygen coverage on the surface, and potentially passivate N-vacancy related defects. After cleaning, the carbon contamination was below the XPS detection limit. The oxygen coverage stabilized at ~1 ML on both Ga- and N-face GaN, which indicated the presence of Ga-O bonding on both Ga- and N-face GaN. In addition, the surface atomic ratio of N to Ga also increased from ~0.9 and 1.0 to ~1.3 and 1.6 for Ga- and N-face GaN, respectively. The passivation of donor-like N-vacancy related defects may be indicated by the increased surface band bending during processing. The respective upwards surface band bending of Ga- and N-face GaN increased from ~0.2 and -0.1 eV to 0.8 ± 0.1 and 0.6 ± 0.1 eV. The similar upward band bending on Ga- and N-face GaN suggested surface defects could accommodate opposite charges to compensate the polarization bound charge. To completely screen the polarization charge by surface defects alone, the potential drop between the defects and polarization charge may be ~0.1V, if the surface defects are located at several angstroms away from the polarization bound charge. The similar surface band bending on both surfaces suggested the net charge of surface defects and polarization charge was similar on both Ga- and N-face GaN. In addition, the similar upward band bending of ~0.7 eV on Ga- and N-face GaN may be caused by the balance between donor-like N-vacancy related defects and acceptor-like Ga-vacancy related defects on the surface [1,2].

The band alignment of the following structures was measured: Al_2O_3/Ga-face GaN, Al_2O_3/N-face GaN, HfO_2/Ga-face GaN, HfO_2/N-face GaN, SiO_2/Ga-face GaN, and SiO_2/N-face GaN. The respective valence band offsets of Al_2O_3, HfO_2, and SiO_2 on both

Ga- and N-face GaN are 1.9±0.2, 1.4±0.1, and 3.1±0.1 eV, independent of dielectric thicknesses and processing conditions. These values were close to the calculated results based on CNL model. Evidently the interface defects effectively screened the polarization charge as suggested by a similar surface band bending after cleaning. The increased dielectric thickness did not affect the binding energy differences between the core level and VBM and the magnitude of the dielectric core level shift during processing, which suggested the plasma induced charge was located near the dielectric/GaN interface.

7.2 Future work

7.2.1 Electron cyclotron resonance plasma clean on GaN

The surface pretreatment of GaN plays a critical role in determining the electronic structure properties and ultimately the device performances. Our previous research has applied NH_4OH wet chemical treatment and *in-situ* NH_3 plasma to remove carbon contamination, retain ~1ML oxygen coverage, and passivate N-vacancy related defects. In this study, to extend this work, it is proposed to employ an *in-situ* electron cyclotron resonance (ECR) H_2/N_2 plasma process. The remote plasma chamber used in the previous study is equipped with a quartz tube, and the o-ring connection between the quartz tube and the chamber is a potential source of background oxygen. Therefore, the ECR system with a higher pumping rate and only metal seals may have a lower oxygen background. In addition, the ECR may have higher density of reactive plasma species. These two advantages may enable further reduction of surface impurities for GaN.

Preliminary experiments have been completed and Fig. 7.1 shows XPS Ga 3d, N 1s, C 1s, and O 1s core levels of n-type, Ga-face GaN after wet chemical NH_4OH

treatment and *in-situ* ECR N_2/H_2 plasma treatment at ~680 ℃. The ECR plasma is operated at 300W for 15min with ~36sccm N_2 and 9sccm H_2 mixed gas flow. After cleaning, the carbon contamination was reduced below the XPS detection limit. In addition, the oxygen concentration was ~ 1.1%, which is close to the XPS detection limit. Fig. 7.2 shows the UPS result after cleaning. The binding energy difference between the Ga 3d and VBM is ~ 17.8 eV, and the value of $(E_F\text{-}E_V)_{GaN}$ is 2.5 eV, which indicates 0.8 eV upward band bending. This value is consisted with the NH_3 plasma cleaned GaN reported in chapter 6. The electron affinity of GaN after ECR plasma cleaning is ~2.9 eV.

Further study will focus on the ECR plasma surface pretreatment processes to achieve atomically clean and stoichiometric surfaces of both Ga- and N-face GaN. In addition, the effect of cleaning process on surface states, charge compensation (e.g., oxygen free surface compared with surface with more than 1ML oxygen coverage), and band offsets between dielectrics on GaN (e.g., Ga-Al bonding compared with Ga-O-Al bonding) will be investigated.

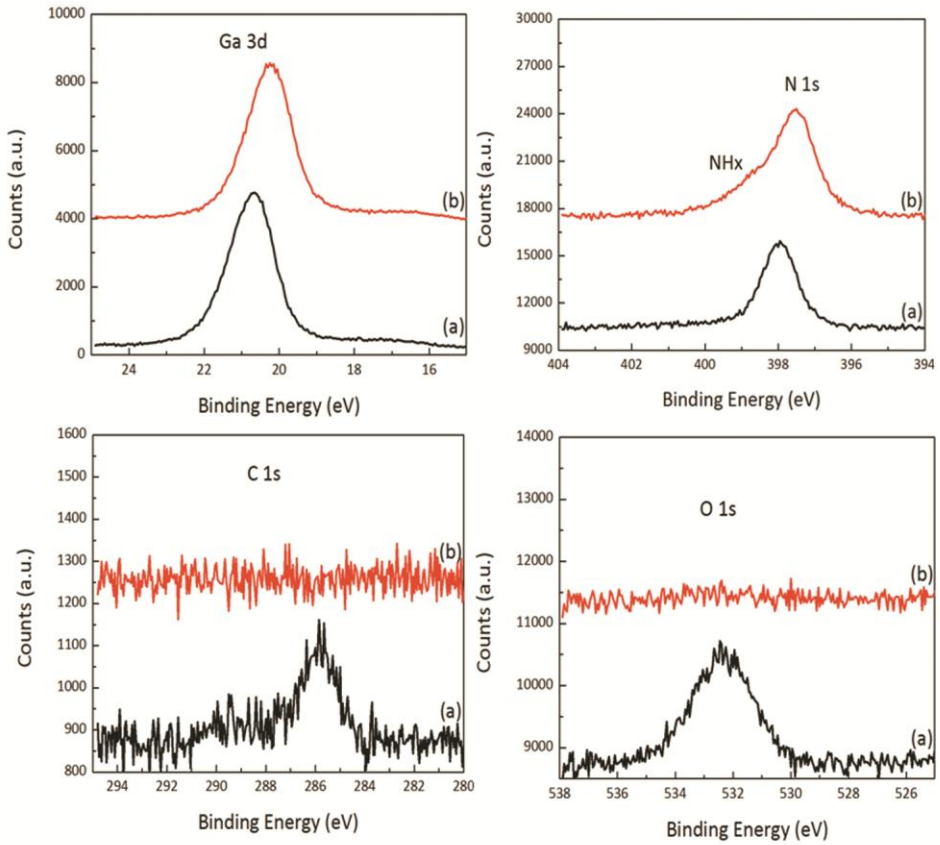

Figure 7.1. The XPS Ga 3d, N 1s, C 1s, and O 1s peaks for n-type, Ga-face GaN after (a) wet chemical clean with NH_4OH and (b) *in-situ* ECR H_2/N_2 plasma treatment.

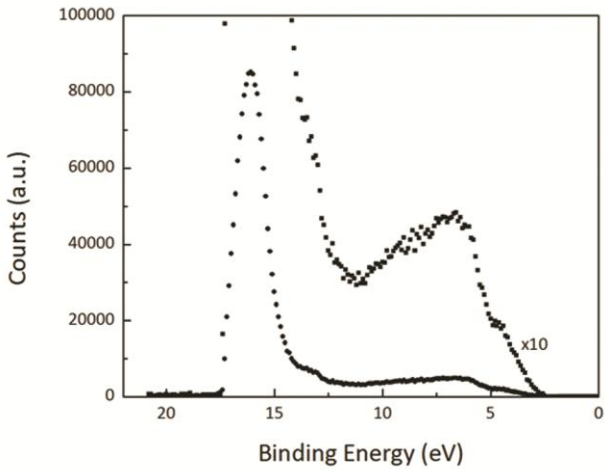

Figure 7.2. The UPS result of n-type, Ga-face GaN after cleaning.

7.2.2 PEALD dielectrics

La_2O_3 remains one of the most promising dielectrics on GaN due to its high dielectric constant and thermal stability [3,4]. However, the relative smaller band gap and unstable chemical properties of La_2O_3 may degrade device performance. In chapter 5, alloying with a wider band gap dielectric or using a chemical stable dielectric as a capping layer are proposed to mitigate this problem. Therefore, a more promising dielectric could be obtained through alloying La_2O_3 and Al_2O_3. The amorphous $La_xAl_{1-x}O_3$ may have improved chemical stability and a greater band gap compared with La_2O_3. According to a calculation by Robertson *et al.* [5], the valence and conduction band offset of $LaAlO_3$ on GaN are 1.3 and 1.1 eV, respectively, which may be sufficient to suppress leakage current. The first part of this proposed project is to use the PEALD method to deposit $La_xAl_{1-x}O_3$ and investigate the surface reaction mechanism. An initial study indicates reduced impurities in $La_xAl_{1-x}O_3$ compared with La_2O_3. Fig. 7.3 shows the XPS spectra for $La_xAl_{1-x}O_3$ on GaN before and after 1 hour 700 ℃ annealing. The atomic ratio of La to Al measured by XPS is 0.87 and 0.90 before and after annealing respectively. This suggests the composition of the alloyed films is $La_{0.47}Al_{0.53}O_3$. For the as-grown film, the carbon concentration is reduced compared with La_2O_3 films on GaN as mentioned in Chapter 5. For $La_{0.47}Al_{0.53}O_3$/GaN, after vacuum annealing, all the core levels shift to higher binding energy. However, for La_2O_3/GaN, the Ga peak shifted to higher binding energy, while the La peak shifted to lower binding energy after annealing. This was explained by the removal of the impurities in La_2O_3 (e.g., La-$(OH)_x$ and/or La-CO_x) through annealing. Therefore, the same shift direction of core levels in $La_{0.47}Al_{0.53}O_3$/GaN suggests the $La_{0.47}Al_{0.53}O_3$ may have much fewer impurities

compared with La_2O_3. Furthermore, the effect of different compositions of La and Al on chemical stability and energy band gap should be measured. The interface chemical and electronic properties of $La_xAl_{1-x}O_3$/GaN should be investigated, with a specific focus on the effect of different deposition sequence on interface bonding states, namely La_2O_3 (e.g., Ga-La-O bonding) or Al_2O_3 (e.g., Ga-Al-O bonding). The second approach is to use Al_2O_3 as a capping layer on top of La_2O_3/GaN to improve the thermal stability and suppress the leakage current. The chemical and electronic properties of the stacked structure Al_2O_3/La_2O_3/GaN should be studied.

Ga_2O_3, as the predominant native oxide on GaN, is also a potential dielectric on GaN [6] that enables enhanced chemical stability. In this study, the Ga_2O_3 films will be deposited by PEALD method using the precursor gallium(III) acetylacetonate (Ga(caca)3). The Ga_2O_3 will be deposited on both Ga- and N-face GaN to investigate carrier confinement properties and the polarization charge compensation mechanism. Considering the smaller band gap of Ga_2O_3, the theoretical valence and conduction band offsets of Ga_2O_3/GaN are only ~0.7 and 0.5 eV, respectively [5]. Therefore, to create a sufficient potential barrier on GaN, it may be necessary to investigate using Al_2O_3 or SiO_2 as capping layers on Ga_2O_3/GaN. The interface electronic structure and interface charge distribution of Al_2O_3/Ga_2O_3/GaN and SiO_2/Ga_2O_3/GaN will then be discussed.

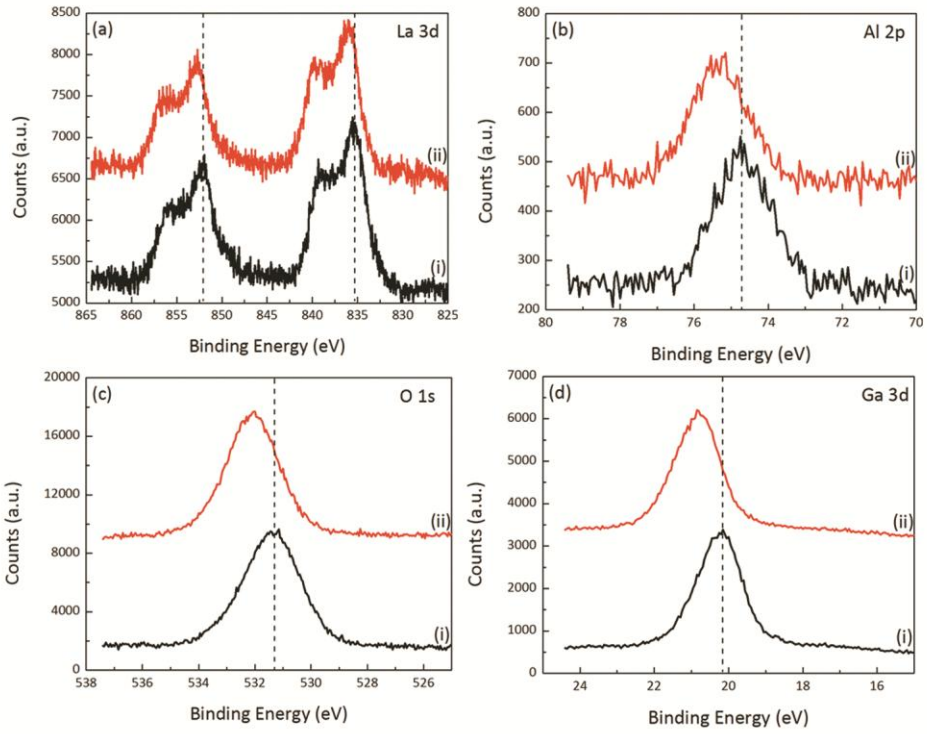

Figure 7.3. The XPS (a) La 3d, (b) Al 2p, (c) O 1s, and (d) Ga 3d peak of $La_xAl_{1-x}O_3$ on GaN before (i) and after (ii) 1 hour 700 ℃ annealing. The initial position of the core levels after $La_xAl_{1-x}O_3$ growth is indicated as dash line.

7.2.3 Surface band bending on p-type GaN

To further investigate the polarization charge compensation mechanism, p-type GaN (Mg doped, carrier concentration ~$2x10^{18}cm^{-3}$) should be investigated. This study would contain two parts: one is the surface band bending and surface photovoltage of n- and p-type GaN, and the second is the interface electronic structure of PEALD dielectrics/p-type GaN.

When using photoemission spectroscopy, the measured binding energy may be affected due to a surface photovoltage, which is related to an illumination-induced

change in the surface potential [7]. The photovoltage effect is usually described as photo-excited holes and electrons that become separated by an electric field in space charge region. This effect leads to partial screening of the electric field and reduced surface band bending [8]. The surface photovoltage effect could be reduced by using a lower intensity photon source to degrease the electron-hole generation rate or increasing the substrate temperature to increase the electron-hole recombination rate [7]. Fig. 7.4 and Fig. 7.5 shows the XPS Ga 3d, N 1s, O 1s, and C 1s peaks and UPS low binding energy cut off of n- and p-type Ga-face GaN after the same cleaning method, respectively, which consisted of wet chemical clean with NH_4OH and *in-situ* 700 ℃ 10min N_2 annealing.

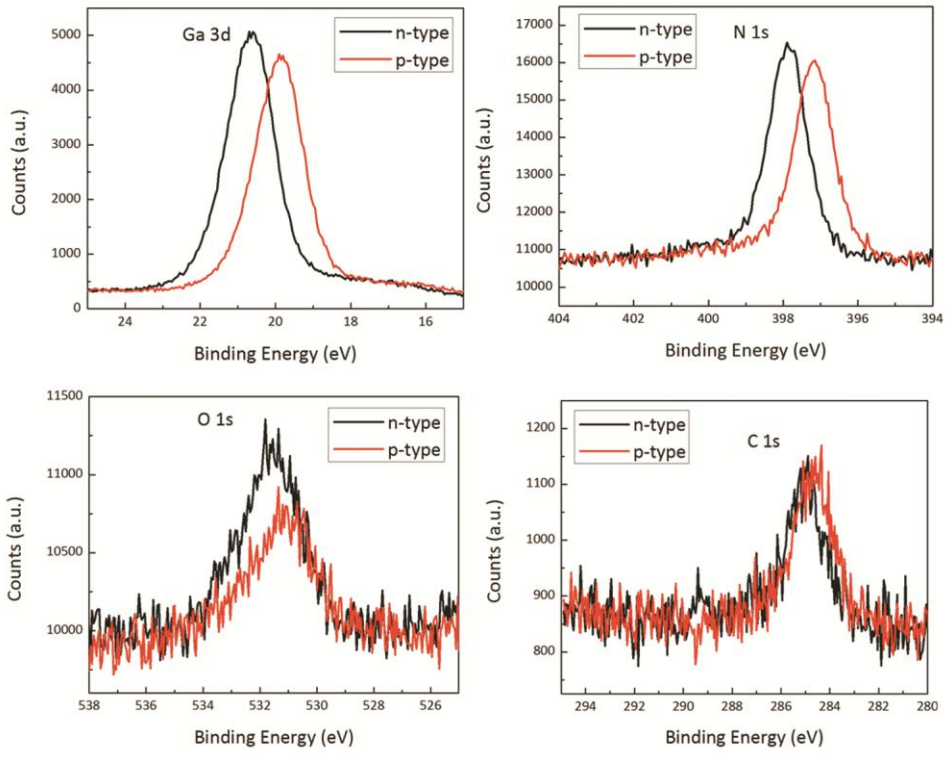

Figure 7.4. The XPS Ga 3d, N 1s, O 1s, and C 1s peaks for n-type and p-type GaN after cleaning.

For both n- and p-type GaN, the binding energy difference between Ga 3d and VBM is ~ 17.8 eV. The n- and p-type GaN also exhibits similar atomic concentrations as shown in Fig. 7.6. For n-type, Ga-face GaN, the value of ($E_F - E_V$) changes from ~2.8 eV at room temperature to 2.5-2.6 eV at 250 ℃, which indicates the surface band bending increases from 0.5 to 0.7-0.8 eV. On the other hand, for p-type, Ga-face GaN, the value of ($E_F - E_V$) increases from 2.0 eV at room temperature to 2.5-2.6 eV at 250 ℃. Considering the value of ($E_F - E_V$) is 0.3 eV in the bulk of p-type GaN [9], the p-type GaN surface exhibits a large downwards band bending, which increases from 1.7 eV at room temperature to 2.2-2.3 eV at 250 ℃. This suggests that the surface photovoltage has a more significant effect on p-type GaN. Furthermore, for both the n- and p-type, Ga-face GaN, the valence band maximum is ~2.5-2.6 eV relative to the Fermi level, indicating a similar surface Fermi level on the different surfaces. This result is consistent with a previous investigation by Long *et al.* as shown in Fig 7.7 [8]. Further research would be focused on the origin of the pinning states and how these states affect the compensation of the polarization bound charge. The effect of surface pretreatment on these pinning states will also be investigated.

In addition, the interface chemistry and electronic structure of PEALD dielectrics (Al_2O_3, HfO_2, and SiO_2)/p-type GaN should be investigated and the effect of different doping types and polarization charge compensations on interface bonding should be discussed.

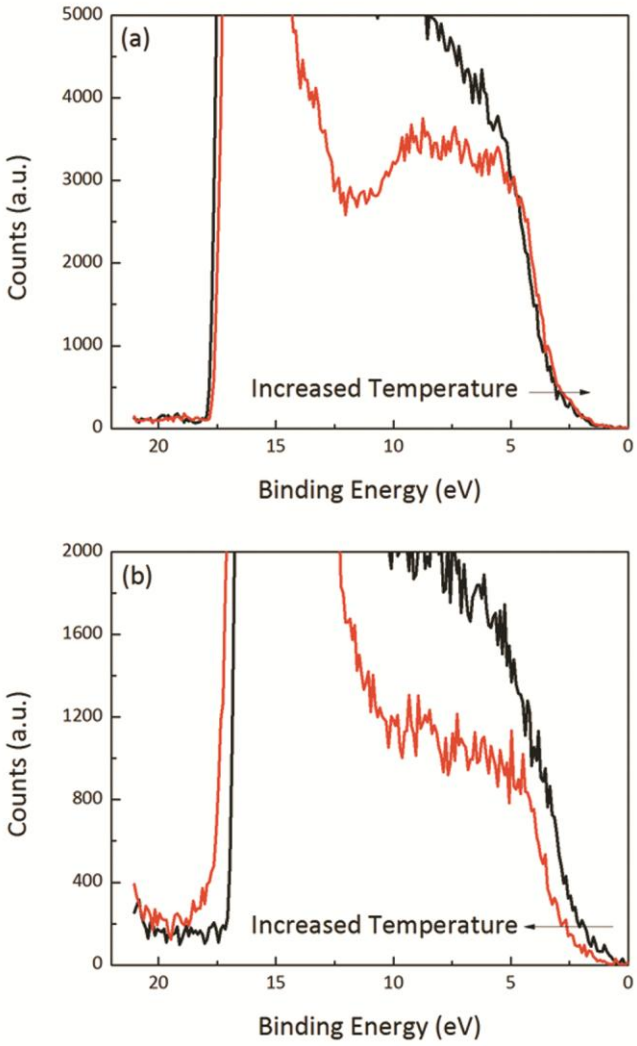

Figure 7.5. The UPS spectra of (a) n-type and (b) p-type GaN at room temperature (black) and 250 ℃ (red).

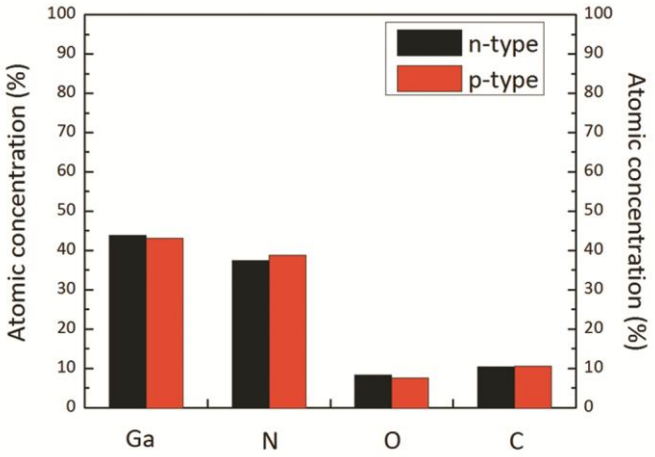

Figure 7.6. The surface atomic concentration of n- and p-type GaN after surface pretreatment.

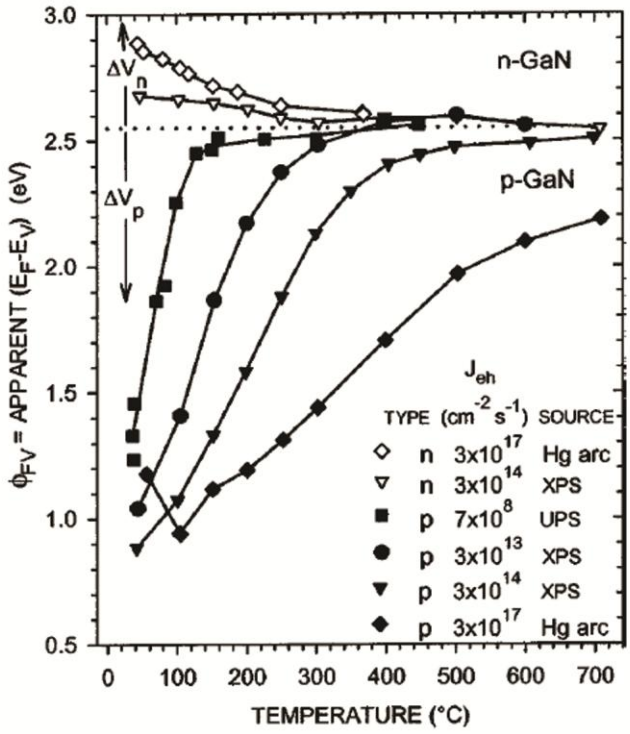

Figure 7.7. The value of ($E_F - E_V$) vs temperatures for n-type (open symbols) and p-type (solid symbols) GaN. The inserted J_{eh} represents the generation rate of electron-hole pairs, and the different photon sources are indicated [8]. J. P. Long *et. al., Phys. Rev. B* **66**, 121308 (2002) "Copyright (2002) by the American Physical Society".

The following discussion shows the preliminary results of Al_2O_3 on p-type GaN. Fig. 7.8 shows the XPS Al 2p and Ga 3d spectra of as-grown and annealed Al_2O_3 films (~2nm) on n-type and p-type, Ga-face GaN. The plasma induced defects in both Al_2O_3/n-type and p-type GaN could be removed by an N_2 annealing process. The binding energy difference between Ga 3d and Al 2p for Al_2O_3/p-type GaN was ~ 0.3 eV higher than that in Al_2O_3/n-type GaN. Considering constant values of $(E_{Ga3d}\text{-}E_V)_{GaN}$ (=~17.8 eV) and $(E_{Al2p}\text{-}E_V)_{Al2O3}$ (=~70.6 eV), the valence band offsets for Al_2O_3 on n- and p-type GaN

were ~1.9 eV and 2.2 eV, respectively, which is shown in Fig. 7.9. The corresponding respective conduction band offsets were ~1.4 eV and 1.1 eV. Further investigation will focus on careful measurement of the band offsets of Al_2O_3 on n- and p- type GaN. The photovoltage effects on n- and p-type GaN before and after Al_2O_3 growth will also be addressed.

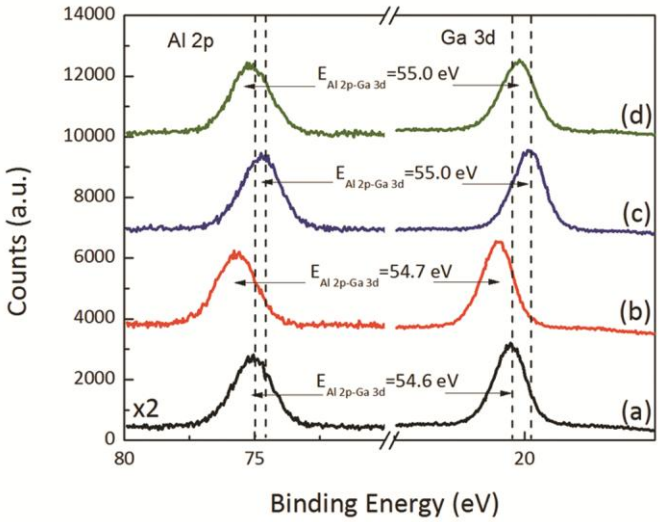

Figure 7.8. The XPS Al 2p and Ga 3d spectra for (a) as-deposited and (b) N_2 annealed ~2nm Al_2O_3 on n-type GaN; and (c) as-deposited and (d) N_2 annealed ~2nm Al_2O_3 on p-type GaN. The initial positions of the core level peaks after Al_2O_3 growth are indicated with dashed lines. The intensity of Al 2p peak is enlarged by twice.

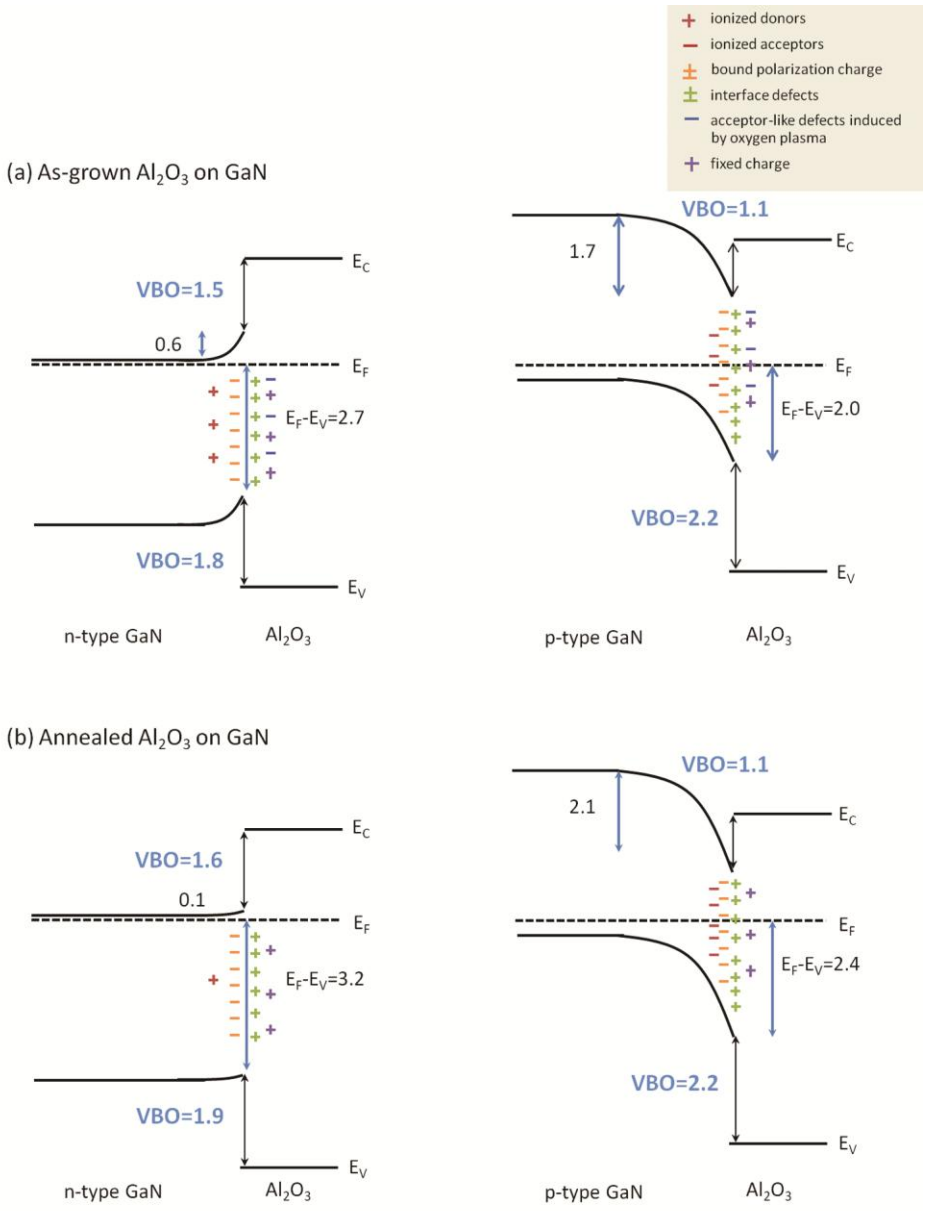

Figure 7.9. A schematic illustration of band alignment of (a) as-grown and (b) annealed Al_2O_3 on n- and p-type GaN.

Reference

[1] V.M. Bermudez, D.D. Koleske, A.E. Wickenden, *Appl. Sur. Sci.*, **126** 69 (1998)

[2] J. Neugebauer, C.G. Van de Walle, Festkörperprobleme **35** 25 (1996)

[3] B. S. Eller, J. Yang, and R. J. Nemanich, *J. Vac. Sci. Technol. A* **31** 050807 (2013)

[4] H. Chiu, C. Lin, C. Chen, C. Yang, C. Lin, J. S. Fu, L. Chang, R. Lin, and K. Hsueh, *J. The Electrochem. Soc.*, **157** H160 (2010)

[5] J. Robertson and B. Falabretti, *J. Appl. Phys.* **100**, 014111 (2006).

[6] B. S. Eller, J. Yang, and R. J. Nemanich, *J. Vac. Sci. Technol. A* **31** 050807 (2013)

[7] L. Kronik, and Y. Shapira, *Surf. Sci. Rep*. **37**, 1 (1999)

[8] J. P. Long and V. M. Bermudez, *Phys. Rev. B* **66**, 121308 (2002)

[9] S. Strite and H. Morkoç, *J. Vac. Sci. Technol. B* **10**, 1237 (1992).

REFERENCES

A. I. Abdulagatov, et. al., *Appl. Mater. Interfaces*, **3**, 4593 (2011).

M. Abraham, et. al., *Appl. Phys. Lett.* **101**, 243504 (2012).

O. Ambacher et. al., *J. Appl. Phys.* **85**, 3222 (1999).

K.-S. An, et. al., *Bull. Korean Chem. Soc.* **24**, 1659 (2003).

R. L. Anderson, *Solid-State Electron*. **5**, 341 (1962).

K. Balachander, et. al., *Phys. Status Solidi A* **202**, R16 (2005).

J. Bardeen, *Phys. Rev*. **71**, 717 (1947).

J. A. Bardwell, et. al., *Electrochem. Solid-State Lett.* 10, H46 (2007).

F. G. Bell, et. al., *Phys. Rev. B* **37**, 8383 (1988).

V.M. Bermudez, et. al., *Phys. Rev. B* **48**, 2436 (1993).

V. M. Bermudez, *J. Appl. Phys.* **80**, 1190 (1996).

V.M. Bermudez, et. al., *J. Appl. Phys.* **79**, 110 (1996).

V.M. Bermudez, et. al., *Appl. Sur. Sci.*, **126** 69 (1998).

F. Bernardini, et. al., *Phys. Rev. B*. **56** R10 024 (1997).

E. Bersch, et. al., *Phys. Rev. B* **78**, 085114 (2008).

O. Blank, et. al., *J. Appl. Phys.* **97**, 044107 (2005).

M. Brause, et. al., *Surf Sci.* **383**, 216 (1997).

O. Bierwagen, et. al., *Appl. Phys. Lett.* **98**, 172101 (2011).

D. Briggs, et. al., Practical Surface Analysis, Vol. 1 Auger and X-ray Photoelectron Spectroscopy, 2nd edition (John Wiley & Sons, West Sussex, 1990).

A. D. Bykhovski, et. al., *J. Appl. Phys.* **81**, 6332 (1997).

P. F. Carcia, et. al., *Appl. Phys. Lett*. **89**, 031915 (2006).

J. C. Carrano, et. al., *Appl. Phys. Lett.* **72**, 542 (1998).

Y.C. Chang, et. al., *Appl. Phys. Lett.* **90**, 232904 (2007).

Y. C. Chang, et. al., *Appl. Phys. Lett.* **93**, 053504 (2008).

Y. C. Chang, et. al., *Microelectron Eng.* **87**, 2042 (2010).

Y. Chiou et. al., *IEEE T Electron Dev.* **58**, 3869 (2011).

H. Chiu, et. al. *J. The Electrochem. Soc.*, **157** H160 (2010)

W. Cho, et. al., *J. Vac. Sci. Technol. A* **21**, 1366 (2003).

M. Choi, et. al., *Appl. Phys. Lett.* **102**, 142902 (2013).

T. E. Cook, et. al., *J. Appl. Phys*. **93**, 3995 (2003).

T. E. Cook, et. al., *J. Appl. Phys.* **94**, 7155 (2003).

I. Costina, et. al., *Appl. Phys. Lett*. **78**, 4139 (2001).

S. Y. Davydov, *Phys. Solid State*, **51** 1231 (2009).

M. Diale, et. al., *Appl. Surf. Sci.* 246, 279 (2005).

R. Dimitrov, et. al., *J. Appl. Phys.* **87**, 3375 (2000).

N. V. Edwards**,** et. al., *Appl. Phys. Lett.* **69**, 2065 (1996).

B. S. Eller, et. al., *J. Vac. Sci. Technol. A* **31** 050807 (2013).

J. Elsner, et. al., *Solid State Commun.*, **106** 739 (1998).

J. Elsner, et. al., *Solid State Commun.* **108** 953 (1998).

M. M. Frank, et. al., *Appl. Phys. Lett.* **86**, 152904 (2005).

R. H. French, *J. Am. Ceram. Soc*. **73**, 477 (1990).

D J. Fu, et. al., *Appl. Phys. Lett.* **80**, 446 (2002).

C. C. Fulton, et. al., *J. Appl. Phys*. **96**, 2665 (2004).

S. P. Grabowski, et. al., *Appl. Phys. Lett.* **78**, 2503 (2001).

S. Gredelj, et. al., *Appl. Surf. Sci*. **174**, 240 (2001).

M. D. Groner, et. al., *Thin Solid Films* **413**, 186 (2002).

M. D. Groner, et. al., *Chem. Mater*. **16**, 639 (2004).

M. D. Groner, et. al., *Appl. Phys. Lett.* **88**, 051907 (2006).

J.-B. Ha, et. al., *Jpn. J. Appl Phys.* **49**, 126501 (2010).

H. Hasegawa, et. al., *J. Vac. Sci. Technol. B* **21**, 1844 (2003).

T. Hashizume, et. al., *J. Appl. Phys*. **88**, 1983 (2000).

T. Hashizume, et. al., *Appl. Phys. Lett*. **76**, 2880 (2000).

T. Hashizume, et. al., *Mater. Sci. Eng. B* **80**, 309 (2001).

T. Hashizume, et. al., *Appl. Phys. Lett.* **83**, 2952 (2003).

T. Hashizume, et. al., *J. Vac. Sci. Technol. B* **21**, 1828 (2003).

T. Hashizume, et. al., *Appl. Phys. Lett.* **84**, 4884 (2004).

A. N. Hattori, et. al., *Surf. Sci.* **604**, 1247 (2010).

J. Hedman, et. al., *Phys. Scr.* **22**, 176 (1980).

S. B. S. Heil, et. al., *Appl. Phys. Lett.* **89**, 131505 (2006).

V. Heine, *Phys. Rev.* **138**, A1689 (1965).

A. Hierro, et. al., *Appl. Phys. Lett.* **77**, 1499 (2000).

M. Hong, et. al., *J. Vac. Sci. Technol. B* **18**, 1453 (2000).

S. Hoshi, et. al., *IEICE Trans Electron.* **E89C**, 1052 (2006).

C. Hu, et. al., *IEEE T Electron Dev.* **59,** 121 (2012).

X. Hu, et. al., *Appl. Phys. Lett*. **79**, 2832 (2001).

M. L. Huang, et. al., *Appl. Phys. Lett*. **87**, 252104 (2005).

T. Inagaki, et. al., *Appl. Surf. Sci.* **216**, 519 (2003).

H. W. Jang, et. al., *Appl. Phys. Lett*. **78**, 2015 (2001).

H. W. Jang, et. al., *Appl. Phys. Lett.* **80**, 3955 (2002).

A. Jimenez-Gonzalez, et. al., *Surf. Sci.*, **250,** 59 (1991).

J. S. Jur, et. al., *Appl. Phys. Lett*. 98, 042902 (2011).

T. O. Kääriäinen, et. al., *Plasma Process. Polym.* **6**, S237 (2009).

C. J. Kao et. al., *J. Appl. Phys*. **98**, 064506 (2005).

U. Karrer, et. al., *Appl. Phys. Lett.* **77**, 2012 (2000).

S. W. King, et. al., *J. Appl. Phys.* **84**, 5248 (1998).

H. Kim, et. al., *IEEE Electron Device Lett.* **24**, 421 (2003).

J. Kim, et. al., *Jpn. J. Appl .Phys.* **49** 04DF05 (2010).

J. J. Kim, et. al., *Jpn. J. Appl. Phys.* **50**, 096501 (2011).

K.-W. Kim, et. al., *Microelectron. Eng.* **88**, 1225 (2011).

C. J. Kirkpatrick, et. al., *IEEE Electr Device L* **33**, 1240 (2012).

P. B. Klein, et. al., *Appl. Phys. Lett.* **79**, 3527 (2001).

J. Koo, et. al., *J. Korean Phys. Soc.* **48**, 131 (2006).

E. A. Kraut, et. al., *Heterojunction Band Discontinuities: Physics and Device Applications*, edited by F. Capasso and G. Margaritondo (Elsevier, New York, 1987).

L. Kronik, et. al., *Surf. Sci. Rep*. **37**, 1 (1999)

E. Langereis, et. al., *Appl. Phys. Lett.* **89**, 081915 (2006).

E. Langereis, et. al., *Appl. Phys. Lett*. **92**, 231904 (2008).

V. Lebedev, et. al., *J. Appl. Phys.***101**, 033705 (2007).

B. Lee, et. al., *Appl. Phys. Lett.* **92**, 203102 (2008).

J. G. Lee, et. al., *Thin Solid Films* **534**, 515 (2013).

K.N. Lee, et. al., *J. Electrochem. Soc.* **147**, 3087 (2000).

S. Y. Lee, et. al., *Appl. Surf. Sci.* **222**, 234 (2004).

C. Liu, et. al., *Appl. Phys. Lett.* **88**, 173504 (2006).

Z. H. Liu, et. al., *Appl. Phys. Lett.* **98**, 163501 (2011).

J. W. Lim, et. al, *Electrochem. Solid-State Lett.* **7**, F45 (2004).

S. J. Lim, et. al., *Appl. Phys. Lett*. **91**, 183517 (2007).

J. P. Long, et. al., *Phys. Rev. B* **66**, 121308 (2002).

R. D. Long, et. al., *Materials* **5**, 1297 (2012).

B. Luo et. al., *Appl. Phys. Lett.* **80**, 1661 (2002).

P. Lorenz, et. al., *Phys. Status Solidi B* **247**, 1658 (2010).

A. J. M. Mackus, et. al., *Chem. Mater.* **24**, 1752 (2012).

R. Mehandru, et. al., *Appl. Phys. Lett.* **82**, 2530 (2003).

T. Maruyama et. al., *Appl. Phys. Lett*. **60**, 322 (1992).

R. Matero, et. al., *J. Phys. IV* **9**, 493 (1999).

Y. Matsuura, et. al., *J. Opt. Soc. Am. A* **14**, 1255 (1997).

W. J. Mecouch, et. al., *J. Vac. Sci. Technol. A* **23**, 72 (2005).

E. J. Miller et. al., *Appl. Phys. Lett.* **84**, 535 (2004).

U. K. Mishra, et. al., *Proc. IEEE* **90**, 1022 (2002).

S. Miyazaki, *J. Vac. Sci. Technol. B* **19**, 2212 (2001).

W. Mönch, *Phy. Rev. Lett.* **58**, 1260 (1987).

W. Mönch, *J. Vac. Sci. Technol. B* **6**, 1270 (1988).

W. Mönch, *J. Appl. Phys.* **109**, 113724 (2011).

N. F. Mott, *Math. Proc. Cambridge* **34**, 568 (1938).

S. Nakamura, et. al., *Jpn. J. Appl. Phys.* **31**, 1258 (1992).

R. Nakasaki, et. al., *Physica E (Amsterdam)* **7**, 953 (2000).

J. Neugebauer, et. al., Festkörperprobleme **35** 25 (1996).

N. V. Nguyen, et. al., *J. Vac. Sci. Technol. A* **23**, 1706 (2005).

N. V. Nguyen, et. al., *Appl. Phys. Lett.* **93**, 082105 (2008).

Y. Niiyama, et. al., *Semicond. Sci. Technol.* **25** 125006 (2010).

H. Nohira, et. al, *J. Non-Cryst. Solids* **303**, 83 (2002).

M. Ochiai, et. al., *Jpn. J. Appl. Phys.* **42**, 2278 (2003).

S. Oyama, et. al., *Appl. Surf. Sci.* **190**, 322 (2002).

K.-Y. Park, et. al., *J. Korean Phys. Soc.* **45**, S898 (2004).

K.-Y. Park, et. al., *Jpn. J. Appl Phys.* **43**, L1433 (2004).

M.Z. Peng , et. al., *Microelectron Eng.* **87** 2638 (2010).

S. J. Pearton, et. al., *J. Appl. Phys*. **86**, 1 (1999).

V. M. Polyakov, et. al., *Semicond. Sci. Technol.* **13**, 1396 (1998).

F. A. Ponce, et. al., *Appl. Phys. Lett*. **69**, 337 (1996).

F. A. Ponce, et. al., *Nature* **386**, 351 (1997).

P. Poodt, et. al., *Adv. Mater*. **22** 3564 (2010).

S. E. Potts, et. al., *J. Electrochem. Soc.* **157**, 66 (2010).

S. E. Potts, et. al., *J. Vac. Sci. Technol. A* **30**, 021505 (2012).

S. E. Potts, et. al., *Chem. Vap. Deposition* **19** 125 (2013).

A.Y. Polyakov, et. al., *J. Electrochem. Soc.* **154**, H115 (2007).

C. Prasittichai, et. al., *J. Phys. Chem. Lett*. **1** 1611 (2010).

H. B. Profijt, et. al., *J. Vac. Sci. Technol. A* **29**, 050801 (2011).

R. L. Puurunen, *J. Appl. Phys.* **97**, 121301 (2005).

M. Ritala, et. al., *Chem. Mater*. **5**, 1174 (1993).

J. Robertson, *J. Vac. Sci. Technol. B* **18**, 1785 (2000).

J. Robertson et. al., *J. Appl. Phys.* **100**, 014111 (2006).

F. C. Sauls, et. al., *Chem. Mater.* **7**, 1361 (1995).

M. Sawada, et. al., *J. Cryst. Growth* **189/190**, 706 (1998).

W. Schottky, *Phys. Z* **41**, 570 (1940).

Ch. Schulz, et. al., *J. Vac. Sci. Technol. A* **29**, 011013 (2011).

C. F. Shih, et. al., *J. Alloys Compd.* **480**, 541 (2009).

A. R. Smith, et. al., *Appl. Phys. Lett.* **72**, 2114 (1998).

L.L. Smith, et. al., *J. Electron. Mater.* **25**, 805 (1996).

S. Strite, et. al., *J. Vac. Sci. Technol. B* 10, 1237 (1992).

M. Stutzmann, et. al., *Phys. Stat. Sol. (b)* **228** 505 (2001).

D. Li, M. Sumiya, et. al., *J. Appl. Phys.* **90** 4219 (2001).

A.R. Smith et. al., *Appl. Phys. Lett.*, **72** 2114 (1998).

S. Suzer, et. al., *J. Vac. Sci. Technol. A* **21**, 106 (2003).

F. Tang, et. al., *J. Vac. Sci. Technol.A* **30**, 01A147 (2012).

C. Tejedor, et. al., *J. Phys. C: Solid State Phys.* **11**, L19 (1978).

J. Tersoff, *Phys. Rev. B* **30**, 4874 (1984).

R. Thielsch, et. al., *Thin Solid Films* **410**, 86 (2002).

K. M. Tracy, et. al., *J. Appl. Phys.* **94**, 3163 (2003).

M. J. Uren, et. al., *IEEE Trans. Electron Devices* **59**, 3327 (2012).

C. G. Van de Walle, et. al., *Microelectron. Eng.* **109**, 211 (2013).

J. L. van Hemmen, et. al., *J. Electrochem. Soc.* **154**, G165 (2007).

R. Vetury, et. al., *IEEE Trans. Electron Devices* **48**, 560 (2001).

J. R. Waldrop, et. al., *Appl. Phys. Lett.* **68**, 2879 (1996).

X. Wang, et. al., *Appl. Phys. Lett.* **101**, 232109 (2012).

C. I. Wu, et. al., *J. Appl. Phys.* **83**, 4249 (1998).

Y.Q. Wu, et. al., *Appl. Phys. Lett.* **90**, 143504 (2007).

Y. Xiong, et. al., *Plasma Sci and Technol*, **15**, 52 (2013).

J. Yang et. al., *J. Appl. Phys.* **112**, 053710 (2012).

J. Yang, et. al, *J. Vac. Sci. Technol. A*. **32**, 021514 (2014).

P.D. Ye, et. al., *Appl. Phys. Lett.* **86**, 063501 (2005).

H. Y. Yu, et. al., *Appl. Phys. Lett.* **81**, 376 (2002).

H. Zhang, et. al., *J. Appl. Phys.* **99**, 023703 (2006).

H. Zhou, et. al., *Appl. Phys. Express*. **4** 104102 (2011).

C. Zhu, et. al., *J. Vac. Sci. Technol. B* **30**, 051807 (2012).

C. Zhu, et. al., *J. Vac. Sci. Technol. B* **32**, 011203 (2014).

D. Zhuang, et. al., *Mat. Sci. Eng. R* **48** 46 (2005).

A. Zoroddu, et. al., *Phys. Rev. B* **64**, 045208 (2001).

APPENDIX

COPYRIGHT STATEMENTS

This dissertation included two published journal articles: J. Yang *et. al.*, J. Vac. Sci. Technol. A **32**, 021514 (2014) as Chapter 4, and J. Yang *et. al.*, J. Appl. Phys. **112**, 053710 (2012) as part of Chapter 5. All co-authors have given their permissions to use these contents in this dissertation.

The following tables and figures are cited from separate journal articles, including table 2.1, 2.2, and 2.3, and figure 2.4, 2.5, 2.6, 2.10, 2.11, and 7.7. The copyright permissions are listed here.

Thesis / Dissertation Reuse

The IEEE does not require individuals working on a thesis to obtain a formal reuse license, however, you may print out this statement to be used as a permission grant:

Requirements to be followed when using any portion (e.g., figure, graph, table, or textual material) of an IEEE copyrighted paper in a thesis:

1) In the case of textual material (e.g., using short quotes or referring to the work within these papers) users must give full credit to the original source (author, paper, publication) followed by the IEEE copyright line © 2011 IEEE.
2) In the case of illustrations or tabular material, we require that the copyright line © [Year of original publication] IEEE appear prominently with each reprinted figure and/or table.
3) If a substantial portion of the original paper is to be used, and if you are not the senior author, also obtain the senior author's approval.

License Number	3363350693668
Order Date	Apr 06, 2014
Publisher	AIP Publishing LLC
Publication	Journal of Vacuum Science & Technology B
Article Title	Mechanisms of current collapse and gate leakage currents in AlGaN/GaN heterostructure field effect transistors
Author	Hideki Hasegawa,Takanori Inagaki,Shinya Ootomo, et al.
Online Publication Date	Aug 5, 2003
Volume number	21
Issue number	4
Type of Use	Thesis/Dissertation
Requestor type	Student
Format	Print and electronic
Portion	Figure/Table
Number of figures/tables	1
Title of your thesis / dissertation	Interface Electronic State Characterization of Plasma Enhanced Atomic Layer Deposited Dielectrics on GaN
Expected completion date	Apr 2014
Estimated size (number of pages)	255
Total	0.00 USD

License Number	3363351161345
Order Date	Apr 06, 2014
Publisher	AIP Publishing LLC
Publication	Journal of Vacuum Science & Technology A
Article Title	Electronic surface and dielectric interface states on GaN and AlGaN
Author	Brianna S. Eller,Jialing Yang,Robert J. Nemanich
Online Publication Date	Jun 7, 2013
Volume number	31
Issue number	5
Type of Use	Thesis/Dissertation
Requestor type	Author (original article)
Format	Print and electronic
Portion	Figure/Table
Number of figures/tables	1
Title of your thesis / dissertation	Interface Electronic State Characterization of Plasma Enhanced Atomic Layer Deposited Dielectrics on GaN
Expected completion date	Apr 2014
Estimated size (number of pages)	255
Total	0.00 USD

License Number	3363410689380
License date	Apr 06, 2014
Licensed content publisher	John Wiley and Sons
Licensed content publication	Journal of Chemical Technology & Biotechnology
Licensed content title	Practical surface analysis, 2nd edn., vol I, auger and X-ray photoelectron spectroscopy. Edited by D. Briggs & M. P. Seah, John Wiley, New York, 1990, 657 pp., price: £86.50. ISBN 0471 92081 9
Licensed copyright line	Copyright © 1992 Society of Chemical Industry
Licensed content author	A. Taylor
Licensed content date	Apr 24, 2007
Start page	215
End page	215
Type of use	Dissertation/Thesis
Requestor type	University/Academic
Format	Print and electronic
Portion	Figure/table
Number of figures/tables	1
Original Wiley figure/table number(s)	Figure
Will you be translating?	No
Title of your thesis / dissertation	Interface Electronic State Characterization of Plasma Enhanced Atomic Layer Deposited Dielectrics on GaN
Expected completion date	Apr 2014
Expected size (number of pages)	255
Total	0.00 USD

License Number	3363360434038
Order Date	Apr 06, 2014
Publisher	AIP Publishing LLC
Publication	Journal of Applied Physics
Article Title	Band offsets of high K gate oxides on III-V semiconductors
Author	J. Robertson,B. Falabretti
Online Publication Date	Jul 13, 2006
Volume number	100
Issue number	1
Type of Use	Thesis/Dissertation
Requestor type	Student
Format	Print and electronic
Portion	Figure/Table
Number of figures/tables	3
Title of your thesis / dissertation	Interface Electronic State Characterization of Plasma Enhanced Atomic Layer Deposited Dielectrics on GaN
Expected completion date	Apr 2014
Estimated size (number of pages)	255
Total	0.00 USD

BIOGRAPHICAL SKETCH

Jialing Yang, son of Baoqin Huang and Chuanhai Yang, was born in Huainan, Anhui, China, March 03, 1987, a city known by the coal resources and Tofu. Jialing lived in Huainan for 18 years before he graduated from No.1 Middle School of Huainan in 2005. While in high school, his interest in physics was fostered and he was blessed with her future wife, Jie Chen. Jialing then enrolled in physics department at the University of Science and Technology of China at Hefei. After he completed the Bachelor's degree, he entered the graduate program in physics department at Arizona State University in 2009, and started his research under Professor Robert Nemanich's mentoring. Jialing's research interest focuses on the interface properties and plasma enhanced atomic layer deposited dielectrics on GaN and Si. The work here represents the partial completion of the Doctor of Philosophy degree.